Report Title:	Computational Design and Discovery of Ni-Based Alloys and Coatings: Thermodynamic Approaches Validated by Experiments
Type of Report:	Final Scientific/Technical Report
Reporting Period Start Date:	01/01/2015
Reporting Period End Date:	12/31/2017
Principal Author(s):	Zi-Kui Liu (Distinguished Professor, PI @ Penn State) Brian Gleeson (Professor, Co-PI @ U Pitt) Shunli Shang (Research Professor @ Penn State) Thomas Gheno (Postdoc @ U Pitt) Greta Lindwall (Postdoc @ Penn State) Bi-Cheng Zhou (Postdoc @ Penn State) Xuan Liu (PhD student @ Penn State) Austin Ross (PhD student @ Penn State)
Date Report was Issued:	April 2018
DOE Award Number:	DE-FE0024056
Name and Address of Submitting Organization:	Pennsylvania State University, University Park, PA 16802 University of Pittsburgh, 4200 Fifth Ave, Pittsburgh, PA 15260

DISTRIBUTION LIMITATION NOTICES

No distribution limitation, all contents in this report are open to the public.

ABSTRACT

This project developed computational tools that can complement and support experimental efforts in order to enable discovery and more efficient development of Ni-base structural materials and coatings. The project goal was reached through an integrated computation-predictive and experimental-validation approach, including first-principles calculations, thermodynamic CALPHAD (CALculation of PHAse Diagram), and experimental investigations on compositions relevant to Ni-base superalloys and coatings in terms of oxide layer growth and microstructure stabilities.

The developed description included composition ranges typical for coating alloys and, hence, allow for prediction of thermodynamic properties for these material systems. The calculation of phase compositions, phase fraction, and phase stabilities, which are directly related to properties such as ductility and strength, was a valuable contribution, along with the collection of computational tools that are required to meet the increasing demands for strong, ductile and environmentally-protective coatings.

Specifically, a suitable thermodynamic description for the Ni-Al-Cr-Co-Si-Hf-Y system was developed for bulk alloy and coating compositions. Experiments were performed to validate and refine the thermodynamics from the CALPHAD modeling approach. Additionally, alloys produced using predictions from the current computational models were studied in terms of their oxidation performance. Finally, results obtained from experiments aided in the development of a thermodynamic modeling automation tool called ESPEI/*pycalphad* – for more rapid discovery and development of new materials.

Table of Contents

1. EXECUTIVE SUMMARY

This collaborative project between the Pennsylvania State University and the University of Pittsburgh aimed to develop a thermodynamic foundation for the accelerated design of Ni-base alloys and coatings. Central to this foundation was the novel combination of atomic-scale first-principles calculations with continuum-scale thermodynamic modeling to arrive at consistent descriptions of the key phases in the Ni-base system in terms of the composition- and temperature-dependent Gibbs energy functions for a CALPHAD (CALculations of Phase DIAgrams) database. Such a database enables prediction of tunable properties, including phase compositions and fractions, solubility limits and driving forces, all of which are very important in the efficient design high-temperature alloys coatings and coating/alloy combinations having long-term resistance to harsh service environments.

This project included composition ranges that correspond to the typical MCrAl based (where M is Ni, Co or Ni+Co) coating compositions, relevant to not only alloys based on γ-Ni and γ-Ni+γ'-Ni_3Al structures, but also to coatings based on γ-Ni and γ-Ni+β-NiAl structures. Thermodynamic database for the Ni-Al-Co-Cr-Hf-Y-O system was created in terms of the CALPHAD modeling approach with input from first-principles calculations and experimental data available in the literature.

In addition to the generated thermodynamic database, this project have **four** major achievaments as shown in the following parts.

First. A method based on thermodynamic modeling was developed to determine optimal amounts of reactive elements such as Hf and Y additions to Al_2O_3-forming γ-γ' NiCrAl alloys.

Additions of this sort can play a profound role in beneficially affecting the protectiveness of oxide layers that form on alloys during high-temperature exposure to oxidizing environments; however, adding too much can be detrimental to protectiveness. Computation-based guidance on optimizing the levels of Y and/or Hf additions in multi-component Ni-based alloys was a much needed and significant outcome of this study. For example, the alloy ability to maintain Hf in solution was set by the Hf concentration required to form HfO_2 at the oxygen activity defined by the alloy/Al_2O_3 equilibrium. It was found that Hf tolerance decreases with increasing temperature and increases with increasing γ′ fraction. The latter is due to the higher solubility of Hf in γ', compared to γ. The validity of the procedure was evaluated by oxidizing a series of NiCrAl-Hf alloys in dry air at 1000-1200°C. The experimental results followed the predicted trends, although the Hf tolerance tended to be overestimated. The applicability of the criterion, and potential routes for improved predictability, were pointed out by considering the influence of the compositional changes occurring at the metal surface during the transient and steady-state stages of the oxidation process.

Second. The present work searched for other beneficial elements to add to the system to increase the Hf-tolerance through an extensive computational and thermodynamic search.

Given the importance of the γ' phase, an initial selection process was established by searching for elements a large solubility in the γ' phase. These elements have the most prominent interactions with Hf for alloys with appreciable equilibrium fractions of γ'. Once these elements are selected, a computational search can be performed to calculate the mixing enthalpies of these phases in the γ phase and the formation enthalpies of the $L1_2$-Hf_3X and $L1_2$-HfX_3 in the Hf-X system. This not only provided valuable thermodynamic information for each Hf-X system but also highlighted which element have the strongest effect on the activity of Hf, since the mixing enthalpy plays a significant role in the partial molar quantities, and hence on the activity. In all, this amounted to a study of the Hf interactions with the elements Al, Co, Cr, Cu, Fe, Ga, Ge, Hf, Mn, Nb, Ni, Pd, Pt, Sc, Si, Ta, Ti, V, and Zn. Of these elements Pt, Pd, Rh and Si were found to have the strongest interaction with Hf.

Third. Origin of slow-growing alumina scale mediated by reactive elements.

We proposed that the interatomic bonding strength (energy) can be quantified by stretching force constants (SFC) after first-principles phonon calculations. A large and positive force constant suggests strong interaction (bonding), while a negative force constant indicates that the atomic pairs tend to separate from each other. We proposed that the diffusion activation energy Q of oxygen, used to break the M-O bonds, can be characterized by the largest SFC, f_{s0} and the associated bond length r_0, i.e.,

$Q \propto f_{s0} r_0^2$. We showed that the origin of slow-growing alumina scale affected by reactive elements (REs) stems from the strong RE-O bonding energy via the present SFC model applied to oxides (Al_2O_3, Cr_2O_3, Ti_2O_3, ZrO_2, HfO_2, Y_2O_3, and La_2O_3), Al_3M, and $Al_{47}MO_{72}$ (M = Cr, Ti, Zr, Hf, Y, and La). It showed that Hf-O has the highest bonding energy, making Hf the best reactive element in retarding the growth of Al_2O_3 scale. The other beneficial REs for the slow-growing Al_2O_3 scale are Zr and Y.

Fourth. Development of high throughput (H-T) CALPHAD modeling based on ESPEI/pycalphad.

Efficient CALPHAD modeling calls for H-T approaches due to the compounding effects, e.g., a change in the binary system affects the description of the corresponding ternary systems, making re-modeling of multicomponent necessary and extremely challenge. To address this issue, a software package named ESPEI (extensible, self-optimizing phase equilibrium computer program)[1] was developed, which establishes a data infrastructure for storing input data used in thermodynamic modeling and output data for thermodynamic analysis. *Pycalphad* [2] is an open source Python code for designing thermodynamic models, calculating phase diagrams, and investigating phase equilibria. H-T CALPHAD modeling based on ESPEI/*pycalphad* relies on extensive thermochemical data from DFT calculations. An important feature of ESPEI/*pycalphad* is the implemented uncertainty quantification through the Markov Chain Monte Carlo (MCMC) sampling method, making it possible to test and develop new models and model parameters. In this project, we tested and developed further the ESPEI/pycalphad code with more details shown in: http://espei.org and https://pycalphad.org.

The delivered ESPEI/*pycalphad* code not only enables for high throughput CALPHAD modeling and more rapid design of materials, but also offers the capability for the community to further develop tools due to its open-source nature.

The above four achievements make it possible the following impacts:

(i) The presently proposed Hf-tolerance (or other tolerances such as Pd, Ir, Rh, or Si) can be used as a bottom-up approach to designing oxidation resistant alloys. This is, the present work can be used to design advanced Ni-based superalloys and coatings tailored towards harsh environments in industrial gas turbines; and in particular

(ii) This project provided the capability for the community to use and develop the open-source ESPEI/*pycalphad* code.

2. ACTUAL ACCOMPLISHMENTS COMPARED WITH PROJECT OBJECTIVES

Objectives set in the proposed project:

"*The project scope will include composition ranges that correspond to typical MCrAl-based (where M is Ni, Co or Ni+Co) coating compositions. Thus, the project will be relevant to not only alloys based on γ-Ni and γ-Ni+γ'-Ni_3Al structures, but also to coatings based on γ-Ni and γ-Ni+β-NiAl structures. Thus the information derived from this project will be essential for the efficient design and performance prediction of alloys, coatings and coating/alloy combinations.*"

"*A further project objective is the application and further development of an automated thermodynamic modeling tool (ESPEI - self-optimizing phase equilibrium computer program) which will more efficiently arrive at accurate thermodynamic descriptions and hence, will have the potential to significantly enhance computational alloy and coating design. All data collected and developed in this project will be stored in an existing ESPEI SQL database structure.*"

Acutal accomplishments with respect to the check points set in the proposal: ALL DONE; see below the decision points, and more details in Section 3: Report Details.

Decision points 1 and 3: Development of a CALPHAD database (Ni-rich system + coating system)
Criteria for success: Completed thermodynamic description of the Ni-Al-Cr-Co-Fe-Hf-Y-O system

Acutal accomplishment w.r.t. decision points 1 and 3: ***DONE.***
A thermodynamic database for the Ni-Al-Co-Cr-Hf-Y-O system was created by CALPHAD modeling approach.

Decision point 2: Calculations of the effect of Hf and Y and Experiments
Criteria for success: Thermodynamic property calculations for the Hf and Y effects correlate with the experimental observations and increase the fundamental understanding of the RE-effect.

Acutal accomplishment w.r.t. decision point 2: ***DONE.***
We studied the effect of Hf and Y on the Al_2O_3-forming Ni-base alloys in terms of first-prinicples calculations and experiments.

Decision point 4: Evaluation and improvement of ESPEI
Criteria for success: ESPEI is further improved and the ESPEI SQL database have been extended to include a large amount of raw data (experimental and DFT data used as input for the modeling) which is well accessible for other future materials design modeling projects.

Acutal accomplishment w.r.t. decision point 4: ***DONE.***
ESPEI/*pycalphad* was developed, see details in https://espei.org and https:/pycalphad.org.

The milestone status is listed in Table 1**.**

Table 1: Milestone status report.

Milestone title /Description	Planned completion date	Actual completion date	Verification method	Comments
Milestone 1: completion of literature survey of thermochemical and phase equilibria data	3/1/2015	3/31/2015	Literature survey report	The surveyed literature information were summarized and collected into one document. Database

and summary of available thermodynamic descriptions.				files for available thermodynamic descriptions were collected.
Milestone 2: Construction of thermodynamic database for the Ni-Al-Cr-Co-Si-Y-Hf (Ni-rich).	11/30/2015	12/31/2015	Completed thermodynamic database file.	The descriptions of Hf-Ni, Al-Hf-Ni and Cr-Hf-Ni were finalized. A thermodynamic database of Ni-Al-Cr-Co-Y-Hf were established
Milestone 3: Conclusion about the effects of Hf and Y based on observations made by thermodynamic calculations and the correlation to experiments.	12/31/2015	03/31/2016	Calculation of thermodynamic properties using the developed thermodynamic description. Correlation to oxidation experiments.	Thermodynamic calculations of oxidation in the Ni-Al-Cr-Hf-O system match well with experiments for most temperature and composition combinations.
Milestone 4: Construction of thermodynamic database for the Ni-Al-Cr-Co-Si-Y-Hf (Ni-rich + coating compositions).	11/1/2016	12/31/2016	Completed thermodynamic database file.	Thermodynamic database for the Ni-Al-Cr-Co-Y-Hf was established. Comparison between oxidation experiments and predictions from the current database were performed.
Milestone 5: Completion of experimental work and validation of calculations.	12/31/2016	07/31/2017	Calculation of thermodynamic properties using the developed thermodynamic description. Correlation to oxidation experiments.	The Hf tolerance plots as a function of alloying compositions and temperatures were calculated based on the current Ni-Al-Cr-Co-Y-Hf thermodynamic database. The alloying effect of Co/Ta/Si/Pt on Hf tolerance were also investigated based on the modified databases using DFT SQS data.
Milestone 6: Final report	07/31/2018	12/31/2017	Final report.	The final report was submitted in April 2018.

3. REPORT DETAILS

Aiming to design advanced Ni-based superalloys and coatings under harsh environments in industrial gas turbines, the present project has the following accomplishments within three years (including no cost extension for one year). For each of the accomplishments, we show the key experimental and/or simulation details, results and discussions, and conclusions.

- Origin of slow-growing alumina scale mediated by reactive elements;
- Insight into γ-Ni/γ'-Ni_3Al interfacial energy affected by alloying elements;
- Thermodynamic modeling of the Ni-Al-Pt, Ni-Al-Cr-Hf, Al-Co-Cr-Ni, and Al-Fe-O systems;
- Thermodynamic approach to guide reactive element doping: Hf additions to NiCrAl; and

- Design for Hf doping and Hf co-doping in high temperature Ni-based alloys

2.1. Origin of slow-growing alumina scale mediated by reactive elements

We proposed that the interatomic bonding strength (energy) can be quantified by stretching force constants (SFC) after first-principles phonon calculations. A large and positive force constant suggests strong interaction (bonding), while a negative force constant indicates that the atomic pairs tend to separate from each other. Here, we showed that the origin of slow-growing alumina scale affected by reactive elements (REs) stems from the strong RE-O bonding energy via the present SFC model applied to oxides (Al_2O_3, Cr_2O_3, Ti_2O_3, ZrO_2, HfO_2, Y_2O_3, and La_2O_3), Al_3M, and $Al_{47}MO_{72}$ (M = Cr, Ti, Zr, Hf, Y, and La).

The reason why REs are so effective in improving scale performance is still unclear,[3] albeit numerous mechanisms have been proposed. We[4] showed that the metal-oxygen (M-O) bonding strength can be used to understand the effectiveness of REs in retarding the rate of alumina-scale growth. This understanding considered that the diffusion of oxygen involves the breaking of M-O bonds and that the diffusion of aluminum, in turn, relies on oxygen diffusion due to charge-compensation reactions.[5,6] The diffusion activation energy Q of oxygen, which can be estimated by the global properties of oxides,[4,7]

$$Q \propto B_0 V_0 \propto RT_m \propto -\Delta H_{298} \quad (1)$$

where the bulk modulus B_0 and volume V_0 are for the oxides of interest, R the gas constant, T_m the melting point, and ΔH_{298} the enthalpy of formation at 298 K. We further proposed that Q, used to break the M-O bonds, can be characterized by the largest SFC, f_{s0} and the associated bond length r_0,

$$Q \propto f_{s0} r_0^2 \quad (2)$$

Table 2 summarizes the M-O bonding energies as shown in Figure 1. It shows that all models in Eqs. (1) and (2) indicate Hf-O has the highest bonding energy, making Hf the best reactive element in retarding the growth of Al_2O_3 scale, agreeing with our experimental result in Figure 2. The other beneficial REs for the slow-growing Al_2O_3 scale are Zr and Y.

Currently one manuscript was submitted to the journal of "Oxidation of Metals"[4] and the other manuscript was published:

- S. L. Shang, Y. Wang, B. Gleeson, and Z. K. Liu, "Understanding slow-growing alumina scale mediated by reactive elements: Perspective via local metal-oxygen bonding strength", *Script. Mater.* 150 (2018) 139-142. https://doi.org/10.1016/j.scriptamat.2018.03.002

Table 2. Summary of alumina (α-Al_2O_3) scale from the slow- to fast-growing rate affected by alloying elements (REs and Cr) characterized by the metal-oxygen bonding energy, which is related to the properties of stretching force constant ($f_{S0}r_0^2$), bulk modulus (B_0V_0), melting point (T_m), and enthalpy of formation at 298 K ($-\Delta H_{298}$) of oxides; see the models in Eqs. (1) and (2).

Properties	Slow-growing scale by	Fast-growing scale by	Details in
$f_{S0}r_0^2$	Hf $\rightarrow$ Cr, Zr $\rightarrow$ Y $\rightarrow$	Ti, La	This work
B_0V_0	Hf $\rightarrow$ Zr $\rightarrow$ Ti $\rightarrow$ Y, Cr $\rightarrow$	La	This work
T_m	Hf $\rightarrow$ Zr $\rightarrow$ Cr, Y $\rightarrow$ La $\rightarrow$	Ti	Expt.[8]
$-\Delta H_{298}$	Hf, Zr $\rightarrow$ Y $\rightarrow$ La $\rightarrow$	Ti $\rightarrow$ Cr	Expt.[8]

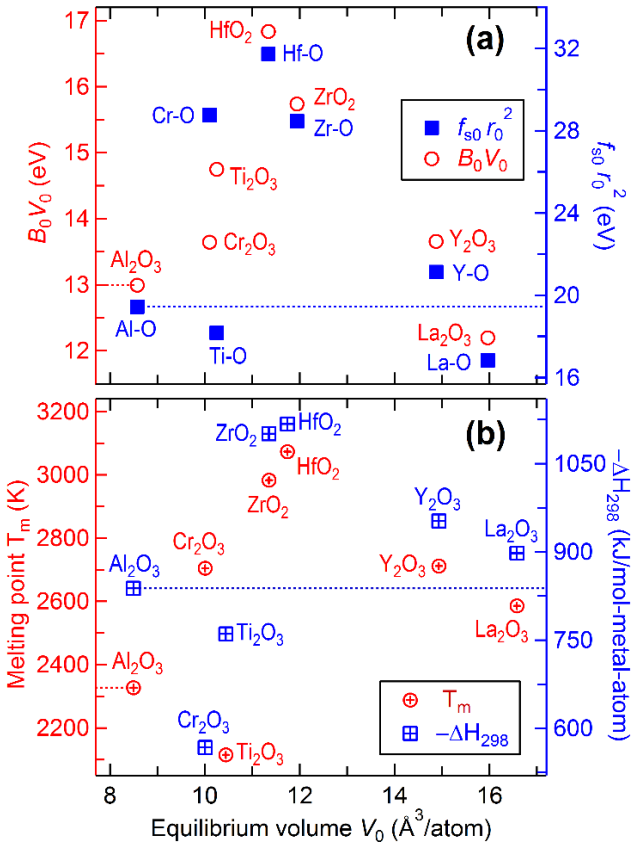

Figure 1. Metal-oxygen bonding energies related to the stretching force constant ($f_{S0}r_0^2$) and bulk modulus (B_0V_0) (a), and the melting point (T_m) and enthalpy of formation at 298 K ($-\Delta H_{298}$) (b); see the models in Eqs. (1) and (2).

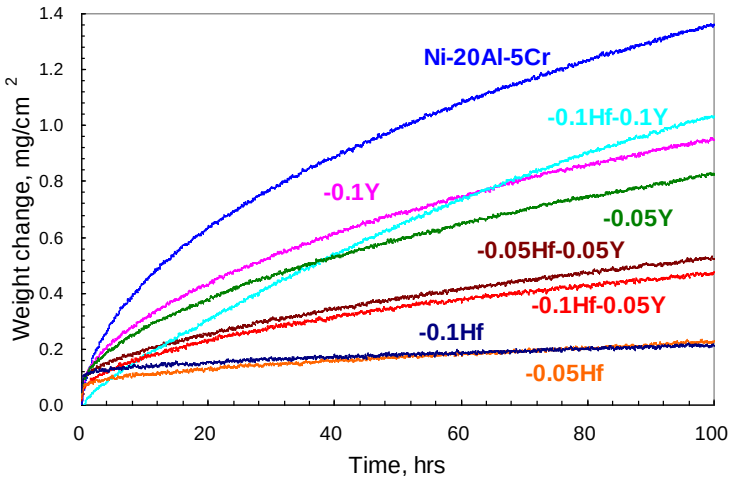

Figure 2. Weight changes of reactive element-doped Ni-20Al-5Cr (at. %) alloys as a function of isothermal exposure time at 1150ºC in air.

2.2. Insight into γ-Ni/γ'-Ni_3Al interfacial energy affected by alloying elements

Interfacial energy ($\sigma_{\gamma/\gamma'}$) of the γ-Ni/γ'-Ni_3Al interface is critical to understand and design Ni-based superalloys. In the present work, a first-principles methodology with constrained relaxations was used to study the effect of dilute alloying element (X) on $\sigma_{\gamma/\gamma'}$ of the (100) coherent interface, where the sixteen

X's include Al, Co, Cr, Fe, Hf, Mo, Nb, Pd, Pt, Re, Ru, Ta, Ti, W, Y, and Zr. $\sigma_{\gamma/\gamma'}$ = 19 mJ/m^2 was predicted for the unalloyed γ/γ' interface, agreeing well with the previous estimations. It was found that the $\sigma_{\gamma/\gamma'}$ value is the lowest when alloying element is in γ-Ni, while the addition to γ'-Ni_3Al increases $\sigma_{\gamma/\gamma'}$ due mainly to the in-plane lattice expansion. Specifically, our calculations showed that alloying elements Mo, W, and Re have the largest effect on the $\sigma_{\gamma/\gamma'}$ value by decreasing it to 4-5 mJ/m^2 when partitioned to γ-Ni; Ru and Pt are shown to increase greatly the $\sigma_{\gamma/\gamma'}$ value up to 25-28 mJ/m^2 when partitioned to γ-Ni; all ternary additions substituting for Ni in γ'-Ni_3Al increase $\sigma_{\gamma/\gamma'}$ except for Pt; and for Ti and Ta, which segregate strongly to γ'-Ni_3Al and substitute for Al, the $\sigma_{\gamma/\gamma'}$ values increase to 32 and 35 mJ/m^2, respectively.

Figure 3 shows the interfacial energy ($\sigma_{\gamma/\gamma'}$) of the γ-Ni/γ'-Ni_3Al interface affected by alloying elements when alloying elements in γ-Ni and γ'-Ni_3Al phases. Currently this work was published:

- X. L. Liu, S. L. Shang, Y. J. Hu, Y. Wang, Y. Du, and Z. K. Liu, "Insight into γ-Ni/γ'-Ni_3Al interfacial energy affected by alloying elements", *Mater. Design* 133 (2017) 39-46.

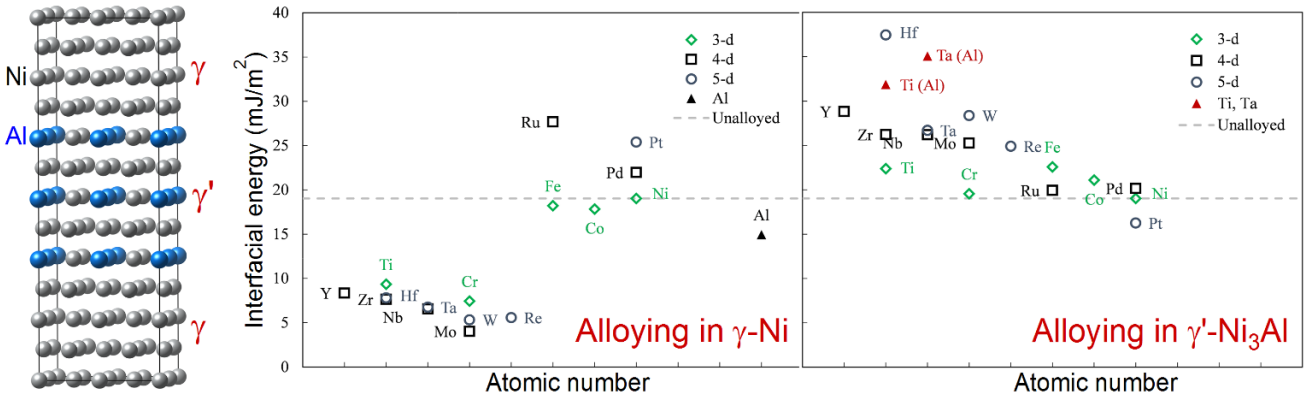

Figure 3. Interfacial energy ($\sigma_{\gamma/\gamma'}$) of the γ-Ni/γ'-Ni_3Al interface (see left figure) affected by alloying elements when they are in the γ-Ni phase or the γ'-Ni_3Al phase. The dashed line indicates the unalloyed γ-Ni/γ'-Ni_3Al interface.[9]

2.3. Thermodynamic modeling in the Ni-Al-Co-Cr-Hf-Y-O system

A complete thermodynamic database for the Ni-Al-Co-Cr-Hf-Y-O system is critical to understand and design advanced Ni-based superalloys and coatings used in harsh environments in industrial gas turbines (see examples in Sections 3.4 and 3.5). To this end, thermodynamic modeling based on the CALPHAD approach[10,11] was used to model Gibbs energy of individual phases using both thermodynamic data of single phase and phase equilibrium data between phases. The density functional theory (DFT) based first-principles calculations have the strength to predict thermodynamic data, while experiments have the strength to determine phase equilibrium data and hence can be used to refine the models developed solely based on DFT calculations; see Figure 4.

The CALPHAD modeling approach for the properties of interest can be written in a general form as follows,[10–12]

$$\Delta\varphi = {}^{0}\varphi + \Delta\varphi_{conf} + \sum_{i}\sum_{j>i} x_i x_j \sum_{L=0} {}^{L}\varphi_{ij}(x_i - x_j)^L + \sum_{i}\sum_{j>i}\sum_{k>j} x_i x_j x_k \varphi_{ijk} \qquad (3)$$

where ${}^{0}\varphi = \sum x_i {}^{0}\varphi_i$ represents the contributions of individual constituents according to their compositions x_i, $\Delta\varphi_{conf}$ is the configurational contribution when applicable, φ_{ij} and φ_{ijk} are the binary and ternary interaction parameters with the subscripts *i*, *j*, and *k* representing different constituents.

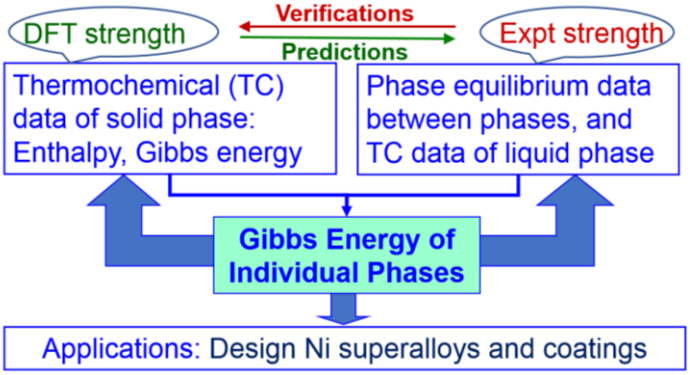

Figure 4. CALPHAD modeling of Gibbs energy.[10–12]

In terms of the CALPHAD modeling approach with input from DFT calculations and experiments available in the literatures, for example, the following systems were modelled as our efforts to build thermodynamic database for the Ni-Al-Co-Cr-Hf-Y-O system.

- Thermodynamic remodeling of the Al-Pt system towards an assessment of the Al-Ni-Pt system. The four sub-lattice (4SL) model for the ordered/disordered fcc and bcc phases was adopted resulting in improved agreement with experiment and first-principles information compared to previous descriptions. First-principles calculations were performed and the results were used in addition to available experimental data as input for the modeling. Modeling results agreed well with most experimental phase equilibria and thermochemical data compiled. Special attention was also paid to the metastable phase diagrams to ensure that the parameters obtained in the modeling do not present unphysical results in the metastable regime. The obtained fcc and bcc descriptions were converted to two sublattice (2SL) models to enable combination with available multi-component Ni-base superalloy descriptions. The converted Al-Pt system was extended into the Al-Ni-Pt ternary system to study its extrapolation characteristics using available thermodynamic and thermochemical data. It was found that the 2SL model is not adequate in capturing the thermodynamic behavior of the fcc-based phases found in the ternary Al-Ni-Pt system. This work was published in: *CALPHAD* 55 (2016) 88-102.

  For example, Figure 5 shows the modelled Al-Pt system using four sublattice model for the ordered and disordered fcc and bcc phases.[13]

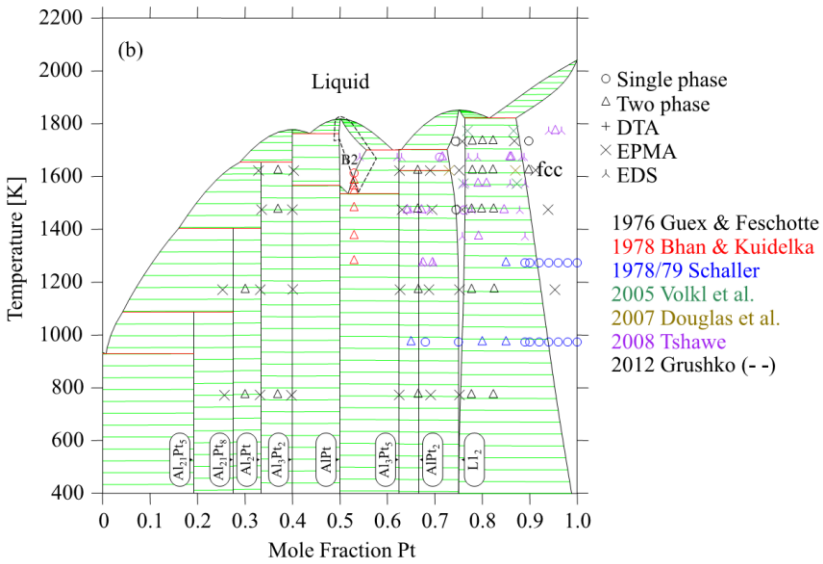

Figure 5. Calculated Al-Pt phase diagram using four sublattice model for fcc and bcc phases.[13]

- Thermodynamic modeling of Al-Co-Cr, Al-Co-Ni, Co-Cr-Ni ternary systems towards a description for Al-Co-Cr-Ni. The phase relations and thermodynamic properties of the Al-Co-Cr, Al-Co-Ni, and Co-Cr-Ni ternary alloys were investigated using first principles calculations. Their thermodynamic descriptions were developed by means of the CALPHAD method using experimental and DFT data. Emphasis was placed on modeling the A2, B2, fcc-γ, L12-γ′ and tetragonal-s phases in the temperature range of 1173-1623 K. Liquid, A2 and fcc-γ phases were modeled using substitutional solution descriptions. A partitioning model was then used for the γ/γ′ and A2/B2 phases to effectively describe the order-disorder transitions. The critically assessed thermodynamic descriptions described all experimentally determined phase equilibria data well. A2/B2 transitions were also shown to agree well with previous experimental findings in the Al-Co-Cr ternary system.
  This work was published in: *CALPHAD* 52 (2016) 125-142. For example, Figure 6 shows the calculated Al-Co-Cr isothermal sections in comparison with experimental data.[14]

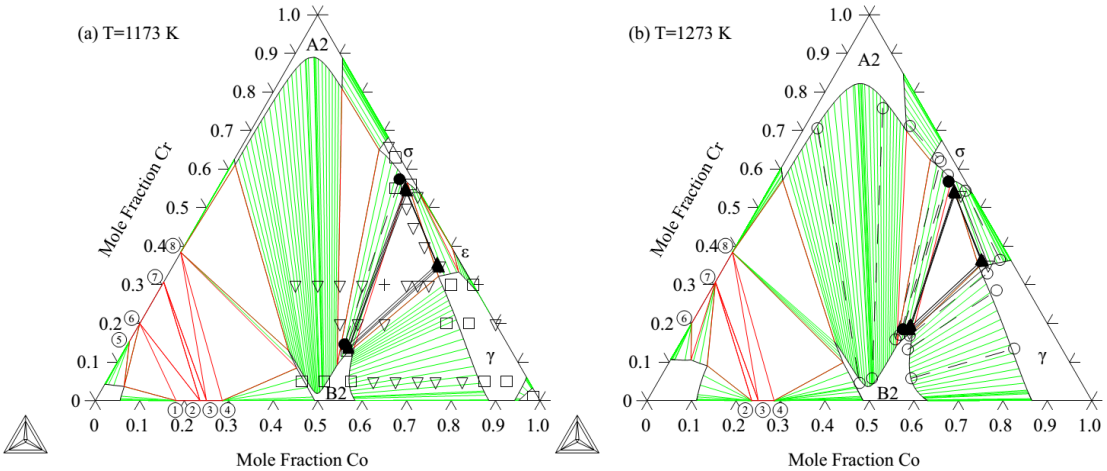

Figure 6. Calculated Al-Co-Cr isothermal sections (solid lines) at 1173 K (a) and 1273 K (b). The symbols are experimental data.[14]

- Thermodynamic modeling of the Al-Fe-O system. This system is an important subsystem within several material classes, especially when considering oxidation of high-performance structural materials or deoxidation of steels during steelmaking. Despite its industrial importance as well as the large amount of experimental information available in literature, no complete phase diagram has been reported for this system. Therefore, a thermodynamic description, by means of the CALPHAD method, was developed in this study. To account for the complexity of the solid oxides including non-stoichiometry, solid solution in the phases and cation distribution between different lattice sites, the compound energy formalism is applied for the modeling. The liquid phase was modeled utilizing the ionic two-sublattice model. The sublattice models were selected with the aim to achieve compatibility with the Al-Ni-O and Fe-Ni-O systems to facility development of a quaternary thermodynamic description. The evaluated model was validated by comparison to available experimental data. Satisfactory agreement with both thermochemical and phase equilibrium data was concluded.
  This work was published in: *CALPHAD* 51 (2015) 178-192. For example, Figure 7 shows the calculated Al_2O_3-FeO-Fe_2O_3 isothermal sections.[15]

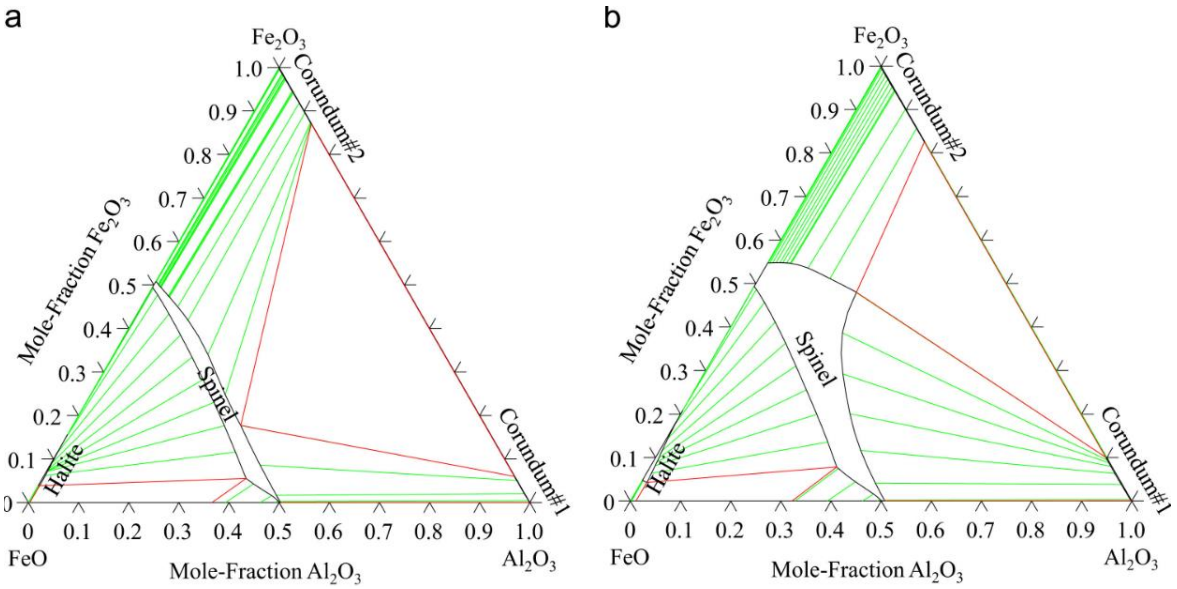

Figure 7. Calculated Al_2O_3-FeO-Fe_2O_3 isothermal sections at 1173 K (a) and 1473 K (b).[15]

- First-principles calculations, experimental study, and thermodynamic modeling of the Al-Co-Cr system. In this work, the phase relations and thermodynamic properties of the condensed Al-Co-Cr ternary alloy system were investigated using first-principles calculations and phase-equilibria experiments that led to X-ray diffraction (XRD) and electron probe micro-analysis (EPMA) measurements. A thermodynamic description was developed by means of the CALPHAD method using experimental and computational data from the present work and the literature. Emphasis was placed on modeling the bcc-A2, B2, fcc-γ, and tetragonal-σ phases in the temperature range of 1173 to 1623 K. Liquid, bcc-A2 and fcc-γ phases were modeled using substitutional solution descriptions. First-principles special quasirandom structures (SQS) calculations predicted a large bcc-A2 (disordered)/B2 (ordered) miscibility gap, in agreement with experiments. A partitioning model was then used for the A2/B2 phase to effectively describe the order-disorder transitions. The critically assessed thermodynamic description described all phase equilibria data well. A2/B2 transitions were also shown to agree well with previous experimental findings.
  This work was published in: *PLoS One* 10 (2015) e0121386. For example, Figure 8 shows the calculated Al-Co-Cr isothermal section.[16]

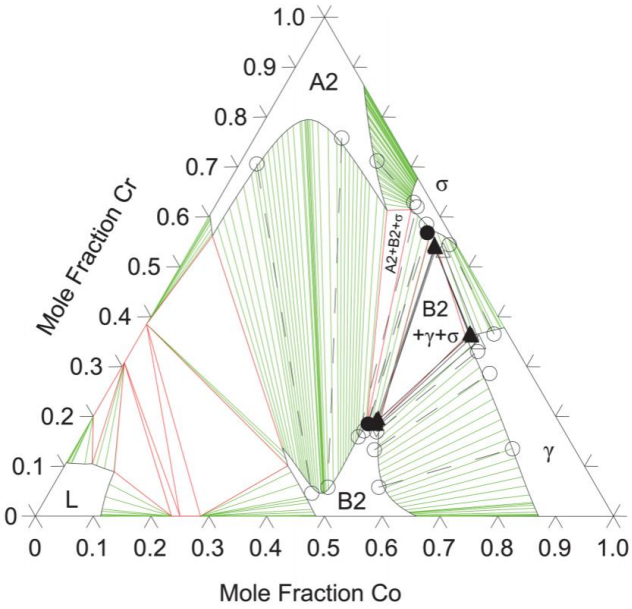

Figure 8. Calculated Al-Co-Cr isothermal section at 1273 K.[16]

- Experimental study and thermodynamic modeling of the Al-Co-Cr-Ni system. In this work, a thermodynamic database for the Al-Co-Cr-Ni system was built via the CALPHAD method by extrapolating re-assessed ternary subsystems. A minimum number of quaternary parameters were included, which are optimized using experimental phase equilibrium data obtained by electron probe micro-analysis and X-ray diffraction analysis of NiCoCrAlY alloys spanning a wide compositional range, after annealing at 900, 1100 and 1200 °C, and water quenching. These temperatures are relevant to oxidation and corrosion resistant MCrAlY coatings, where M corresponds to some combination of nickel and cobalt. Comparisons of calculated and measured phase compositions showed excellent agreement for the β-γ equilibrium, and good agreement for three-phase β-γ-σ and β-γ-α equilibria. An extensive comparison with existing Ni-base databases was presented in terms of phase compositions.
  This work was published in *Sci. Technol. Adv. Mater.* 16 (2015) 55001. For example, Figure 9 shows the calculated isothermal sections of the Al-Co-Cr-Ni system.[17]

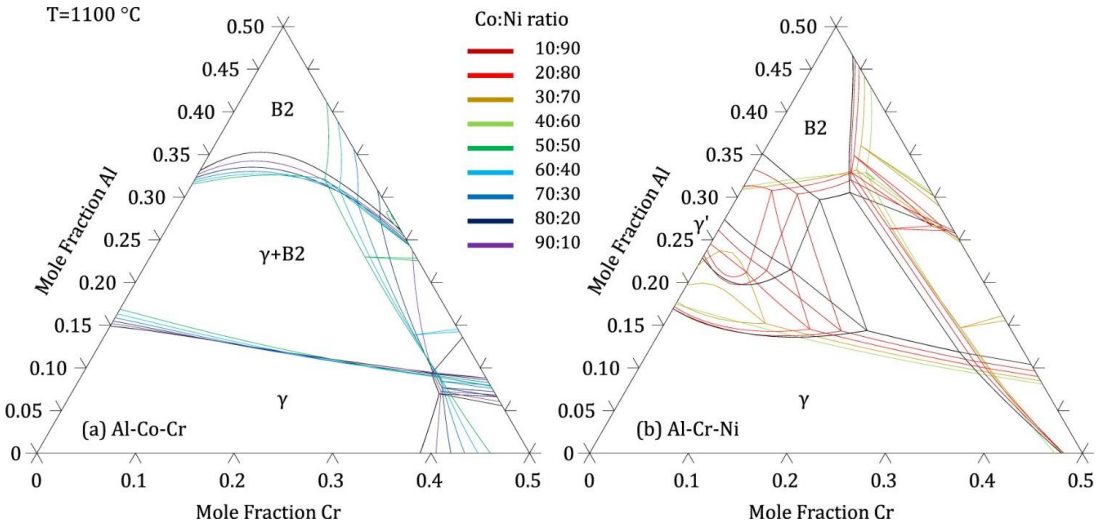

Figure 9. Isothermal (1100 °C) sections of the Al-Co-Cr-Ni system for constant Co:Ni ratios. Co-rich and Ni-rich sections are superimposed on the (a) Al-Co-Cr and (b) Al-Cr-Ni diagram, respectively.[17]

Currently these modeling works were published in **five** peer-reviewed journals and **two** PhD theses:

- X. L. Liu, G. Lindwall, R. Otis, H. Kim, and Z.-K. Liu, “Thermodynamic remodeling of the Al-Pt system towards an assessment of the Al-Ni-Pt system”, *CALPHAD* 55 (2016) 88-102.
- X. L. Liu, G. Lindwall, T. Gheno, and Z. K. Liu, “Thermodynamic modeling of Al-Co-Cr, Al-Co-Ni, Co-Cr-Ni ternary systems towards a description for Al-Co-Cr-Ni”, *CALPHAD* 52 (2016) 125-142.
- G. Lindwall, X. L. Liu, A. Ross, H. Z. Fang, B. C. Zhou, and Z. K. Liu, “Thermodynamic modeling of the aluminum-iron-oxygen system”, *CALPHAD* 51 (2015) 178-192.
- X. L. Liu, T. Gheno, B. B. Lindahl, G. Lindwall, B. Gleeson, and Z. K. Liu, “First-principles calculations, experimental study, and thermodynamic modeling of the Al-Co-Cr system”, PLOS One, 10 (2015) e0121386.
- T. Gheno, X. L Liu, G. Lindwall, Z. K. Liu, and B. Gleeson, “Experimental study and thermodynamic modeling of the Al-Co-Cr-Ni system”, *Sci. Technol. Adv. Mater.* 16 (2015) 055001.
- Xuan Liu, “Design of Ni-base superalloys and MCrAlY coatings from first-principles and computational thermodynamics”, Pennsylvania State University, Ph.D. thesis, 2015.
- Austin Ross, “Solubility of oxygen and hydrogen and diffusivity of oxygen in the fcc phase of the Al-Fe-Ni-H-O system with application to the formation of a protective α-Al_2O_3 scale at high temperatures”, Pennsylvania State University, Ph.D. thesis, 2017.

2.4. Thermodynamic approach to guide reactive element doping: Hf additions to NiCrAl

A method based on thermodynamic modeling was developed to determine optimal amounts of Hf additions to Al_2O_3-forming, γ-γ′ NiCrAl alloys. The alloy ability to maintain Hf in solution was set by the Hf concentration required to form HfO_2 at the oxygen activity defined by the alloy/Al_2O_3 equilibrium. This Hf tolerance decreased with increasing temperature and increased with increasing γ′ fraction. The latter was due to the higher solubility of Hf in γ′, compared to γ. The validity of the procedure was evaluated by oxidizing a series of NiCrAl-Hf alloys in dry air at 1000-1200 °C. The experimental results followed the predicted trends, although the Hf tolerance tended to be overestimated. The applicability of the criterion, and potential routes for improved predictability, were discussed by considering the influence of the compositional changes occurring at the metal surface during the transient and steady-state stages of the oxidation process.

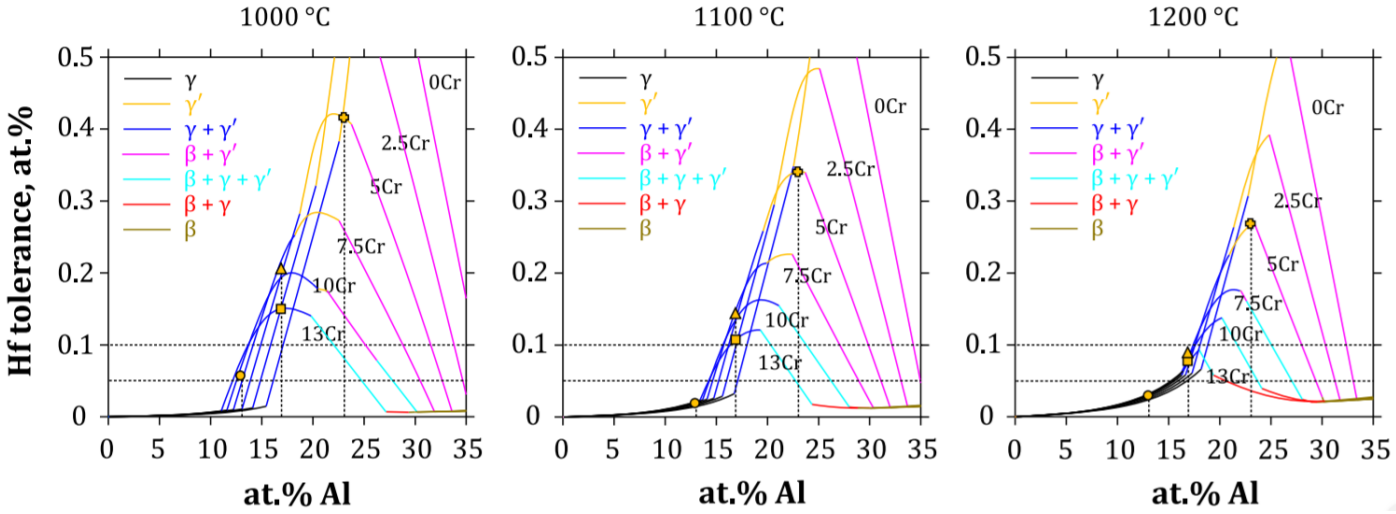

Figure 10. Calculated Hf concentration required to form HfO_2 at the O activity defined by the alloy/Al_2O_3 equilibrium at varying Cr levels. This “Hf tolerance” is the maximum Hf concentration which can be included in an alloy to avoid HfO_2 formation, based on the equilibrium alloy phase compositions. The yellow symbols represent the base NiCrAl compositions.[18]

The Hf concentration for HfO_2 formation, or Hf tolerance, was predicted to be larger in γ′ than in γ (or in β, which dissolves very little Hf). For example, plots of the Hf tolerance as a function of Cr and Al concentrations at 1000-1200 °C are given in Figure 10.

This work was published in *Oxidation of Metals* 87 (2017) 297-310.

2.5. Design for Hf Doping and Hf co-doping in high temperature Ni-based alloys

The performance of reactive elements in MCrAlYs can often be improved by the addition of other elements in the alloy such as Si, Pt, or Pd. However, the exact mechanism of the improvement in performance is unclear. Si has been shown to be beneficial to oxide growth rates in Cr_2O_3 forming alloys by forming a continueous layer of SiO_2 beneath the scale. For Al_2O_3 forming alloys, small concentrations (~2 at.%) have been proven to have little effect on oxidation properties[19] but at larger concentrations (~6 at.%) Si has been proven useful in reducing the amount of Al required to form Al_2O_3.[20] Pt has a plethora of beneficial effects for the oxidation.[21] This is not for alloys containing reactive elements but also for Ni-Al alloys where Pt has been shown to reduce the amount of Al required to form Al_2O_3 by promoting uphill diffusion of Al during oxidation.[22] This shows that Pt has the ability to modify and reduce the activity of Al in the alloy. Pd has been shown to have similar benefits to Pt when added to Al-rich alloys.[23]

Previous work has shown that thermodynamic considerations of the underlying alloy and oxide can be used to model the interface reaction between Al_2O_3 and the alloy to form HfO_2.[18] The onset of HfO_2 is typically referred to as over-doping and results in increased oxide growth rates and decreased oxide adhesion during cylclic oxidation.[24] The thermodynamic boundary for this behavior in composition space has been termed the Hf-tolerance and this value has been used to predict the onset of HfO_2 precipitation in several NiAlCrHf alloys.[18]

The most important contribution to the Hf tolerance is the activity of Hf relative to the activity of Al. When the Hf activity is below a certain threshold level at the interface between Al_2O_3 and the alloy, HfO_2 is unlikely to precipitate. The ordered intermetallic γ' phase has a much larger solubility for Hf relative to the disordered fcc phase (γ). Given the Al concentrations needed to form γ', this means that the Hf activity relative to the Al activity will drop appreciably when the γ' phase is present in the alloy. Hence, the two most important factors to consider when designing a Hf containing alloy is the phase fraction of the γ' phase and how the Hf activity is affected relative to the Al activity in all phases.

The concept of Hf-tolerance has already been applied to alloys in the Ni-rich Al-Cr-Hf-Ni system,[18] see Section 3.4. The present work searched for other beneficial elements to add to the system to increase the Hf-tolerance through an extensive computational and thermodynamic search. Given the importance of the γ' phase, an initial selection process was established by searching for elements a large solubility in the γ' phase. These elements have the most prominent interactions with Hf for alloys with appreciable equilibrium fractions of γ'. Once these elements were selected, a computational search is performed to calculate the mixing enthalpies of these phases in the γ phase and the formation enthalpies of the $L1_2$-Hf_3X and $L1_2$-HfX_3 in the Hf-X system. This not only provided valuable thermodynamic information for each Hf-X system but also highlighted which element will have the strongest effect on the activity of Hf since the mixing enthalpy will play a significant role in the partial molar quantities, and hence on the activity. In all, this amounted to a study of the Hf interactions with the elements Al, Co, Cr, Cu, Fe, Ga, Ge, Hf, Mn, Nb, Ni, Pd, Pt, Sc, Si, Ta, Ti, V, and Zn. Of these elements Pt, Pd, Rh and Si were found to have the strongest interaction with Hf.

For example, the Hf-tolerance was calculated in the present work in the Ni-rich Al-Hf-Ni-Pt and Al-Cr-Hf-Ni-Pt alloy system and compared with oxidation observations in the literatures, see Figure 11 and Figure 12. Calculations matched well with experimental oxidation results for most cases in this system with the exception of samples with high Al concentrations where experimental observations had HfO_2 precipitates in the oxide scale. It was hypothesized that these formed as a consequence of the transient oxidation stage and did not represent the steady state oxidizing behavior.

Pt was shown to decrease the Hf activity relative to the Al activity as well as decreasing the amount of Al required to form γ' when substituting for Ni. The calculated Hf tolerance had a maximum of ~ 0.21 at.% Hf at 1150 °C for the the Ni-xAl-5Cr-5Pt-y Hf system compared to a maximum of 0.17 at.% Hf at 1150 ° C for the Ni-xAl-5Cr-y Hf system. This showed a clear demonstration of the ability of Pt to improve oxidation resistance in the Ni-rich Al-Cr-Hf-Ni-Pt alloy system.

The present culmination of work represented a bottom-up approach to designing oxidation resistant alloys. A similar first-principles based modeling procedure carried out for Pd, Ir, Rh, or Si additions which could yield similar models for the design space of oxidation resistant alloys.

More details of this work can be found in:

- Austin Ross, “Solubility of oxygen and hydrogen and diffusivity of oxygen in the fcc phase of the Al-Fe-Ni-H-O system with application to the formation of a protective α-Al_2O_3 scale at high temperatures”, Pennsylvania State University, Ph.D. thesis, 2017.

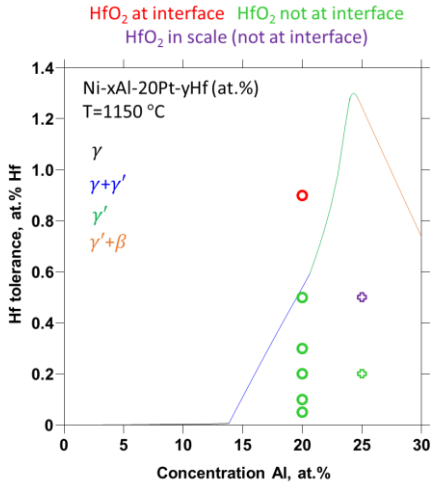

Figure 11. Hf tolerance in the Ni-20Pt-xAl-yHf system compared to cyclic oxidation experiments by Mu *et al.*[21] (✚) and isothermal oxidation experiments by Mu *et al.*[25] (○). Symbols indicate when HfO_2 was observed at the interface (green), when it was not observed at the interface (red), and when it was observed in the scale but not at the interface (purple).

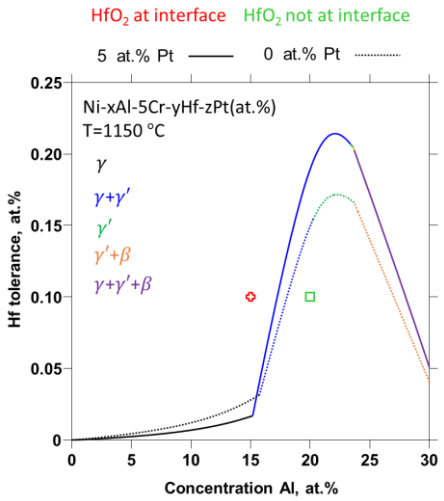

Figure 12. Hf tolerance in the Ni-xAl-5Cr-5Pt-yHf system at 1150 °C compared to cyclic oxidation experiments by Mu *et al.*[21] (✚) and unpublished work by Gleeson(□). Symbols indicate when HfO_2 was observed at the interface (green) and when it was not observed at the interface (red).

2.6. Development of ESPEI/*pycalphad* for high throughput CALPHAD modeling

Efficient CALPHAD modeling calls for high throughput (H-T) approaches due to the compounding effects, e.g., a change in the binary system affects the description of the corresponding ternary systems, making re-modeling of multicomponent necessary and extremely challenge. To address this issue, a software package named ESPEI (extensible, self-optimizing phase equilibrium computer program)[1] was been developed, which establishes a data infrastructure for storing input data used in thermodynamic modeling and output data for thermodynamic analysis. *Pycalphad* [2] is an open source Python code for designing thermodynamic models, calculating phase diagrams, and investigating phase equilibria. H-T CALPHAD modeling based on ESPEI/*pycalphad* relies on extensive thermochemical data from DFT calculations. An important feature of ESPEI/*pycalphad* is the implemented uncertainty quantification through the Markov Chain Monte Carlo (MCMC) sampling method, making it possible to test and develop new models and model parameters.

In this project, we tested and developed the ESPEI/pycalphad code. For example, Figure 13 shows the modelled Cu-Mg system using ESPEI/pycalphad. More details are shown in:

- http://espei.org/en; and
- https://pycalphad.org.

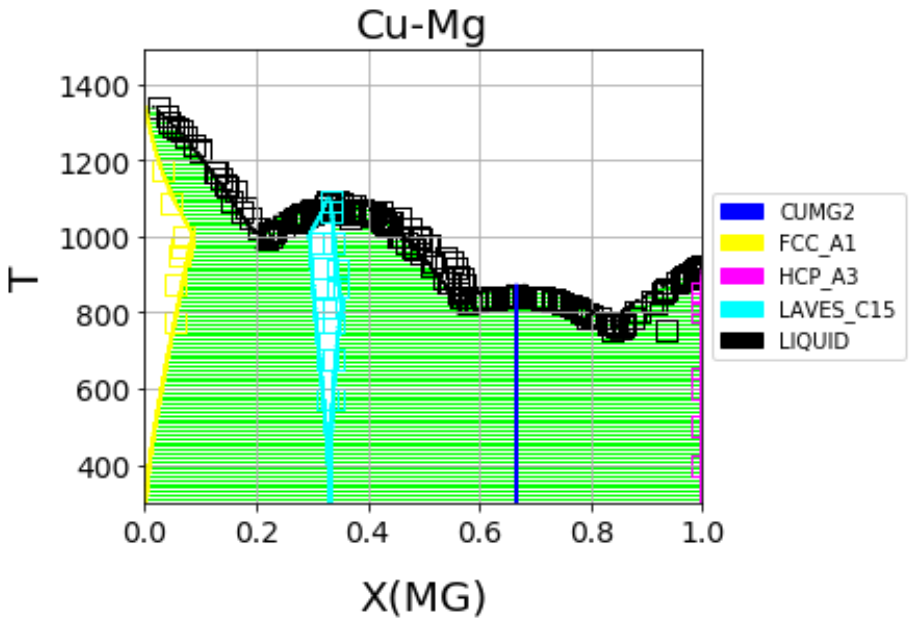

Figure 13. Cu-Mg phase diagram from a database created with and optimized by ESPEI/*pycalphad*.

3. GRAPHICAL MATERIALS LIST(S)

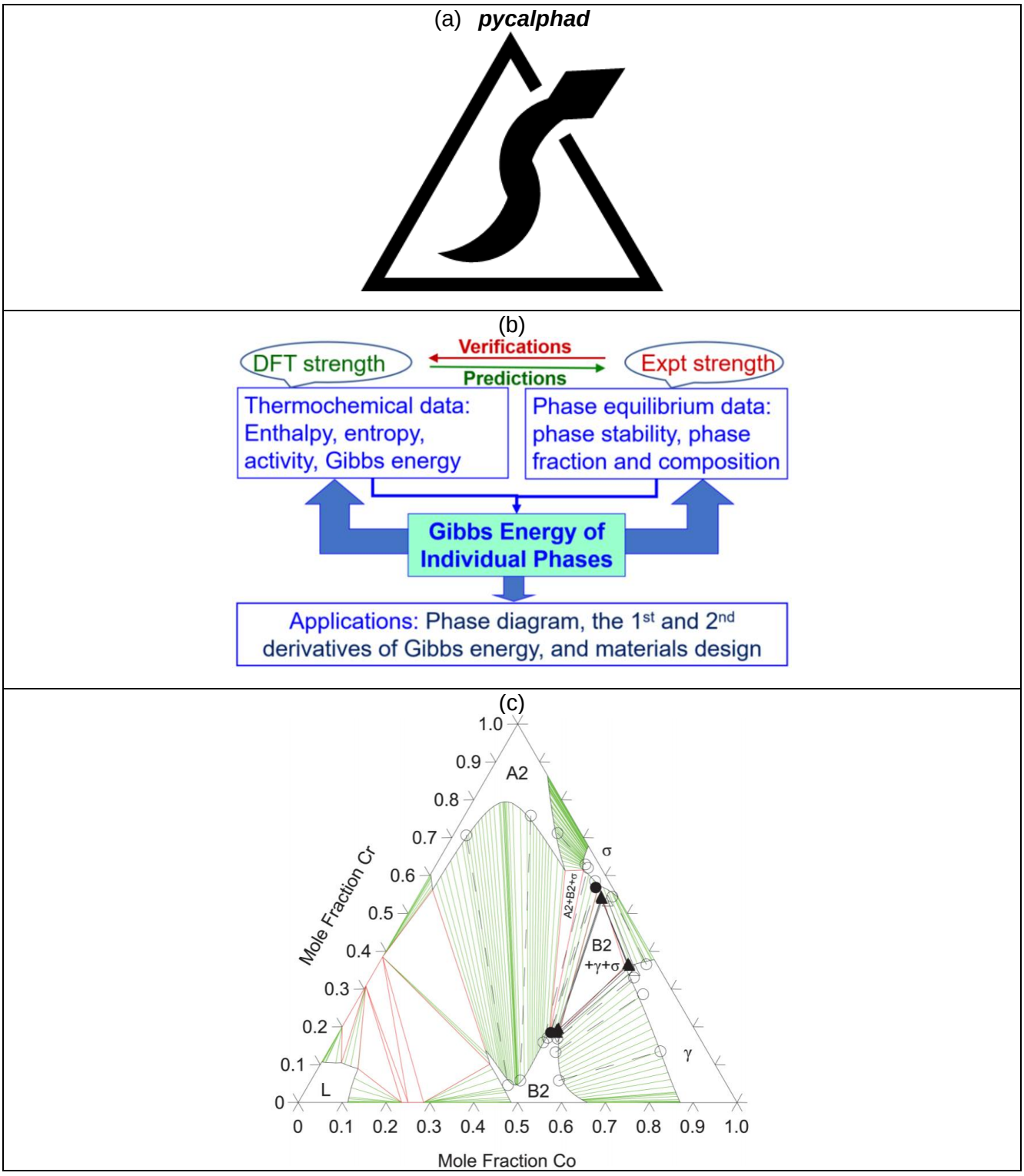

Figure 14. Key graphical materials for this project (a) the logo of *pycalphad*, (b) the idea of CALPHAD modeling, and (c) the modelled modelled phase diagram such as Al-Co-Cr at 1273 K.

4. REFERENCES

(1) Shang, S.-L.; Wang, Y.; Liu, Z.-K. ESPEI: Extensible, Self-Optimizing Phase Equilibrium Infrastructure for Magnesium Alloys. *Magnes. Technol. 2010 - TMS 2010 Annu. Meet. Exhib. Febr. 14-18, 2010* **2010**, No. iv, 617–622.

(2) Otis, R. A.; Liu, Z.-K. Pycalphad: CALPHAD-Based Computational Thermodynamics in Python. *J. Open Res. Softw.* **2017**, *5* (1), 1.

(3) Naumenko, D.; Pint, B. A.; Quadakkers, W. J. Current Thoughts on Reactive Element Effects in Alumina-Forming Systems: In Memory of John Stringer. *Oxid. Met.* **2016**, *86* (1–2), 1–43.

(4) Kim, D. E.; Shang, S.-L.; Li, Z. Q.; Gleeson, B.; Liu, Z.-K. Effects of Hf, Y, and Zr on Alumina Scale Growth on NiAlCr and NiAlPt Alloys. *Oxid. Met.* **2018**, Submitted.

(5) Heuer, A. H.; Hovis, D. B.; Smialek, J. L.; Gleeson, B. Alumina Scale Formation: A New Perspective. *J. Am. Ceram. Soc.* **2011**, *94* (s1), s146–s153.

(6) Heuer, A. H.; Nakagawa, T.; Azar, M. Z.; Hovis, D. B.; Smialek, J. L.; Gleeson, B.; Hine, N. D. M.; Guhl, H.; Lee, H.-S.; Tangney, P.; et al. On the Growth of Al2O3 Scales. *Acta Mater.* **2013**, *61* (18), 6670–6683.

(7) Shang, S.-L.; Zhou, B.-C.; Wang, W. Y.; Ross, A. J.; Liu, X. L.; Hu, Y.-J.; Fang, H.-Z.; Wang, Y.; Liu, Z.-K. A Comprehensive First-Principles Study of Pure Elements: Vacancy Formation and Migration Energies and Self-Diffusion Coefficients. *Acta Mater.* **2016**, *109*, 128–141.

(8) Scientific Group Thermodata Europe (SGTE). Thermodynamic Properties of Inorganic Materials. In *Landolt-Boernstein New Series, Group IV*; Lehrstuhl fuer Theoretische Huettenkunde, Ed.; Springer: Verlag Berlin Heidelberg, 1999; Vol. 19.

(9) Liu, X. L.; Shang, S.-L.; Hu, Y.-J.; Wang, Y.; Du, Y.; Liu, Z.-K. Insight into γ-Ni/γ′-Ni3Al Interfacial Energy Affected by Alloying Elements. *Mater. Des.* **2017**, *133*.

(10) Saunders, N.; Miodownik, A. P. *CALPHAD (Calculation of Phase Diagrams): A Comprehensive Guide*; Pergamon: Oxford; New York, 1998; Vol. 1.

(11) Liu, Z. K.; Wang, Y. *Computational Thermodynamics of Materials*; Cambridge University Press: Cambridge, UK, 2016.

(12) Liu, Z.-K. First-Principles Calculations and CALPHAD Modeling of Thermodynamics. *J. Phase Equilibria Diffus.* **2009**, *30* (5), 517–534.

(13) Liu, X. L.; Lindwall, G.; Otis, R.; Kim, H.; Liu, Z.-K. Thermodynamic Remodeling of the Al–Pt System towards an Assessment of the Al–Ni–Pt System. *Calphad* **2016**, *55*, 88–102.

(14) Liu, X. L.; Lindwall, G.; Gheno, T.; Liu, Z.-K. Thermodynamic Modeling of Al–Co–Cr, Al–Co–Ni, Co–Cr–Ni Ternary Systems towards a Description for Al–Co–Cr–Ni. *Calphad* **2016**, *52*, 125–142.

(15) Lindwall, G.; Liu, X. L.; Ross, A.; Fang, H.; Zhou, B.-C.; Liu, Z.-K. Thermodynamic Modeling of the Aluminum–iron–oxygen System. *Calphad* **2015**, *51*, 178–192.

(16) Liu, X. L.; Gheno, T.; Lindahl, B. B.; Lindwall, G.; Gleeson, B.; Liu, Z.-K. First-Principles Calculations, Experimental Study, and Thermodynamic Modeling of the Al-Co-Cr System. *PLoS One* **2015**, *10* (4), e0121386.

(17) Gheno, T.; Liu, X. L.; Lindwall, G.; Liu, Z.-K.; Gleeson, B. Experimental Study and Thermodynamic Modeling of the Al–Co–Cr–Ni System. *Sci. Technol. Adv. Mater.* **2015**, *16* (5), 55001.

(18) Gheno, T.; Zhou, B.-C.; Ross, A.; Liu, X.; Lindwall, G.; Liu, Z.-K.; Gleeson, B. A Thermodynamic Approach to Guide Reactive Element Doping: Hf Additions to NiCrAl. *Oxid. Met.* **2017**, *87* (3–4), 297–310.

(19) Susan, D. F.; Marder, A. R. Oxidation of Ni–Al-Base Electrodeposited Composite Coatings. I: Oxidation Kinetics and Morphology at 800°C. *Oxid. Met.* **2002**, *57* (1/2), 131–157.

(20) Niu, Y.; Wu, Y.; Gesmundo, F. The Oxidation of Three Ni–6Si–xAl Alloys in 1atm O2 at 1000°C. *Corros. Sci.* **2006**, *48* (1), 1–22.

(21) Mu, N.; Izumi, T.; Zhang, L.; Gleeson, B. The Development and Performance of Novel Pt+Hf-

Modified γ′-Ni3Al-γ-Ni Bond Coatings for Advanced Thermal Barrier Coatings Systems. In *Proceedings of the International Symposium On Superalloys*; 2008; pp 629–637.
(22) Gleeson, B.; Wang, W.; Hayashi, S.; Sordelet, D. J. Effects of Platinum on the Interdiffusion and Oxidation Behavior of Ni-Al-Based Alloys. *Mater. Sci. Forum* **2004**, *461–464*, 213–222.
(23) Li, M. J.; Sun, X. F.; Guan, H. R.; Jiang, X. X.; Hu, Z. Q. Effect of Palladium Incorporation on Isothermal Oxidation Behavior of Aluminide Coatings. *Oxid. Met.* **2003**, *59* (5/6), 483–502.
(24) Pint, B. A. Optimization of Reactive-Element Additions to Improve Oxidation Performance of Alumina-Forming Alloys. *J. Am. Ceram. Soc.* **2003**, *86* (4), 686–695.
(25) Mu, N. High Temperature Oxidation Behavior of γ-Ni + γ'-Ni3Al Alloys and Coatings Modified with Pt and Reactive Elements, Iowa State University, 2007.

5. LIST OF ACRONYMS AND ABBREVIATIONS

ABBREVIATIONS	EXPLANATIONS
CALPHAD	Calculation of phase diagram
DFT	Density functional theory
ESPEI	Extensible, self-optimizing phase equilibrium computer program
H-T	High throughput
MCMC	Markov Chain Monte Carlo
pycalphad	Python based CALPHAD modeling code
RE	Reactive element
SFC	Stretching force constants
γ	FCC based Ni alloys
γ'	$L1_2$ based Ni_3Al phase
$\sigma_{\gamma/\gamma'}$	Interfacial energy of the γ-Ni/γ'-Ni_3Al interface

6. PRODUCTS

6.1. Two Ph.D. Students Graduated with Two Theses Published

- Xuan Liu, "Design of Ni-base superalloys and MCrAlY coatings from first-principles and computational thermodynamics", Pennsylvania State University, Ph.D. thesis, 2015. https://etda.libraries.psu.edu/paper/24917/
- Austin Ross, "Solubility of oxygen and hydrogen and diffusivity of oxygen in the fcc phase of the Al-Fe-Ni-H-O system with application to the formation of a protective α-Al_2O_3 scale at high temperatures", Pennsylvania State University, Ph.D. thesis, 2017. https://etda.libraries.psu.edu/catalog/26535

6.2. Eight Peer-Reviewed Journal Publications

- S. L. Shang, Y. Wang, B. Gleeson, and Z. K. Liu, "Understanding slow-growing alumina scale mediated by reactive elements: Perspective via local metal-oxygen bonding strength", *Script. Mater.* 150 (2018) 139-142. https://doi.org/10.1016/j.scriptamat.2018.03.002
- X. L. Liu, S. L. Shang, Y. J. Hu, Y. Wang, Y. Du, and Z. K. Liu, "Insight into γ-Ni/γ'-Ni_3Al interfacial energy affected by alloying elements", *Mater. Design* 133 (2017) 39-46. http://dx.doi.org/10.1016/j.matdes.2017.07.028

- T. Gheno, B. C. Zhou, A. J. Ross, X. Liu, G. Lindwall, Z. K. Liu, and B. Gleeson, “A thermodynamic approach to guide reactive element doping: Hf additions to NiCrAl”, *Oxidation of Metals* 87 (2017) 297-310. http://dx.doi.org/10.1007/s11085-016-9706-0
- X. L. Liu, G. Lindwall, R. Otis, H. Kim, and Z.-K. Liu, “Thermodynamic remodeling of the Al-Pt system towards an assessment of the Al-Ni-Pt system”, *CALPHAD* 55 (2016) 88-102. http://dx.doi.org/10.1016/j.calphad.2016.08.002
- X. L. Liu, G. Lindwall, T. Gheno, and Z. K. Liu, “Thermodynamic modeling of Al-Co-Cr, Al-Co-Ni, Co-Cr-Ni ternary systems towards a description for Al-Co-Cr-Ni”, *CALPHAD* 52 (2016) 125-142. http://dx.doi.org/10.1016/j.calphad.2015.12.007
- G. Lindwall, X. L. Liu, A. Ross, H. Z. Fang, B. C. Zhou, and Z. K. Liu, “Thermodynamic modeling of the aluminum-iron-oxygen system”, *CALPHAD* 51 (2015) 178-192. http://dx.doi.org/10.1016/j.calphad.2015.09.004
- T. Gheno, X. L Liu, G. Lindwall, Z. K. Liu, and B. Gleeson, “Experimental study and thermodynamic modeling of the Al-Co-Cr-Ni system”, *Sci. Technol. Adv. Mater.* 16 (2015) 055001. http://dx.doi.org/10.1088/1468-6996/16/5/055001
- X. L. Liu, T. Gheno, B. B. Lindahl, G. Lindwall, B. Gleeson, and Z. K. Liu, “First-principles calculations, experimental study, and thermodynamic modeling of the Al-Co-Cr system”, PLOS One, 10 (2015) e0121386. http://dx.doi.org/10.1371%2Fjournal.pone.0121386

6.3. Websites related to the results of this projects

- http://espei.org/: ESPEI has been developed for automated thermodynamic database development within the CALPHAD method
- https://pycalphad.org/: pycalphad is a Python library for computational thermodynamics using the CALPHAD method.

6.4. Other products

- Thermodynamic database for the Ni-Al-Co-Cr-Hf-Y-O system

7. APPENDICES

7.1. Peer-Reviewed Journal Publications

Eight peer-reviewed journal publications as shown in Section 6.2 are listed in the following pages.

Scripta Materialia 150 (2018) 139–142

Contents lists available at ScienceDirect

Scripta Materialia

journal homepage: www.elsevier.com/locate/scriptamat

Regular article

Understanding slow-growing alumina scale mediated by reactive elements: Perspective via local metal-oxygen bonding strength

Shun-Li Shang [a,*], Yi Wang [a], Brian Gleeson [b], Zi-Kui Liu [a]

[a] Department of Materials Science and Engineering, The Pennsylvania State University, University Park, PA 16802, United States
[b] Department of Mechanical Engineering and Materials Science, University of Pittsburgh, Pittsburgh, PA 15261, United States

ARTICLE INFO

Article history:
Received 11 February 2018
Received in revised form 28 February 2018
Accepted 1 March 2018
Available online xxxx

Keywords:
Alumina scale
Reactive elements
Oxides
Phonon
First principles calculations

ABSTRACT

Interatomic bonding strength/energy can be quantified by stretching force constants (SFC) after first-principles phonon calculations. Here, we show that the slow-growing alumina (α-Al_2O_3) scale mediated by reactive elements (REs) can be understood via the strong RE—O bonding energy from the present SFC model applied to oxides (Al_2O_3, Cr_2O_3, Ti_2O_3, ZrO_2, HfO_2, Y_2O_3, and La_2O_3), Al_3M, and $Al_{47}MO_{72}$ (M = Cr, Ti, Zr, Hf, Y, and La). The present model indicates that Hf is the best RE in retarding alumina scale growth, agreeing with the analyses from bulk modulus, melting point, and enthalpy of formation of oxides, and experimental observations.

A dense, continuous, slow-growing, relatively chemically inert and adherent oxide scale is essential for protecting an underlying alloy from oxidation and hot corrosion [1,2]. For example, the thermally grown oxide (TGO) layer within the thermal barrier coating (TBC) system, commonly alumina (α-Al_2O_3), forms in the high-temperature environments of aircraft and industrial gas-turbine engines [3,4]. The Al_2O_3 scale is believed to grow predominantly by oxygen (O) inward diffusion, combined with non-trivial aluminum (Al) outward diffusion, on alumina grain-boundaries [1,5]. Adding reactive elements (REs) such as the present focus of Ti, Zr, Hf, Y, and La, has been found to significantly reduce the growth rate of Al_2O_3 scale [1,5–7]. In particular, Hf shows exceptional effectiveness in comparison with such as Y and Zr [8,9].

The reason why REs are so effective in improving scale performance is still unclear [7], albeit numerous mechanisms have been proposed. Cho et al. [10] suggested a "site-blocking" effect on diffusion by oversized segregant cations within the TGO grain-boundaries, but this hypothesis fails to explain the fact that the smaller size Hf has a more beneficial effect than the larger size Y and Zr [8]. Heuer et al. [5,11] proposed that the segregation of REs on alumina grain-boundaries could reduce Al ionization by modifying the grain-boundary donor and acceptor states, rather than any blocking of diffusion pathways. They suggested that the grain-boundary diffusion occurs via charged jogs instead of the jumping of isolated point defects in the high-angle grain-boundaries, indicating the connection of production/annihilation of the charged Al and O vacancies, and in turn, their diffusivities on grain-boundaries. In a different paper, the present authors [8] recently showed that the metal-oxygen (M—O) bonding strength can be used to understand the effectiveness of REs in retarding the rate of alumina-scale growth. This understanding considers that the diffusion of oxygen involves the breaking of M—O bonds and that the diffusion of aluminum, in turn, relies on oxygen diffusion due to charge-compensation reactions [5,11].

Qualitative M—O bonding strength can be estimated by global properties of oxides due to the dominated M—O bonding in oxides, for example, bulk modulus, melting point, and enthalpy of formation [8]. Due to the local nature of interatomic bonding, quantitative bonding strength between two atoms of interest can be evaluated by force constants, i.e., the Hessian matrix of second derivatives of energy with respect to displacement. Force constants allow quantitative analyses of the extent of interaction or bonding between atomic pairs [12,13]. A large and positive force constant suggests strong interaction (bonding), while a negative force constant indicates that the atomic pairs tend to separate from each other. A zero force constant implies that the two atoms do not interact under the given atomic environments. We believe that force constants are more suitable to characterize bonding strength between atomic pairs in comparison with such as electronegativity which describe the tendency of an atom to attract electrons towards itself.

Force constants between every two atoms (separated by vector $\mathbf{u}$) can be represented by a 3×3 matrix (denoted by $\mathbf{F}$) with nine components. It is more convenient to quantify interatomic bonding using only the bending force constant (BFC) and especially the major contribution

* Corresponding author.
E-mail address: sus26@psu.edu (S.-L. Shang).

https://doi.org/10.1016/j.scriptamat.2018.03.002
1359-6462/

of the stretching force constant (SFC or f_s for short) [12,13]. Both BFC and SFC can be calculated using the projections of force constants **F** perpendicular and parallel to **u**, respectively. For instance,

$$f_s = \hat{\mathbf{u}} \cdot \mathbf{F} \cdot \hat{\mathbf{u}}^T \quad (1)$$

where $\hat{\mathbf{u}}$ is a 1×3 unit vector of **u** and the superscript T indicates transposition. SFC and the associated bond length between every two atoms can be used to probe the origin of alumina-scale growth affected by the reactive elements such as the present focus: Ti, Zr, Hf, Y and La. In addition, alloying constituent Cr is also studied herein since it is another key element to form a protective α-Cr_2O_3 scale, which is isostructural with α-Al_2O_3 (i.e., corundum, hexagonal close-packed).

Metal-oxygen (M—O) and metal-aluminum (M—Al) force constants in the present work are calculated based on the stable oxides (α-Al_2O_3, α-Cr_2O_3, Ti_2O_3, ZrO_2, HfO_2, Y_2O_3, and La_2O_3), dilute M in alumina (i.e., $Al_{47}MO_{72}$, see Supplementary Fig. S1), and Al_3M compounds (Al_3Cr, Al_3Ti, Al_3Zr, Al_3Hf, Al_3Y, and Al_3La); see Supplementary Table S1 for details. It is noted that force constants as a function of bond length are usually transferable across different and especially similar atomic environments [14], making the present analysis reasonable.

All force constants in the present work are calculated using the Vienna Ab initio Simulation Package (VASP) [15]. The ion-electron interaction is described by the projector augmented wave (PAW) method [16]. The exchange-correlation (X-C) energy functional is mainly described by the improved generalized gradient approximation for densely packed solids and their surfaces, i.e., PBEsol [17]. During VASP calculations, the plane wave cutoff energies are set at 500 eV for oxides (including $Al_{47}MO_{72}$) and 350 eV for Al_3M, and the spin polarization is included for all Cr-containing calculations. The selected valence-electron configurations for each element are the same as those used by Materials Project [18,19]. More details of first-principles calculations are given in Supplementary Table S1, including structural details, supercell sizes, and *k*-point meshes for sampling the Brillouin zone for each oxide, $Al_{47}MO_{72}$, or Al_3M. The Supplementary Material also shows additional results from first-principles calculations, including (i) equilibrium properties (volume V_0, bulk modulus B_0, and its pressure derivative B') fitted by a four-parameter Birch-Murnaghan equation of state (EOS) [20], see Supplementary Table S1; (ii) a comparison of the calculated and experimental V_0 and B_0 for oxides, see Supplementary Fig. S2; and (iii) phonon densities of states for oxides and Al_3M predicted by the YPHON code [21], see Supplementary Fig. S3. These properties are not the present focus but can be used to judge the quality of the present first-principles calculations.

Fig. 1a shows the calculated SFCs at 0 K for various metal-oxygen (M—O) pairs based on the stable oxides and the dilute alloying elements M in α-Al_2O_3 (i.e., $Al_{47}MO_{72}$). Note that the key SFC is the largest SFC (denoted by f_{s0}) with usually the shortest bond length r_0, for example, $f_{s0} = 5.62$ eV/Å^2 with $r_0 = 1.86$ Å for the Al—O bond in bulk Al_2O_3 (see the black and filled triangle on the left side of Fig. 1a). It can be seen that all the r_0 values of RE—O (RE = Ti, Zr, Hf, Y, and La) and Cr—O are longer than those of Al—O based on the oxides and $Al_{47}MO_{72}$ (i.e., r_0 = 1.95–2.35 Å versus r_0 = 1.80–1.86 Å). However, the largest SFC (i.e., f_{s0} with length r_0) of each RE—O or Cr—O in oxide case (see the filled symbols) is comparable with and even higher than the f_{s0} of Al—O, with the largest f_{s0} value being for the Hf—O bond followed by those of Cr—O and Zr—O. When REs or Cr dissolve in α-Al_2O_3, the largest SFCs with the shortest M—O bonds (viz., f_{s0} with length r_0) increase dramatically due mainly to the decrease of M—O bond lengths in α-Al_2O_3, especially for the Y—O and La—O bonds with f_{s0} = 3–4 eV/Å^2 increased to 13–14 eV/Å^2; see the symbols connected by the dotted lines in Fig. 1a. In addition, the increased f_{s0} values of M—O bonds in $Al_{47}MO_{72}$ (here, M ≠ Al) are more significant than the corresponding increase of f_{s0} of Al—O; see the open symbols connected by the dot-dashed lines in Fig. 1a. It should be noted that Cr may be expected to dissolve in Al_2O_3 instead of segregated to grain-boundaries [1]. However, the solubility

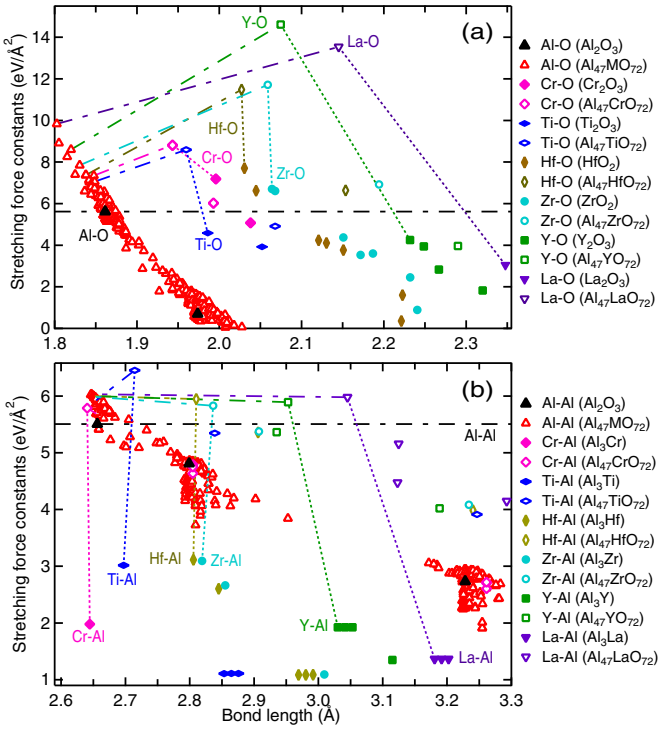

Fig. 1. Calculated stretching force constants (SFCs) at 0 K by PBEsol between the metal-oxygen (M—O) (a) and metal-aluminum (M—Al) (b) atoms based on oxides, Al_3M, and the dilute M-containing α-Al_2O_3 ($Al_{47}MO_{72}$). The dot lines connect the maximal M—O (or M—Al) SFCs in oxides (or Al_3M) and $Al_{47}MO_{72}$. The dot-dashed lines connect the maximal M—O (or M—Al) and Al—O (or Al—Al) SFCs in $Al_{47}MO_{72}$.

of REs in Al_2O_3 is very low, for example, the HfO_2 doping level was found to be 100–200 ppm in Al_2O_3 at 1400 °C [22]. In the real system, the REs are mainly segregated on the Al_2O_3 grain boundaries [1,5], where diffusion would mostly take place. In these lower-symmetry environments, the RE—O (here, RE ≠ Cr) bonds can probably relax close to their equilibrium lengths as shown in the RE-containing concentrated oxides. Correspondingly, the SFCs of these RE—O bond lengths are expected to be similar to those in the RE-containing concentrated oxides, but these SFCs may change up to the cases in $Al_{47}MO_{72}$ when REs dissolve in Al_2O_3, see Fig. 1a.

The variations of bond lengths and SFCs of M—Al in Al_3M and $Al_{47}MO_{72}$ are similar to the M—O case in Fig. 1a; see Fig. 1b. However, the Al-M SFCs (here, M ≠ Al) in Fig. 1b are much lower than the Al—Al SFCs in α-Al_2O_3, for example, f_{s0} = 2–3 eV/Å^2 for Al—M versus f_{s0} = 5.5 eV/Å^2 for Al—Al; see the symbols connected by the dotted lines in Fig. 1b. The M—Al bonding strengths in Fig. 1b are hence ignored during the analyses of alumina scale growth. Force constants in Fig. 1 suggest that the REs influence the diffusion of oxygen due to the strong RE—O bonding, and in turn, the diffusion of aluminum, on the grain-boundaries of alumina via a mechanism such as the charge compensation reactions to generated the Al/O charged vacancies proposed by Heuer et al. [5,11].

The growth of alumina scale relates to the diffusion of oxygen through the breaking of M—O bonds by exceeding the diffusion activation energy *Q* of oxygen. The *Q* values can be estimated via the global properties of oxides [8,23], since the properties of oxides are mainly controlled by the M—O bonds (see such as Supplementary Fig. S4):

$$Q \propto B_0 V_0 \propto RT_m \propto -\Delta H_{298} \quad (2)$$

where the bulk modulus B_0 and volume V_0 for the oxides of interest are shown in Supplementary Table S1, *R* is the gas constant, T_m the melting point, and ΔH_{298} the enthalpy of formation at 298 K. The introduction of Eq. (2) considers the facts that (i) the M—O bonds with shorter bond

lengths are stronger than the O—O bonds with longer bond lengths, see such as Supplementary Fig. S4 for the cases of Al_2O_3 and HfO_2; (ii) the bond stretching can be characterized by bulk modulus, and the work done in stretching bond to failure is proportional to B_0V_0 [23,24]; and (iii) heat can break bonds, causing melting (or sublimation), and the thermal energy at the melting point is RT_m for each principal vibrational mode [24]. Similar to Eq. (2), we propose that the diffusion activation energy Q used to break the M—O bonds can be characterized by the largest SFC, f_{s0} (its unit is energy per unit area such as eV/Å^2; see Fig. 1), and the associated bond length r_0,

$$Q \propto f_{s0} r_0^2 \tag{3}$$

Fig. 2a shows the variations of B_0V_0 of oxides and $f_{s0}r_0^2$ of M—O bonds in oxides as a function of equilibrium volume based on the present first-principles results by PBEsol. Both B_0V_0 and $f_{s0}r_0^2$ show that Y, Zr, and especially Hf increase the M—O bonding energy with respect to the Al—O case, whereas the La—O bonding energy is weaker. However, the predicted Cr—O and especially Ti—O bonding energies have large differences from B_0V_0 and $f_{s0}r_0^2$. For example, it shows that a faster-growing Al_2O_3 scale results from Ti addition based on $f_{s0}r_0^2$; whereas, a slower-growing Al_2O_3 scale results from Ti addition based on B_0V_0. Fig. 2b shows the measured T_m values and the $-\Delta H_{298}$ values for the oxides of interest (estimated by the SSUB5 database) [25]. Note that (i) the gas constant R in Eq. (2) is ignored since it is a constant and (ii) the unit of ΔH_{298} is energy per mole metal atoms to normalize the number of M—O bonds in oxygen-rich MO_2 and M_2O_3. Similar to the conclusions from Fig. 2a, Y, Zr, and especially Hf have unambiguously stronger M—O bonding energy than that of Al—O in terms of T_m and $-\Delta H_{298}$. In addition, Ti—O has a weaker bonding energy than Al—O. However, Cr—O has a stronger bonding energy from T_m whereas a weaker bonding energy from $-\Delta H_{298}$ with respect to the Al—O case.

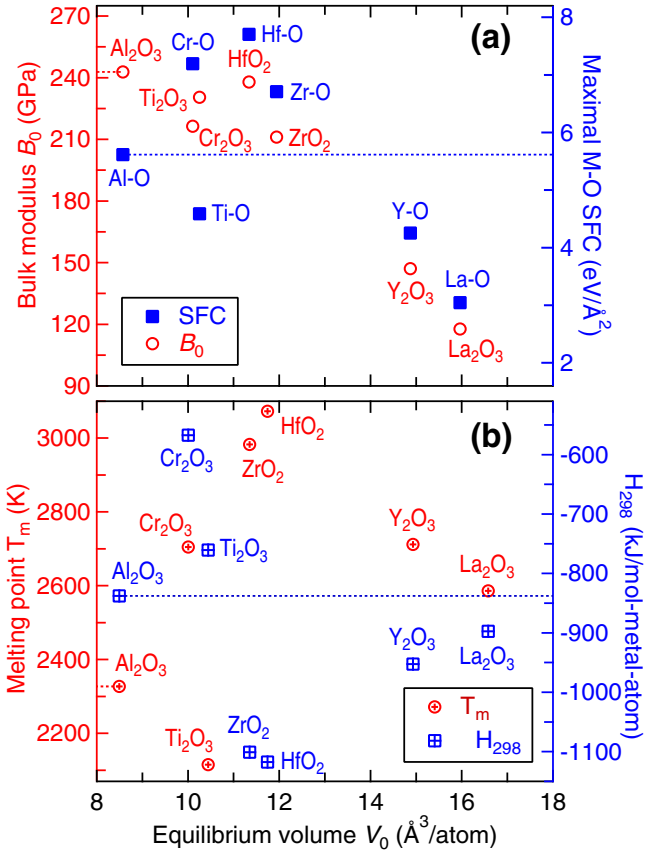

Fig. 2. Metal-oxygen bonding energies related to the stretching force constant ($f_{s0}r_0^2$) and bulk modulus (B_0V_0) predicted by PBEsol in the present work (a), and the melting point (T_m) and enthalpy of formation at 298 K ($-\Delta H_{298}$) from experiments [25] (b); see the models in Eqs. (2) and (3).

Table 1
Summary of alumina (α-Al_2O_3) scale from the slow- to fast-growing rate affected by alloying elements (REs and Cr) characterized by the metal-oxygen bonding energy, which is related to the properties of stretching force constant ($f_{s0}r_0^2$), bulk modulus (B_0V_0), melting point (T_m), and enthalpy of formation at 298 K ($-\Delta H_{298}$) of oxides; see the models in Eqs. (2) and (3).

Properties	Slow-growing scale by	Fast-growing scale by	Details in
$f_{s0}r_0^2$	Hf → Cr, Zr → Y→	Ti, La	Fig. 2a (this work)
B_0V_0	Hf → Zr → Ti → Y, Cr→	La	Fig. 2a (this work)
T_m	Hf → Zr → Cr, Y → La→	Ti	Fig. 2b (expt.) [25]
$-\Delta H_{298}$	Hf, Zr → Y → La→	Ti → Cr	Fig. 2b (expt.) [25]

Table 1 summarizes the M—O bonding energies presented in Fig. 2. It shows that all models in Eqs. (2) and (3) indicate Hf—O has the highest bonding energy, making Hf the best reactive element in retarding the growth of Al_2O_3 scale. The other beneficial REs for the slow-growing Al_2O_3 scale are Zr and Y. However, the discrepancies are for Cr, Ti and La, which may promote or retard the Al_2O_3-scale growth rate. Alloying element Cr can dissolve in Al_2O_3 [1], increasing Cr—O SFCs (see Fig. 1a), and in turn, a stronger Cr—O bonding energy. It is therefore concluded that Cr should retard the growth of Al_2O_3 scale. Reactive element La (as well as Y) has quite a large ionic size, such as r_0 = 2.35 Å for La—O versus r_0 = 1.86 Å for Al-O; see Supplementary Table S1. Any decrease of La—O bond length when La locates on the grain-boundary of Al_2O_3 will increase greatly the La—O bonding strength (see Fig. 1a). This suggests that La could retard the growth of Al_2O_3 scale. For the smaller ionic size of Ti, we conclude that Ti promotes the growth of Al_2O_3 scale to some extent.

It should be mentioned that over-doping of REs will promote the formation RE-containing oxides and hence result in an accelerated oxidation process. An optimal amount of RE addition needs to be determined by using such as thermodynamic modeling, see the approach to guide Hf-doping in the Al_2O_3-forming NiCrAl alloys [9]. Note also that the RE—O bonding strength/energy cannot explain the observation that Hf only suppressed Al diffusion during polycrystalline alumina wafers exposed to oxygen potential [26], albeit this experiment is not fully consistent with the observations in alumina scales [7].

In summary, the determination of local bonding energy between two atoms of interest has been proposed in terms of the stretching force constants (SFC), see Eq. (3). Based on force constants from first-principles phonon calculations of oxides (Al_2O_3, Cr_2O_3, Ti_2O_3, ZrO_2, HfO_2, Y_2O_3, and La_2O_3), Al_3X compounds, and the dilute M-containing $Al_{47}MO_{72}$ (M = Cr, Ti, Zr, Hf, Y, and La), we quantify the M-O bonding energies using the present SFC model. Together with the M—O bonding energies estimated from the global properties of oxides, i.e., bulk modulus, melting point, and enthalpy of formation; see the models in Eq. (2), we conclude that the slow-growing alumina scale tuned by reactive elements (REs) can be explained by the strong RE—O bonding energy. It is found that Hf is the best RE to retard the growth of alumina scale, followed by Zr, Y, and La. Our predictions are in good agreement with experimental observations [1,5,6,8,9], indicating the capability of the present SFC model to understand the slower-growing alumina scale affected by reactive elements.

Acknowledgments

This work was funded by the U.S. Department of Energy through Grant DE-FE0024056. First-principles calculations were carried out partially on the LION clusters supported by the Materials Simulation Center and the Research Computing and Cyber infrastructure unit at the Pennsylvania State University, partially on the resources of NERSC supported by the Office of Science of the U.S. DOE under Contract No. DE-AC02-05CH11231, and partially on the resources of XSEDE supported by National Science Foundation with Grant ACI-1053575.

Appendix A. Supplementary data

Supplementary data to this article can be found online at https://doi.org/10.1016/j.scriptamat.2018.03.002.

References

[1] P.Y. Hou, J. Am. Ceram. Soc. 86 (2003) 660–668.
[2] B.A. Pint, M. Treska, L.W. Hobbs, Oxid. Met. 47 (1997) 1–20.
[3] N.P. Padture, Science 296 (2002) 280–284.
[4] B.W. Veal, A.P. Paulikas, P.Y. Hou, Nat. Mater. 5 (2006) 349–351.
[5] A.H. Heuer, T. Nakagawa, M.Z. Azar, D.B. Hovis, J.L. Smialek, B. Gleeson, N.D.M. Hine, H. Guhl, H.-S. Lee, P. Tangney, W.M.C. Foulkes, M.W. Finnis, Acta Mater. 61 (2013) 6670–6683.
[6] Y. Chen, R.C. Reed, E.A. Marquis, Oxid. Met. 82 (2014) 457–467.
[7] D. Naumenko, B.A. Pint, W.J. Quadakkers, Oxid. Met. 86 (2016) 1–43.
[8] D.E. Kim, S.-L. Shang, Z.Q. Li, B. Gleeson, Z.-K. Liu, Oxid. Met. (2018) (Submitted).
[9] T. Gheno, B.-C. Zhou, A. Ross, X. Liu, G. Lindwall, Z.-K. Liu, B. Gleeson, Oxid. Met. 87 (2017) 297–310.
[10] J. Cho, H.M. Chan, M.P. Harmer, J.M. Rickman, J. Am. Ceram. Soc. 81 (2005) 3001–3004.
[11] A.H. Heuer, D.B. Hovis, J.L. Smialek, B. Gleeson, J. Am. Ceram. Soc. 94 (2011) s146–s153.
[12] S.L. Shang, L.G. Hector Jr., Y. Wang, H. Zhang, Z.K. Liu, J. Phys. Condens. Matter 21 (2009) 246001.
[13] S. Shang, Y. Wang, P. Guan, W.Y. Wang, H. Fang, T. Anderson, Z.-K. Liu, J. Mater. Chem. A 3 (2015) 8002–8014.
[14] J.Z. Liu, G. Ghosh, A. van de Walle, M. Asta, Phys. Rev. B 75 (2007) 104117.
[15] G. Kresse, J. Furthmüller, Phys. Rev. B 54 (1996) 11169–11186.
[16] G. Kresse, D. Joubert, Phys. Rev. B 59 (1999) 1758–1775.
[17] J.P. Perdew, A. Ruzsinszky, G.I. Csonka, O.A. Vydrov, G.E. Scuseria, L.A. Constantin, X. Zhou, K. Burke, Phys. Rev. Lett. 100 (2008) 136406.
[18] S.P. Ong, W.D. Richards, A. Jain, G. Hautier, M. Kocher, S. Cholia, D. Gunter, V.L. Chevrier, K.A. Persson, G. Ceder, Comput. Mater. Sci. 68 (2013) 314–319.
[19] A. Jain, S.P. Ong, G. Hautier, W. Chen, W.D. Richards, S. Dacek, S. Cholia, D. Gunter, D. Skinner, G. Ceder, K.A. Persson, APL Mater. 1 (2013) 11002.
[20] S.-L. Shang, Y. Wang, D. Kim, Z.-K. Liu, Comput. Mater. Sci. 47 (2010) 1040–1048.
[21] Y. Wang, S.-L. Shang, H. Fang, Z.-K. Liu, L.-Q. Chen, NPJ Comput. Mater. 2 (2016) 16006.
[22] Q. Wu, H.M. Chan, J.M. Rickman, M.P. Harmer, J. Am. Ceram. Soc. 98 (2015) 3346–3351.
[23] S.-L. Shang, B.-C. Zhou, W.Y. Wang, A.J. Ross, X.L. Liu, Y.-J. Hu, H.-Z. Fang, Y. Wang, Z.-K. Liu, Acta Mater. 109 (2016) 128–141.
[24] M.F. Ashby, Proc. R. Soc. A Math. Phys. Eng. Sci. 454 (1998) 1301–1321.
[25] Lehrstuhl fuer Theoretische Huettenkunde (Ed.), Scientific Group Thermodata Europe (SGTE), Landolt-Boernstein New Ser. Gr. IV, Springer, Verlag Berlin Heidelberg, 1999.
[26] T. Matsudaira, M. Wada, T. Saitoh, S. Kitaoka, Acta Mater. 59 (2011) 5440–5450.

Materials and Design 133 (2017) 39–46

Contents lists available at ScienceDirect

Materials and Design

journal homepage: www.elsevier.com/locate/matdes

Insight into γ-Ni/γ′-Ni_3Al interfacial energy affected by alloying elements

Xuan L. Liu [a], Shun-Li Shang [a,*], Yong-Jie Hu [a], Yi Wang [a], Yong Du [b], Zi-Kui Liu [a]

[a] Department of Materials Science and Engineering, The Pennsylvania State University, University Park, PA 16802, USA
[b] State Key Laboratory of Powder Metallurgy, Central South University, Changsha, Hunan 410083, PR China

HIGHLIGHTS

- Constrained relaxations are used to predict γ-Ni/γ′-Ni_3Al interfacial energy $\sigma_{\gamma/\gamma'}$.
- $\sigma_{\gamma/\gamma'}$ is the lowest when alloying elements in γ-Ni phase.
- $\sigma_{\gamma/\gamma'}$ increases when alloying elements substituting for Ni in γ′-Ni_3Al except Pt.
- Mo, W, and Re in γ phase have the largest effect and decrease $\sigma_{\gamma/\gamma'}$ to 4–5 mJ/m^2.

GRAPHICAL ABSTRACT

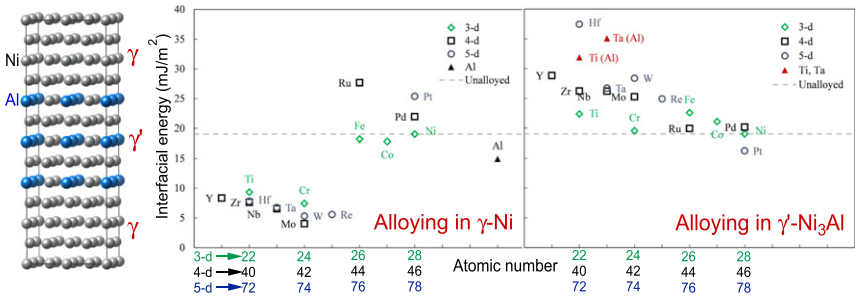

ARTICLE INFO

Article history:
Received 5 May 2017
Received in revised form 22 June 2017
Accepted 14 July 2017
Available online 15 July 2017

Keywords:
First-principles calculations
γ-Ni/γ′-Ni_3Al interfacial energy
Ni-based superalloys
Sixteen alloying elements

ABSTRACT

Interfacial energy ($\sigma_{\gamma/\gamma'}$) of the γ-Ni/γ′-Ni_3Al interface is critical to understand and design Ni-based superalloys. In the present work, a first-principles methodology with constrained relaxations has been used to study the effect of dilute alloying element (X) on $\sigma_{\gamma/\gamma'}$ of the (100) coherent interface, where the sixteen X's include Al, Co, Cr, Fe, Hf, Mo, Nb, Pd, Pt, Re, Ru, Ta, Ti, W, Y, and Zr. $\sigma_{\gamma/\gamma'} = 19$ mJ/m^2 has been predicted for the unalloyed γ/γ′ interface, agreeing well with the previous estimations. It is found that the $\sigma_{\gamma/\gamma'}$ value is the lowest when alloying element is in γ-Ni, while the addition to γ′-Ni_3Al increases $\sigma_{\gamma/\gamma'}$ due mainly to the in-plane lattice expansion. Specifically, our calculations show that alloying elements Mo, W, and Re have the largest effect on the $\sigma_{\gamma/\gamma'}$ value by decreasing it to 4–5 mJ/m^2 when partitioned to γ-Ni; Ru and Pt are shown to increase greatly the $\sigma_{\gamma/\gamma'}$ value up to 25–28 mJ/m^2 when partitioned to γ-Ni; all ternary additions substituting for Ni in γ′-Ni_3Al increase $\sigma_{\gamma/\gamma'}$ except for Pt; and for Ti and Ta, which segregate strongly to γ′-Ni_3Al and substitute for Al, the $\sigma_{\gamma/\gamma'}$ values increase to 32 and 35 mJ/m^2, respectively.

1. Introduction

Single-crystal (SX) nickel (Ni) based superalloys, one of the most important gas turbine 'hot section' materials, derive their excellent high-temperature mechanical properties from the strengthening γ′-Ni_3Al ($L1_2$) phase in its γ-Ni (face-centered cubic, fcc) matrix [1]. To improve their creep resistances, precipitate hardened SX superalloys, such as CMSX-4 (CM indicates Cannon-Muskegon Corporation), can contain up to 70% γ′ phase by volume after aging treatments [2]. The presence of cuboidal γ/γ′ microstructure is one of the responsibilities to strengthen the previous and the current generations of SX superalloys [3]. These cuboidal γ′ precipitates create γ/γ′ interfaces that have predominantly ⟨100⟩ orientations after aging [4]. Due to the very small differences in lattice parameters of the ordered γ′ phase and the disordered γ matrix (<0.5% in lattice parameters in most cases), lattice misfits are quite small [1]. This small lattice misfit creates highly coherent γ/γ′ interfaces in the microstructure.

Interfacial energies ($\sigma_{\gamma/\gamma'}$) at the γ/γ′ interface affect a vast of kinetic processes such as microstructure evaluation [5–7], nucleation, growth, and coarsening of precipitates [8,9], and grain refinement [10], which are highly influential on the final bulk mechanical properties of the SX

* Corresponding author.
E-mail address: sus26@psu.edu (S.-L. Shang).

http://dx.doi.org/10.1016/j.matdes.2017.07.028
0264-1275/

superalloys [11,12]. Attempts to model phase transformations such as solidification, coarsening, and grain growth require kinetic as well as thermodynamic data [13]. In terms of thermodynamics, coarsening is driven by lowering the overall energy of the system, which is strongly affected by the interfacial properties [14]. Investigating atomic level interactions, for example the interface itself, has always been challenging due to the length-scale limitations. High resolution techniques such as transmission electron microscopy, grazing incident X-ray scattering [15], and atom probe tomography [16] can only examine certain aspects of interfaces; leaving theoretical simulations as the main methodology [17] such as the density functional theory (DFT) based first-principles calculations.

Interfacial energies in Ni-based superalloys are mainly estimated from experiments and parametrically studied. Experimental interfacial energies are usually back-calculated using the Lifshitz-Slyozov-Wagner (LSW) and the trans interface diffusion-controlled (TIDC) theories [18] for averaged precipitate interface orientations. These methods produce the γ/γ′ interfacial energy values between 6.9 and 60 mJ/m^2 [19]. Atomistic models have only been used to look at the binary Ni—Al system. Interfacial energies at 0 K between the pristine (only Al and Ni considered) γ and γ′ interfaces have been calculated by several groups [11,16,19,20] using various computational techniques. First-principles calculations performed by Mao et al. [16] include detailed analyses of the ⟨100⟩, ⟨011⟩, and ⟨111⟩ orientations of the γ/γ′ interface as well as vibrational effects. Woodward et al. [21] recently performed a similar study and found the similar conclusions as by Mao et al. [16] concerning the sharp γ/γ′ interfaces at low temperatures. Compared to calculations, very few experimental coarsening studies relating to interfacial energies have been performed on the Ni—Al system with addition of a ternary alloying element. Some of these studies include the Ni-Al-Co [22,23] and Ni-Al-Ti [24] systems. Davies et al. [22] studied the multiple Ni-Al-Co samples and found that the small addition of Co decreases slightly the coarsening rate when compared to a binary Ni—Al sample. Additionally, the studies by Njah and Dimitrov [24] showed retardation of the coarsening process in a Ni-10.6%Al-2.5%Ti alloy. On another note, addition of transition metal to the Ni—Al system imparts the partitioning/segregation effects where elemental preference for either γ or γ′ was seen by Jia et al. [25]. It was found, in a series of Ni-Al-X (dilute X) alloys, that Ti, Ta, and Nb strongly segregate to the γ′ phase while Co, Cr, and Fe have slight preferences for the γ phase across 900–1300 °C. Also, it was shown that Mo and W prefer to be in γ′ at lower temperatures and γ at higher temperatures [25]. Therefore, it is important to understand how the change of interfacial energies when alloying elements partition to either phase.

The present work aims to investigate the effects of dilute ternary elements on the γ-Ni/γ′-Ni$_3$Al (100) interface in terms of the DFT-based first-principles calculations according to the constrained relaxations. Sixteen alloying elements are considered, including Al; the 3-d transition metals Ti, Cr, Fe, Co, and Ni; 4-d transition metals Y, Zr, Nb, Mo, Ru, and Pd; and 5-d transition metals Hf, Ta, W, Re, and Pt. In addition, magnetic effects on the γ/γ′ interfacial energy are also examined in the present work. It is worth mentioning that the focus of the present work is the effect of alloying elements on γ-Ni/γ′-Ni$_3$Al interfacial energy. Interfacial energy affected by Ni-rich fcc solid solution, such as the case of γ-(Ni-10 at.%Al)/γ′-Ni$_3$Al, is beyond the scope of the present work due to the time-consuming calculations.

2. Computational methodology

2.1. Interfacial energy via constrained relaxations

Due to the facts that the γ-Ni/γ′-Ni$_3$Al interfaces have predominantly the ⟨100⟩ orientations after aging [4] and the (100) interfacial energy is the lowest one compared with those of (110) and (111) [21], the present focus is the (100) interfacial energy. In order to create a chemical sharp interface between γ/γ′ particles, a simplification of geometry must be implemented, since the current DFT simulations are limited in size to a few nanometers with a few hundred atoms. In the present work, the 96-atom 2 × 2 × 6 supercells with respect to the fcc lattice, consisting of the repeating γ and γ′ phases connected by their (100) planes, are used (see Fig. 1); each half of the supercell consists of the γ and γ′ phases, respectively. The resulting supercells contain periodic slabs and two interfaces due to boundary constraints. There are no misfit dislocations at the interface due to forced coherency, unlike in a real interface [17].

Note that the equal amount of γ and γ′ phases in the 96-atom supercell is adopted in the present work to make the calculations easy, and there are six atomic layers to separate the two neighbor-interfaces (see Fig. 1) based on our ancillary calculations using the 24-, 48-, 72-, 96-, and 144-atom supercells. Note also that interfacial energy from first-principles will keep constant regardless of the supercell size and the ratio of γ and γ′ phases in the supercell, once the two neighbor-interfaces are separated as far as possible (such as greater than six atomic layers based on our tests).

In the present work, the (100) interfacial energy ($\sigma_{\gamma/\gamma'}$ in the unit of mJ/m^2) is calculated using [26]:

$$\sigma_{\gamma/\gamma'} = \left\{ E_{\gamma/\gamma'}(a,b,c) - \frac{1}{2}\left[E_{\gamma}(a,b,c) + E_{\gamma'}(a,b,c)\right] \right\} / 2A \quad (1)$$

where $E_{\gamma/\gamma'}(a,b,c)$ is the bulk energy of a 96-atom supercell (with lattice parameters a, b, and c) constructed by γ and γ′ phases with two interfaces separating them (see Fig. 1). $E_{\gamma}(a,b,c)$ and $E_{\gamma'}(a,b,c)$ denote the bulk energies of the corresponding 96-atom supercells that consist of only γ and γ′, respectively. A is the cross-sectional area of the supercell since interfacial energies are defined on a per unit area basis (e.g., mJ/m^2). Given the current setup, an overall composition of 12.5 at.% Al is achieved, which is representative of many experimental Ni—Al alloys [27–30].

To account for the effect of alloying elements on the interfacial energy $\sigma_{\gamma/\gamma'}$, the methodology shown in Eq. (1) is modified by using four supercells for the calculations, see Eq. (2) below. Here, two alloying elements are placed symmetrically and equivalently in relation to the two interfaces due to symmetry (for example, see the places marked by red circles in Fig. 1, more meanings about the red circles are discussed in Section 3.2), viz., each interface contains only one alloying element. For alloyed interfaces, the γ/γ′ interfacial energy with an alloying element X ($\sigma^{X}_{\gamma/\gamma'}$) is calculated by the following equation. For (two) alloying elements in the γ phase, the interfacial energy is defined as:

$$\sigma^{X}_{\gamma/\gamma'} = \left\{ \Xi_{\gamma/\gamma'}(a,b,c) - \frac{1}{2}E_{\gamma'}(a,b,c) - \left[E_{\mathrm{Alloyed},\gamma}(a,b,c) - \frac{1}{2}E_{\gamma}(a,b,c)\right] \right\} / 2A \quad (2)$$

The additional $E_{\mathrm{Alloyed},\gamma}(a,b,c)$ term is required to calculate the interaction effects on the bulk energy of the phase γ with alloying elements placed in (see Fig. 1b). Note that $\Xi_{\gamma/\gamma'}(a,b,c)$ in Eq. (2) and $E_{\gamma/\gamma'}(a,b,c)$ in Eq. (1) are bulk energies with and without alloying elements included (see Fig. 1a), respectively. In short, $E_{\gamma/\gamma'}(a,b,c)$ is employed to represent both cases in the present work. Eq. (2) shows that the chemical potential contributions of the alloying element will be *effectively* removed. Otherwise, energies between the interface-supercell and the reference supercells cannot be compared. This is done by replacing the bulk energies between the two interacting atoms with the bulk energies of a supercell that does not have the alloying elements or interactions, see Eq. (2). The same approach is also used for dilute additions to γ′. In both cases, an overall composition of 12.5% Al and 1% X (ternary element) is achieved. Alloying elements Ta and Ti are special cases in the present work as they have extremely strong tendencies to partition to the Al-site in γ′ [25,31]. Therefore, calculations are performed for the cases where Ta and Ti substitute for either Al or Ni in γ′.

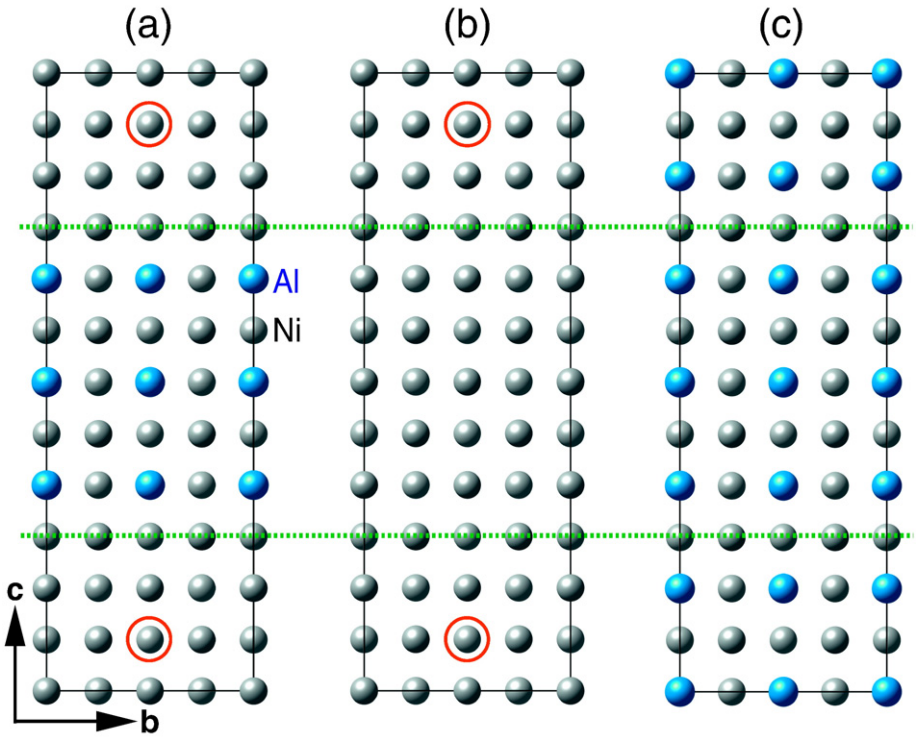

Fig. 1. 96-Atom 2 × 2 × 6 supercell with respect to the fcc lattice viewed along the a-axis direction: (a) the coherent (100) γ-Ni/γ′-Ni_3Al interface, (b) the single phase γ-Ni, and (c) the single phase γ′-Ni_3Al. The two dotted lines cross the Ni atoms indicate the two equivalent interface locations and the red circles indicate the major sites to place alloying elements (corresponding to the lowest interfacial energy, see Supplementary Fig. S2).

Lattice misfit between the γ/γ′ phases must be accounted for in the relaxation scheme. The scheme for the present calculations are implemented using suggestions from Wang et al. [26], Benedek et al. [17], and Christensen and Wahnström [32]. Woodward et al. [21] has also proven the effectiveness of this method for calculating the energetics of the γ/γ′ interface. Interface-supercells to calculate bulk energies $E_{\gamma/\gamma'}(a,b,c)$ are relaxed in all directions to the equilibrium volume. Lattice parameters for the interface-supercell will have a and b, which are between that of the pure γ and γ′ phases. Once the equilibrium volume of these interface-supercells have been found, the obtained lattice parameters a and b are used as input to calculate the $E_{\gamma}(a,b,c)$, $E_{\gamma'}(a,b,c)$, and $E_{\mathrm{Alloyed},\gamma}(a,b,c)$. These three supercells are only allowed to be relaxed perpendicular to the interface, i.e., only in the c direction with a and b fixed. Such a relaxation scheme eliminates the need to calculate strain energy during the determination of interfacial energy. Previously, multiple supercells were calculated and extrapolated to a zero-atom supercell size in order to determine the interfacial energy [19] that do not contain strain effects. As noted by Benedek et al. [17], it is possible to constrain the chemical potentials of alloying elements by precluding the strain-related contributions as well, but this method is beyond the present scope.

2.2. First-principles calculations

In the present work, all DFT-based first-principles calculations were performed using the Vienna ab-initio Simulation Package (VASP) [33]. The electron-ion interactions were described by the projector augmented-wave (PAW) method [34,35]. The generalized gradient approximation (GGA), as implemented by Perdew, Burke, and Ernzerhof (PBE) [36], was used as the exchange-correlation approximation. Additionally, the spin-state dependent correlation was described using the Vosko, Wilk and Nusair [37] interpolation for a homogenous electron gas to accurately capture ferromagnetism. A plane-wave cutoff energy of 350 eV was consistently used — a value that was >1.3 times of the highest plane wave energy cutoff for the elements in the system. Due to the large supercell sizes and convergence considerations, Γ-centered k-points scheme (usually 3 × 3 × 3) was consistently employed. The structures were relaxed by utilizing the Methfessel-Paxton method [38] in order to minimize the forces acting on the atoms. Spin-polarization was applied to account for the ferromagnetic nature of Ni and Ni_3Al.

Equilibrium volumes and the corresponding energies were obtained using an equation of state (EOS). The static energy at 0 K as a function of volume (V), $E_{0K}(V)$, was obtained using a four-parameter Birch-Murnaghan (BM4) EOS fitting [39,40]. Calculations of five volumes were used in EOS fitting according to the following procedure. An initial supercell was relaxed with respect to atomic positions, cell shape, and cell size. Thereafter, four additional volumes with up to 6% difference in lattice parameter in expansion and compression were constructed. These additional supercells with fixed volumes were relaxed with respect to atomic positions and cell shape. A similar technique was implemented for supercells that were only relaxed in the c direction with fixed volume and shape. By fitting the first-principles calculated data points to the BM4 equation, the equilibrium volume and energy (as well as the corresponding lattice parameters) can be determined [39].

3. Results and discussion

3.1. Ni—Al system

It is important to first validate the calculated results for the binary Ni—Al system and investigate how the interface affects the adjacent atomic layers (bulk phases). Differential charge density, see definition in [41,42] and the plot in Supplementary Fig. S1, indicates that the atomic Ni layer shared by γ and γ′ is the interface layer and suggests that the interface interactions are localized to the atomic layers adjacent to it. Fig. 2 as well as Table 1 compares the calculated lattice parameters with the previous computational results [16,20,39,43,44] and

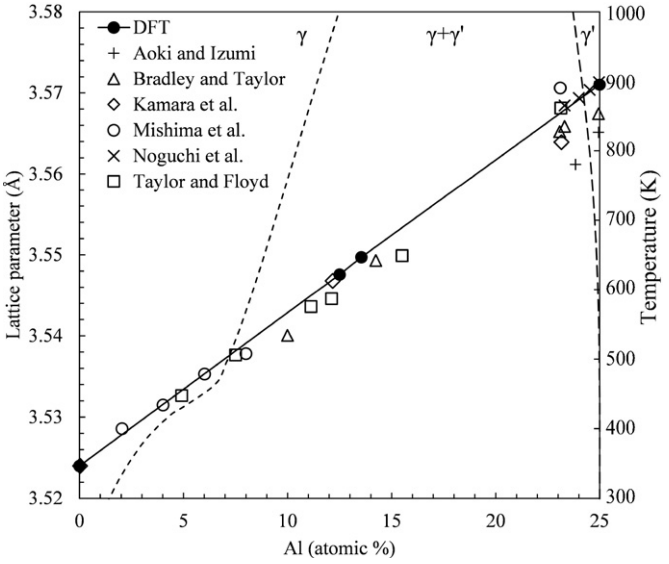

Fig. 2. First-principles calculated lattice parameters at 0 K for single phases γ-Ni and γ′-Ni_3Al, and two sharp γ/γ′ interface superlattices at different Al compositions (12.5 and 13.5 at.%). Calculated γ (short dashed) and γ′ (long dashed) phase boundaries from 300 to 1000 K are also shown using the modelled data by Dupin et al. [54]. Experimental lattice parameters are taken from Aoki and Izumi [49], Bradley and Taylor [50], Kamara et al. [46], Mishima et al. [51], Noguchi et al. [52], and Taylor and Floyd [53].

experimental data [45–53]. A good agreement is seen for the single phases as well as for the γ/γ′ interface. It is shown that the calculated in-plane lattice parameter (i.e., $a = 3.548$ Å within the *a-b* plane, see Table 1) of the interface-supercell are between those calculated for the pure γ ($a = 3.524$ Å) and γ′ ($a = 3.571$ Å); viz., γ is in tension and γ′ compression. Lattice parameter of the interface-supercell shows a 0.68% increase compared to pure Ni and 0.64% decrease relative to pure Ni_3Al. While not directly comparable, the present results for the supercell in-plane lattice parameter compares favorably to the measured lattice parameters in the γ + γ′ region modelled by Dupin et al. [54], as seen in Fig. 2. According to Eq. (1), the spin-polarized calculations for the sharp unalloyed γ/γ′ interface results in $\sigma_{\gamma/\gamma'} = 19$ mJ/m^2. This is in line with the previous first-principles results in the ranges of 20–60 mJ/m^2 [11,16,19–21], and especially, is closer to the extrapolated experimental values as discussed below.

In an effort to estimate the interfacial energy $\sigma_{\gamma/\gamma'}$ from experiments, Ardell [55] implemented a magnetic technique to measure the coarsening rates of two Ni—Al alloys with Al compositions of 12.85 and 13.14 at.%, respectively. Coarsening data at high temperatures were fitted to the LSW diffusion-controlled coarsening equation, which has been shown to work exceptionally well for the Ni—Al system, in order to back calculate the interfacial energies. The calculated energies, using both alloys, are 14.4 and 14.2 mJ/m^2 at 898 K and 988 K, respectively [55]. Chellman and Ardell [56] conducted additional studies on four Ni—Al alloys with 14.07, 15.91, 17.70, and 19.46 at.% Al at 1073 K and found the corresponding $\sigma_{\gamma/\gamma'}$ values of 6.2, 8.9, 11.9, and 8.3 mJ/m^2, respectively. Marsh and Chen [57] found the $\sigma_{\gamma/\gamma'}$ values of 16.9, 21.7, 16.6, and 10.3 mJ/m^2 at 823, 873, 923, and 973 K, respectively, for an alloy with 12.5 at.% Al. Recent studies using a trans interface diffusion-controlled model by Ardell and Ozolins [18] indicated the $\sigma_{\gamma/\gamma'}$ value may be as low as 3.71–4.29 mJ/m^2 for an alloy containing 12.86 at.% Al at high temperatures. The most recent values took into account the Gibbs energy corrections [58], yielding the $\sigma_{\gamma/\gamma'}$ values of 20 and 30 mJ/m^2 for the TIDC and LSW cases, respectively. In this approach, the second derivative of Gibbs energy for the Ni—Al system is calculated using the CALPHAD (calculation of phase diagram) approach for the real, non-ideal, case [59,60]. While there is no an "accepted" value, it can be seen that most interfacial energies hover around 10–20 mJ/m^2 for this interface at 800–1000 K.

In the present work, the Ni—Si and Ni—Ti binary systems are also investigated in the same fashion to validate the methodology. Ardell [60] predicted, using the methods previously described, that the Ni—Si and Ni—Ti γ/γ′ interfaces would have energies higher than that of Ni—Al (84–109 and 56–84 mJ/m^2, respectively). The present result for the Ni—Si interface (162 mJ/m^2), shown in Table 1, agrees well with the predictions by Ardell (84–109 mJ/m^2) [60]. However, due to the metastable $L1_2$-Ni_3Ti and its decomposition path to an ordered hexagonal phase, direct comparison with the real alloy data is difficult [60]. Albeit, the calculated Ni—Ti γ/γ′ interfacial energy in Table 1 is slightly higher than that of Ni—Al (22.1 vs. 19.0 mJ/m^2).

Through the agreement between the calculated and experimental $\sigma_{\gamma/\gamma'}$ values is satisfactory to some extent, differences exist in the calculated $\sigma_{\gamma/\gamma'}$ values in the present work (19 mJ/m^2) and the scattered values derived from coarsening data (4–20 or 30 mJ/m^2 as aforementioned), which takes into account diffuse interfaces at finite temperatures. As noted by Ardell [60], the sharp interface implemented in the present work at 0 K would represent the upper bound of the interfacial energy since interface widening and entropic contributions above 0 K will cause the interfacial excess free energy to decrease. Recent studies by Woodward et al. [21], using Monte Carlo method, found that configurational entropy near the interface and interface widening decrease the 0 K (100) interfacial energy from approximately 41 mJ/m^2 to 11 mJ/m^2 at 800–1000 K. A supplementary Ni—Al supercell was constructed with the addition of an Al atom near the interface in the γ phase to study its effects on the interfacial energy (13.5 at.% Al in Fig. 2). The dilute addition of Al is shown to decrease the interfacial energy to 15 mJ/m^2. While this is not representative of a diffuse interface, the disruption of the completely sharp interface with perfect ordering actually decreases the interfacial energy. This effect becomes amplified with the disordering of the interface at high temperatures as the interfacial width increases [21].

Table 1
Calculated lattice parameters for the single phases as well as the interface-supercell compared to the previous calculations and experiments in the Ni—Al, Ni—Si and Ni—Ti systems. Calculated interfacial energies $\sigma_{\gamma/\gamma'}$ in the present work are also shown. Additional experimental data points are shown in Fig. 2.

Phase(s)	This work (Å)	Calc. (Å)	Expt. (Å)	$\sigma_{\gamma/\gamma'}$ (mJ/m^2)
γ-Ni	3.524	3.523 [39]	3.530 [45]	
		3.520 [20]	3.524 [46]	
		3.524 [16]		
γ′-Ni_3Al	3.571	3.569 [39]	3.570 [45]	
		3.570 [20]	3.563 [46]	
		3.568 [16]		
γ′-Ni_3Si	3.507	3.512 [44]	3.506 [47]	
			3.510 [46]	
γ′-Ni_3Ti	3.612	3.618 [43]	3.589 [48]	
γ-Ni + γ′-Ni_3Al	3.548[a]	3.545 [20]	3.546 [46]	19.0
γ-Ni + γ′-Ni_3Si	3.525[a]		3.518 [46]	161.9
γ-Ni + γ′-Ni_3Ti	3.577[a]			22.1

[a] In-plane lattice parameter in the *a-b* plane.

3.2. Ni-Al-X systems

The present work includes studies on 16 alloying elements commonly found in Ni-based superalloys with their interfacial energies shown in Table 2. The positions of alloying element X occupied in the interface-supercell are examined in order to get a low $\sigma_{\gamma/\gamma'}$ value, for example, Fig. 1 shows the general Ni-site for substitution (marked by red circles) and Supplementary Fig. S2 shows the examinations with X = Re and W.

3.2.1. Effects of 3-d transition metals Ti, Cr, Fe, Co, and Ni

The effects of 3-d transition metals on the γ/γ′ in-plane lattice parameters are presented in Figs. 3 and 4. Experimental measurements on Ni-X solid solutions with dilute transition metal additions by

Table 2
Calculated (100) γ-Ni/γ′-Ni_3Al interfacial energies (unit of mJ/m^2) with the dilute 3-d, 4-d, or 5-d alloying element X (or Al) in γ or γ′ phase. Note that the Ni site in γ′-Ni_3Al is substituted by X except for the marked alloying elements Ta and Ti.

Affected by 3-d X (Al)			Affected by 4-d X			Affected by 5-d X		
X (or Al)	γ-Ni	γ′-Ni_3Al	X	γ-Ni	γ′-Ni_3Al	X	γ-Ni	γ′-Ni_3Al
Ti	9.3	22.4	Y	8.4	28.8	Hf	7.8	37.5
Cr	7.4	19.6	Zr	7.6	26.2	Ta	6.8	26.7
Fe	18.2	22.6	Nb	6.6	26.2	W	5.3	28.4
Co	17.8	21.1	Mo	4.0	25.3	Re	5.6	24.9
Ni	19.0		Ru	27.7	19.9	Pt	25.4	16.3
Ti[a]		31.9	Pd	22.0	20.2	Ta[a]		35.1
Al	14.9							

[a] Al-site in γ′-Ni_3Al is substituted by Ti or Ta.

Mishima et al. [51] are also plotted for comparison in Fig. 4(a). It can be seen that Ti increases the in-plane lattice parameter of the supercell by 0.5% when alloyed in γ, in agreement with experimental Ni—Ti solid solutions [51]. Note that the magnitude of the increase is larger for the experimental Ni-X solid solutions since γ′ is absent in those systems. Cr, Fe, and Co are shown to have small effects on the supercell lattice parameters, which is in agreement with solid solution measurements [51]. In γ′, however, Ti, Cr, and Fe that substitute for Ni all increase the in-plane lattice parameters with Ti having the largest effect. For Ti, this is no longer the case when it favorably substitutes for an Al atom due to site preference [31]. Fig. 5(a) and 6(a) show that when a ternary dilute atom resides γ, there is no direct correlation between the lattice expansion induced by the alloying element and its effects on the interfacial energy. It can be seen that Co and Fe decrease the interfacial

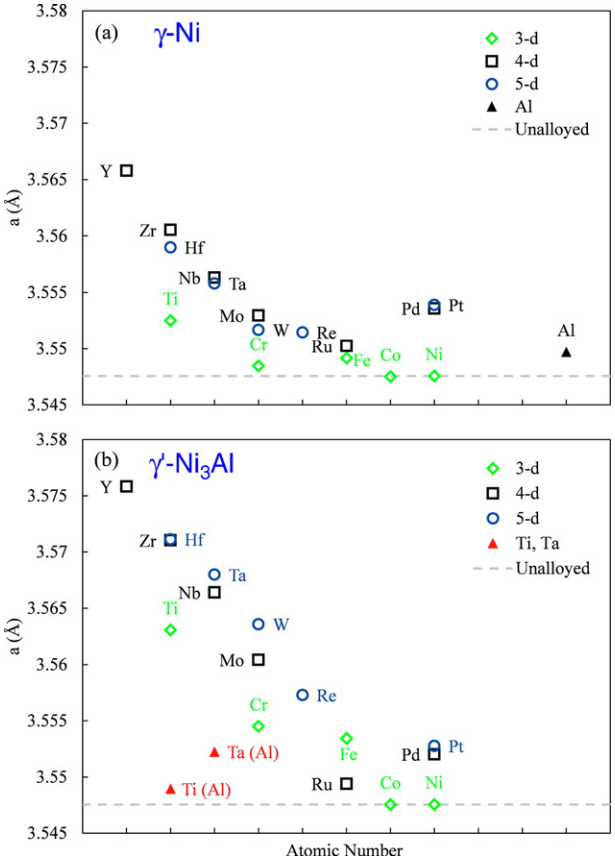

Fig. 3. In-plane lattice parameter (Å) in the *a-b* plane when a ternary element X (plotted with respect to atomic number) substitutes for a Ni atom in (a) γ-Ni and (b) γ′-Ni_3Al. Note that Al atom in γ′-Ni_3Al substituted by Ta and Ti is also calculated and shown.

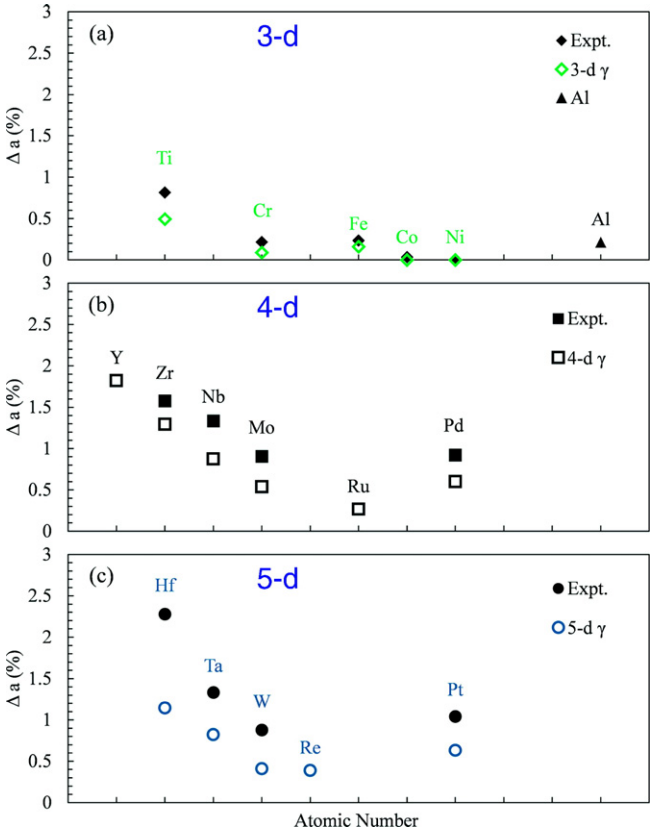

Fig. 4. Supercell in-plane lattice parameter change (%) when a 3-d (a), 4-d (b), or 5-d (c) alloying element X (plotted with respect to atomic number) substitutes for a Ni atom in the γ phase. Experimental data measured by Mishima et al. [51] are also shown for comparison.

energy by only 1–2 mJ/m^2. On the other hand, Cr and Ti in γ can lower the interfacial energy to around 10 mJ/m^2.

Shown in Figs. 5(b) and 6(b), Ti increases the interfacial energy when it resides in γ′ and substitutes for an Al or Ni atom. Interestingly, the interfacial energy is higher when it substitutes for Al, which is the favorable site for Ti [31]; the energies are expectedly different due to different site occupations. Cr, Fe, and Co all increase the interfacial energy slightly when substituting for Ni in γ′ with Cr having the smallest effect. It is also important to note that no atomistic level experimental values for interfacial energies exist on these systems. However, qualitative comparisons can be made with energies calculated using coarsening theories for a few experiments that do exist. Ardell [61] found, by applying TDIC theory to coarsening data, that a Ni-7.5Al-8.5Cr alloy yields $\sigma_{\gamma/\gamma'} = 15$ mJ/m^2, which is in the middle of present predictions (7.4 mJ/m^2 when Cr in γ-Ni and 19.6 mJ/m^2 when Cr in γ′-Ni_3Al, see also Table 2).

3.2.2. Effects of 4-d transition metals Y, Zr, Nb, Mo, Ru, and Pd

Similar effects on the in-plane lattice parameters are seen in Figs. 3 and 4 for the 4-d transition metals as seen for the 3-d. Alloying elements Y and Zr, given their large atomic sizes, distort the interface-supercell the greatest. Fig. 4(b) shows that the relative change of in-plane lattice parameter caused by the ternary addition in γ is in good agreement with the measurements [51]. Fig. 6(a) again indicates that the interfacial energy is not directly attributed to lattice expansion effects caused by the addition of the alloying elements. Pd and Mo introduce similar atomic volumes to the lattice but have opposite effects on the interfacial energy. Pd increases the interfacial energy slightly while Mo, Nb, Zr and Y all decrease it. Mo is shown to have the greatest effect on the interfacial energy as it can decrease the interfacial energy to as low as 4 mJ/m^2.

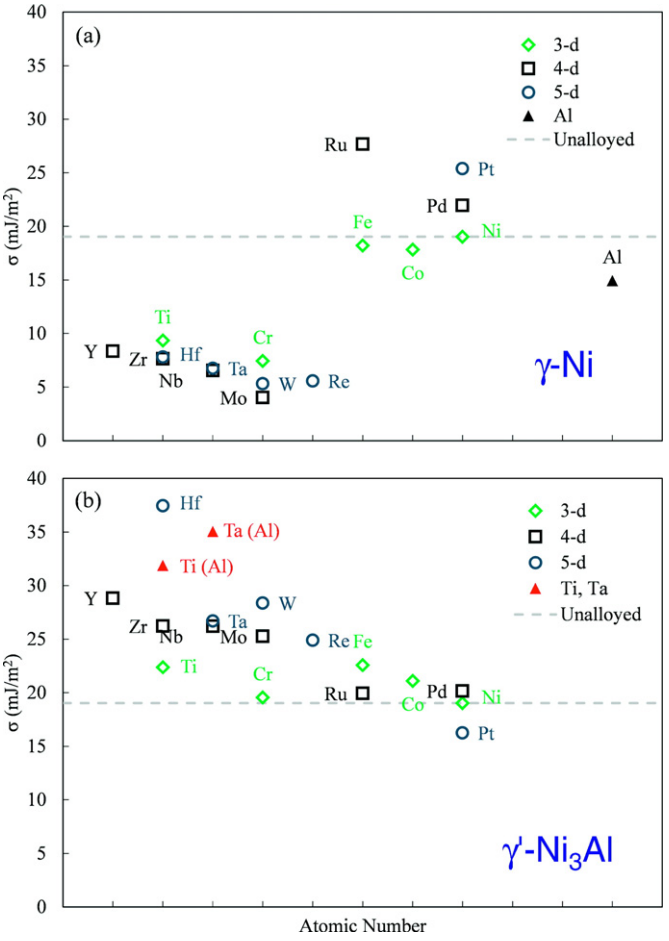

Fig. 5. γ-Ni/γ′-Ni_3Al interfacial energy (σ) when a ternary alloying element X (plotted with respect to atomic number) is in (a) γ phase or (b) γ′ phase. Note that the Ni site in γ′-Ni_3Al is substituted by X except for the marked alloying elements (Ta and Ti).

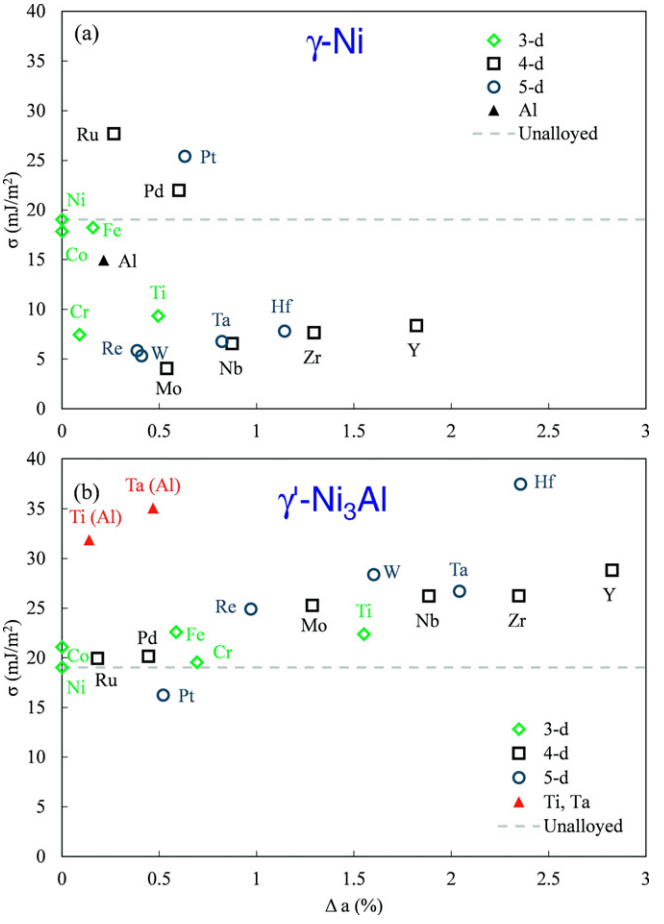

Fig. 6. γ-Ni/γ′-Ni_3Al interfacial energy (σ) when a ternary alloying element X (plotted with respect to atomic size change) is in (a) γ phase or (b) γ′ phase. Note that the Ni site in γ′-Ni_3Al is substituted by X except for the marked alloying elements (Ta and Ti).

Figs. 5(b) and 6(b) show that Y, Zr, Nb, and Mo all increase the interfacial energy when in γ′. Ru and Pd are shown to have minor effects. It is seen that lattice expansions caused by the ternary additions in the in-plane lattice parameters generally increase the interfacial energies accordingly for γ′.

3.2.3. Effects of 5-d transition metals Hf, Ta, W, Re, and Pt

Much like the 3-d and 4-d transition metals, larger atoms of 5-d transition metals increase the lattice parameters of the interface-supercells in γ. These effects are shown in Figs. 3 and 4 and are in agreement with the measurements [51]. Fig. 6(a) also present no direct correlation between the lattice expansion induced by the ternary element and the apparent interfacial energy. For example, Pt increases the interfacial energy while Re, W, Ta, and Hf all decrease this value. With the alloying element in γ′, only Pt is shown to decrease the interfacial energy. This can be attributed to the fact that the Pt—Al binary is the only system other than Ni—Al that forms a stable γ′ [62]. Ternary additions to γ′ increase the interfacial energy as a function of lattice expansion. In fact, as seen in Fig. 6(b), Hf is shown to increase the interfacial energy to 37 mJ/m^2. Much like Ti, Ta sitting on its preferred Al-site produces a higher interfacial energy. Few data points are available for comparison in these ternary systems as well. Atom probe tomography experiments were used to investigate the effect of W on a ⟨100⟩ oriented superalloy by Amouyal et al. [63], showing that W can effectively decrease the $\sigma_{\gamma/\gamma'}$ value by approximately 6 mJ/m^2, consistent with the present DFT calculations (5.3 mJ/m^2 when W in γ-Ni).

3.2.4. Magnetic effects on the γ/γ′ interfacial energy

Initial calculations without employing spin-polarization resulted in negative interfacial energies, denoting the interfaces are more stable than the bulk [63]. Previous calculations by Price and Cooper [11] also showed that removing spin-polarization lowers the energy to a point of infinite interfaces, which is unphysical. From the performed calculations, it quickly becomes apparent that magnetic spin contributes strongly to the interfacial energy. Woodward et al. [21] stated that the interfacial energies are extremely sensitive to local spin moments often induced by bad optimization of the electronic structure in elongated supercells. Therefore, special attention is paid to the magnetic convergence of each supercell where the overall magnetic moment of a supercell is checked [64]. Mao et al. [16] indicated that ferromagnetism can change the average magnetic moment of Ni atoms across the interface and decrease the (100) interfacial energy by 15 mJ/m^2. In the present work, this effect has been analyzed by looking at how alloying elements can affect the average Ni magnetic moment in γ, see Fig. 7. It is seen that ferromagnetic elements Fe and Co increase the average Ni magnetic moment and magnetic spin is not disturbed across the interface, resulting in a small change in the interfacial energy. However, alloying elements that are paramagnetic or antiferromagnetic will alter and disrupt the magnetic ordering across the interface. Alloying elements such as Mo, Re, and W that decrease the average Ni magnetic moment greatly will drop the interfacial energy. Alloying elements such as Ru and Pt are seen to have little effect on the average Ni magnetic moment and all increase the interfacial energy. Disregarding the ferromagnetic elements, there is a linear trend, for each row of elements,

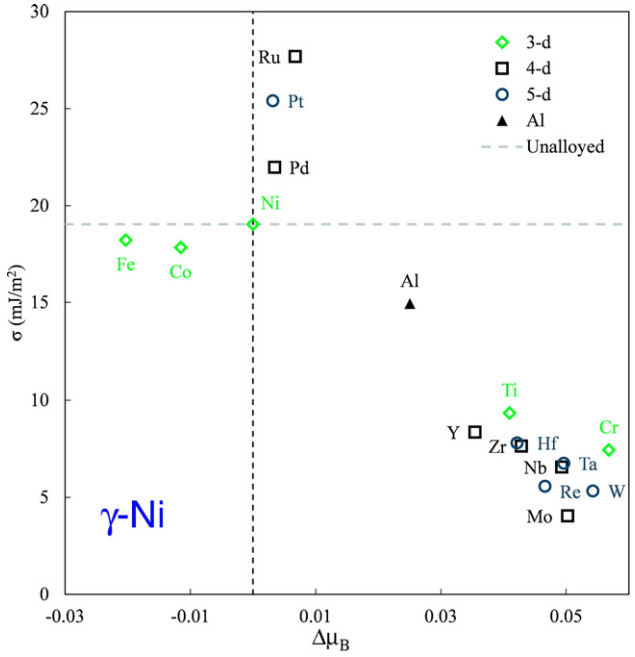

Fig. 7. γ-Ni/γ′-Ni_3Al interfacial energy (σ) when a ternary element X (plotted with respect to the change in average Ni magnetic moment, $\Delta\mu_B$) is in γ phase.

which exists between the interfacial energy and how the average Ni magnetic moment is changed with respect to alloying element. It is shown that one of the strongest contributions to the interfacial energy is indeed the magnetic spin moments presented in the system. Alloying elements which induce the largest changes in the Ni magnetic moment near the interface lead to a rapid decrease in the interfacial energy.

It should be remarked that the present interfacial energy data can also be used to understand and model complex Ni-based superalloys such as IN718 and CMSX-4 by using a general CALPHAD (calculations of phase diagram) modeling approach [65,66] or a linear combination approach as follows,

$$\sigma = \sigma_0 + \sum_i \Delta\sigma_i x_i \tag{3}$$

where σ_0 is the unalloyed interfacial energy (i.e., $\sigma_0 = \sigma_{\gamma/\gamma'} = 19$ mJ/m^2 based on the present work), and $\Delta\sigma_i$ is the change of interfacial energy with respect to σ_0 due to alloying element i, and x_i is the mole fraction of alloying element i. Note that Eq. (3) is only validated for the dilute alloying elements case. If interfacial energy as a function of temperature is expected, a quasistatic approach can be used just like the cases to predict elasticity [67] and stacking fault energy [68] at finite temperatures.

4. Conclusions

A first-principles methodology with constrained relaxations of lattice vectors for the reference states has been used to investigate the effects of dilute alloying elements on the interfacial energy $\sigma_{\gamma/\gamma'}$ of the coherent (100) γ-Ni/γ′-Ni_3Al interface with composition of Ni-12.5 at.%Al-1 at.%X. Sixteen alloying elements are considered including Al; the 3-d transition metals Ti, Cr, Fe, Co, and Ni; 4-d transition metals Y, Zr, Nb, Mo, Ru, and Pd; and 5-d transition metals Hf, Ta, W, Re, and Pt. Specially, the following conclusions have been found.

- First-principles calculations for the pure γ/γ′ interface yields a $\sigma_{\gamma/\gamma'}$ value of 19 mJ/m^2, which is in agreement with previous atomistic and experimental estimations;
- Calculations show that Mo, W, and Re have the largest effect on $\sigma_{\gamma/\gamma'}$ by decreasing it to 4–5 mJ/m^2 when partitioned to γ. Ru and Pt are shown to increase $\sigma_{\gamma/\gamma'}$ the greatest amount, up to 25–28 mJ/m^2 when partitioned to γ;
- In γ′, all ternary alloying elements substituting for Ni increase $\sigma_{\gamma/\gamma'}$ except for Pt, which decreases it to 16 mJ/m^2. Hf is seen to increase $\sigma_{\gamma/\gamma'}$ to 37 mJ/m^2;
- For Ti and Ta, which segregate strongly to γ′ and substitute for Al, $\sigma_{\gamma/\gamma'}$ values increase to 32 and 35 mJ/m^2, respectively;
- It is found that the interfacial energy is the lowest when the ternary alloying element is in γ and decrease the average Ni magnetic moment the most, such as Mo, Re, and W; and
- Ternary alloying elements to γ′ increase the interfacial energies as a function of the in-plane lattice expansion within the *a*-*b* plane.

Acknowledgements

This work was funded partially by the Department of Energy (DOE) under Grant DE-FE0024056, partially by the Office of Naval Research (ONR) under Contract No. N0014-07-1-0638, and partially by the National Natural Science Foundation of China (NSFC) with Grant No. 51429101. First-principles calculations were carried out partially on the LION clusters supported by the Materials Simulation Center and the Research Computing and Cyber infrastructure unit at the Pennsylvania State University, partially on the resources of NERSC supported by the Office of Science of the U.S. DOE under Contract No. DE-AC02-05CH11231, and partially on the resources of XSEDE supported by National Science Foundation with Grant ACI-1053575.

Appendix A. Supplementary data

Supplementary data to this article can be found online at http://dx.doi.org/10.1016/j.matdes.2017.07.028.

References

[1] R.C. Reed, The Superalloys, 1st ed. Cambridge University Press, Cambridge, UK, 2006.
[2] B.C. Wilson, J.A. Hickman, G.E. Fuchs, The effect of solution heat treatment on a single-crystal Ni-based superalloy, JOM 55 (2003) 35–40, http://dx.doi.org/10.1007/s11837-003-0158-z.
[3] S.V. Prikhodko, A.J. Ardell, Coarsening of γ′ in Ni-Al alloys aged under uniaxial compression: III. Characterization of the morphology, Acta Mater. 51 (2003) 5021–5036, http://dx.doi.org/10.1016/S1359-6454(03)00328-8.
[4] T.M. Pollock, A.S. Argon, Directional coarsening in nickel-base single crystals with high volume fractions of coherent precipitates, Acta Metall. Mater. 42 (1994) 1859–1874.
[5] N. Ta, L. Zhang, Y. Tang, W. Chen, Y. Du, Effect of temperature gradient on microstructure evolution in Ni-Al-Cr bond coat/substrate systems: a phase-field study, Surf. Coat. Technol. 261 (2015) 364–374, http://dx.doi.org/10.1016/j.surfcoat.2014.10.061.
[6] Y. Huang, Z. Mao, R.D. Noebe, D.N. Seidman, The effects of refractory elements on Ni-excesses and Ni-depletions at γ(f.c.c.)/γ′($L1_2$) interfaces in model Ni-based superalloys: atom-probe tomographic experiments and first-principles calculations, Acta Mater. 121 (2016) 288–298, http://dx.doi.org/10.1016/j.actamat.2016.09.005.
[7] S. Zhang, P. Wang, D. Li, Y. Li, Investigation of the evolution of retained austenite in Fe-13%Cr-4%Ni martensitic stainless steel during intercritical tempering, Mater. Des. 84 (2015) 385–394, http://dx.doi.org/10.1016/j.matdes.2015.06.143.
[8] I.J. Moore, M.G. Burke, E.J. Palmiere, Modelling the nucleation, growth and coarsening kinetics of γ″ ($D0_{22}$) precipitates in the Ni-base alloy 625, Acta Mater. 119 (2016) 157–166, http://dx.doi.org/10.1016/j.actamat.2016.08.027.
[9] H. Chen, Y.Q. Si, D.G. McCartney, An analytical approach to the β-phase coarsening behaviour in a thermally sprayed CoNiCrAlY bond coat alloy, J. Alloys Compd. 704 (2017) 359–365, http://dx.doi.org/10.1016/j.jallcom.2017.02.002.
[10] X. Zhao, J. Zhang, S. Liu, C. Zhao, C. Wang, X. Ren, Q. Yang, Investigation on grain refinement mechanism of Ni-based coating with $LaAlO_3$ by first-principles, Mater. Des. 110 (2016) 644–652, http://dx.doi.org/10.1016/j.matdes.2016.08.040.
[11] D.L. Price, B.R. Cooper, Full-potential LMTO calculation of Ni/Ni_3Al interface energies, Mater. Res. Soc. Symp. Proc. 408 (1995) 463–468, http://dx.doi.org/10.1557/PROC-408-463.
[12] K. Wu, S. Chen, F. Zhang, Y.A. Chang, Integrating CALPHAD into phase field simulations for practical applications, J. Phase Equilib. Diffus. 30 (2009) 571–576, http://dx.doi.org/10.1007/s11669-009-9567-1.
[13] L.-Q. Chen, Phase-field models for microstructure evolution, Annu. Rev. Mater. Res. 32 (2002) 113–140, http://dx.doi.org/10.1146/annurev.matsci.32.112001.132041.
[14] X. Li, N. Saunders, A.P. Miodownik, The coarsening kinetics of γ′ particles in nickel-based alloys, Metall. Mater. Trans. A 33 (2002) 3367–3373, http://dx.doi.org/10.1007/s11661-002-0325-9.
[15] S. Wang, H. Ye, Theoretical studies of solid–solid interfaces, Curr. Opin. Solid State Mater. Sci. 10 (2006) 26–32, http://dx.doi.org/10.1016/j.cossms.2006.06.001.

[16] Z. Mao, C. Booth-Morrison, E. Plotnikov, D.N. Seidman, Effects of temperature and ferromagnetism on the γ-Ni/γ′-Ni_3Al interfacial free energy from first principles calculations, J. Mater. Sci. 47 (2012) 7653–7659, http://dx.doi.org/10.1007/s10853-012-6399-x.

[17] R. Benedek, D.N. Seidman, C. Woodward, The effect of misfit on heterophase interface energies, J. Phys. Condens. Matter 14 (2002) 2877–2900.

[18] A.J. Ardell, V. Ozolins, Trans interface diffusion-controlled coarsening, Nat. Mater. 4 (2005) 309–316, http://dx.doi.org/10.1038/nmat1340.

[19] Y. Mishin, Atomistic modeling of the γ and γ′-phases of the Ni–Al system, Acta Mater. 52 (2004) 1451–1467, http://dx.doi.org/10.1016/j.actamat.2003.11.026.

[20] D. Farkas, Atomistic structure of the coherent Ni/Ni_3Al interface, Scr. Metall. Mater. 30 (1994) 367–371, http://dx.doi.org/10.1016/0956-716X(94)90390-5.

[21] C. Woodward, A. van de Walle, M. Asta, D.R. Trinkle, First-principles study of interfacial boundaries in Ni–Ni_3Al, Acta Mater. 75 (2014) 60–70, http://dx.doi.org/10.1016/j.actamat.2014.04.056.

[22] C.K.L. Davies, P. Nash, R.N. Stevens, Precipitation in Ni-Co-Al alloys: part 1 continuous precipitation, J. Mater. Sci. 15 (1980) 1521–1532, http://dx.doi.org/10.1007/BF00752134.

[23] C.K.L. Davies, P. Nash, R.N. Stevens, L.C. Yap, Precipitation in Ni-Co-Al alloys: part 2: discontinuous precipitation, J. Mater. Sci. 20 (1985) 2945–2957, http://dx.doi.org/10.1007/BF00553059.

[24] N. Njah, O. Dimitrov, Microstructural evolution of nickel-rich Ni-Al-Ti alloys during aging treatments: the effect of composition, Acta Metall. 37 (1989) 2559–2566, http://dx.doi.org/10.1016/0001-6160(89)90054-0.

[25] C.C. Jia, K. Ishida, T. Nishizawa, Partition of alloying elements between γ (A1), γ′ ($L1_2$), and β (B2) phases in Ni-Al base systems, Metall. Mater. Trans. A 25A (1994) 473–485, http://dx.doi.org/10.1007/BF02651589.

[26] Y. Wang, Z.-K. Liu, L.-Q. Chen, C. Wolverton, First-principles calculations of β″-Mg_5Si_6/α-Al interfaces, Acta Mater. 55 (2007) 5934–5947, http://dx.doi.org/10.1016/j.actamat.2007.06.045.

[27] A.J. Ardell, Interfacial free energies and solute diffusivities from data on Ostwald ripening, Interface Sci. 3 (1995) 119–125, http://dx.doi.org/10.1007/BF00207013.

[28] A.J. Ardell, R.B. Nicholson, The coarsening of γ′ in Ni-Al alloys, J. Phys. Chem. Solids 27 (1966) 1793–1794, http://dx.doi.org/10.1016/0022-3697(66)90110-7.

[29] C. Schmuck, P. Caron, A. Hauet, D. Blavette, Ordering and precipitation of γ′ phase in low supersaturated Ni-Cr-Al model alloy: an atomic scale investigation, Philos. Mag. A 76 (1997) 527–542, http://dx.doi.org/10.1080/01418619708214021.

[30] C.S. Jayanth, P. Nash, Review factors affecting particle-coarsening kinetics and size distribution, J. Mater. Sci. 24 (1989) 3041–3052, http://dx.doi.org/10.1007/BF01139016.

[31] C. Jiang, B. Gleeson, Site preference of transition metal elements in Ni_3Al, Scr. Mater. 55 (2006) 433–436, http://dx.doi.org/10.1016/j.scriptamat.2006.05.016.

[32] M. Christensen, G. Wahnström, Effects of cobalt intergranular segregation on interface energetics in WC-Co, Acta Mater. 53 (2004) 2199–2207, http://dx.doi.org/10.1016/j.actamat.2004.01.013.

[33] G. Kresse, J. Furthmüller, Efficient iterative schemes for ab initio total-energy calculations using a plane-wave basis set, Phys. Rev. B 54 (1996) 11169–11186, http://dx.doi.org/10.1103/PhysRevB.54.11169.

[34] P.E. Blöchl, Projector augmented-wave method, Phys. Rev. B 50 (1994) 17953–17979, http://dx.doi.org/10.1103/PhysRevB.50.17953.

[35] G. Kresse, D. Joubert, From ultrasoft pseudopotentials to the projector augmented-wave method, Phys. Rev. B 59 (1999) 1758–1775, http://dx.doi.org/10.1103/PhysRevB.59.1758.

[36] J.P. Perdew, K. Burke, M. Ernzerhof, Generalized gradient approximation made simple, Phys. Rev. Lett. 77 (1996) 3865–3868, http://dx.doi.org/10.1103/PhysRevLett.77.3865.

[37] S.H. Vosko, L. Wilk, M. Nusair, Accurate spin-dependent electron liquid correlation energies for local spin density calculations: a critical analysis, Can. J. Phys. 58 (1980) 1200–1211, http://dx.doi.org/10.1139/p80-159.

[38] M. Methfessel, A.T. Paxton, High-precision sampling for Brillouin-zone integration in metals, Phys. Rev. B 40 (1989) 3616–3621, http://dx.doi.org/10.1103/PhysRevB.40.3616.

[39] S.L. Shang, Y. Wang, D. Kim, Z.K. Liu, First-principles thermodynamics from phonon and Debye model: application to Ni and Ni_3Al, Comput. Mater. Sci. 47 (2010) 1040–1048.

[40] F. Birch, Finite elastic strain of cubic crystals, Phys. Rev. 71 (1947) 809–824, http://dx.doi.org/10.1103/PhysRev.71.809.

[41] S.L. Shang, W.Y. Wang, B.C. Zhou, Y. Wang, K.A. Darling, L.J. Kecskes, S.N. Mathaudhu, Z.K. Liu, Generalized stacking fault energy, ideal strength and twinnability of dilute Mg-based alloys: a first-principles study of shear deformation, Acta Mater. 67 (2014) 168–180, http://dx.doi.org/10.1016/j.actamat.2013.12.019.

[42] W.Y. Wang, S.L. Shang, Y. Wang, K.A. Darling, S.N. Mathaudhu, X.D. Hui, Z.K. Liu, Electron localization morphology of the stacking faults in Mg: a first-principles study, Chem. Phys. Lett. 551 (2012) 121–125, http://dx.doi.org/10.1016/j.cplett.2012.09.028.

[43] Y. Cao, J. Zhu, Y. Liu, Z. Lai, Z. Nong, First-principles studies of the structural, elastic, electronic and thermal properties of γ′-Ni_3Ti, Phys. B Condens. Matter 412 (2013) 45–49, http://dx.doi.org/10.1016/j.physb.2012.12.020.

[44] D. Connétable, O. Thomas, First-principles study of nickel-silicides ordered phases, J. Alloys Compd. 509 (2011) 2639–2644, http://dx.doi.org/10.1016/j.jallcom.2010.10.118.

[45] P. Villars, L.D. Calvert, Pearson's Handbook of Crystallographic Data for Intermetallic Phases, American Society for Metals, Metals Park, Ohio, 1986http://dx.doi.org/10.1002/crat.2170221117.

[46] A.B. Kamara, A.J. Ardell, C.N.J. Wagner, Lattice misfits in four binary Ni-Base γ/γ′ alloys at ambient and elevated temperatures, Metall. Mater. Trans. A 27 (1996) 2888–2896, http://dx.doi.org/10.1007/BF02663837.

[47] Y. Oya, T. Suzuki, The nickel-rich portion of the Ni-Si phase diagram, Z. Metallkd. 74 (1983) 21–24.

[48] J.R. Mihalisin, R.F. Decker, Phase transformations in nickel-rich nickel-titanium- aluminum alloys, Trans. Metall. Soc. AIME. 218 (1960) 507–515.

[49] K. Aoki, O. Izumi, Defect structures and long-range-order parameters in off-stoichiometric Ni_3Al, Phys. Status Solidi 32 (1975) 657–664, http://dx.doi.org/10.1002/pssa.2210320240.

[50] A.J. Bradley, A. Taylor, An X-ray analysis of the nickel-aluminium system, Proc. R. Soc. Lond. A Math. Phys. Eng. Sci. 159 (1937) 56–72, http://dx.doi.org/10.1098/rspa.1937.0056.

[51] Y. Mishima, S. Ochiai, T. Suzuki, Lattice parameters of Ni(γ), Ni_3Al(γ′) and Ni_3Ga(γ′) solid solutions with additions of transition and B-subgroup elements, Acta Metall. 33 (1985) 1161–1169, http://dx.doi.org/10.1016/0001-6160(85)90211-1.

[52] O. Noguchi, Y. Oya, T. Suzuki, The effect of nonstoichiometry on the positive temperature dependence of strength of Ni_3Al and Ni_3Ga, Metall. Trans. A. 12 (1981) 1647–1653, http://dx.doi.org/10.1007/BF02643570.

[53] A. Taylor, R.W. Floyd, The constitution of nickel-rich alloys of the nickel-titanium-aluminum system, J. Inst. Met. 81 (1952) 25–32.

[54] N. Dupin, I. Ansara, B. Sundman, Thermodynamic re-assessment of the ternary system Al-Cr-Ni, Calphad 25 (2001) 279–298, http://dx.doi.org/10.1016/S0364-5916(01)00049-9.

[55] A.J. Ardell, An application of the theory of particle coarsening: the γ′ precipitate in Ni-Al alloys, Acta Metall. 16 (1968) 511–516, http://dx.doi.org/10.1016/0001-6160(68)90125-9.

[56] D. Chellman, A. Ardell, The coarsening of γ′ precipitates at large volume fractions, Acta Metall. 22 (1974) 577–588, http://dx.doi.org/10.1016/0001-6160(74)90155-2.

[57] C. Marsh, H. Chen, An in situ X-ray diffraction study of precipitation from a supersaturated solid solution: the γ′ precipitate in a Ni-12.5 at.% A1 alloy, Acta Metall. Mater. 38 (1990) 2287–2298, http://dx.doi.org/10.1016/0956-7151(90)90096-Y.

[58] H.A. Calderon, P.W. Voorhees, J.L. Murray, G. Kostorz, Ostwald ripening in concentrated alloys, Acta Metall. Mater. 42 (1994) 991–1000, http://dx.doi.org/10.1016/0956-7151(94)90293-3.

[59] I. Ansara, N. Dupin, H.L. Lukas, B. Sundman, Thermodynamic assessment of the Al-Ni system, J. Alloys Compd. 247 (1997) 20–30, http://dx.doi.org/10.1016/S0925-8388(96)02652-7.

[60] A.J. Ardell, A1-$L1_2$ interfacial free energies from data on coarsening in five binary Ni alloys, informed by thermodynamic phase diagram assessments, J. Mater. Sci. 46 (2011) 4832–4849, http://dx.doi.org/10.1007/s10853-011-5395-x.

[61] A.J. Ardell, Trans interface-diffusion-controlled coarsening of γ′ precipitates in ternary Ni–Al–Cr alloys, Acta Mater. 61 (2013) 7828–7840, http://dx.doi.org/10.1016/j.actamat.2013.09.021.

[62] A.J. McAlister, D.J. Kahan, The Al—Pt (aluminum-platinum) system, Bull. Alloy Phase Diagr. 7 (1986) 47–51, http://dx.doi.org/10.1007/BF02874982.

[63] Y. Amouyal, Z. Mao, D.N. Seidman, Segregation of tungsten at γ′($L1_2$)/γ(fcc) interfaces in a Ni-based superalloy: an atom-probe tomographic and first-principles study, Appl. Phys. Lett. 93 (2008) 201905, http://dx.doi.org/10.1063/1.3026745.

[64] V.R. Manga, J.E. Saal, Y. Wang, V.H. Crespi, Z.-K. Liu, Magnetic perturbation and associated energies of the antiphase boundaries in ordered Ni_3Al, J. Appl. Phys. 108 (2010) 103509, http://dx.doi.org/10.1063/1.3513988.

[65] S. Shang, Y. Wang, Y. Du, M.A. Tschopp, Z.-K. Liu, Integrating computational modeling and first-principles calculations to predict stacking fault energy of dilute multicomponent Ni-base alloys, Comput. Mater. Sci. 91 (2014) 50–55, http://dx.doi.org/10.1016/j.commatsci.2014.04.040.

[66] Z.-K. Liu, First-principles calculations and CALPHAD modeling of thermodynamics, J. Phase Equilib. Diffus. 30 (2009) 517–534, http://dx.doi.org/10.1007/s11669-009-9570-6.

[67] S.-L. Shang, H. Zhang, Y. Wang, Z.-K. Liu, Temperature-dependent elastic stiffness constants of α- and θ-Al_2O_3 from first-principles calculations, J. Phys. Condens. Matter 22 (2010) 375403.

[68] S.L. Shang, C.L. Zacherl, H.Z. Fang, Y. Wang, Y. Du, Z.K. Liu, Effects of alloying element and temperature on the stacking fault energies of dilute Ni-base superalloys, J. Phys. Condens. Matter 24 (2012), 505403. http://dx.doi.org/10.1088/0953-8984/24/50/505403.

Oxid Met (2017) 87:297–310
DOI 10.1007/s11085-016-9706-0

ORIGINAL PAPER

A Thermodynamic Approach to Guide Reactive Element Doping: Hf Additions to NiCrAl

Thomas Gheno[1,3] · Bi-Cheng Zhou[2] · Austin Ross[2] · Xuan Liu[2] · Greta Lindwall[2,4] · Zi-Kui Liu[2] · Brian Gleeson[1]

Received: 20 December 2016 / Published online: 5 January 2017

Abstract A method based on thermodynamic modeling was developed to determine optimal amounts of Hf additions to Al_2O_3-forming, γ-γ' NiCrAl alloys. The alloy ability to maintain Hf in solution was set by the Hf concentration required to form HfO_2 at the oxygen activity defined by the alloy/Al_2O_3 equilibrium. This Hf tolerance decreased with increasing temperature and increased with increasing γ' fraction. The latter was due to the higher solubility of Hf in γ', compared to γ. The validity of the procedure was evaluated by oxidizing a series of NiCrAl–Hf alloys in dry air at 1000–1200 °C. The experimental results followed the predicted trends, although the Hf tolerance tended to be overestimated. The applicability of the criterion, and potential routes for improved predictability, were discussed by considering the influence of the compositional changes occurring at the metal surface during the transient and steady-state stages of the oxidation process.

Keywords Reactive elements · Thermodynamic modeling · Coatings · High-temperature oxidation

✉ Thomas Gheno
thomas.gheno@gmail.com

[1] Department of Mechanical Engineering and Materials Science, University of Pittsburgh, Pittsburgh, PA 15261, USA

[2] Department of Materials Science and Engineering, Pennsylvania State University, University Park, PA 16802, USA

[3] Present Address: DEN-Service de la Corrosion et du Comportement des Matériaux dans leur Environnement, CEA, Université Paris-Saclay, 91191 Gif-sur-Yvette, France

[4] Present Address: Materials Science and Engineering Division, National Institute of Standards and Technology, Gaithersburg, MD 20899-8555, USA

Introduction

Reactive element (RE) addition to high-temperature materials is a widespread method of improving their oxidation resistance. Mechanistic and practical aspects of RE effects have been discussed extensively in the literature; reviews are found in Refs. [1–6] for example. Most common dopants include Y, Hf and Zr in Al_2O_3-forming systems, Ce and La in Cr_2O_3-forming systems. Their influence on oxidation behavior takes multiple forms, some of which are still open to interpretation. In particular, REs are known to yield significantly slower scale growth and improved scale adhesion. Although the two effects are related since a thinner scale will produce less growth stress, RE effects on scale adhesion appear to be more important than reduced scaling rates in determining the lifetime of a thermally cycled material [7]. A commonly accepted view is that REs neutralize S impurities and thus prevent a weakening of the metal/oxide interface [8–13]. Other aspects of improved scale adhesion are system-dependent, as they are related to the metal coefficient of thermal expansion, strength and microstructure, all of which influence the stress state and integrity of the metal-oxide assemblage. In particular, RE additions are known to mitigate interfacial void formation, which is often associated with scale spallation from β-NiAl and FeCrAl systems, but not necessarily NiCrAl or Ni-base superalloys [14]. MCrAlY systems (M = Ni, Co or both) typically benefit from the formation of Y oxide particles (pegs) at the base of the Al_2O_3 scale, which are thought to improve the scale adhesion via "mechanical keying" [1], although some disagreement exists as to their actual role [6].

As beneficial as REs may be when added in the right proportion, overdoping can have detrimental consequences on oxidation resistance. Not only does overdoping increase overall scaling rates, but more critically, it produces oversized pegs which may favor scale failure during thermal cycling [15, 16], or act as initiation sites for accelerated corrosion under sulfate [17] or oxide–sulfate deposits [18]. Controlling RE additions, together with impurities such as S or C, is therefore a critical aspect of material design and manufacturing. To this end, computational thermodynamics provides a valuable tool in integrating experimental phase equilibrium data and predicting microstructures.

The present paper presents a study of Hf additions to Al_2O_3-forming NiCrAl alloys. Based on thermodynamic equilibrium in the alloy system, a simple criterion is devised to predict the maximum amount of Hf which can be added without producing HfO_2 below the Al_2O_3. The applicability of such a criterion, and potential routes for improved predictability, are discussed based on experimental results obtained with γ, γ-γ′ and γ′ alloys at 1000–1200 °C (γ and γ′ designate the fcc A1 solid solution based on Ni and the ordered cubic $L1_2$ compound based on Ni_3Al, respectively).

Experimental and Computational Procedures

Materials

The NiCrAl–Hf alloys used for the oxidation experiments were based on four NiCrAl compositions, which are plotted on an isothermal section of the Al–Cr–Ni

phase diagram in Fig. 1. These were chosen so as to obtain γ, γ-γ′ and γ′ microstructures at 1000–1200 °C with varying Cr levels, while maintaining the ability to form an Al_2O_3 scale. Nominal compositions and equilibrium phase constitutions are summarized in Tables 1 and 2, respectively. Four alloys were cast with 0.1 at.% Hf; in two cases, 0.05 at.% Hf additions were also used. These Hf levels were low enough to avoid the formation of Hf-containing intermetallics. A version of the Ni–8Cr–17Al–0.1Hf alloy was made with 0.5 at.% Si.

The ingots were made by argon arc melting, followed by drop casting into 10-mm-diameter rods which were then homogenized in vacuum for 6 h at 1200 °C plus another 48 h at 1150 °C. All processing was conducted at the Materials Preparation Center of the Ames Laboratory [20]. Compositions measured by ICP-OES (Evans Analytical Group, Liverpool, NY, USA) for selected alloys were very close to the nominal compositions, as shown in Table 1. In particular, Hf concentrations, albeit small, were controlled with satisfactory accuracy.

Specimens approximately 1 mm thick were vacuum-encapsulated in quartz capsules and annealed in a tube furnace at 1000, 1100 and 1200 °C for 217, 100 and 50 h, respectively. Based on past experience, these durations were thought to be long enough to reach thermodynamic equilibrium. The heat treatments were terminated by water quenching to retain the equilibrated microstructures.

Polished sections of the equilibrated alloys were prepared by standard metallographic procedures. Phase compositions were determined by electron probe micro-analysis (EPMA) using a JEOL JXA-8530F field emission gun instrument. The measured intensities were converted to concentrations via a built-in ZAF calibration procedure using pure metals as standards. The γ and γ′ compositions were found to be in good agreement with equilibrium values calculated from Dupin

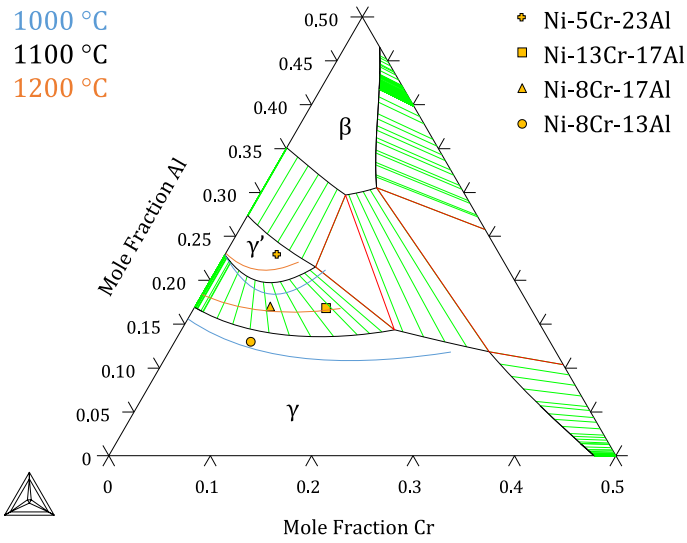

Fig. 1 Isothermal section of the Al–Cr–Ni system at 1100 °C, calculated from data in Ref. [19]. Portions of the γ/γ-γ′ and γ-γ′/γ′ phase boundaries at 1000 and 1200 °C are superimposed, and the base NiCrAl alloy compositions used for oxidation experiments are indicated (Color figure online)

Table 1 Nominal composition of the alloys, at.%, balance: Ni

Reference	Nominal				Measured (ICP-OES)			
	Cr	Al	Hf	Si	Cr	Al	Hf	Si
Ni–8Cr–13Al–0.1Hf	7.5	13	0.1					
Ni–8Cr–17Al–0.1Hf	7.5	16.8	0.1		7.6	16.6	0.098	
Ni–8Cr–17Al–0.1Hf–0.5Si	7.5	16.8	0.1	0.5	7.5	16.6	0.101	0.66
Ni–8Cr–17Al–0.05Hf	7.5	16.8	0.05		7.6	16.4	0.054	
Ni–13Cr–17Al–0.1Hf	13	16.8	0.1					
Ni–5Cr–23Al–0.1Hf	5	23	0.1					
Ni–5Cr–23Al–0.05Hf	5	23	0.05					

Included results of ICP-OES analysis of selected alloys are very close to nominal values

Table 2 Phases observed after annealing at the indicated temperatures and water quenching

	T (°C)		
	1000	1100	1200
Ni–8Cr–13Al	γ-γ′	γ	γ
Ni–8Cr–17Al	γ-γ′	γ-γ′	γ-γ′
Ni–13Cr–17Al	γ-γ′	γ-γ′	γ
Ni–5Cr–23Al	γ′	γ′	γ′

Additions of Hf or Si did not modify the phase constitutions

et al.'s Al–Cr–Ni assessment [19]. Plots of measured versus calculated concentrations are given in Fig. 2 for Ni–13Cr–17Al–0.1Hf. In γ-γ′ alloys, the Hf solubility in γ was too small to be accurately measured; however, the Hf concentration measured in γ′ was in good agreement with the Hf solubility calculated using our developmental Al–Cr–Hf–Ni database (see modeling section below).

Oxidation Experiments

Oxidation experiments were conducted at 1000, 1100 and 1200 °C using specimens equilibrated at the same temperatures. Approximately 100 μm of material was ground off the specimen surfaces using SiC paper so as to remove any layer affected by oxidation or sublimation during the equilibration treatment. The specimens were then ground down to a P1200-grit finish, degreased with detergent and ultrasonically cleaned in ethanol. This procedure was used to have well-defined, equilibrium microstructures at the alloy surfaces from the beginning of the oxidation process.

The oxidation experiments were carried out in flowing dry air using a horizontal tube furnace. Gas flow rates were set to 100 ml/min (about 2 mm/s in the hot zone), with a pressure slightly over 1 atm. Prior to a given experiment, the furnace was stabilized at the desired temperature with the specimens positioned in a cold zone of the reaction tube, and the gas allowed to flow for 2 h. To start the experiment, the specimens were magnetically pushed in the hot zone. All alloys were oxidized 20 h at the three temperatures; shorter exposures were done in selected cases. After

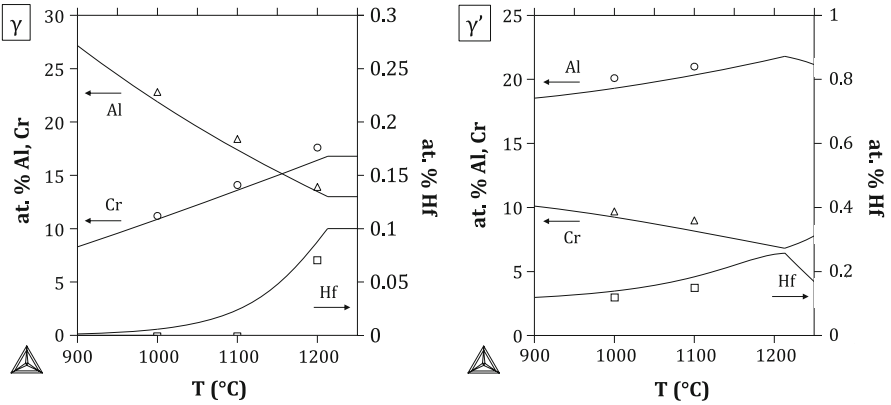

Fig. 2 Calculated phase compositions of γ-γ′ alloy Ni–13Cr–17Al–0.1Hf as a function of temperature. Compositions measured by EPMA after equilibration heat treatments (*symbols*) are included

exposure, polished sections of the reacted alloys were examined by SEM (JEOL JSM 6510) and by EPMA in some cases.

Thermodynamic Modeling

The Al–Cr–Hf–Ni system was modeled using the CALPHAD (CALculation of PHase Diagrams) method [21], where multicomponent sublattice models based on the compound energy formalism were used to describe the Gibbs free energy of the solid solution phases. Details of the modeling procedure will be described in separate publications. Briefly, the description of the Al–Cr–Ni system by Dupin et al. [19] was adopted and combined with that of the most relevant Hf-containing binary and ternary systems. The Hf-Ni system was remodeled based on the work by Wang et al. [22] with new experimental data (EPMA, DSC) and finite-temperature first-principles data (Debye, SQS) obtained by density functional theory. The Al–Hf–Ni and Cr–Hf–Ni systems were modeled by considering the ternary compounds as well as the Al and Cr solubility in the Hf_2Ni_7 phase.

The ability of NiCrAl–Hf alloys to maintain Hf in solution and hence limit the formation of pegs was determined by considering a simple variable, the Hf concentration required to form HfO_2 at the O activity defined by the alloy/Al_2O_3 equilibrium (i.e., below a thermally growing Al_2O_3 scale at steady-state). HfO_2 is more stable than Al_2O_3 at unit activity of the respective metals; yet for a sufficiently low Hf activity in an alloy, HfO_2 will not be stable at the reduced p_{O_2} prevailing below the Al_2O_3. This threshold activity is related to the energy of mixing of Hf, which also determines its solubility in a given alloy phase. Since Hf is more soluble in γ′ than in γ (Fig. 2), at a given Hf activity, the Hf concentration is larger in γ′. Thus, the Hf concentration for HfO_2 formation, or Hf tolerance, is predicted to be larger in γ′ than in γ (or in β, which dissolves very little Hf). Plots of the Hf tolerance as a function of Cr and Al concentrations at 1000–1200 °C are given in Fig. 3. All calculations were made using Thermo-Calc [23, 24].

Figure 3 shows that the Hf tolerance is affected both by phase changes and by composition changes within a given phase field. Within γ or β, increasing the Al content causes a slight increase in Hf tolerance, while Cr variations have little effect. In γ′, however, the effects of Al and Cr variations are non-monotonic and can be large. Increasing Al generally causes the Hf tolerance to increase, especially at low Cr levels. The effect is limited and locally opposite at higher Cr levels, near the γ-γ′-β triangle. Conversely, increasing Cr leads to a decrease in Hf tolerance, except at low Cr levels where an opposite effect is observed. These variations reflect the complex interplay between phase equilibria in the metal system and in the alloy-HfO_2–Al_2O_3 pseudo-ternary system: Al and Cr concentrations determine Al and Cr activities via activity coefficients in the Al–Cr–Ni ternary; the Al activity defines an equilibrium p_{O_2} at the alloy/Al_2O_3 interface, which in turn yields an Hf activity for HfO_2 formation; finally, the threshold Hf concentration (Hf tolerance) depends on both this equilibrium Hf activity and the Al and Cr concentrations, via the topology of the quaternary Al–Cr–Hf–Ni system.

Results and Discussion

General Observations

Cross-sections of the NiCrAl–0.1Hf alloys after 20-h oxidation at 1000, 1100 and 1200 °C are shown in Fig. 4. The Ni–8Cr–13Al–0.1Hf alloy was a marginal Al_2O_3-former at 1000 and 1100 °C, in that it locally formed nodules of NiO and mixed Ni–Cr–Al oxide in addition to Al_2O_3 at these temperatures. Similarly, the Ni–5Cr–23Al–0.1/0.05Hf alloys locally formed mixed oxide scales with internal Al_2O_3 at 1000 and 1100 °C. The other alloys produced thin Al_2O_3 scales at all three temperatures. Particles of a Hf-rich oxide, referred to as HfO_2 hereafter, formed in varying quantities within or below the Al_2O_3. In order to assess the results of the thermodynamic calculation, the alloys were divided into three categories, based on

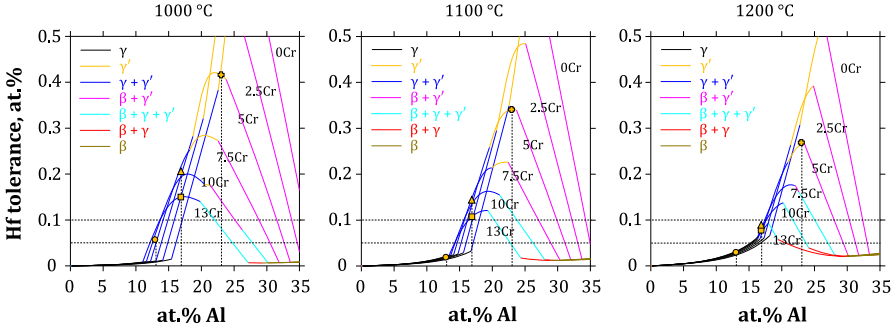

Fig. 3 Calculated Hf concentration required to form HfO_2 at the O activity defined by the alloy/Al_2O_3 equilibrium, i.e., below a growing Al_2O_3 scale, as a function of Al concentration, at varying Cr levels. This "Hf tolerance" is the maximum Hf concentration which can be included in an alloy to avoid HfO_2 formation, based on the equilibrium alloy phase compositions. The *yellow symbols* represent the base NiCrAl compositions used for oxidation experiments (see Fig. 1) (Color figure online)

whether HfO_2 particles were (1) not observed (see for example Ni–5Cr–23Al–0.1Hf at 1200 °C in Fig. 4), (2) observed locally (see Ni–8Cr–17Al–0.1Hf at 1100 °C) or (3) observed consistently (see Ni–13Cr–17Al–0.1Hf at 1200 °C).

Due to the discrete nature of the HfO_2 particles, their varying size and volume fraction, the outcome of any classification necessarily depends on the methods used. Here, Hf oxidation was deemed localized when micron-scale HfO_2 particles were spaced by more than $\sim$5 μm apart along the Al_2O_3 scale, as observed by SEM. Smaller ($\sim$50 nm), isolated HfO_2 particles were observed at high magnification, including in the case of alloys classified as "no HfO_2," and it is recognized that particles too small to be detected by SEM likely also existed. These submicron HfO_2 particles are believed to form, in part, in the transient initial stage of the oxidation process. Increasing the oxidation temperature generally accelerates the establishment of a continuous α-Al_2O_3 scale and limits the formation of transient oxides, i.e., θ-Al_2O_3 and oxides of Ni and Cr. Indeed, from 1000 to 1200 °C, the

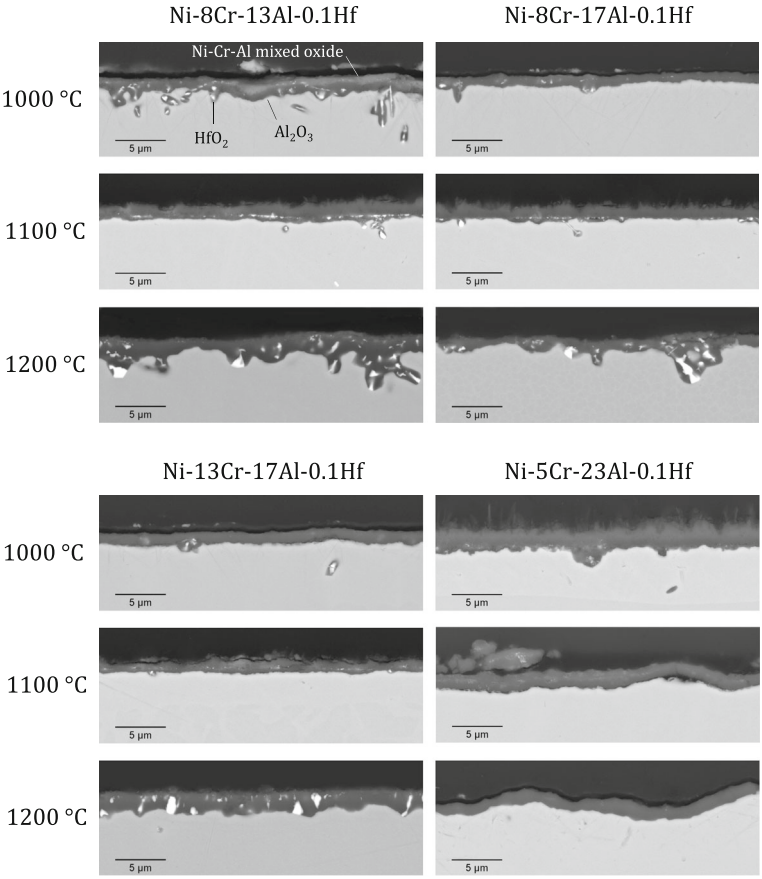

Fig. 4 Cross-sections of the Ni–8Cr–13Al–0.1Hf, Ni–8Cr–17Al–0.1Hf, Ni–13Cr–17Al–0.1Hf and Ni–5Cr–23Al–0.1Hf alloys oxidized 20 h at 1000, 1100 and 1200 °C. The bright particles visible within or below the Al_2O_3 scales consist of Hf-rich oxide, referred to as HfO_2

amount of submicron HfO_2 particles decreased (see Ni–5Cr–23Al–0.1Hf in Fig. 4), despite a predicted rise in the driving force for Hf oxidation.

Factors Affecting Hf Tolerance

The observed presence or absence of HfO_2 is compared in Fig. 5, for each alloy and temperature, with the prediction based on the Hf tolerance plots (Fig. 3). In general, the prediction was rather good, in that whenever Hf was predicted to oxidize, HfO_2 was indeed observed, and when Hf was predicted not to oxidize, HfO_2 was either not observed or observed locally. Factors affecting the Hf tolerance are now addressed individually.

- *γ/γ' phase fractions* The experimental results followed the trend expected from the equilibrium calculation, i.e., alloys with a larger γ' fraction tended to form less HfO_2, due to the larger solubility of Hf in γ' (compare Ni–8Cr–13Al–0.1Hf with Ni–8Cr–17Al–0.1Hf and Ni–5Cr–23Al–0.1Hf, and Ni–8Cr–17Al–0.05Hf with Ni–5Cr–23Al–0.05Hf).
- *Cr concentration* The Hf tolerance is predicted to slightly decrease with increasing Cr in Ni–Cr–17Al alloys. This was verified to some extent, as larger amounts of HfO_2 formed in Ni–13Cr–17Al–0.1Hf than in Ni–8Cr–17Al–0.1Hf; however, no significant difference between the two alloys was observed at 1000 or 1200 °C. Other factors affecting Hf oxidation in these alloys are discussed subsequently. It is noted that a much sharper decrease in Hf tolerance with increasing Cr concentration is predicted to occur at high Al and low Cr concentrations, within the single-phase γ' field and into the γ'-β field. This region of the phase diagram was not explored experimentally.
- *Si concentration* Although Si is not included in the thermodynamic modeling at present, previous experimental results [25] indicated that 0.5–1.0 at.% Si additions to Hf-Y co-doped γ-γ' alloys reduced Hf oxidation, suggesting that Si lowered the Hf activity. At variance with those results, it was found in the

	Prediction			Observation		
	T (°C)			T (°C)		
	1000	1100	1200	1000	1100	1200
Ni-8Cr-13Al-0.1Hf	yes	yes	yes	yes	yes	yes
Ni-8Cr-17Al-0.1Hf	no	no	yes	loc	loc	yes
Ni-8Cr-17Al-0.05Hf	no	no	no	loc	loc	loc
Ni-13Cr-17Al-0.1Hf	no	no	yes	loc	yes	yes
Ni-5Cr-23Al-0.1Hf	no	no	no	loc	loc	no
Ni-5Cr-23Al-0.05Hf	no	no	no	no	no	no

Agreement
Disagreement

Fig. 5 Summary of predicted formation of HfO_2 below an Al_2O_3 scale based on calculation shown in Fig. 3, compared with experimental observations after 20-h oxidation of equilibrated alloys. Experimental results were divided into three categories, based on whether HfO_2 particles were not observed (="no"), observed locally ("loc") or observed consistently ("yes"). See details in text (Color figure online)

present study that adding 0.5 at.% Si to Ni–8Cr–17Al–0.1Hf had no significant effect. Further investigation of the role of Si is in progress.

- *Temperature* For a given alloy, the Hf tolerance is expected to decrease with increasing temperature, and indeed, the extent of Hf oxidation in γ-γ' alloys Ni–8Cr–17Al–0.1Hf and Ni–13Cr–17Al–0.1Hf increased from 1000 to 1200 °C. This is consistent with the simultaneous decrease in γ' fraction in this temperature range. Although this trend is also expected within the single-phase γ' field, the Ni–5Cr–23Al–0.1Hf alloy formed less HfO_2 as the temperature increased. As discussed earlier, this is inferred to be due to the faster establishment of Al_2O_3 and reduced transient oxidation at higher temperatures, a factor which is independent from the thermodynamic considerations involved in the Hf tolerance calculation.

Role of Subsurface Compositional Changes Due to Oxidation

The equilibrium calculation failed to predict the local HfO_2 formation observed in the γ-γ' alloys. In examining this discrepancy, we note that while the Hf tolerance is calculated based on equilibrium phase compositions, i.e., on the composition of the alloy surfaces prior to oxidation, the composition of an alloy at the metal/oxide interface changes as oxidation proceeds, due to selective Al removal to form Al_2O_3 (if scale growth is parabolic, a constant interfacial composition is reached at steady state [26–29]). An obvious manifestation of this change is the dissolution of γ' below the scale.

Composition profiles measured by EPMA in the Ni–8Cr–13Al–0.1Hf, Ni–8Cr–17Al–0.1Hf and Ni–13Cr–17Al–0.1Hf alloys after oxidation at 1100 °C are shown in Fig. 6. In the case of Ni–8Cr–17Al–0.1Hf, the interfacial concentrations of Cr and Al are measured to be $\sim$9 and 11 at.%, respectively. If these values are used instead of the bulk concentrations, Fig. 3 predicts an Hf tolerance of about 0.01 at.%, well below 0.1 at.%. Qualitatively, this is consistent with the observed Hf oxidation in this alloy. Yet the Hf tolerance obtained this way is probably underestimated, since Hf oxidation was only local. Furthermore, a detailed analysis of depletion kinetics during the initial stage of selective oxidation shows that the interfacial alloy composition goes through a minimum before attaining the steady-state value [27, 29]. Taking this minimum into account would lead to an even larger underestimation of the Hf tolerance.

It may be argued that by the time the metal/oxide interface reaches its steady-state composition, much of the Hf initially present in the subsurface could be consumed to form HfO_2, and Al depletion is of little importance. Indeed, is Hf oxidation governed by transient processes, or does the scale equilibrate with the underlying alloy at steady-state? A related question concerns the influence of Hf segregation on the local Hf concentration at the alloy surface in the early stage of oxidation. Elucidation of these questions would require a quantitative mass balance on Hf in the scale and the alloy after varying reaction times, which would be challenging in practice given the small size of HfO_2 precipitates in the scale and the low Hf solubility in the alloy γ phase. In considering the relative importance of

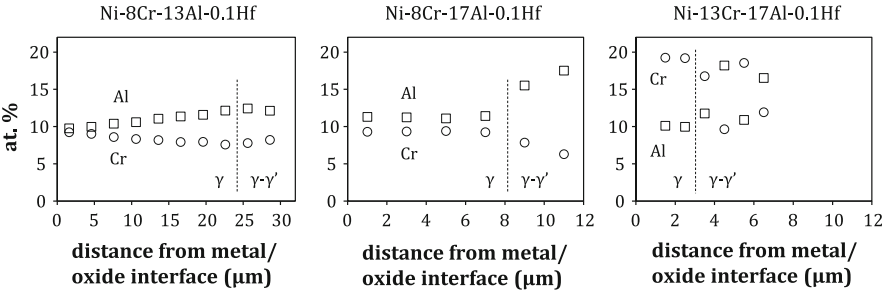

Fig. 6 Composition profiles measured by EPMA below Al_2O_3 scales after 20-h oxidation at 1100 °C. For each alloy, two profiles were recorded at random locations, and found to be consistent; only one is showed for clarity. In the case of Ni–8Cr–13Al–0.1Hf, the γ′ present in the bulk precipitated during air cooling at the end of the oxidation test. No γ′ was observed when the alloy was water-quenched. Interdiffusion work in Ref. [30] showed that both $\widetilde{D}^{Ni}_{Al,Al}$ and $\widetilde{D}^{Ni}_{Al,Cr}$ varied significantly with Al concentration but not with Cr. These thermodynamic interactions and the relative values of the main and cross terms explain why the Al depletion profiles measured here were flat for both Ni–8Cr–17Al–0.1Hf and Ni–13Cr–17Al–0.1Hf, but not for Ni–8Cr–13Al–0.1Hf

transient oxidation, we note that cases of localized Hf oxidation were observed for the γ-γ′ alloys Ni–8Cr–17Al–0.1Hf and Ni–13Cr–17Al–0.1Hf. The question of whether local Hf oxidation in the early stage is related to the initial two-phase alloy microstructure is examined next.

Early Stage Oxidation Processes

Short-term, 3-min oxidation tests were conducted on the γ-γ′ alloys Ni–8Cr–17Al–0.1Hf and Ni–13Cr–17Al–0.1Hf at 1100 °C. Based on past experience, it takes about two minutes for the specimens to heat to 1100 °C after being pushed in the hot zone in these experimental conditions. Thus, the 3-min exposure was mostly anisothermal, with only about a minute at 1100 °C.

After short-term exposure, a thin Al_2O_3 scale had formed, γ′ had started to dissolve, and HfO_2 particles were observed within the Al_2O_3 and at the metal/oxide interface (Fig. 7). The scale and subscale regions were analyzed by EPMA; an example of X-ray maps obtained from Ni–13Cr–17Al–0.1Hf is given in Fig. 8. In the Al map, a band of γ′-free material (i.e., a γ-band) is seen below the scale, which is also visible in the back-scattered image. Remarkably, the Cr concentration is not evenly distributed in this γ-band: it is lower in regions located directly above γ′ and higher above γ. Point analysis confirmed that concentrations in the γ-band were all between the bulk γ and γ′ values, but with differences of up to 3 at.% depending on whether the phase located directly below was γ or γ′. A similar trend was observed for the Hf level, which was slightly higher above γ′ than above γ.

Chemical and microstructural analysis of the subscale region suggests that following Al removal and γ′ dissolution, Cr and Hf diffusion was not fast enough to remove the original γ-γ′ partitioning, which resulted in a local Cr undersaturation and Hf supersaturation in the newly formed γ. Thus, in the first minutes of exposure, the γ-band was in a state of non-equilibrium with respect to Cr and Hf, resulting in

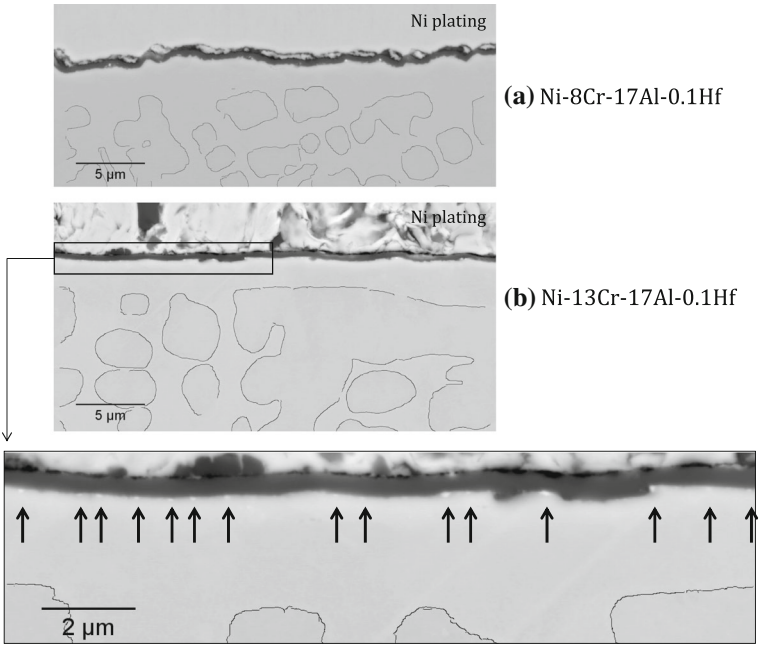

Fig. 7 Cross-sections of the **a** Ni–8Cr–17Al–0.1Hf and **b** Ni–13Cr–17Al–0.1Hf alloys oxidized 3 min at 1100 °C. An automatic edge detection routine was used to outline the γ/γ' phase boundaries. In **b** a zoomed view of the Al_2O_3 scale is shown, with *arrows* pointing to the location of HfO_2 precipitates

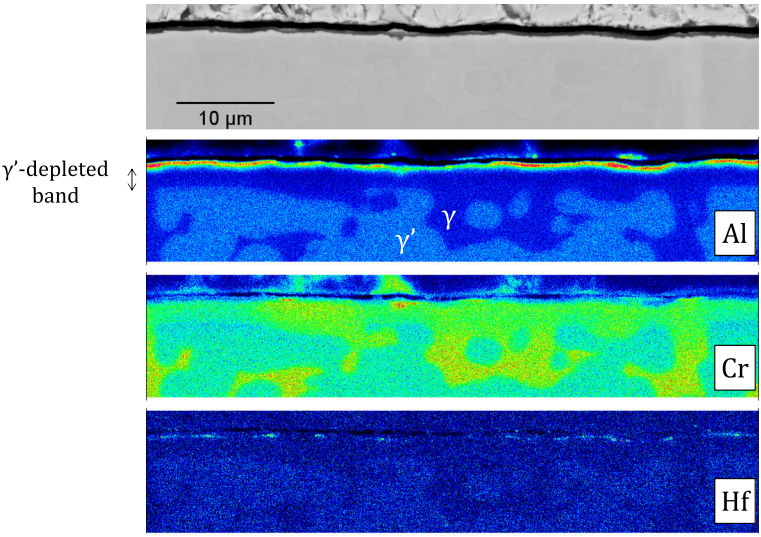

Fig. 8 Back-scattered image and corresponding Al, Cr and Hf X-ray maps recorded by EPMA after 3-min oxidation of alloy Ni–13Cr–17Al–0.1Hf at 1100 °C. The Cr concentration is non-uniform in the γ'-depleted band (Color figure online)

local variations of the Hf activity (a_{Hf}) across the prior-γ/γ′ assemblage. In particular, because of the difference of Hf solubility between γ and γ′, the phase change involved a rise of a_{Hf} in prior-γ′ regions. This is represented in Fig. 9, where a_{Hf} in the non-equilibrium γ-band was obtained by suspending γ′ in the equilibrium calculation. For each region of the γ-band, γ′ dissolution is seen to cause both an increase in a_{Hf} and a decrease in the a_{Hf} required to form HfO_2 at the p_{O_2} defined by the metal/Al_2O_3 equilibrium. The difference between these two activities represents the driving force for HfO_2 formation, and is seen to be the largest in the prior-γ′. This local supersaturation is expected to favor preferential HfO_2 nucleation. Close examination did not show any significant difference in the quantity of HfO_2 precipitates between the regions identified as prior-γ and prior-γ′ (see Fig. 7b). An even shorter exposure might provide more conclusive results, although an added complication would be that this would necessarily be anisothermal.

Whether Hf oxidation occurred preferentially in prior-γ′ regions or not, HfO_2 particles were formed during a transient stage, before a steady-state was reached. By definition, this limits the applicability of an Hf tolerance criterion based solely on thermodynamic equilibrium. However, two limiting cases can be studied, defined by the initial and steady-state alloy composition at the metal/oxide interface. Qualitatively, in an alloy with an Hf content slightly below the tolerance calculated on the basis of the initial composition, removing Al by oxidation would rapidly lower the tolerance and cause HfO_2 nucleation. The fact that Hf oxidized locally even in Ni–8Cr–17Al–0.05Hf (Figs. 4, 5) suggests that in the γ-γ′ field, reducing the Hf

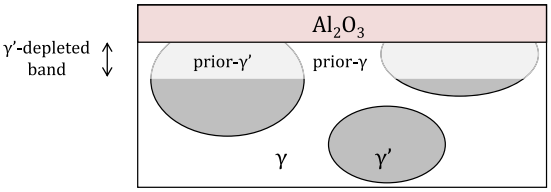

Phase φ	Definition				Hf activity at 1100 °C	
	x_{Al} EPMA, at. %	x_{Cr}	x_{Hf}	γ′	in phase φ	at φ-HfO_2-Al_2O_3 equilibrium
original γ	14	$(x^{\gamma}_{Cr})_{eq}$	$(x^{\gamma}_{Hf})_{eq}$	included	$4.2 \cdot 10^{-11}$	$4.6 \cdot 10^{-11}$
prior-γ	11	$(x^{\gamma}_{Cr})_{eq}$	$(x^{\gamma}_{Hf})_{eq}$	suspended	$3.0 \cdot 10^{-11}$	$1.8 \cdot 10^{-11}$
prior-γ′	13	$(x^{\gamma'}_{Cr})_{eq}$	$(x^{\gamma'}_{Hf})_{eq}$	suspended	$9.1 \cdot 10^{-11}$	$9.1 \cdot 10^{-12}$

Fig. 9 Hf activity changes induced by selective oxidation of Ni–13Cr–17Al–0.1Hf at 1100 °C. After 3-min exposure, the γ′-depleted band is in a non-equilibrium state, with partial retention of the original Cr and Hf partitioning, because of the slow diffusion of these elements, relative to Al. The non-equilibrium regions were modeled by suspending γ′ and setting the Cr and Hf concentrations to those of the original γ and γ′, while using experimentally measured Al concentrations. For each phase, the calculated Hf activity is compared with that required to form HfO_2 at a p_{O_2} defined by the alloy/Al_2O_3 equilibrium (which determines the Hf tolerance). The difference represents the driving force for HfO_2 formation and is largest in the prior-γ′ (Color figure online)

concentration to a level where HfO_2 is totally avoided is on the limit of being impractical, at least for the NiCrAl–Hf system considered in this study. A Calphad-guided strategy to increase the Hf tolerance would be to judiciously add elements that either increase the fraction of γ' or have a negative interaction parameter such that they cause the Hf activity to decrease. Platinum is an example [31], but for most applications it is too expensive to be a viable alloying addition. Future work by our group is being directed at determining cost-effective alloying additions that act to decrease the Hf (and Y) activity in NiCrAl-based systems. It is noted, however, that a relatively high Hf tolerance is more easily sustained for single-phase γ' compositions.

Conclusions

A criterion based on thermodynamic equilibrium was devised to predict the Hf tolerance of Hf-doped, Al_2O_3-forming NiCrAl alloys, i.e., the maximum amount of Hf that can be added without forming HfO_2 beneath the Al_2O_3 scale. This criterion was applied considering the equilibrium composition of alloys in the γ, γ-γ' and γ' fields. Since the Hf solubility in γ' is larger than that in γ, the tolerance is predicted to increase with increasing γ' fraction.

The experimental results followed this trend, although some discrepancy existed: in particular, the model failed to account for localized HfO_2 formation in γ-γ' alloys, i.e., it slightly overestimated the Hf tolerance. This is in part due to the fact that selective oxidation of Al causes γ' dissolution, which reduces the Hf tolerance. In addition, short-term oxidation tests showed that following γ' dissolution, a non-equilibrium situation prevailed in the subscale γ-band, where prior-γ' regions were supersaturated in Hf. The local rise in Hf activity increased the driving force for Hf oxidation. The specifics of HfO_2 nucleation in this non-equilibrium state remain to be elucidated.

Routes for improving the tolerance criterion can be found in the thermodynamic model and in the boundary conditions chosen to represent the oxidation process. A more complete analysis would, for example, include the evolution of HfO_2 solubility in Al_2O_3 with temperature, and account for the compositional changes due to Hf segregation to the metal surface as it is heated. Nevertheless, the approach adopted here proved useful in predicting the formation of micron-sized HfO_2 particles, which may have adverse effects in practice, in terms of Al_2O_3 adhesion during thermal cycling or reactivity with molten sulfates. Future work to optimize reactive-element doping of NiCrAl-based systems includes the expansion of the thermodynamic model to other alloying elements.

Acknowledgements This work was supported by the US Department of Energy through Grant DE-FE0024056.

References

1. D. P. Whittle and J. Stringer, *Philosophical Transactions of the Royal Society of London A* **295**, 309 (1980).

2. H. Hindam and D. P. Whittle, *Oxidation of Metals* **18**, 245 (1982).
3. J. Stringer, *Materials Science and Engineering A* **120**, 129 (1989).
4. D. P. Moon, *Materials Science and Technology* **5**, 754 (1989).
5. R. Prescott and M. J. Graham, *Oxidation of Metals* **38**, 233 (1992).
6. B. A. Pint, in *Proceedings of the John Stringer Symposium on High Temperature Corrosion*, eds P.F. Tortorelli et al (ASM International, Materials Park, OH, 2003), p. 9.
7. B. A. Pint, *Journal of the American Ceramic Society* **86**, 686 (2003).
8. A. W. Funkenbusch, J. G. Smeggil and N. S. Bornstein, *Metallurgical Transactions A* **16**, 1164 (1985).
9. J. G. Smeggil, A. W. Funkenbusch and N. S. Bornstein, *Metallurgical Transactions A* **17**, 923 (1986).
10. J. L. Smialek, *Metallurgical Transactions A* **18**, 164 (1987).
11. D. R. Sigler, *Oxidation of Metals* **32**, 337 (1989).
12. J. L. Smialek and B. A. Pint, *Materials Science Forum* **369**, 459 (2001).
13. P. Y. Hou, T. Izumi and B. Gleeson, *Oxidation of Metals* **72**, 109 (2009).
14. B. A. Pint and I. G. Wright, High Temperature Corrosion and Materials Chemistry. in *Electrochemical Society Proceedings*, vol. 98–99, eds. P. Y. Hou, et al. (Electrochemical Society, Pennington, NJ, 1998), p. 263.
15. J. D. Kuenzly and D. L. Douglass, *Oxidation of Metals* **8**, 139 (1974).
16. Z. Tang and B. Gleeson, unpublished work.
17. M. Task, B. Gleeson, F. S. Pettit and G. H. Meier, *Oxidation of Metals* **80**, 125 (2013).
18. T. Gheno and B. Gleeson, *Oxidation of Metals* (2016). doi:10.1007/s11085-016-9669-1.
19. N. Dupin, I. Ansara and B. Sundman, *Calphad* **25**, 279 (2001).
20. Materials Preparation Center, Ames Laboratory, US DOE Basic Energy Sciences, Ames, IA. https://www.ameslab.gov/mpc.
21. N. Saunders and A. P. Miodownik, *CALPHAD (Calculation of Phase Diagrams): A Comprehensive Guide* (Elsevier, Amsterdam, 1998).
22. T. Wang, Z. P. Jin and J. C. Zhao, *Zeitschrift für Metallkunde* **92**, 441 (2001).
23. B. Sundman, B. Jansson and J.-O. Andersson, *Calphad* **9**, 153 (1985).
24. J.-O. Andersson, T. Helander, L. Höglund, P. Shi and B. Sundman, *Calphad* **26**, 273 (2002).
25. Z. Li, Investigation of the minor-element effects on the oxidation behavior of γ-Ni + γ'-Ni_3Al alloys, Ph.D. Thesis, University of Pittsburgh (2015).
26. H. Y. Ku, *Journal of Applied Physics* **35**, 3391 (1964).
27. D. P. Whittle, D. J. Evans, D. B. Scully and G. C. Wood, *Acta Metallurgica* **15**, 1421 (1967).
28. B. D. Bastow, D. P. Whittle and G. C. Wood, *Oxidation of Metals* **12**, 413 (1978).
29. T. J. Nijdam, L. P. H. Jeurgens and W. G. Sloof, *Acta Materialia* **51**, 5295 (2003).
30. J. A. Nesbitt and R. W. Heckel, *Metallurgical Transactions A* **18**, 2075 (1987).
31. B. Gleeson, W. Wang, S. Hayashi and D. Sordelet, *Materials Science Forum* **461–464**, 213 (2004).

CALPHAD: Computer Coupling of Phase Diagrams and Thermochemistry 55 (2016) 88–102

Contents lists available at ScienceDirect

CALPHAD: Computer Coupling of Phase Diagrams and Thermochemistry

journal homepage: www.elsevier.com/locate/calphad

Thermodynamic remodeling of the Al–Pt system towards an assessment of the Al–Ni–Pt system

Xuan L. Liu *, Greta Lindwall [1], Richard Otis, Hojong Kim, Zi-Kui Liu

Department of Materials Science and Engineering, The Pennsylvania State University, University Park, PA 16802, United States

ARTICLE INFO

Article history:
Received 1 December 2014
Received in revised form
11 August 2016
Accepted 12 August 2016
Available online 21 August 2016

Keywords:
CALPHAD
Platinum Aluminides
Al–Pt system
Thermodynamic modeling
Corrigendum
4 sublattice model

ABSTRACT

The thermodynamic CALPHAD description of the Al–Pt system is remodeled. The four sub-lattice (4SL) model for the ordered/disordered fcc and bcc phases is adopted resulting in improved agreement with experiment and first-principles information compared to previous descriptions. First-principles calculations are performed and the results are used in addition to available experimental data as input for the modeling. Modeling results agree well with most experimental phase equilibria and thermochemical data compiled. Special attention is also paid to the metastable phase diagrams to ensure that the parameters obtained in the modeling do not present unphysical results in the metastable regime. The obtained fcc and bcc descriptions are converted to two sublattice (2SL) models to enable combination with available multi-component Ni-base superalloy descriptions. The converted Al–Pt system is extended into the Al–Ni–Pt ternary system to study its extrapolation characteristics using available thermodynamic and thermochemical data. It is found that the 2SL model is not adequate in capturing the thermodynamic behavior of the fcc-based phases found in the ternary Al–Ni–Pt system. Possible approaches for future work is discussed.

1. Introduction

The calculated phase diagrams included in the most previous publication for thermodynamic modeling of the Al–Pt system [1] fail to show the global minimum of the Al–Pt system's total energy. If the suggested thermodynamic description is used to find the global minimum, disagreement with experiments is found as the *B*2 phase becomes too stable on the Al-rich side of the phase diagram, see Fig. 1. These phase diagram thus only represents metastable phase equilibria at these conditions. Removal of vacancies from the substitutional sublattices in *A*2 and *B*2 in that description yields a phase diagram identical to the phase diagram included in the article but with $L1_0$ being stable at conditions for which *B*2 previously was stable. It is therefore realized that the energetics for all the phases need to be modified to accommodate a revision of the *B*2 phase. This work includes a remodeling of the Al–Pt system. Available experimental data and the first-principles results from the original article are accounted for. Some additional data sets are further included in the present modeling work to improve the overall thermodynamics of the system.

Thermodynamic models in this work have a direct applicability in designing oxidation/corrosion-resistant platinum-based alloys for process industries such as glass manufacturer to produce high quality glass products. In glass industry, platinum group metals are extensively employed in glass melting apparatus due to their high melting temperature and superior corrosion resistance, including refiners ($T > 1600$ °C), stirring chambers, and heating elements [2]. However, these platinum alloys suffer from high temperature degradation mechanisms where volatile oxides (e.g., PtO_2) are formed by oxidation, escape the substrate by gaseous transport, and decompose back to platinum condensates at temperatures below 650 °C [$Pt + O_2(g) \leftrightarrow PtO_2(g)$], leading to the premature failure of glass melting apparatus and/or Pt inclusion defects in the glass products [3–5]. For rational design and selection of platinum alloys and coatings for enhanced high temperature oxidation resistance (e.g., Pt–Al), accurate thermodynamic models can provide essential information on the formation of alloy phases [6–8]. Hence, special attention is paid to the modeling of fcc- and bcc-based phases in this work due to their importance in high temperature diffusion coatings such as Pt-modified *B*2-(Ni, Pt)Al or Pt-based γ/γ' [9–11].

Platinum-modified *B*2-(Ni, Pt)Al or Pt-based γ/γ' coatings can be represented by the Al–Ni–Pt ternary system and prove crucial to Ni-base superalloys as protective coating systems. Unlike overlay coatings such as MCrAlYs, Al–Ni–Pt or so-called "platinum aluminide" coatings are often diffused into the surface of superalloy substrates [12]. For example, Jackson and Rairden [13] found that

* Corresponding author.
E-mail address: xul119@psu.edu (X.L. Liu).
[1] Present address: National Institute of Standards and Technology, Gaithersburg, MD 20899, United States.

http://dx.doi.org/10.1016/j.calphad.2016.08.002
0364-5916/

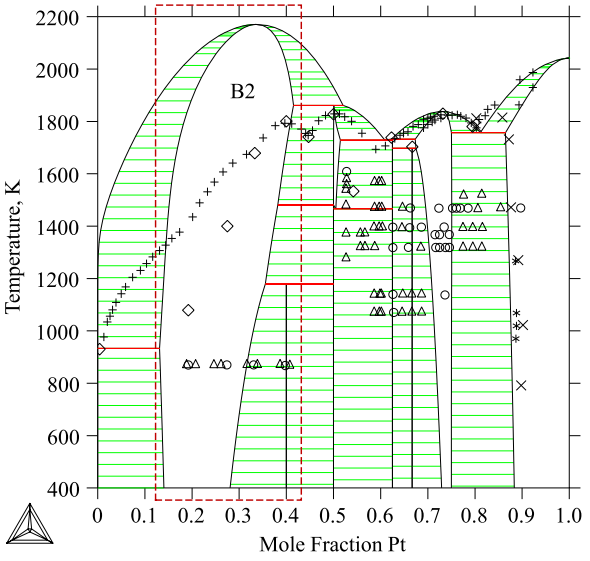

Fig. 1. (Fig. 6 in the previous publication [1]): Calculated erroneous phase (erroneous region marked in red dashed line) diagram of the Al–Pt system using the model parameters in the previous manuscript and experimental data (+) [57], (×) [67], (✱) [78], (▵, ○, ◇) [33].

sputtering Pt on an investment cast IN-738 substrate followed by a pack aluminization produced an outer layer (~25 μm) that is essentially all Al, Ni, and Pt. Recent key phase stability results from Gleeson et al. [9], Zhu et al. [14] and Grushko et al. [15] have contributed to a better understanding of the Al–Ni–Pt ternary though some discrepancies still exist [16]. Experimental [17–19] and first-principles works [11,20–22] have also attempted to shed light on this complex system. In fact, the most recent studies by Grushko et al. [15] and Grushko and Kapush [16] reveals a gamut of new Al–Ni–Pt ternary phases. One such interesting phase is the superstructure ordering of the $L1_0$-$AlNiPt_2$ into an orthorhombic phase, γ^*, with four-times larger volume of the unit cell as the Al content increases [15,16]. This new phase γ^* is believed to be the ternary extension of the Al_3Ni_5 phase and could potentially order from the $L1_0$. Modeling the ordering phenomena fcc » $L1_0$ »γ^* would require at least a 8-sublattice model under the CALPHAD framework. To complicate things even further, $B2$ transforms to $L1_0$ martensite when cooling below approximately 973 K near the γ^* phase region. The uncertainty of the phase stabilities in this region of the phase diagram provides a challenge in the current modeling efforts.

Since the thermodynamic description of the Al–Ni–Pt ternary is important for understanding the thermodynamic behavior of coating to Ni-base superalloy interactions during processing and use, a description of the Al–Ni–Pt system has also been modeled in this work and made compatible with the current Thermo-Calc Nickel Database (TCNI) [23] and the NIST Superalloy Database [24]. Previous modeling efforts on the Al–Ni–Pt [1,14,22,25] system focused on implementing 4SL order-disorder models to describe the fcc, $L1_2$ and $L1_0$ phases in one Gibbs energy framework. Lu et al. [11] and Kim [22] developed 4SL order-disorder model for the Al–Ni–Pt system based on the framework by Kusoffsky et al. [25] in the Ni-rich region of the phase diagram. Zhu et al. [14] also implemented a 4SL cluster/site approximation (CSA) model to assess the Al–Ni–Pt ternary in the Ni-rich region. For the implementation of these models into a Ni-base superalloy database such as the ones mentioned previously, conversion of those databases to 4SL models would be needed which would require an inordinate amount of work. Therefore, a new preliminary 2SL model is developed here to be compatible with the already established superalloy databases. It should be noted that the use of a 2SL model also compromises the correct phase diagram topologies seen with

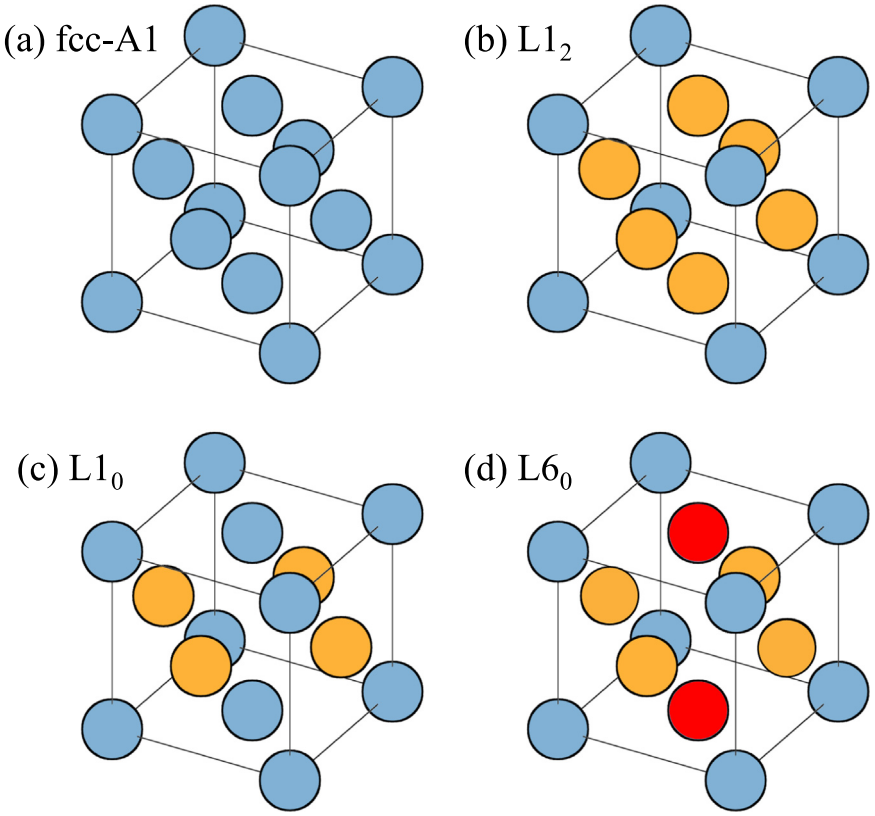

Fig. 2. The 4 fcc-based phases present in the current modeling of Al–Pt: disordered fcc-A1 (a), $L1_2$ (b), $L1_0$ (c), and $L6_0$ (d) with only two sites having the same fractions. Lattice sites with the same colors have the same compositions.

Table 1
Compilation of experimental and theoretical studies involving the Al–Pt and Al–Ni–Pt systems from 1964 to the present.

References	Experimental or theoretical method	Comments
Al–Pt		
Huch and Klemm [57]	XRD	(Phase stability) Investigation of intermetallic phases, Al–Pt liquidus across entire composition
Ferro et al. [61]	Solution calorimetry	(Thermochemical) Heats of formation of intermetallics from 18 to 94 at% Pt
Darling et al. [67]	XRD, EPMA	(Phase stability) Pt-$AlPt_3$ phase equilibria, phase boundaries/compositions by EPMA
Tonejc et al. [74]	XRD	(Phase stability) Al-rich Al–Pt non-equilibrium alloys
Chattopadhyay and Schubert [69]	XRD	(Phase stability) Investigation of intermetallic phases for Pt-rich alloys; $AlPt_3$ low and high temperature variants
Chatterji et al. [68]	XRD, EPMA	(Phase stability) Al–Pt alloys made from pack-aluminizing process; EPMA analysis of resulting layers
Chattopadhyay and Schubert [75]	XRD	(Phase stability) Low and high temperature variants of $AlPt_2$
Guex and Feschotte [70]	XRD, EPMA	(Phase stability) Phase boundaries of Al–Pt intermetallics
Jackson and Rairden [13]	EPMA	(Phase stability) Pack aluminized Pt at 1060 °C for 3 h indicates presence (detectable) of Pt, Al_3Pt_2, AlPt, $AlPt_2$ and $AlPt_3$
Bhan and Kudielka [71]	XRD	(Phase stability) High temperature XRD of arc-melted $Al_{47}Pt_{53}$ sample from 1007 to 1340 °C
Schaller [50]	EMF	(Thermochemical) Al activity in Al–Pt alloys (0–35 at% Al) were measured at 973–1073 K using CaF_2 as a solid electrolyte
Schaller [72]	XRD, Magnetic analysis	(Phase stability) Determination of the range of Al in Pt solid solution at 1000 °C
Piatti and Pellegrini [76]	XRD	(Phase stability) Determination of the $Al_{21}Pt_5$ phase and its related eutectic on the Al-Rich side of the phase diagram
Worrell and Ramanarayanan [62]	EMF	(Thermochemical) Gibbs energy of mixing of $AlPt_3$
Ellner et al. [77]	XRD	(Phase stability, Thermochemical) Phase stabilities and lattice parameter changes as a function of composition; inclusion of enthalpies of formation for Al–Pt intermetallics
McAlister and Kahan [33]	Compilation	Compilation of all Al–Pt experimental data up to 1986
Colinet et al. [63]	Calorimetry	(Thermochemical) Partial enthalpy measurements in Al–Pt at very low Pt levels; prediction of full composition range based on surrounded atom model and compared to one set of Al–Pt liquid data
Oya et al. [34]	XRD, DTA, Dilatometry	(Phase stability) Detailed studies of the phase transformations of $AlPt_3$ (LT) and $AlPt_3$ (HT) at various temperatures
Jung et al. [35]	High temperature calorimetry	(Thermochemical) AlPt enthalpy of formation at 1473 K
Meschel and Kleppa [36]	XRD, Single unit differential microcalorimetry	(Thermochemical) $AlPt_3$ and Al_3Pt_2 enthalpy of formation at 1473 K
Kobayashi et al. [37]	XRD, EMF	(Thermochemical) Al activity in Al–Pt alloys with 35, 42, and 55 at% Al using CaF_2 as a solid electrolyte
Nanko et al. [38]	XRD, EPMA, EMF	(Phase stability, Thermochemical) Al activity in Al–Pt alloys with 4.6, 9.4, and 13.1 at% Al using CaF_2 as a solid electrolyte
de Waal and Pretorius [39]	NMP	(Phase stability) Phase stability in vacuum deposited Al–Pt diffusion couples; effective heat of formation model
Völkl et al. [40]	XRD, EPMA	(Phase stability) Phase stability of arc melted $Al_{15}Pt_{85}$ samples heat treated at 1300 (96 h) and 1500 °C (48 h)
Douglas et al. [41]	EDS, HRTEM	(Phase stability) Phase stability of arc melted $Al_{14}Pt_{86}$ samples heat treated 1350 °C (96 h)
Tshawe [42] – Masters Thesis	EDS, XRD	(Phase stability) Phase stability studies of mostly Pt-rich compositions using arc melted samples heat treated for 1000 h. Most samples heat treated between 1000 and 1400 °C. As-cast microstructures also characterized showing some weight loss in certain samples. Also included a detailed study of the LT and HT polymorphs of $AlPt_3$
Chauke et al. [43]	F-P	(Phase stability, Thermochemical) Theoretical stability of $AlPt_3$ polymorphs based on mechanical stability calculations; 0 K enthalpies of formation
Feng et al. [44]	F-P	(Thermochemical) Theoretical stabilities of Al–Pt intermetallics; 0 K enthalpies of formation
Grushko [45]	XRD, DTA	(Phase stability) Determination of stabilities of AlPt polymorphs using ternary alloys
Grushko et al. [46]	XRD, DTA	(Phase stability) Discovery of a new Al-rich intermetallic in Al–Pt around 25 at% Al
Al–Ni–Pt		
Kamm and Milligan [17]	XRD, EPMA	(Phase stability) Arc melted alloys were heat treated at 1373 K for 7 days. Compositions spanned the $AlNi_3$ to $AlPt_3$ section to determine stabilities of $L1_2$ and $L1_0$ structures
Gleeson et al. [9]	XRD, EDS, EPMA, DTA	(Phase stability) Arc melted alloys were annealed at 1373 and 1423 K for at least one week to study phase stabilities across a range of Al–Ni–Pt compositions
Jiang et al. [20]	F-P	(Phase stability, Thermochemical) First-principles study of $B2$ in the Al–Ni–Pt system
Jiang et al. [21]	F-P	(Phase stability, Thermochemical) First-principles study of $L1_0$ and $L1_2$ phases in the Al–Ni–Pt system. Monte Carlo and SQS calculations were used to predict mixing behavior and transformation/disordering temperatures of $L1_0$ into $L1_2$
Copland [18]	KEMS	(Thermochemical) KEMS activity measurements of 2 Al–Ni and 2 Al–Ni–Pt $B2$ alloys in their solid states
Copland [19]	KEMS	(Thermochemical) KEMS activity measurements of 4 Ni–24Al–xPt and 4 Ni–27Al–xPt alloys in solid and liquid states
Lu et al. [11]	F-P	(Thermochemical) First-principles calculations of bcc- and fcc-based phases in the Al–Ni–Pt system including a CALPHAD assessment using the 4SL model for the fcc phase
Zhu et al. [14]	XRD, EPMA	(Phase stability) Arc melted Al–Ni–Pt alloys were annealed at 1433 K for 30 days and 1523 K for 30 days to study phase stabilities of fcc, $L1_2$ and $B2$. CALPHAD assessment was also performed using the 4SL CSA model for the fcc phase
Kim[22] Ph.D. Thesis	F-P	(Thermochemical) First-principles calculations of bcc- and fcc-based phases in the Al–Ni–Pt system including a CALPHAD assessment using the 4SL model for the fcc phase (chapter 5)
Grushko et al.[15]	XRD, EDS	(Phase stability) Induction melted Al–Ni–Pt alloys were annealed at 1373 K for 165 h and at 1573 K for 90 h to study phase stabilities across a range of ternary compositions. Ternary alloys were arc melted from previously melted Pt containing alloys with alloy mixtures due to the expense of Pt.

Table 1 (*continued*)

References	Experimental or theoretical method	Comments
Grushko and Kapush [16]	XRD, EDS	(Phase stability) Induction melted Al–Ni–Pt alloys were annealed at 1063 K for 330 h, 1173 K for 403 h, 1273 K for 260 h and 1373 K for 660 h to study phase stabilities across a range of ternary compositions. Ternary alloys were arc melted from previously melted Pt containing alloys with alloy mixtures due to the expense of Pt.

DFT – Density Functional Theory; DTA – Differential Thermal Analysis; EDS – Energy-Dispersive X-ray Spectroscopy; EMF – Electro-Motive Force; EPMA – Electron Probe Micro-Analysis; F-P – First-principles; KEMS – Knudsen Effusion Mass Spectrometry; NMP – Nuclear microprobe; XRD – X-ray diffraction.

the 4SL model where configurational entropy and SRO dominate. After decoupling the 4SL model, the $L1_2$ phase is modeled as an ordered part of the fcc phase with the $L1_0$ phase modeled as a separate phase entirely.

The first part of the current work details the remodeling of the Al–Pt binary using the 4SL sublattice model for fcc and the 2SL sublattice model for bcc. In the second part, the 4SL model for the fcc phase is converted to a 2SL model to enable combination with available multi-component Ni-base superalloy databases. Finally, the results are discussed along with suggestions for future work.

2. Remodeling of the Al–Pt system

2.1. Modeling of the fcc and bcc-based phases using the 4SL model

The model parameters for the fcc-A1/$L1_2$ phase are modified by introducing the formalism presented by Kusoffsky et al. [25] where the values for the disordered interaction parameters are derived from the ordered parameters. The original expressions for the fcc end-members and interactions used to describe the 4SL fcc ordering, imposed no relationships between the disordered and ordered phases. This, indirectly, produced unphysical, ordered phases that never disorder even at extremely high temperatures (>6000 K). The fcc-A1, $L1_0$ and $L1_2$ phases can be better described using disordered interaction parameters derived from the ordered state with the introduction of order-*dependent* parameters only if needed. In binary systems, model parameters can be related closely to a bond energy between the two components, in this case Al and Pt. The bond energy, U_{AlPt}, can often be derived from first-principles calculations discussed in great detail by Kusoffsky et al. [25]. Following Kusoffsky et al. [25] reciprocal interaction parameters are added which are important as they approximate short range ordering (SRO) in the compound energy formalism (CEF) framework [26]. The disordered interaction parameters for the disordered fcc-A1 state can be expressed as the following [25,27]:

$$
\begin{aligned}
{}^0L^{fcc}_{Al,Pt} &= G^{4SL}_{Al_3Pt} + 1.5G^{4SL}_{Al_2Pt_2} + G^{4SL}_{AlPt_3} + 1.5L^{4SL}_{Al,Pt:Al,Pt:*:*} + 4^0L^{4SL}_{Al,Pt:*:*:*}\\
{}^1L^{fcc}_{Al,Pt} &= 2G^{4SL}_{Al_3Pt} - 2G^{4SL}_{AlPt_3} + 4^1L^{4SL}_{Al,Pt:*:*:*}\\
{}^2L^{fcc}_{Al,Pt} &= G^{4SL}_{Al_3Pt} - 1.5G^{4SL}_{Al_2Pt_2} + G^{4SL}_{AlPt_3} - 1.5L^{4SL}_{Al,Pt:Al,Pt:*:*} + 4^2L^{4SL}_{Al,Pt:*:*:*} \quad (1)
\end{aligned}
$$

where the interaction parameters for the disordered fcc phase are related to the ordering parameters by the terms ${}^{0,1,2}L^{4SL}_{Al,Pt:*:*:*}$ as shown by Hallstedt and Kim [27]. The parameters $G^{4SL}_{Al_xPt_y}$ and $L^{4SL}_{Al,Pt:k:l:m}$ describe the ordered state end-members and interactions, respectively. In the notation, a comma separates interacting elements in the same sublattice, while a column separates sublattices (alternatively, the end-member $G^{4SL}_{Al_3Pt}$ can be written as $G^{4SL}_{Al:Al:Al:Pt}$ or its equivalent permutations). As such, $L^{4SL}_{Al,Pt:k:l:m}$ describes the interactions between Al and Pt while the other sublattices are occupied by species *k*, *l*, and *m*, respectively. Simultaneous reciprocal interactions are described with interactions $L^{4SL}_{Al,Pt:Al,Pt:k:l}$ where Al and Pt interact on the first and second sublattices while the remaining sublattices are occupied by species *k* and *l*. In Eq. (1), the reciprocal interaction parameters $L^{4SL}_{Al,Pt:Al,Pt:*:*}$ represent an estimate of SRO and can be set equal to the nearest neighbor bond energies U_{AlPt} as a first approximation [25,26]. These interactions are important in producing the correct phase diagram topologies. It can now be seen that the model parameters for the disordered state are expressed by the parameters of the ordered states. By evaluating the coupled model parameters, systems with only one of the phases fcc-*A*1, $L1_2$, or $L1_0$ stable, can be described effectively as well. In the current model, the fcc-*A*1 and Pt-rich $L1_2$ phases are stable while the Al-rich $L1_2$, $L1_0$ and $L6_0$ ($L6_0$ is presented as *F* by Kusoffsky et al. [25]) phases are metastable. Fig. 2 details the possible order and disordered states present in the current system and the site ordering associated with each. The phase $L6_0$ is an intermediate ordered state between $L1_2$ and $L1_0$ where only two sites have the same site fractions.

The bcc-A2 and *B*2 phases are modified in two versions; one description where they are described by the sublattice formalism (SL) and one description when they are described by the modified sublattice (MSL) formalism. The two versions can be used interchangeably and details concerning the conversions between them are described by Dupin and Ansara [28]. Vacancies are retained in the substitutional sites to allow compatibility with other *B*2 containing systems such as Al–Ni [29]; e.g. to enable modeling of the Al–Ni–Pt ternary [11].

Franke [30] suggested that a non-zero value for the vacancy end-member, G^{bcc-A2}_{Va}, in the sublattice model $(A, Va)_1(Va)_3$ for the bcc-A2 phase has to be selected to make it possible to find the global minimum at high temperatures. In fact, in models where $G^{bcc-A2}_{Va}=0$, equilibria are only found as a result of small starting vacancy concentrations. This was the case with the model in the original manuscript where global minimum was not found when calculating an equilibrium at 20 at% Pt at 5500 K. In this work, G^{bcc-A2}_{Va} is to set to a value of $0.2RT$ as recommended by Franke [30]. However, other values have been used; e.g. in recent work by Stein et al. [31] where $G^{bcc-A2}_{Va}=30T$ was adopted. Further, depending on which systems the Al–Pt description is intended to be combined with, a change of this value may also be required and the *B*2 modified accordingly. This would for example be needed if the system was to be combined with the Al–Fe system [32]. In the latter part of this manuscript, due to the use of $G^{bcc-A2}_{Va}=0.2RT$, the Al–Ni binary modeled by Dupin et al. [29] (which used $G^{bcc-A2}_{Va}=0$) shows a difference in the Al3Ni melting temperature compared to the original description [29]. Remodeling of Al–Ni using new values of G^{bcc-A2}_{Va} has not been performed in the current work but should be investigated in the future for this very important system.

2.2. Inclusion of new data

Numerous authors have studied the phase stabilities of intermetallics near the Pt-rich portion of the phase diagram and come to various conclusions. These are summarized in Table 1. Since the

Table 2
(Table 3 in the original publication [1]): Revised thermodynamic parameters of the Al-Pt system [J/mol atoms] with a 4SL fcc-based model.

Phase	Evaluated parameters	Reference
Liquid	${}^{0}L^{liq}_{Al,Pt} = -246324 - 0.506 \times T$	This work
	${}^{1}L^{liq}_{Al,Pt} = -61241 + 32.061 \times T$	This work
	${}^{2}L^{liq}_{Al,Pt} = +63347$	This work
fcc-A1 (disordered fcc)	${}^{0}L^{fcc}_{Al,Pt} = +ALPTG0 + 1.5 \times RECALPT + 4 \times UL0ALPT$	[25,27]
	${}^{1}L^{fcc}_{Al,Pt} = +ALPTG1 + 4 \times UL1ALPT$	[25,27]
	${}^{2}L^{fcc}_{Al,Pt} = +ALPTG2 - 1.5 \times RECALPT + 4 \times UL2ALPT$	[25,27]
$L1_0$, $L1_2$ (ordered part of fcc)	$G^{4SL}_{Al:Al:Al:Pt} = \cdots = G^{4SL}_{Pt:Al:Al:Al} = +AL3PT$	This work
	$G^{4SL}_{Al:Al:Pt:Pt} = \cdots = G^{4SL}_{Pt:Pt:Al:Al} = +AL2PT2$	This work
	$G^{4SL}_{Pt:Pt:Pt:Al} = \cdots = G^{4SL}_{Al:Pt:Pt:Pt} = +ALPT3$	This work
	${}^{0}L^{4SL}_{Al,Pt:*:*:*} = +UL0ALPT$	This work
	${}^{1}L^{4SL}_{Al,Pt:*:*:*} = +UL1ALPT$	This work
	$L^{4SL}_{Al,Pt:Al,Pt:*:*} = +RECALPT$	This work
	$ALPTG0 = +AL3PT + 1.5 \times AL2PT2 + ALPT3$	[25]
	$ALPTG1 = +2 \times AL3PT - 2 \times ALPT3$	[25]
	$ALPTG2 = +AL3PT - 1.5 \times AL2PT2 + ALPT3$	[25]
	$UALPT = -32900$	This work
	$RECALPT = UALPT$	This work
	$AL3PT = -43582 + 2.000 \times T$	This work
	$AL2PT2 = -93413 + 11.089 \times T$	This work
	$ALPT3 = -65861 + 7.013 \times T$	This work
	$UL0ALPT = +3820 + 2.032 \times T$	This work
	$UL1ALPT = +1069$	This work
bcc-A2 (disordered bcc)	$G^{A2}_{Va:Va} = 0.2 \times R \times T$	[30]
	${}^{0}L^{bcc}_{Al,Pt} = +B2ALPT + LB2ALPT$	This work
	${}^{1}L^{bcc}_{Al,Pt} = +L1A2ALPT$	This work
	${}^{0}L^{bcc}_{Al,Va} = B2ALVA + LB2ALVA$	[28]
	${}^{0}L^{bcc}_{Pt,Va} = B2APTA + LB2PTVA$	This work
B2 (ordered part of bcc)	$G^{B2}_{Al:Pt} = G^{B2}_{Pt:Al} = +0.5 \times B2ALPT - 0.5 \times LB2ALPT$	This work
	${}^{0}G^{B2}_{Al:Va} = {}^{0}G^{B2}_{Va:Al} = 0.5 \times B2ALVA - 0.5 \times LB2ALVA$	[28]
	${}^{0}G^{B2}_{Pt:Va} = {}^{0}G^{B2}_{Va:Pt} = 0.5 \times B2PTVA - 0.5 \times LB2PTVA$	This work
	$B2ALPT = --205828 + 23.000 \times T$	This work
	$LB2ALPT = -15000 - 25 \times T$	This work
	$L1A2ALPT = +25000$	This work
	$B2ALVA = +10000 - T$	[28]
	$LB2ALVA = +150000$	[28]
	$B2PTVA = B2ALVA - B2ALPT$ - same formulation as for Al-Ni	[28]
	$LB2PTVA = -51322 + 25 \times T$	This work
Intermetallic phases		
$Al_{21}Pt_5$	$\frac{21}{26}{}^{0}G^{fcc}_{Al} + \frac{5}{26}{}^{0}G^{fcc}_{Pt} - 53729 + 7.894 \times T$	This work
$Al_{21}Pt_8$	$\frac{21}{29}{}^{0}G^{fcc}_{Al} + \frac{8}{29}{}^{0}G^{fcc}_{Pt} - 81677 + 142.227 \times T - 24.4824018*T*\mathrm{LN}(T) - .00180259094 *T**2 - 5.07905199E-08*T**3 + 73439.4837*T**(-1)$	This work
Al_2Pt	$\frac{2}{3}{}^{0}G^{fcc}_{Al} + \frac{1}{3}{}^{0}G^{fcc}_{Pt} - 94901 + 149.044 \times T - 25.3879657*T*\mathrm{LN}(T) - 9.76971043E-04*T**2 - 1.24939625E-07*T**3 + 57838.2515*T**(-1)$	This work
Al_3Pt_2	$\frac{3}{5}{}^{0}G^{fcc}_{Al} + \frac{2}{5}{}^{0}G^{fcc}_{Pt} - 104171 + 149.609 \times T - 25.5546046*T*\mathrm{LN}(T) - 5.42160693E-04*T**2 - 1.70115474E-07*T**3 + 93033.608*T**(-1)$	This work
AlPt	$\frac{1}{2}{}^{0}G^{fcc}_{Al} + \frac{1}{2}{}^{0}G^{fcc}_{Pt} - 108753 + 150.500 \times T - 25.5681815*T*\mathrm{LN}(T) - 6.07797546E-04*T**2 - 1.62526769E-07*T**3 + 80317.0116*T**(-1)$	This work
Al_3Pt_5	$\frac{3}{8}{}^{0}G^{fcc}_{Al} + \frac{5}{8}{}^{0}G^{fcc}_{Pt} - 95922 + 144.916 \times T - 25.2063775*T*\mathrm{LN}(T) - .00123884732 *T**2 - 1.57112248E-07*T**3 + 49147.617*T**(-1)$	This work
$AlPt_2$	$\frac{1}{3}{}^{0}G^{fcc}_{Al} + \frac{2}{3}{}^{0}G^{fcc}_{Pt} - 91610 + 143.517 \times T - 25.1147341*T*\mathrm{LN}(T) - .00118339103 *T**2 - 9.63850253E-08*T**3 + 47285.6272*T**(-1)$	This work

Table 3
(New table): Thermodynamic parameters of the Al-Ni–Pt system [J/mol atoms] with a 2SL fcc/$L1_2$ model. A set of constraints as implemented by Dupin et al. [29] are used to describe some of the following $L1_2$ parameters.

Phase	Evaluated parameters	Reference
Liquid	${}^0L^{liq}_{Al,Ni,Pt} = +25000$	This work
fcc-*A*1 (disordered fcc)	Al-Ni fcc binary interactions from Dupin et al. [29]	[29]
	Al-Pt fcc binary interactions taken from 4SL model shown in this work	This work
	Ni–Pt fcc binary interactions taken from Lu et al. [11]	[11]
	${}^0L^{fcc}_{Al,Ni,Pt} = +150219 - 102.276 \times T$	This work
$L1_2$ (ordered part of fcc) $(Al,Ni)_{0.75}(Al,Ni)_{0.25}$	$AL3PT = -40695+11.430 \times T$	This work
	$AL2PT2 = -92911 + 29.284 \times T$	This work
	$ALPT3 = -69052+11.430 \times T$	This work
	$L04ALPT = -7424$	This work
	$L14ALPT = +4617$	This work
	Al-Ni 2SL-$L1_2$ end-member and interaction parameter values from Dupin et al. [29]	[29]
	Ni–Pt 4SL order end-member values from Lu et al. [11] modified to 2SL model by using the following approximation after removal of SRO parameter $L^{4SL}_{Ni,Pt:Ni,Pt:*:*}$ $NI3PT = GNI3PT1 + 9 \times T$	This work
	$NI2PT2 = GNI2PT2 + 10 \times T$	
	$NIPT3 = GNI1PT3 + 9 \times T$	
	$U1ALNIPT = -10003 + 1.905 \times T$	This work
	$U2ALNIPT = +0$	This work
	$U3ALNIPT = +10754$	This work
bcc-*A*2 (disordered bcc)	Al-Ni bcc binary interactions from Dupin et al. [29]	[29]
	Al-Pt bcc binary interactions taken from current work	This work
	${}^0L^{bcc}_{Al,Ni,Pt} = -35.030 \times T$	This work
	${}^0L^{bcc}_{Ni,Pt} = +B2NIPT + LB2NIPT$	This work
*B*2 (ordered part of bcc)	$G^{B2}_{Ni:Pt} = G^{B2}_{Pt:Ni} = +0.5 \times B2NIPT - 0.5 \times LB2NIPT$	This work
	$B2NIPT = -22697 - 11.985 \times T$	This work
	$LB2NIPT = 0$	This work
$L1_0$ (separate phase) $(Al,Ni,Pt)_{0.25}(Al,Ni,Pt)_{0.25}(Ni,Pt)_{0.5}$	$G^{L10}_{Ni:Ni:Ni} = {}^0G^{fcc}_{Ni} + 0.5 \times T$	This work
	$G^{L10}_{Pt:Pt:Pt} = {}^0G^{fcc}_{Pt} + 0.5 \times T$	This work
	$G^{L10}_{Al:Al:Ni} = +0.5{}^0G^{fcc}_{Al} + 0.5{}^0G^{fcc}_{Ni} + GALNIL10$	This work
	$G^{L10}_{Al:Ni:Ni} = G^{L10}_{Ni:Al:Ni} = +0.25{}^0G^{fcc}_{Al} + 0.75{}^0G^{fcc}_{Ni} + ALNI3 + 2015 - 3 \times T$	This work
	$G^{L10}_{Al:Al:Pt} = +0.5{}^0G^{fcc}_{Al} + 0.5{}^0G^{fcc}_{Pt} + GALPTL10$	This work
	$G^{L10}_{Al:Pt:Pt} = G^{L10}_{Pt:Al:Pt} = +0.25{}^0G^{fcc}_{Al} + 0.75{}^0G^{fcc}_{Pt} + ALPT3 + 4118$	This work
	$G^{L10}_{Ni:Ni:Pt} = G^{L10}_{Pt:Pt:Ni} = +0.5{}^0G^{fcc}_{Ni} + 0.5{}^0G^{fcc}_{Pt} + GNIPTL10$	This work
	$G^{L10}_{Pt:Ni:Ni} = G^{L10}_{Ni:Pt:Ni} = +0.25{}^0G^{fcc}_{Pt} + 0.75{}^0G^{fcc}_{Ni} + NI3PT + 6014 - 6 \times T$	This work
	$G^{L10}_{Ni:Pt:Pt} = G^{L10}_{Pt:Ni:Pt} = +0.25{}^0G^{fcc}_{Ni} + 0.75{}^0G^{fcc}_{Pt} + NIPT3 + 8834 - 6 \times T$	This work
	$G^{L10}_{Al:Ni:Pt} = G^{L10}_{Ni:Al:Pt} = +0.25{}^0G^{fcc}_{Al} + 0.25{}^0G^{fcc}_{Ni} + 0.5{}^0G^{fcc}_{Pt} + GALNIPT2$	This work
	$G^{L10}_{Al:Pt:Ni} = G^{L10}_{Pt:Al:Ni} = +0.25{}^0G^{fcc}_{Al} + 0.25{}^0G^{fcc}_{Pt} + 0.5{}^0G^{fcc}_{Ni} + GALNI2PT$	This work
	${}^0L^{L10}_{Al,Ni:Al:Ni} = {}^0L^{L10}_{Al:Al,Ni:Ni} = {}^0L^{L10}_{Ni:Al,Ni:Ni} = {}^0L^{L10}_{Al,Ni:Ni:Ni} = +1000$	This work
	${}^0L^{L10}_{Pt,Ni:Pt:Ni} = {}^0L^{L10}_{Pt:Pt,Ni:Ni} = {}^0L^{L10}_{Ni:Pt,Ni:Ni} = {}^0L^{L10}_{Pt,Ni:Ni:Ni} = +1000$	This work
	${}^0L^{L10}_{Pt,Ni:Pt:Pt} = {}^0L^{L10}_{Pt:Pt,Ni:Pt} = {}^0L^{L10}_{Ni:Pt,Ni:Pt} = {}^0L^{L10}_{Pt,Ni:Ni:Pt} = +1000$	This work
	${}^0L^{L10}_{Ni:Ni:Ni,Pt} = {}^0L^{L10}_{Ni:Pt:Ni,Pt} = +2000$	This work
	${}^0L^{L10}_{Al:Al:Ni,Pt} = {}^0L^{L10}_{Al:Ni:Ni,Pt} = {}^0L^{L10}_{Pt:Al:Ni,Pt} = +0$	This work
	$GALNIL10 = -67000 + 11 \times T$	This work
	$GALPTL10 = -92000 + 10 \times T$	This work
	$GNIPTL10 = -14250$	This work
	$GALNIPT2 = -66500 + 4.917 \times T$	This work
	$GALNI2PT = -56298 + 5.000 \times T$	This work
	Binary $L1_0$ end-member values ALNI3, ALPT3, NI3PT, and NIPT3 same as from 2SL-$L1_2$	This work
Intermetallic phases		
AlPt - $(Al)_{0.5}(Ni,Pt)_{0.5}$	$\frac{1}{2}{}^0G^{fcc}_{Al} + \frac{1}{2}{}^0G^{fcc}_{Ni} - 63481 + 9 \times T$	This work
	${}^0L^{AlPt}_{Al:Ni,Pt} = -4651$	This work

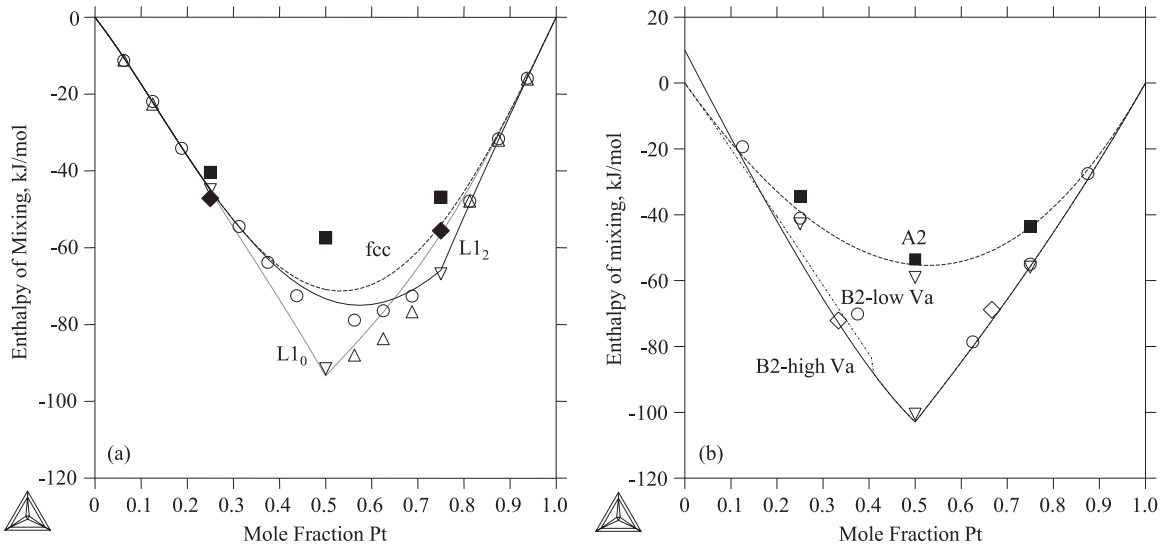

Fig. 3. Enthalpies of mixing of (a) fcc-based and (b) bcc-based phases in the Al–Pt system with lines from the present CALPHAD modeling (4SL_AL_PT_2015.TDB) at 298 K and symbols from the first-principles calculations at 0 K [1]. The disordered and ordered phases have been plotted separately for both the fcc- and bcc-based phases. Symbols for SQS calculations: disordered state volume-only relaxed (■), disordered state fully relaxed (◆), ordered state volume-only relaxed (○), order-state fully relaxed (△). Fully ordered compounds ($L1_2$-Al_3Pt, $L1_0$-AlPt, $L1_2$-$AlPt_3$, $B2$-AlPt) are shown with (▽). SQS calculations involving vacancies (Va) in $B2$ are shown with (◇). Note that pure Al in the $B2$-(high Va) structure is metastable with respect to the A2 state (itself metastable with respect to the stable phases of Al) and the enthalpy value resides above the 0-point, similar to the Al–Ni system [29].

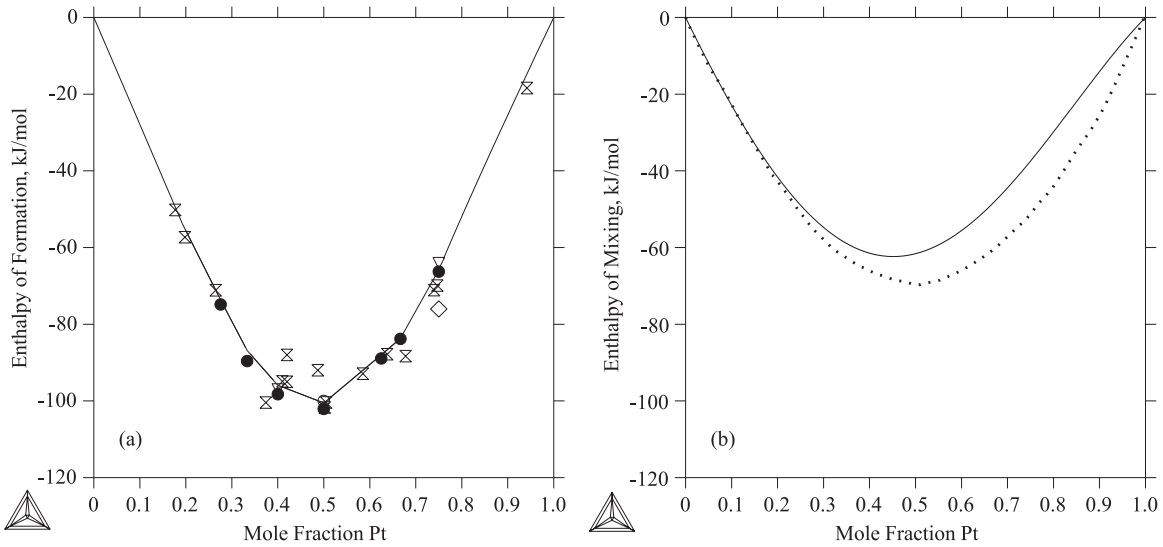

Fig. 4. (a) Calculated enthalpy of formation at 298 K as a function of Pt concentration in the Al–Pt system using the developed description (4SL_Al_PT_2015.TDB) along with measurements (⧖) [61], (▽) [36], (○) [35], (◇) [79] from the literatures and first-principles results (●) from the present work. (b) Enthalpy of mixing of the liquid phase at 1000 K from the present CALPHAD modeling (b, solid line) and the surrounded atom model by Colinet et al. [63] (dotted line).

review paper by McAlister and Kahan [33] in 1986, a number of new experiments and calculations have been performed on the Al–Pt system in the Pt-rich region of the phase diagram [34–46].

The presence of a low-temperature (LT) $AlPt_3$ phase has marred the understanding of Pt-rich Al–Pt alloys, especially at low and high temperatures where there are indications of martensitic transformations. Experimental results by Oya et al. [34] suggested that there may be two LT variants of $AlPt_3$ that destabilize at 400 and 613 K. However, more recent experiments [40,41,42] as well as first-principles calculations [43] suggest that there is only one stable form of LT-$AlPt_3$ with the probable crystal structures tP16 or DO_c'. Long duration high temperature anneals at 1573 [40], 1623 [41] and 1773 K [42] all indicated the presence of LT-$AlPt_3$ and hence, are in conflict with the findings by Oya et al. [34]. The transition electron microscope (TEM) studies by Douglas et al. [41] indicated that large HT-$AlPt_3$ $L1_2$ precipitates in their samples contained twin domains where LT-$AlPt_3$ existed as plates. Interestingly, first-principles calculations by Chauke et al. [43] showed that the ground state crystal structure for the composition $AlPt_3$ is tP16 rather than $L1_2$. This is in contrast to the Al–Ni system where $L1_2$ indeed represent the ground state. These phenomena are indicative of martensitic transformations and would require further analysis. Two crystallographic variants of $AlPt_2$ have also been reported with the low temperature form not being observed by all researchers [33,47]. The resolution of the debate about the stability of LT-$AlPt_3$ and LT-$AlPt_2$ is outside the scope of this work and consequently, the thermodynamics of these compounds are not modeled here.

Since the publication of the previous Al–Pt description [1], Grushko et al. [15,16,45,46,48] has performed a series of extensive experiments with regards to the Al–Pt and Al–Ni–Pt systems in order to rectify some of the disagreements present in the

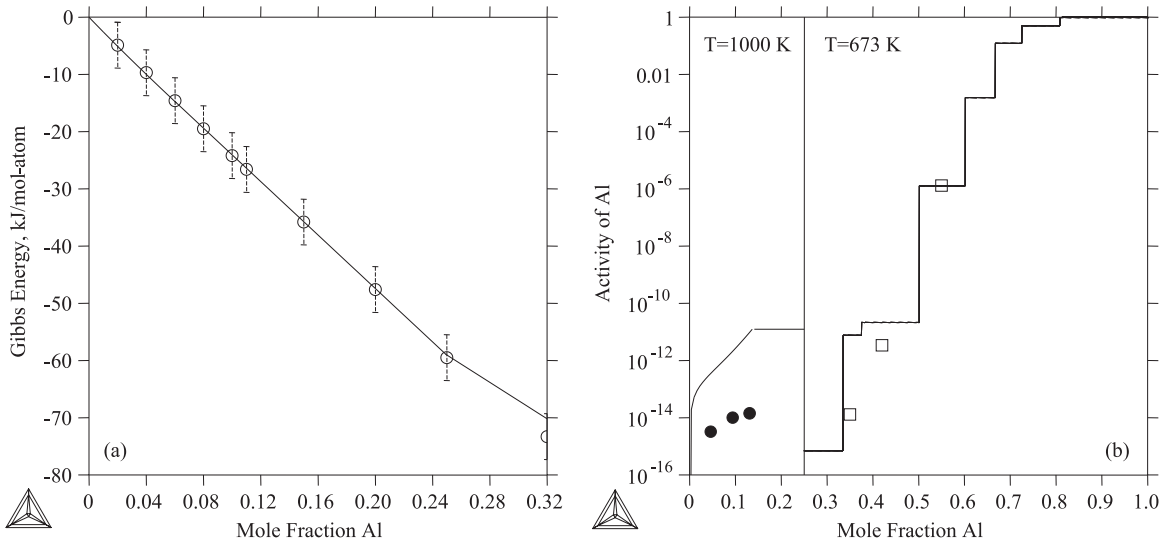

Fig. 5. (a) Gibbs energy of formation calculated at 973 K (solid line) using the developed description (4SL_AL_PT_2015.TDB) compared to EMF measurements by Schaller (○) [50]. (b) Activity of Al at 1000 K (left pane in b) and 673 K (right pane) compared to measurements by Nanko et al. (●) [38], and Kobayashi et al. (□) [37].

literature. These include the stability of *B*2 [45] and Al-rich intermetallics in the Al–Pt binary system [46]. McAlister and Kahan [33], based on the experiments by Bhan and Kudielka [49], rationalized that *B*2 is stable from approximately 1533 to 1783 K at ~52 at% Pt while AlPt-*B*20 melts congruently at 50 at% Pt. However, based on results of DTA and XRD investigations, Grushko [45] suggested that *B*2 becomes more stable than *B*20 at 50 at% Pt at high temperatures and melts congruently based in binary and ternary systems. Grushko [45] also proposed a new *B*2 phase region (Fig. 7b) based on his experimental findings that attempts to resolve some of the conflicts present in the literature concerning this area of the phase diagram. This experimental investigation is judge to be the most complete analysis of the *B*2 phase in the Al–Pt system and is therefore accounted for in the modeling of the *B*2 phase in the current work. Grushko [46] also discovered a new phase ξ at ~25 at% Pt with an orthorhombic structure that exists between 1074 and 1188 K. Structural determination for this phase is still ongoing [46] and the phase is not included in the current assessments.

In addition to the data sets accounted for in the previous assessment of the Al–Pt system [1], further data sets are included in this work to aid in the revision. In terms of thermochemical data, activity measurements [37,38,50] are accounted for as well as first-principles calculations by Feng et al. [44]. Due to a lack of thermodynamic information on the important $L1_2$-$AlPt_3$ compound, the Debye–Grüneisen model is used to calculate the finite temperature properties of the phase at the stoichiometric composition. The same settings as in the previous work [1] are used and an appropriate scaling factor is applied [51,52]. This method is also used to compute the thermodynamic properties of all other intermetallics except that of $Al_{21}Pt_5$, which is disregarded due to its massive unit cell size. Previously, only off-stoichiometry *B*2 anti-site defects were calculated where Al resides on Pt sites and vice versa. However, off-stoichiometry energies in *B*2 involving vacancies are highly important to the stability of this phase. For this reason, the special quasirandom structures (SQS) calculations with vacancies replacing either Al or Pt in *B*2 are performed following the method described by Jiang et al. [53]. The PARROT module [54] of Thermo-Calc [55,56] is used to evaluate the model parameters for the end-members and interactions based on the selected experimental and calculated information. The resulting values are shown in Table 2.

To the authors knowledge, only one complete set of liquidus and solidus measurements is available in the literature for the Al–Pt binary system [57]. The solid to liquid transformations at high temperatures were studied using DTA measurements for alloy compositions spanning the entirety of the phase diagram. However, it is difficult to determine the validity and accuracy of those measurements given some of the discrepancies shown in the phase diagram by Huch and Klemm [57]. At around ~56 at% Pt, there is a sheer drop in the liquidus from 1397 to 1260 K, which is unphysical.

3. Extension into the Ni-rich part of Al–Ni–Pt

The Al–Pt binary developed here is extended into the Al–Ni–Pt ternary to determine its extrapolation "fitness" as well as the parameterization required to obtain a reasonable ternary phase diagram assessment. As is described in the introduction, the extrapolation is done using the 2SL "order-disorder" model where only the $L1_2$ is captured as the ordered phase to ensure compatibility with the TCNI [23] and NIST Superalloy Databases [24]. To convert the 4SL fcc model presented in this work into the 2SL fcc model, thermodynamic parameters determined for all phases except for the ordered part of the fcc-A1, i.e. 4SL-fcc, are retained. A set of constraints as implemented by Dupin et al. [29], are then used as the ordered part of the fcc describing only the $L1_2$ phase with 2SL (Al, Ni, Pt)$_{0.75}$(Al, Ni, Pt)$_{0.25}$ model. The implementation of these constraints for Al–Ni–Pt are essentially the same as Al–Cr–Ni presented by Dupin et al. [29] and the reader is referred to Ref. [29] for more on its background and derivation. Gibbs energy parameters for the 2SL-$L1_2$ ordered part are re-assessed to the same Al–Pt data used for the 4SL that is relevant to the $L1_2$. The new 2SL-$L1_2$ parameters are shown in Table 3 for the converted Al–Pt system. As a result of this conversion, the $L1_0$ must be modeled as a separate phase.

To capture the ordering of Ni- and Pt-rich $L1_0$ in Al–Ni–Pt, a 3SL model is used with the following sublattices: (Al, Ni, Pt)$_{0.25}$(Al, Ni, Pt)$_{0.25}$(Ni, Pt)$_{0.5}$. Such a model allows both binary $L1_0$-NiPt, and ternary $L1_0$-$AlNi_2Pt$, $L1_0$-$AlNiPt_2$ to be described as ordered compositions and mirrors the treatment of a similar $L2_1$ phase by Dupin [58]. For example, binary $L1_0$-AlNi can be described as (Al)$_{0.25}$(Al)$_{0.25}$(Ni)$_{0.5}$ while ternary $L1_0$-$AlNiPt_2$ can be described as (Al)$_{0.25}$(Ni)$_{0.25}$(Pt)$_{0.5}$. The end-member (A)$_{0.25}$(B)$_{0.25}$(B)$_{0.5}$ is evaluated to always be less stable than the $L1_2$ phase with the same

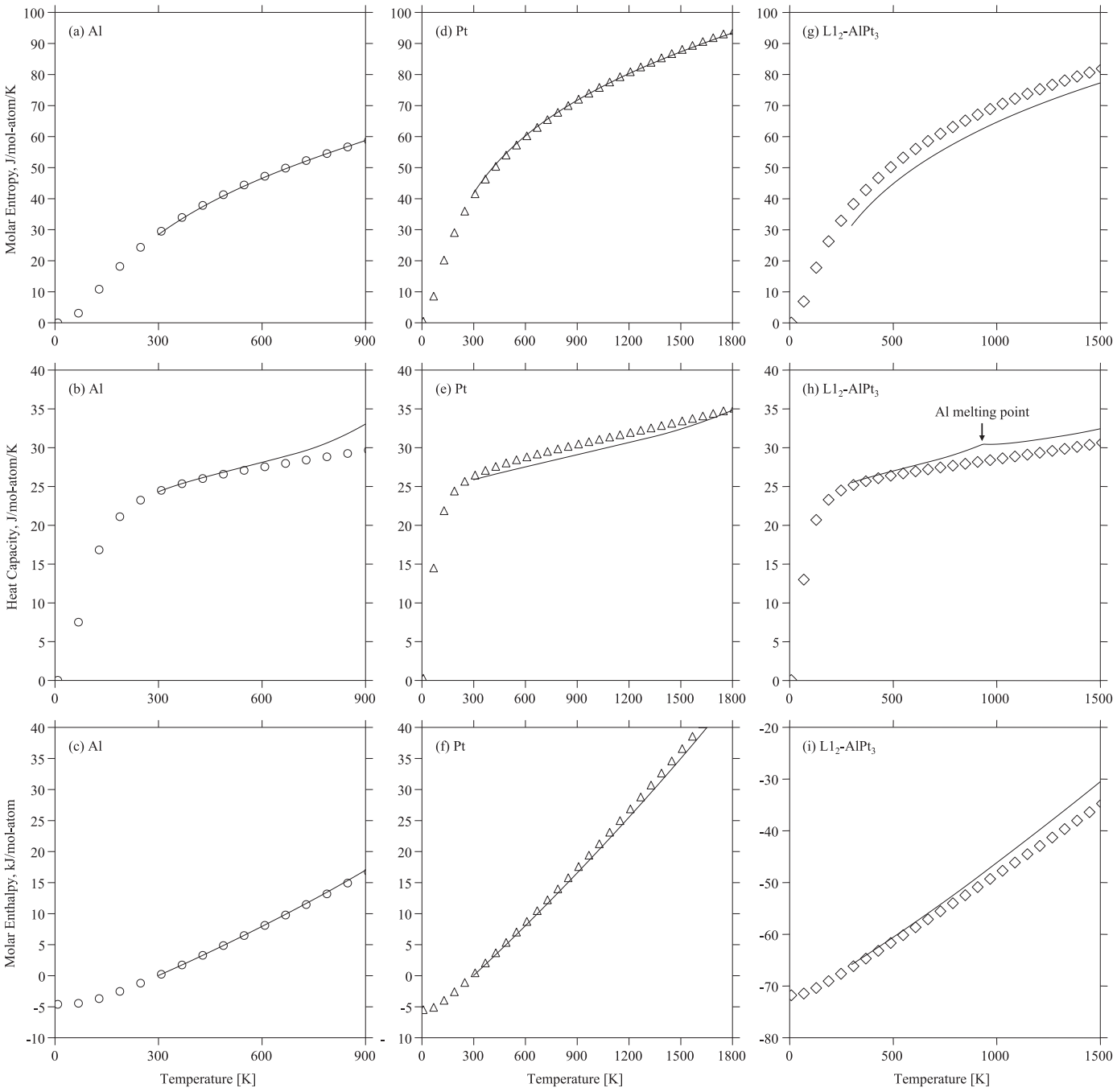

Fig. 6. Calculated Al, Pt, and $L1_2$-AlPt3 molar entropies (a, d, g), heat capacities (b, e, h), and enthalpies (c, f, i) from the current model (4SL_AL_PT_2015.TDB) compared to the predictions from the Debye-Grüneisen model (○, △, ◇).

composition, $(A)_{0.25}(B)_{0.75}$. This treatment assumes that the tetragonal $L1_0$ is less stable than the cubic $L1_2$ phase at compositions such as $AlNi_3$. This new ordered part of the fcc and $L1_0$ are then re-evaluated using the same Al–Pt dataset to obtain the 2SL $L1_2$ ordered parameters and the 3SL $L1_0$ parameters.

Since no 2SL-fcc model of Ni–Pt exists in the open literature to the authors' knowledge, the conversion presented above is also performed on the 4SL Ni–Pt binary by Lu et al. [11] to convert it to 2SL-fcc/$L1_2$ and $3SLl_0$ models for the purpose of modeling the ternary. Additionally, $L1_0$-AlNi was added to the 2SL Al–Ni binary by Dupin et al. [29] to approximate the 4SL Al–Ni assessment [59] referenced by Lu et al. [11]. Due to the current poor understanding of the γ^* phase and the boundaries associated, it is precluded in the current modeling efforts. The preliminary conversion performed for Ni–Pt presented in this work requires more detailed assessments to finalize its 2SL-$L1_2$ and 3SL-$L1_0$ parameters.

4. Results and discussion

4.1. Al–Pt system

The model parameters of the liquid phase and all intermetallics published by Kim et al. [1] are remodeled in the present work alongside those of the fcc- and bcc-based phases. Calculated enthalpies of mixing for fcc-*A*1, bcc-*A*2, $L1_0$, $L1_2$ and *B*2 agree well with the values from first-principles calculations (Fig. 3(a and b)). Fig. 3(b) also shows the importance of including substitutional

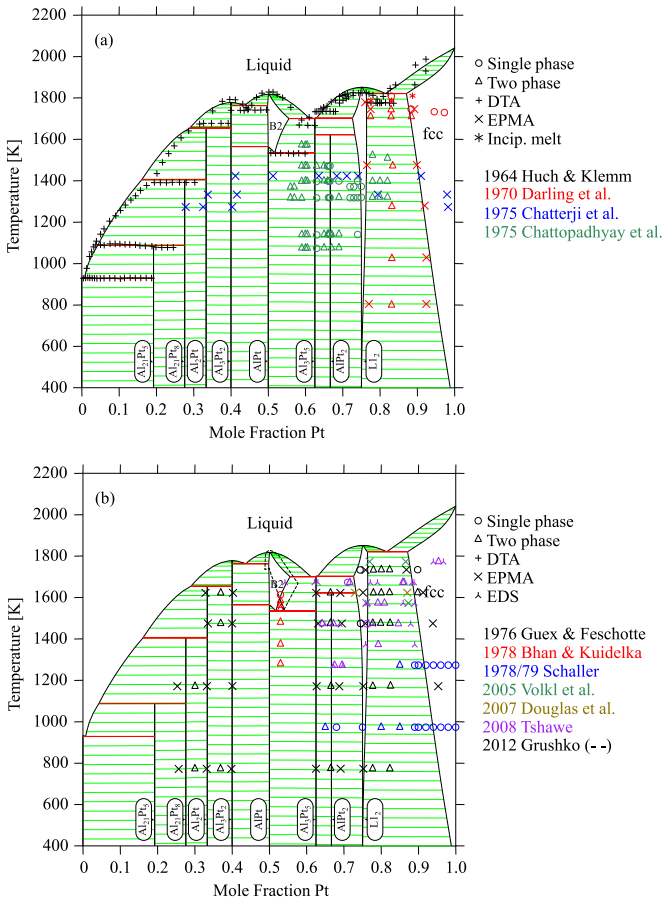

Fig. 7. (a) Calculated phase diagram of the Al–Pt system using the revised model (4SL_AL_PT_2015.TDB) with data from 1964 to 1975 [57,67–69]. (b) Calculated phase diagram of the Al–Pt system using the revised model (4SL_AL_PT_2015.TDB) with data from 1976-present [70,71,40–42,45,50,72].

vacancies in *B*2. When the *A*2-*B*2 phase is modeled with vacancies, it exists not only in two states (*A*2 and *B*2-Va), but in three states: *A*2, *B*2-(high Va) and *B*2-(low Va). This marks the distinction in the two different *B*2 curves seen in Fig. 3(b). Comparing the calculated B2 formation energies with and without vacancies for off-stoichiometric compositions on the Al-rich side, the introduction of vacancies on Pt sites lowers the energies substantially. On the Pt-rich side, vacancies are shown to increase the formation energies slightly (Fig. 3(b)). Similar results are obtained in other *B*2 containing systems such as Al–Ni [53] and In-Pd [60]. Fig. 4(a) shows the calculated enthalpies of formation at 298 K for all the modeled phases. Agreement with experiments [35,36,61,62] as well as first-principles results from the previous Al–Pt work [1] can be concluded. The liquid energies seen in Fig. 4(b) are close to predicted energies using the surrounded atom model by Colinet et al. [63]. Presented in Fig. 5(a), the calculated Gibbs energies of formation in the fcc-*A*1 and $L1_2$ regions (up to 32 at% Al) at 973 K are shown to agree with the EMF measurements by Schaller [50] within expected experimental uncertainty. In Fig. 5(b), activities of Al at 1000 and 673 K are shown to be in line with EMF measurements by Nanko et al. [38] and Kobayashi et al. [37]. Fig. 6 indicates that the Debye-Grüneisen predictions for pure Al and Pt (Fig. 6(a)–(f)) agree very well with the SGTE values [64–66]. Additionally, Fig. 6 (g) and (h) show that the calculated molar entropy, heat capacity and enthalpy of $L1_2$-$AlPt_3$ are in accordance with predictions from the Debye-Grüneisen model. It is important to note that the hump seen in Fig. 6(h) results from the use of the Neumann-Kopp approximation for the heat capacity of the fcc phase from which the $L1_2$ orders from. The heat capacity of pure fcc Al is ill-defined above its melting point and discontinuous, producing this artifact. It is expected that future redefinition of the pure elements expressions could resolve this issue. By the use of first-principles calculations coupled with experiments the theoretical heat capacity could be defined at temperatures above the melting point until the phase becomes unstable.

Fig. 7(a) and (b) present the remodeled Al–Pt phase diagram compared to a series of experiments performed after 1964. The solubility in the fcc-A1+$L1_2$ two-phase region is expected to decrease significantly at low temperatures and this is now captured by the revised description. Good agreement is seen for the majority of data sets [40–42,45,50,57,67–72] with some exceptions. The measurements of the Pt-rich fcc+$L1_2$ phase boundary show a large scatter ranging from as high as 98 at% [68] to as low as 89 at% Pt [50,72] (Fig. 7). The current assessment shows good agreement with the boundaries measured by Darling et al. [67], Völkl et al. [40], Douglas et al. [41], and Tshawe [42]. Also the $AlPt_2$ phase boundary

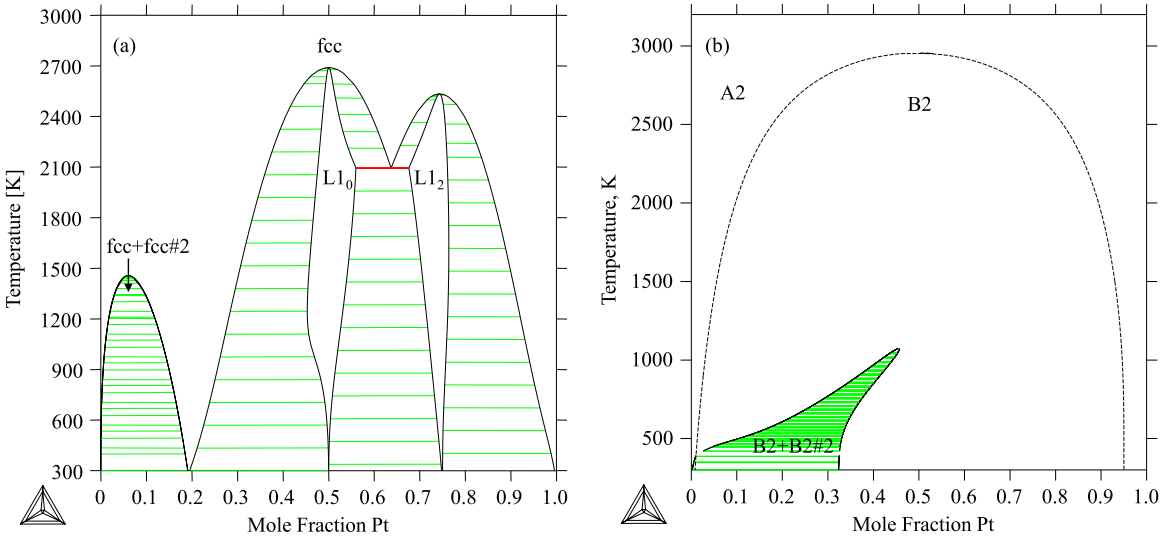

Fig. 8. Calculated metastable phase diagrams for the fcc-based (a) and bcc-based (b) phases showing the variety of ordered phases (Detailed in Fig. 2) using the developed description (4SL_AL_PT_2015.TDB). Second order transitions are shown for both cases (dashed line). Note the presence of low Va and high Va *B*2 phases at low temperatures.

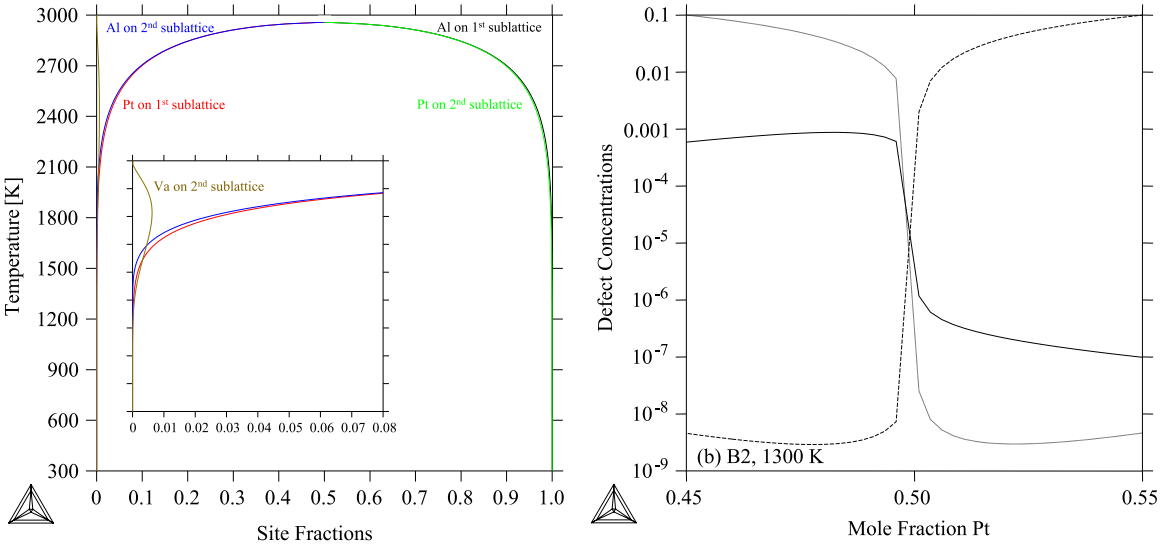

Fig. 9. Calculated temperature-site fraction diagrams for AlPt-*B2* (a), showing order and disorder of the phase using the developed description (4SL_AL_PT_2015.TDB). In (a), small vacancy fractions can be seen near the edge of the figure (zoomed inset). In (b), calculated defect concentrations in the *B2* at 1300 K are shown: Vacancies on Pt sites (solid line), Pt on Al anti-site (dashed line), and Al on Pt anti-site (dotted line).

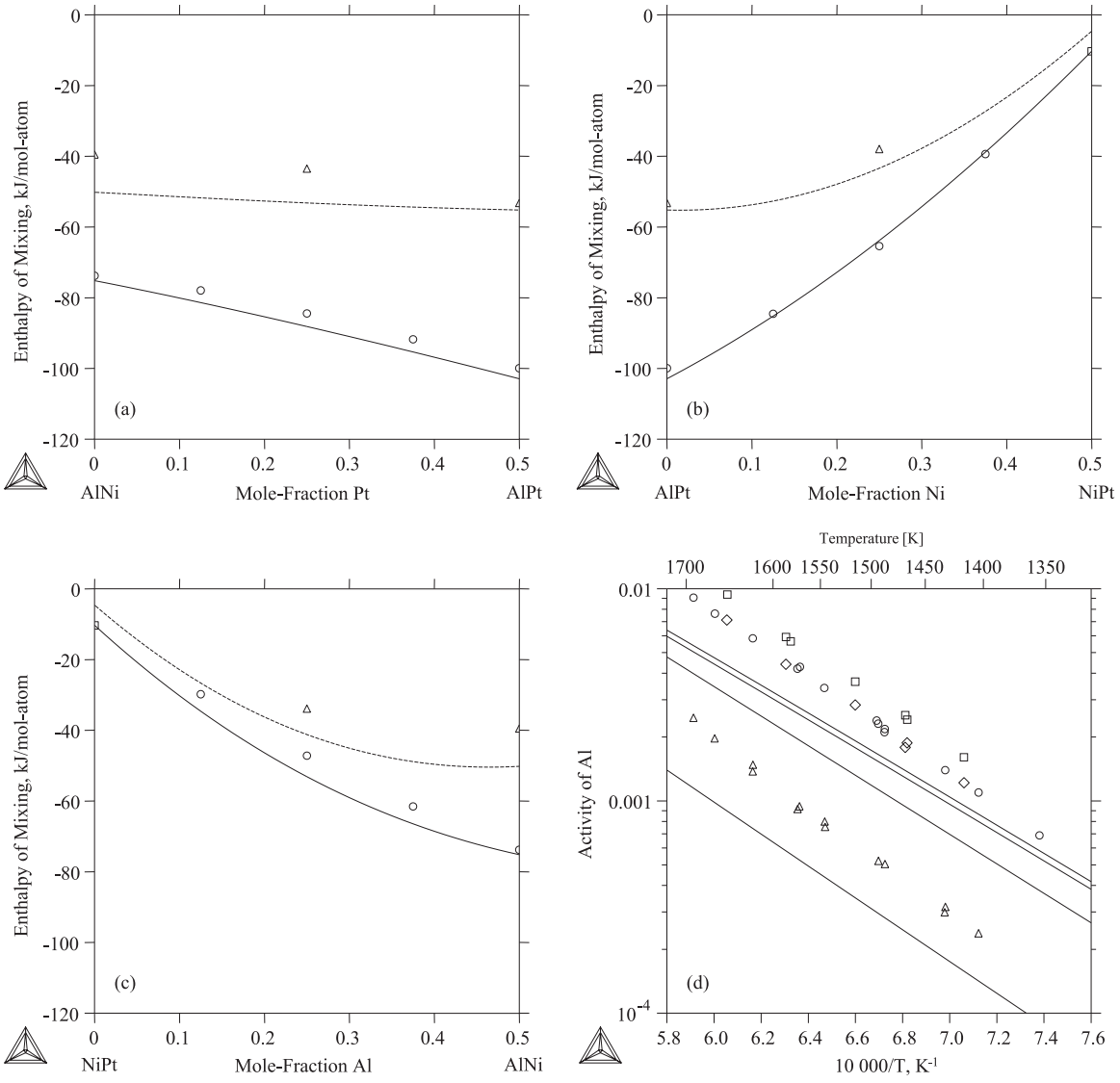

Fig. 10. Enthalpies of mixing of A2 (dashed lines) and B2 (solid lines) phases in the Al–Ni–Pt system with lines from the present CALPHAD modeling (2SL_AL_NI_PT.TDB) at 298 K and symbols from the first-principles calculations at 0 K by Kim [22]. The AlNi-AlPt (a), AlPt-NiPt (b), and NiPt-AlNi (c) sections are shown here. The enthalpy of mixing for *B2*-NiPt (□) comes from Jiang et al. [20]. For insets a, b, and c, reference states for Al, Ni, and Pt are bcc-*A2* and symbols (Δ) and (○) represent first-principles SQS calculations for the *A2* and *B2* phases, respectively. Calculated Al activities at four different compositions in *B2* are shown in (d) and compared to KEMS measurements by Copland [18] from Al–Ni and Al–Ni–Pt alloys. In (d), symbols from experiments and lines from the current calculations are defined as Ni–47.2Al (○, dashed), Ni–47.5Al (□, dotted), Ni–39.5Al–15.0Pt (▵, solid), and Ni–46.9Al–14.9Pt (◇, dot dashed).

with $L1_2$ poses some challenges. The current model agrees with Al_3Pt_5-$L1_2$ phase boundaries suggested by Tshawe [42] at high temperatures but disagrees with alloys from Chattopadhyay [69] at lower temperatures. Chatterji et al. [68] noted the difficulty of $AlPt_2$ to form in a series of diffusion studies using aluminized Pt samples and Guex and Feschotte [70] were unable to find the $AlPt_2$ phase in their anneals. These results question the stability of $AlPt_2$ altogether and its phase boundaries with the phases in proximity.

The calculated *B*2 phase region seen in Fig. 7(b) reproduced the phase region proposed by Grushko [45] where *B*2 becomes the stable phase instead of B20 before melting congruently. Fig. 8 (a) and (b) demonstrate the calculated metastable phase diagram when only the fcc- and bcc-based phases are present. As can be deduced from the first-principles results, $AlPt_3$-$L1_2$ and AlPt-$L1_0$ are seen in the metastable phase diagram while the less stable Al_3Pt-$L1_2$ is not. The presence of $L1_0$ ordering in the center of the metastable phase diagram is not surprising given its highly exothermic formation energy of −90 kJ/mol-atom predicted by DFT, rivaling the formation energy of the stable AlPt-B20 phase and metastable *B*2. Additionally, $L1_0$ ordering is seen near the Al–Pt side of the Al–Ni–Pt phase diagram at temperatures as high as 1573 K [15] which further suggests its metastability. In Fig. 8 (a) and (b), $AlPt_3$-$L1_2$, AlPt-$L1_0$, and *B*2 all disorder at reasonable temperatures (less than 3000 K). This occurs through 1st order transformations for the fcc-based phases and a 2nd order transformation for the bcc-based *B*2. The associated site fraction changes are shown in Fig. 9(a) for *B*2 at its stoichiometric composition. In Fig. 9(b), the calculated defect concentrations in *B*2 at 1300 K are shown. Finally, the introduction of the 4SL model for the bcc-based phases can capture D03 and B32 ordering seen at lower temperatures such as in Al–Fe by Sundman et al. [73]. It is possible to then also model Al_2Pt as a Va-ordered structure using the 4SL bcc frame-work. Such a model could account for the ordering phenomena seen by Grushko et al. near the $B2 + Al_2Pt$ region of the phase diagram [16].

4.2. Ni-rich part of the Al–Ni–Pt system

The resulting model parameters from the current assessment are shown in Table 3. First the bcc-based A2 and *B*2 phases are compared to thermochemical properties measured [18] and calculated [20,22] by various authors. Fig. 10(a)–(c) compares the calculated CALPHAD enthalpies of mixing for the bcc-A2 and *B*2 phases to first-principles values calculated by Kim [22] and Jiang et al. [20]. In all three isopleths, showing the composition ranges AlNi-AlPt, AlPt-NiPt, and NiPt-AlNi, good agreement is seen. Aluminum activities measured using Knudsen Effusion Mass Spectrometry (KEMS) [18] for four different alloys (Ni–47.2Al, Ni–47.5Al, Ni–39.5Al–15.0Pt, and Ni–46.9Al–14.9Pt) shown in Fig. 10 (d) parallel the calculated CALPHAD values as well. Copland [19] made additional KEMS measurements for activities of species in a series of Ni–24Al–*x*Pt and Ni–27Al–*x*Pt alloys with the first set shown in Fig. 11(a). Calculated CALPHAD Al activities in $L1_2$ and liquid phases compared to those measured by Copland [19] via KEMS show good agreement. One of the most important regions of the phase diagram is the $AlNi_3$ to $AlPt_3$ vertical section and modeling its phase stability first requires the correct thermochemical properties of the phases involved. Fig. 11(b) shows that the calculated CALPHAD enthalpies of mixing for the fcc, $L1_0$ and $L1_2$ phases are congruent with first-principles calculations by Kim [22], Jiang et al. [21] and Lu et al. [11].

Fig. 12(a) plots the AlNi3-AlPt3 phase diagram with some melting information inferred from KEMS measurements by Copland in a series of alloys that are close in composition to this vertical section [19]. From this series of Ni–24Al–*x*Pt and Ni–27Al–*x*Pt alloys, the highest temperature solid and lowest temperature liquid observed are in accord with the calculated liquidus and solidus temperatures shown in Fig. 12(a). It can be seen from Fig. 12(b) that the calculated *L*10 disordering temperatures have the same trend as those predicted by Jiang et al. [21] using Monte-Carlo and SQS methods. Due to experimental observations of *L*10-AlNiPt2 at temperatures as high as 1573 K, however, the current assessment places its disordering temperatures much higher. Additionally, Fig. 12(b) shows that *L*10-AlNi2Pt and *L*10-AlNiPt2 both first disorder to *L*12 and then finally to fcc as suggested by predictions from first-principles [21].

Fig. 13(a) presents the Ni-rich partial isothermal section of the Al–Ni–Pt system at 1373 K. While most calculations are in consensus with the measured EPMA data by Gleeson et al. [9], Grushko et al. [15] and Kamm and Milligan [17], discrepancies exist near the $B2$-$L1_0$ phase boundary. Recent experiments by Grushko et al. [15,16] indicate that $L1_0$-$AlNiPt_2$ orders into an

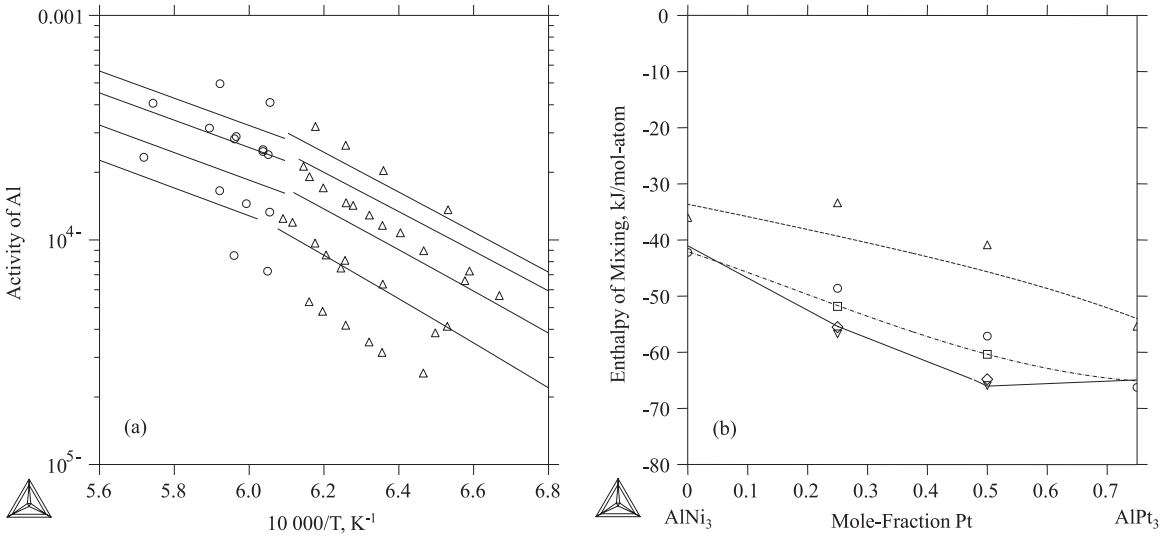

Fig. 11. Calculated Al activities at 4 different Al–Ni–Pt compositions using the developed description (2SL_AL_NI_PT_2015.TDB) compared to KEMS measurements of solid (△) and liquid phases (○) by Copland [19] (a). In (a), lines from the current calculations are defined as Ni–24Al–2Pt (dotted), Ni–24Al–10Pt (dashed), Ni–24Al–18Pt (dot dashed), and Ni–24Al–25Pt (solid). For inset (b), calculated enthalpies of mixing in the $AlNi_3$-$AlPt_3$ vertical section are plotted with first-principles calculations by Kim [22] shown in symbols. In (b), CALPHAD and first-principles results from Kim [22] are shown for fcc (▵, dashed), $L1_2$ (○, dot dashed) and $L1_0$ (solid) phases. Additional first-principles calculations by Jiang et al. [21] and Lu et al. [11] for the $L1_2$ (□) and $L1_0$ (◇,▽) phases are also shown in (b).

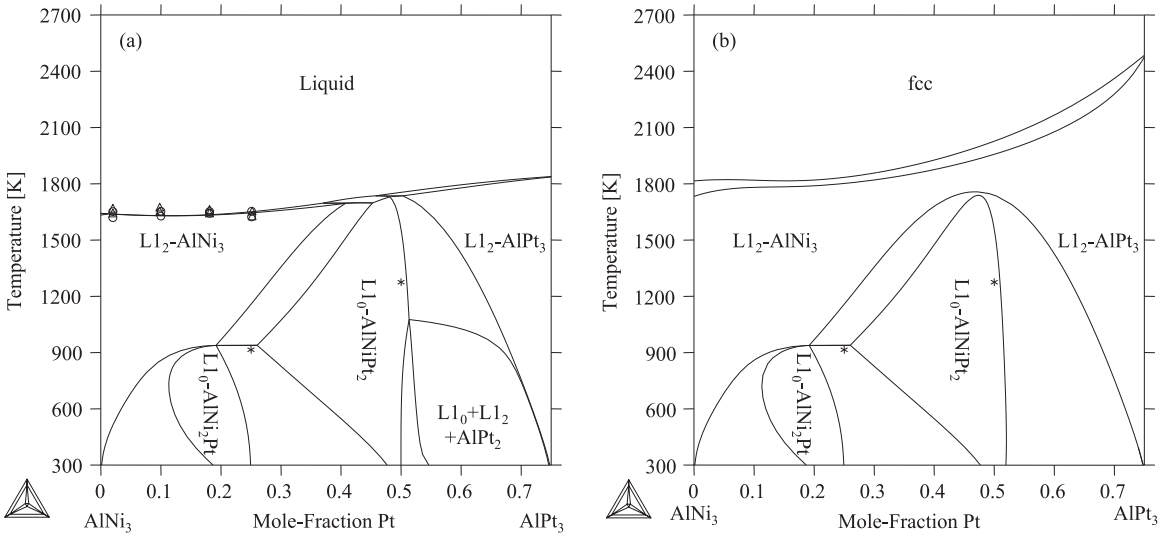

Fig. 12. Calculated stable (a) and metastable fcc-based (b) $AlNi_3$-$AlPt_3$ vertical sections using the developed description (2SL_AL_NI_PT_2015.TDB). Highest temperature solid (○) and lowest liquid (△) points from Copland are shown for a series of Ni–24Al–*x*Pt and Ni–27Al–*x*Pt alloys [19]. $L1_0$ to $L1_2$ transition/disorder temperatures calculated from first-principles for the compositions $L1_0$-$AlNi_2Pt$ and $L1_0$-$AlNiPt_2$ by Jiang et al. [21] are shown with (∗).

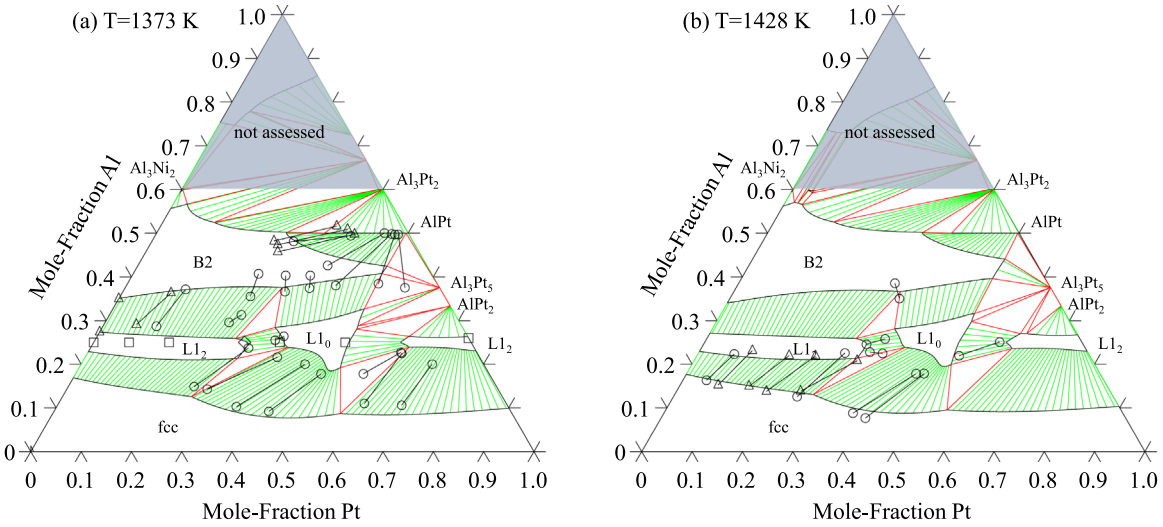

Fig. 13. Calculated partial isothermal section at 1373 K (a) using the developed description (2SL_AL_NI_PT_2015.TDB) together with two-phase EPMA measurements by Gleeson et al. [9] (△) and EDS measurements by Grushko et al. [15] (○). Single- (□) and two-phase alloys (◇) from Kamm and Milligan [17] are also included in (a). Calculated partial isothermal section (b) using the developed description (2SL_AL_NI_PT_2015.TDB) at 1428 K together with two-phase EPMA measurements by Gleeson et al. (○) at 1423 K [9] and by Zhu et al. at 1433 K (△) [14].

orthorhombic superlattice phase, γ^*, with four-times larger volume of the unit cell as Al content increases near B2. It is suggested that this phase is the ternary extension of Al3Ni5 given their similar crystal structures [15,16]. Currently, there is no data to suggest if phase separation occurs in the *L*10-γ^* phase field. It is not expected that the calculated $L1_0$-*B*2 phase boundaries could capture the EPMA data given that it really is the γ^*-*B*2 phase boundary. One sees the same story in Fig. 13(b) where the calculated isothermal section at 1428 K is in agreement with two-phase EPMA measurements by Gleeson et al. at 1423 K [9] and by Zhu et al. at 1433 K [14] except for the $L1_0$-*B*2 phase region.

The 1523 K partial isothermal section shown in Fig. 14 (a) indicates that the calculated phase boundaries are in reasonable agreement with EPMA measurements from Zhu et al. [14]. EPMA data from Zhu et al. [14] would suggest that the fcc+*L*12 phase region is actually growing wider as temperature increases despite the fact that it is shrinking rapidly in the Al–Ni binary. Such a contradictive result is non-intuitive and requires further experimental investigation. Fig. 14(b) shows that the calculated isothermal section is in accordance with the EDS measurements by Grushko et al. [15] with discrepancies again involving the *L*10-*B*2 phase boundaries. It is expected that a model which captures the γ^* phase correctly, once enough experimental data is generated, should also improve the phase boundaries near the B2 phase.

5. Conclusions and suggestions for future work

This work presents a complete remodeling of the Al–Pt system. Calculated energies, especially in the Pt-rich section of the phase diagram are shown to agree well with experiments and DFT calculations. The *B*2 phase has been modified according to new results by Grushko [45]. Metastable phase diagrams are also presented to show the various ordered fcc phases that exist in the

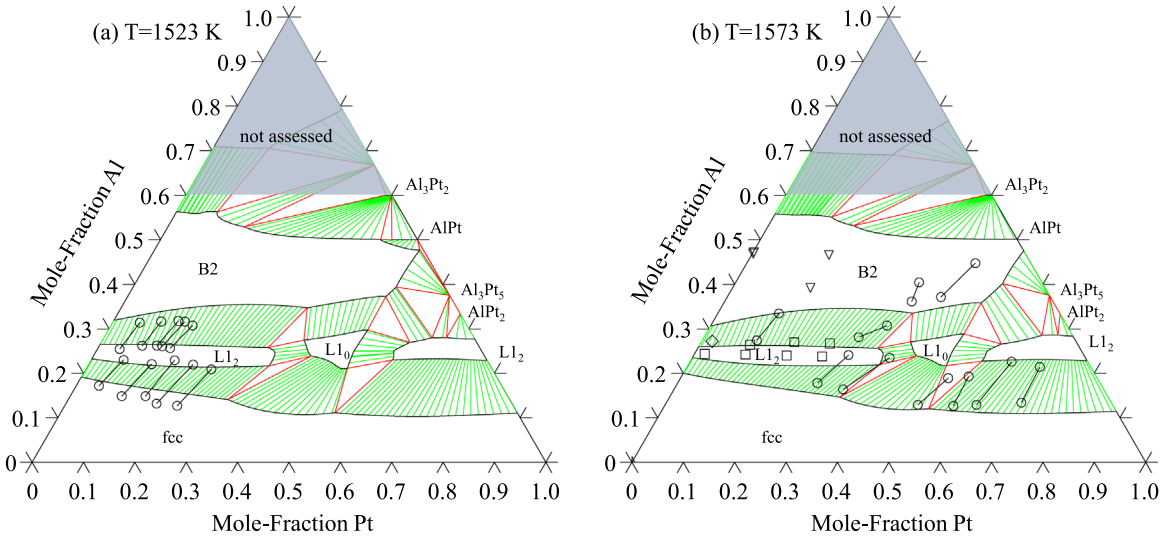

Fig. 14. Calculated partial isothermal section at 1523 K (a) using the developed description (2SL_AL_NI_PT_2015.TDB) with two-phase EPMA measurements by Zhu et al. [14] (○). Calculated partial isothermal section at 1573 K (b) using the developed description (2SL_AL_NI_PT_2015.TDB) together with two-phase EDS measurements by Grushko et al. [15] (○). Single- (□,▽) and two-phase alloys (◇) from Copland [19] and Copland [18] are also included in (b).

system. The 4SL binary Al–Pt model was converted to a 2SL model for ease of integration into existing Ni-base superalloy databases. This 2SL Al–Pt model was then extrapolated into the Ni-rich portion of the Al–Ni–Pt system to determine its extrapolation characteristics as well as the parameterization required to obtain a reasonable assessment. Preliminary modeling of the fcc, $L1_0$, $L1_2$, and $B2$ phases indicate that the 2SL model presented here provides a reasonable assessment of the Ni-rich part of Al–Ni–Pt without the need of excessive ternary interaction parameters for the solution phases. Poor agreement was found for the phase boundaries involving $L1_0$ and $B2$ due to the presence of another superlattice phase, denoted γ^*, which orders from $L1_0$ near the B2 phase field.

The authors recommend the following to improve the assessment presented here:

- Additional experiments near the LT/HT-$AlPt_3$, B2 and LT/HT-$AlPt_2$, regions of the phase diagram to improve the understanding of their phase boundaries
- Phase stability studies to determine the LT phases for AlPt2 and AlPt3 and their possible martensitic characteristics
- Phase stability of γ^* and its relationship to Al_3Ni_5 near B2-(Ni, Pt)Al
- $L1_0$-γ^* phase boundaries and if phase separation occurs at certain temperatures
- Introduction of the appropriate model (ordering from $L1_0$ or separate phase) for γ^*.

The revised thermodynamic database is included in the supplemental document.

Acknowledgments

The authors would like to thank Austin Ross of the Pennsylvania State University and Dr. Brian Gleeson of the University of Pittsburgh for stimulating discussions. We would also like to thank Dr. Maria Emelianenko of George Mason University for finding the erroneous stability of the B2 phase in the original article. This work is supported partially by the Department of Energy under grant DE-FE0024056 and partially by the NASA Space Technology Research Fellowships (NSTRF) program under grant NNX14AL43H.

Appendix A. Supplementary material

Supplementary data associated with this article can be found in the online version at http://dx.doi.org/10.1016/j.calphad.2016.08.002.

References

[1] D.E. Kim, V.R. Manga, S.N. Prins, Z.-K. Liu, First-principles calculations and thermodynamic modeling of the Al–Pt binary system, Calphad 35 (2011) 20–29, http://dx.doi.org/10.1016/j.calphad.2010.10.008.
[2] C. Couderc, Platinum group metals in glass making, Platin. Met. Rev. 54 (2010) 186–191, http://dx.doi.org/10.1595/147106710 × 514012.
[3] H. Jehn, Platinum losses during high temperature oxidation, J. Less Common Met. 78 (1981) 33–41, http://dx.doi.org/10.1016/0022-5088(81)90141-7.
[4] H. Jehn, High temperature behaviour of platinum group metals in oxidizing atmospheres, J. Less Common Met. 100 (1984) 321–339, http://dx.doi.org/10.1016/0022-5088(84)90072-9.
[5] H. Kim, D.A. Nolet, Apparatus for Homogenizing a Glass Melt, US8650910, 2014. http://dx.doi.org/10.1197/jamia.M1139.Adar.
[6] a Watson, R. Süss, L. a Cornish, Building a thermodynamic database for platinum-based superalloys: Part II, Platin. Met. Rev. 51 (2007) 189–198, http://dx.doi.org/10.1595/147106707 × 232893.
[7] L.A. Cornish, R. Süss, A. Watson, S.N. Prins, Building a thermodynamic database for platinum-based superalloys: Part I, Platin. Met. Rev. 51 (2007) 104–115.
[8] J. Preußner, S.N. Prins, M. Wenderoth, R. Völkl, U. Glatzel, Building a thermodynamic database for platinum-based superalloys: Part III, Platin. Met. Rev. 52 (2008) 48–51, http://dx.doi.org/10.1595/147106708 × 255167.
[9] B. Gleeson, W. Wang, S. Hayashi, D.J. Sordelet, Effects of platinum on the interdiffusion and oxidation behavior of Ni-Al-based alloys, Mater. Sci. Forum 461–464 (2004) 213–222, 10.4028/www.scientific.net/MSF.461-464.213.
[10] S. Hayashi, S.I. Ford, D.J. Young, D.J. Sordelet, M.F. Besser, B. Gleeson, α-NiPt(Al) and phase equilibria in the Ni-Al-Pt system at 1150 °C, Acta Mater. 53 (2005) 3319–3328, http://dx.doi.org/10.1016/j.actamat.2005.03.046.
[11] X.-G. Lu, B. Sundman, J.A. gren, Thermodynamic assessments of the Ni–Pt and Al–Ni–Pt systems, Calphad 33 (2009) 450–456, http://dx.doi.org/10.1016/j.calphad.2009.06.002.
[12] S. Bose, High Temperature Coatings, Butterworth-Heinemann, Elsevier, New York, NY, 2007.
[13] M.R. Jackson, J.R. Rairden, The aluminization of platinum and platinum-coated IN-738, Metall. Trans. A 8 (1977) 1697–1707.
[14] J. Zhu, C. Zhang, D. Ballard, P. Martin, J. Fournelle, W. Cao, et al., Study of the Ni-rich multi-phase equilibria in Ni–Al–Pt alloys using the cluster/site approximation for the face-centered cubic phases, Acta Mater. 58 (2010) 180–188, http://dx.doi.org/10.1016/j.actamat.2009.08.068.
[15] B. Grushko, D. Kapush, V. Konoval, V. Shemet, A study of the Al-Ni-Pt alloy system. Phase equilibria at 1100 and 1300°C, Powder Metall. Met. Ceram. 50

(1978) 1–9, http://dx.doi.org/10.1007/s11106-011-9350-9.
[16] B. Grushko, D. Kapush, A refinement of the Al-Ni-Pt phase diagram, J. Alloy. Compd. 594 (2014) 127–132, http://dx.doi.org/10.1016/j.jallcom.2014.01.114.
[17] J.L. Kamm, W.W. Milligan, Phase stability in (Ni, Pt)3Al alloys, Scr. Metall. Mater. 31 (1994) 1461–1464, http://dx.doi.org/10.1016/0956-716X(94)90056-6.
[18] E. Copland, Thermodynamic Effect of Platinum Addition to β-NiAl: An Initial Investigation, Cleveland, Ohio, 2005.
[19] E. Copland, Partial thermodynamic properties of γ′-(Ni,Pt)3Al in the Ni-Al-Pt system, J. Phase Equilibria Diffus. 28 (2007) 38–48, http://dx.doi.org/10.1007/s11669-006-9004-7.
[20] C. Jiang, M.F. Besser, D.J. Sordelet, B. Gleeson, A combined first-principles and experimental study of the lattice site preference of Pt in B2 NiAl, Acta Mater. 53 (2005) 2101–2109, http://dx.doi.org/10.1016/j.actamat.2004.12.038.
[21] C. Jiang, D.J. Sordelet, B. Gleeson, First-principles study of phase stability in pseudobinary $(Ni_{1-x}Pt_x)$3Al alloys, Phys. Rev. B – Condens. Matter Mater. Phys. 72 (2005) 1–7, http://dx.doi.org/10.1103/PhysRevB.72.184203.
[22] DongEung Kim, Thermodynamic Modeling and Prediction of Elastic and Thermal Expansion Properties of Ni-base Superalloys: Application to Ni-Al-Pt-Cr-Hf System with gamma and gamma prime Phases (Ph.D. Thesis), University Park, Pennsylvania, USA, 2011.
[23] N. Dupin, B. Sundman, A thermodynamic database for Ni-base superalloys, Scand. J. Metall. 30 (2001) 184–192.
[24] U.R. Kattner, Construction of a Thermodynamic Database for Ni-Base Superalloys: A Case Study, in: TMS CALPHAD Alloy Thermodynamics, 2002, pp. 147–164.
[25] A. Kusoffsky, N. Dupin, B. Sundman, On the compound energy formalism applied to fcc ordering, Calphad 25 (2001) 549–565.
[26] T. Abe, B. Sundman, A description of the effect of short range ordering in the compound energy formalism, Calphad Comput. Coupling Phase Diagr. Thermochem. 27 (2003) 403–408, http://dx.doi.org/10.1016/j.calphad.2004.01.005.
[27] B. Hallstedt, O. Kim, Thermodynamic assessment of the Al-Li system, Int. J. Mater. Res. (Z. Für Met.) 98 (2007) 961–969.
[28] N. Dupin, I. Ansara, On the sublattice formalism applied to the B2 phase, Z. Für Met. 90 (1999) 76–85.
[29] N. Dupin, I. Ansara, B. Sundman, Thermodynamic Re-assessment of the ternary system Al-Cr-Ni, Calphad 25 (2001) 279–298.
[30] P. Franke, Modeling of thermal vacancies in metals within the framework of the compound energy formalism, J. Phase Equilibria Diffus. 35 (2014) 780–787, http://dx.doi.org/10.1007/s11669-014-0348-0.
[31] F. Stein, C. He, N. Dupin, Melting behaviour and homogeneity range of B2 CoAl and updated thermodynamic description of the Al–Co system, Intermetallics 39 (2013) 58–68.
[32] D. Connetable, J. Lacaze, P. Maugis, B. Sundman, A. Calphad, assessment of Al–C–Fe system with the carbide modelled as an ordered form of the fcc phase, Calphad 32 (2008) 361–370, http://dx.doi.org/10.1016/j.calphad.2008.01.002.
[33] A.J. McAlister, D.J. Kahan, The Al–Pt (Aluminum-Platinum) system, Bull. Alloy Phase Diagr. 7 (1986) 47–51, http://dx.doi.org/10.1007/BF02874982.
[34] Y. Oya, Y. Mishima, T. Suzuki, The Pt-Al and Pt-Ga phase diagram with emphasis on the polymorphism of Pt3Al and Pt3Ga, Z. Für Met. 78 (1987) 485–490.
[35] W.-G. Jung, O.J. Kleppa, L. Topor, Standard molar enthalpies of formation of PdAl, PtAl, ScAl1.78, YAl2 and LaAl2, J. Alloy. Compd. 176 (1991) 309–318, http://dx.doi.org/10.1016/0925-8388(91)90039-X.
[36] S.V. Meschel, O.J. Kleppa, Standard enthalpies of formation of 5d aluminides by high-temperature direct synthesis calorimetry, J. Alloy. Compd. 197 (1993) 75–81, http://dx.doi.org/10.1016/0925-8388(93)90621-S.
[37] Y. Kobayashi, T. Egawa, S. Tamura, N. Imanaka, G. Adachi, Trivalent Al3+ ion conduction in aluminum tungstate solid, Chem. Mater. 9 (1997) 1649–1654.
[38] M. Nanko, Y. Kishi, T. Maruyama, Activity of aluminum in Pt–Al solid solution by EMF method with CaF2 solid electrolyte, Mater. Trans. – Jpn. Inst. Met. 39 (1998) 1238–1242.
[39] H. de Waal, R. Pretorius, Lateral diffusion study of the Pt-Al system using the NAC nuclear microprobe, Nucl. Instrum. Methods Phys. Res. Sect. B Beam Interact. Mater. At. 158 (1999) 717–721, http://dx.doi.org/10.1016/S0168-583X(99)00310-9.
[40] R. Völkl, C. Huang, H. Harada, Stabilizing the L12 structure of Pt3Al(r) in the Pt-Al-Sc system, Metall. Mater. Trans. A 36 (2005) 2881–2892.
[41] A. Douglas, J.H. Neethling, R. Santamarta, D. Schryvers, L. a Cornish, Unexpected ordering behaviour of Pt3Al intermetallic precipitates, J. Alloy. Compd. 432 (2007) 96–102, http://dx.doi.org/10.1016/j.jallcom.2006.05.106.
[42] W. Tshawe, The Behaviour of Pt-Based Alloys at High Temperature (Ph.D. Thesis), University of the Witwatersrand, Johannesburg, South Africa, 2008.
[43] H.R. Chauke, B. Minisini, R. Drautz, D. Nguyen-Manh, P.E. Ngoepe, D.G. Pettifor, Theoretical investigation of the Pt3Al ground state, Intermetallics 18 (2010) 417–421, http://dx.doi.org/10.1016/j.intermet.2009.08.016.
[44] J. Feng, B. Xiao, J. Chen, Y. Du, J. Yu, R. Zhou, Stability, thermal and mechanical properties of PtxAly compounds, Mater. Des. 32 (2011) 3231–3239, http://dx.doi.org/10.1016/j.matdes.2011.02.043.
[45] B. Grushko, On the constitution of Al-Pt-(Pd or Ni) around 50 at% Al, J. Alloy. Compd. 541 (2012) 88–93, http://dx.doi.org/10.1016/j.jallcom.2012.06.114.
[46] B. Grushko, D. Kapush, J. Su, W. Wan, S. Hovmöller, Al-rich region of Al–Pt, J. Alloy. Compd. 580 (2013) 618–625, http://dx.doi.org/10.1016/j.jallcom.2013.07.178.
[47] R. Süss, L. a Cornish, M.J. Witcomb, Investigation of as-cast alloys in the Pt-Al-Cr system, J. Alloy. Compd. 490 (2010) 124–144, http://dx.doi.org/10.1016/j.jallcom.2009.10.032.
[48] B. Grushko, D. Kapush, L. Meshi, A study of the Al-rich part of the Al-Ni-Pt alloy system, J. Alloy. Compd. 514 (2012) 60–63, http://dx.doi.org/10.1016/j.jallcom.2011.10.076.
[49] S. Bhan, H. Kudielka, Ordered bcc-phases at high temperature in alloys of transition metals and B-subgroup elements, Z. Met. 69 (1978) 333–336.
[50] H.-J. Schaller, Der Einfluß der Fermi-Energie auf das thermodynamische Verhalten von Platin-Mischkristallen, Z. Phys. Chem. 112 (1978) 85–99 (in German).
[51] X.L. Liu, B.K. VanLeeuwen, S.S.-L. Shang, Y. Du, Z.-K. Liu, On the scaling factor in Debye-Grüneisen model: a case study of the Mg-Zn binary system, Comput. Mater. Sci. 98 (2015) 34–41.
[52] S.L. Shang, Y. Wang, D. Kim, Z.-K. Liu, First-principles thermodynamics from phonon and Debye model: application to Ni and Ni3Al, Comput. Mater. Sci. 47 (2010) 1040–1048.
[53] C. Jiang, L.-Q. Chen, Z.-K. Liu, First-principles study of constitutional point defects in B2 NiAl using special quasirandom structures, Acta Mater. 53 (2005) 2643–2652.
[54] B. Jansson, Evaluation of Parameters in Thermochemical Models using Different Types of Experimental Data simultaneously, Technical Report TRITA-MAC-0234, Stockholm, Sweden, 1984.
[55] B. Sundman, B. Jansson, J.-O. Andersson, The Thermo-Calc databank system, Calphad 9 (1985) 153–190, http://dx.doi.org/10.1016/0364-5916(85)90021-5.
[56] J.-O. Andersson, T. Helander, L. Höglund, P. Shi, B. Sundman, Thermo-Calc & DICTRA, computational tools for materials science, Calphad 26 (2002) 273–312.
[57] R. Huch, W. Klemm, Das system platin-aluminium, Z. Für Anorg. Allg. Chem. 329 (1964) 123–135, http://dx.doi.org/10.1002/zaac.19643290116 (in German).
[58] N. Dupin, Contribution A L'Evaluation Thermodynamique Des Alliages Polyconstitues A Base De Nickel (Ph.D. Thesis), Grenoble Institute of Technology, Grenoble, France, 1992.
[59] B. Sundman, N. Dupin, No Title, in: JEEP Conf., Lyon, 2003.
[60] C. Jiang, L.Q. Chen, Z.K. Liu, First-principles study of constitutional and thermal point defects in B2 PdIn, Intermetallics 14 (2006) 248–254, http://dx.doi.org/10.1016/j.intermet.2005.05.012.
[61] R. Ferro, R. Capelli, A. Borsese, G. Centineo, Research on alloys of nobel metals with less electropositive elements. XII – Heats of formation of AL-Pt Alloys, Atti Della Accad. Naz. Dei Lincei Cl. Di. Sci. Fis. Mat. Nat. 45 (1968) 54–59.
[62] W.L. Worrell, T.A. Ramanarayanan, Electrochemical cell investigations of platinum binary systems at elevated temperature, Chem. Metall.: Tribut. Carl Wagner (1981) 69–74.
[63] C. Colinet, A. Bessoud, A. Pasturel, Thermodynamic investigation of (NI, Pd, Pt)-(AL, in) alloys, Z. Met. 77 (1986) 798–804.
[64] A.T. Dinsdale, SGTE data for pure elements, Calphad 15 (1991) 317–425.
[65] Scientific Group Thermodata Europe (SGTE), A.T. Dinsdale, In: SGTE Pure Element Database (UNARY) v. 4.6, 2008.
[66] Scientific Group Thermodata Europe (SGTE), Thermodynamic Properties of Inorganic Materials Compiled by SGTE, Springer, New York, NY, 1999.
[67] A.S. Darling, G.L. Selman, R. Rushforth, Platinum and the refractory oxides I-compatibility and decomposition processes at high temperature, Platin. Met. Rev. 14 (1970) 54–60 ⟨http://www.platinummetalsreview.com/dynamic/article/view/pmr-v14-i2-054-060⟩.
[68] D. Chatterji, R.C. Devries, J.F. Fleischer, Investigation of sub-solidus equilibria in the platinum-aluminium system using diffusion couples, J. Less Common Met. 42 (1975) 187–198, http://dx.doi.org/10.1016/0022–5088(75)90004-1.
[69] T. Chattopadhyay, K. Schubert, Kristallstruktur von Pt3Ga(r) und einigen phasen der mischung Pt-Al, J. Less Common Met. 41 (1975) 19–32, http://dx.doi.org/10.1016/0022–5088(75)90090-9 (in German).
[70] P. Guex, P. Feschotte, Les Systemes Binaries Platine-Aluminium, Platine-Gallium et Platine-Indium, J. Less-Common Met. 46 (1976) 101–116 (in French).
[71] S. Bhan, H. Kudielka, Ordere bcc-phases at high temperatures in alloys of transition metals and B-subgroup elements, Z. Für Met. 69 (1978) 333–336.
[72] H.-J. Schaller, Magnetische Eigenschaften un Gitterparameter von Platin-Mischkristallen, Z. Für Met. 70 (1979) 318–321.
[73] B. Sundman, I. Ohnuma, N. Dupin, U.R. Kattner, S.G. Fries, An assessment of the entire Al–Fe system including D03 ordering, Acta Mater. 57 (2009) 2896–2908.
[74] A.M. Tonejc, A. Tonejc, A. Bonefacic, Non-equilibrium phases in Al-rich Al-Pt alloys, J. Mater. Sci. 9 (1974) 523–526.
[75] T. Chattopadhyay, K. Schubert, Kristallstruktur von Pt2Al.r, J. Less-Common Met. 45 (1976) 79–83 (in German).
[76] G. Piatti, G. Pellegrini, The structure of the unidirectionally solidified Al-Al21Pt5 eutectic alloys, J. Mater. Sci. 15 (1980) 2403–2408, http://dx.doi.org/10.1007/BF00552339.
[77] M. Ellner, U. Kattner, B. Predel, Konstitutionelle und strukturelle untersuchungen im aluminiumreichen teil der systeme Ni-Al und Pt-Al, J. Less-Common Met. 87 (1982) 305–325 (in German) ⟨http://www.sciencedirect.com/science/article/pii/0022508882900972⟩.
[78] K. Schubert, On the binding in phases of mixtures T 10 B N 3, Z. Krist. 148 (1978) 193–206, http://dx.doi.org/10.1524/zkri.1978.148.3-4.193.
[79] W.L. Worrell, T.A. Ramanarayanan, Electrochemical cell investigations of Pt binary systems, Chem. Metall.: Tribut. Carl Wagner (1981) 69–74.

CALPHAD: Computer Coupling of Phase Diagrams and Thermochemistry 52 (2016) 125–142

Contents lists available at ScienceDirect

CALPHAD: Computer Coupling of Phase Diagrams and Thermochemistry

journal homepage: www.elsevier.com/locate/calphad

Invited article

Thermodynamic modeling of Al–Co–Cr, Al–Co–Ni, Co–Cr–Ni ternary systems towards a description for Al–Co–Cr–Ni

Xuan L. Liu [a,*], Greta Lindwall [a], Thomas Gheno [b], Zi-Kui Liu [a]

[a] Department of Materials Science and Engineering The Pennsylvania State University, University Park, PA 16802, United States
[b] Department of Mechanical Engineering and Materials Science University of Pittsburgh, Pittsburgh, PA 15261, United States

ARTICLE INFO

Article history:
Received 6 July 2015
Received in revised form
19 December 2015
Accepted 22 December 2015
Available online 6 January 2016

Keywords:
Al–Co–Cr
Al–Co–Ni
Co–Cr–Ni
MCrAlY
NiCoCrAlY
B2

ABSTRACT

The phase relations and thermodynamic properties of the Al–Co–Cr, Al–Co–Ni, Co–Cr–Ni ternary alloys are investigated using first principles calculations based on DFT (density functional theory). Their thermodynamic descriptions are developed by means of the CALPHAD (calculations of phase diagrams) method using experimental and computational data from the present work and the literature. Emphasis is placed on modeling the A2, B2, fcc-γ, L12-γ′ and tetragonal-σ phases in the temperature range of 1173–1623 K. Liquid, A2 and fcc-γ phases are modeled using substitutional solution descriptions. A partitioning model is then used for the γ/γ′ and A2/B2 phases to effectively describe the order–disorder transitions. The critically assessed thermodynamic descriptions describe all experimentally determined phase equilibria data well. A2/B2 transitions are also shown to agree well with previous experimental findings in the Al–Co–Cr ternary system.

1. Introduction

Overlay MCrAlY (M=Ni, Co or NiCo) coatings are critical in the protection of high-temperature Ni- and Co-base superalloys operating in corrosive environments such as gas turbine hot sections. These coatings are used either solely or in conjunction with a ceramic topcoat such as yttria-stabilized zirconia as a part of the thermal barrier coating system [1–4]. Phase fractions and compositions in the coatings change as a result of selective oxidation and interdiffusion during service. It is important to thoroughly understand the thermodynamics of these alloys in order to predict their microstructural evolution, as it affects the corrosion resistance and mechanical properties of the overall system.

In the base Al–Co–Cr–Ni system, there are 6 binaries (Al–Co, Al–Cr, Al–Ni, Co–Cr, Co–Ni, and Cr–Ni) and 4 ternaries (Al–Co–Cr, Al–Co–Ni, Al–Cr–Ni, Co–Cr–Ni) to be studied. In previous work on the Al–Co–Cr system [5], the effectiveness of a computational approach in predicting accurate phase relations by implementing the CALPHAD method (Calculation of Phase Diagrams) has been demonstrated. This method has also been used extensively and successfully to study the thermodynamics of multi-component Ni-base superalloys [6,7]. In the literature, there is no complete description of the Al–Co–Cr–Ni alloy system. The present work focuses on the modeling of the subsystems, especially Al–Co–Ni and Co–Cr–Ni, necessary in building a coherent Al–Co–Cr–Ni quaternary description. Some modifications are made in the description of the Al–Co–Cr [5] system and are discussed in detail later in the manuscript. The quaternary Al–Co–Cr–Ni system is studied in a separate publication [8].

While B2 (β, $Pm\bar{3}m$, simple cubic type) and fcc-A1 (γ, $Fm\bar{3}m$, disordered f.c.c.) are the desired phases in MCrAlY coatings, all other phases must be modeled to give an accurate overall description of phase stability in the system. These include bcc-A2 (α, $Im\ \bar{3}m$, disordered b.c.c.), hcp-A3 (ε, $P6_3/mmc$, disordered h.c.p.), $L1_2$ (γ′, $Pm\bar{3}m$, simple cubic type), sigma (σ, $P4L_2/mnm$, Frank–Kasper, Fig. 1(a)) and the binary intermetallics.

The present paper focuses on evaluating and modeling the important ternary alloy systems found in the Al–Co–Cr–Ni quaternary in order to produce meaningful extrapolations without the need of excessive higher order parameters. First-principles calculations based on density functional theory (DFT) are performed to supplement the lack of experimentally measured thermochemical data. By effectively combining these results with experimental information from the literature, energetically accurate parameters in the lower order systems are evaluated. Ultimately, this model will be used in the construction of a multicomponent Al–Co–Cr–Ni database in future work.

* Corresponding author.
E-mail address: xul119@psu.edu (X.L. Liu).

http://dx.doi.org/10.1016/j.calphad.2015.12.007
0364-5916/

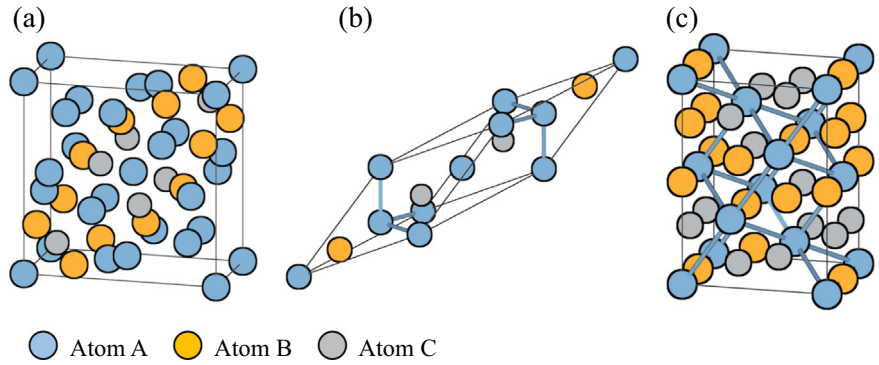

Fig. 1. Atomic structures for the σ (a), the SQS 8-atom B2 (b) and the SQS for the 24-atom γ′ (c). The different colors denote different atomic species and some bonds have been added to aid in the visualization of the unit cell crystal structures. Structures shown are used for ternary DFT calculations: σ-$(B)_8(A)_{18}(C)_4$, B2-$(A)_4(B)_2(C)_2$, γ′ -$(B)_9(C)_9(A)_6$. (For interpretation of the references to color in this figure legend, the reader is referred to the web version of this article.)

2. Literature review

2.1. Binary models used in the present work

The assessment of the Al–Co binary by Dupin and Ansara [9] reproduces all experimental results available in the literature satisfactorily and is hence adopted in the present work. The model for B2 in the original Al–Co binary was asymmetrical and was changed to the order–disorder model by Liu et al. in previous work on the system [5], which is adopted here. The Al–Cr assessment by Saunders, which can be found in the COST507 [10] database, is also accepted without modification. The assessment for the Al–Ni binary by Ansara et al. [11], (later modified by Dupin et al. [6]) has been used extensively previously and is, therefore, adopted in the present work. There are two descriptions of the Co–Cr binary available which both reproduce certain experiments well, one by Oikawa et al. [12] and another by Kusoffsky et al. [13]. However, it has been found that the Oikawa description has σ end-member energies which disagree with experiments by Downie and Arslan [14] though it was adopted in the previous modeling of Al–Co–Cr [5]. It is important to have correct energies in the binary subsystems to produce accurate extrapolations to the higher order systems and for this reason, the model by Kusoffsky et al. [13] is used here. The Co–Ni and Cr–Ni binary descriptions are taken from SGTE [15], based on works by Guillermet [16] and Lee [17], respectively. In addition, the present Cr–Ni description includes a metastable description of σ following the work by Gustafson [18] in the ternary Ni–Cr–W system which is later modified by Kattner [7]. Recently, the Al–Co system has been reassessed by Stein et al. [19] with slight improvements in the B2 phase boundaries. Al–Ni has also been reassessed recently by Chen et al. [20] to improve the B2 solidus and liquidus. However, both descriptions offer different values for the substitutional A2 vacancy end-members and cannot be adopted in the current work without significant remodeling of the Al–Cr–Ni system also adopted in the current work.

2.2. Ternary models and experiments

A summary of the experimental techniques from the literature for the ternary systems is shown in Table 1.

2.2.1. Al–Co–Cr

In previous work [5], the Al–Co–Cr description was assessed using experimental findings from Ishikawa et al. [21] supplemented with new phase equilibrium experiments and first-principles data. While the model by Oikawa et al. [12] better reproduces A2+σ phase boundaries, the model by Kusoffsky et al. [13] better reproduces formation energies for the σ when

Table 1
Summary of relevant experimental information used in the modeling.

References	Exp. method	Exp. data
Al–Co–Cr		
Moskvitina et al. [92]	XRD	Isothermal section at 1173 using cast alloys; no phase compositions
Ishikawa et al. [21]	EDS, TEM	Isothermal sections at 1273, 1473, 1573 and 1623 K determined using cast alloys and diffusion couples, order–disorder transition; phase compositions given
Liu et al. [5]	XRD, EPMA	Isothermal sections at 1173, 1273 and 1373 K
Al–Co–Ni		
Schramm [23]	OM, XRD	Isothermal sections at 1173, 1273, 1373, 1473, 1573 K and room temperature using cast alloys. Vertical sections at Ni:Co concentrations of 90:10, 80:20, 50:50, and 20:80; no phase compositions
Kek et al. [25]	Calorimetry	γ′ enthalpies of formation for various Co additions
Jia et al. [24]	SEM, EDS, TEM, XRD	B2, γ, and γ′ phase boundaries near γ′ at 1073, 1173, 1273, 1373, 1473, and 1573 K; phase compositions given
Kainuma et al. [27]	SEM, EDS, TEM, XRD, DSC	Isothermal sections at 1173, 1373, and 1573 K; phase compositions given
Albers et al. [28]	SEM, KEMS	Solubility of Co in γ′ at 1473 K, activities from 1326 to 1581 K; phase compositions given
Grün et al. [29]	DSC	B2 enthalpies of formation at 1073 K
Co–Cr–Ni		
Kubaschewski and Hack [42]	Adiabatic calorimetry	Enthalpies of formation for A2, γ, and σ alloys at 1523 K, some at 1523–1648 K
Zhanpeng [41]	EPMA	Isothermal section at 1473 K; phase compositions given
Zhmurko et al. [39]	SEM, EDS, XRD	Isothermal section at 1073 K using cast alloys; phase compositions given
Omori et al. [40]	EPMA, XRD, DSC	Isothermal sections at 1073, 1173, 1273, 1373, 1473, and 1573 K, liquidus and solidus temperatures at 10–40% Cr concentrations; phase compositions given

compared to measurements by Downie and Arslan [14]. Switching to the description by Kusoffsky et al. [13] will yield better higher order extrapolations for this complex intermetallic. The A2/B2 phases are modeled using a single Gibbs energy function in the previous work [5] and will be retained in the present modeling.

2.2.2. Al–Co–Ni

The Al–Co–Ni ternary system was first modeled by Dupin [22] and reproduces experimental phase equilibria from Schramm [23] and Jia et al. [24] as well as enthalpies from Kek et al. [25]. This system has been remodeled recently by Zhu et al. [26] for incorporation into a Al–Co–Ni–W quaternary database. Since an A2/B2 transition is expected to be present in the quaternary Al–Co–Cr–Ni system, the Al–Co–Ni system will be remodeled with the A2/B2 as one Gibbs energy function in the present work.

We further use new experimental phase equilibria on the γ, γ′ and B2 from Kainuma et al. [27] and Albers et al. [28] as well as enthalpies of formation data from Grün et al. [29]. Schramm [23] originally investigated isothermal/vertical sections pertaining to γ, γ′ and B2 from room temperature to 1350 °C, and Gödecke et al. [30–33] studied the Al-rich corner of the Al–Co–Ni phase diagram in a series of experiments focusing on Al-rich intermetallics. In addition to the above experimental information available in the literature, first-principles calculations of the solution phases are performed in the present work to aid the modeling.

A complete experimental review of the Al–Co–Ni system was performed by Velikanova et al. [34] which shows the presence of numerous ternary phases in the Al-rich corner of the phase diagram. The current work attempts to address the thermodynamic description of only the Ni–Co rich section of the Al–Co–Ni ternary system for bond coat alloy applications. Al-rich ternary phases will be studied in future work.

2.2.3. Al–Cr–Ni

The Al–Cr–Ni ternary by Dupin et al. [6] is adopted in the present work. Both the A2/B2 and γ/γ′ phases use partitioned Gibbs energy models which is compatible with the Al–Co–Cr ternary model in the present work. All experimental data found in the literature is well reproduced except for the A2/B2 phase boundary near the Cr-rich region of the system at 1423 K compared to EPMA measurements by Oforka and Argent [35]. This was recently investigated, using diffusion couples and EPMA, by Cutler [36] at 1473 K and the A2/B2 phase boundary is found to disagree with those found by Oforka and Argent [35]. More experiments must be performed to determine the phase boundaries in this region at temperatures above 1373 K. A summary of experiments relevant to this ternary can be found in Dupin et al. [6] and is not repeated in detail in the present manuscript. The model by Dupin et al. [6] describes mostly the Cr–Ni rich region of the phase diagram. In order for this system to be compatible with the other ternary subsystems within the Al–Co–Cr–Ni quaternary system, σ is introduced as a metastable ternary phase in the present work with data obtained from first-principles calculations. An earlier description of Al–Cr–Ni by Huang and Chang [37], which is used in the NIST superalloy database by Kattner [7], uses the asymmetrical B2 model is not adopted in the current work.

2.2.4. Co–Cr–Ni

Yang et al. [38] modeled the Co–Cr–Ni ternary using binary descriptions different from those implemented here as well as superfluous ternary interaction parameters. Here, the system is remodeled using the following binary models due to ternary compatibility with the Al–Co–Cr, Al–Co–Ni and Al–Cr–Ni systems: Co–Cr by Kusoffsky et al. [13], Co–Ni by Guillermet [16], and Cr–Ni by Lee. [17]. As is shown in Table 1, phase equilibrium data by Zhmurko et al. [39], Omori et al. [40], and Zhanpeng [41] are accounted for in the evaluation. Additionally, A2, γ, and σ formation enthalpies measured by Kubaschewski and Hack [42] are used. First-principles calculations of the solution phases are performed and accounted for in the modeling work.

3. Thermodynamic models

The thermodynamic modeling methodology remains the same as in previous work on Al–Co–Cr [5]. However, γ′ was not modeled as it is not stable in Al–Co–Cr. In the present work γ′ is stable in the Al–Co–Ni and Al–Cr–Ni ternary extensions of the Al–Ni binary and hence, γ′ must be included as a metastable phase in the Al–Co–Cr and Co–Cr–Ni systems. To account for the A2/B2 order–disorder transition and γ′ ordering from γ, each of the bcc and fcc phases is modeled using a partitioning model, which treats the ordered and disordered components separately and with the same Gibbs energy functions [43]. Additionally, in B2-containing systems such as Al–Co [9], Al–Fe [44] or Al–Ni [6], triple-defect mechanisms are especially important and have to be accounted for when considering site ordering. Ordering of the bcc phase was described in Ref. [5]. The ordering of the fcc phase is described in the following section.

The PARROT module [45] within Thermo-Calc [46,47] is used to assess all model parameters for each phase in the system using phase equilibrium data from the experimental measurements listed in Table 1 as well as first-principles data obtained in the present work. Discrepancies in higher order systems can sometimes stem from inappropriate parameter choices in lower order systems in which distinct sets of parameters can describe phase equilibria equally well [48]. Therefore, the optimized ternary parameters are systematically extrapolated to the quaternary Al–Co–Cr–Ni system to ensure consistency and agreement with quaternary data from Ref. [8]. Finalized parameters included in the Appendix are those that reproduce the ternary as well as the quaternary system best.

3.1. Modeling of fcc-γ and L12-γ′

The γ and γ′ phases are modeled with a single Gibbs energy function using a partitioned two sublattice model (2SL) $(Al,Co,Cr,Ni)_3(Al,Co,Cr,Ni)$ to be compatible with the Al–Cr–Ni binary by Dupin et al. [6]:

$$\boldsymbol{G_m^{\gamma/\gamma'} = G_m^{\gamma}(x_i) + \Delta G_m^{Order}\left(y_i^{(s)}\right)} \quad (1)$$

where $y_i^{(s)}$ denotes the site fraction of element i on sublattice s, $G_m^{\gamma}(x_i)$ describes the contributions from the disordered solution with only mole fractions taken into account and $\Delta G_m^{Order}(y_i^{(s)})$ describes the site-fraction dependent ordering energy. The ordering term can be expressed as the difference of two terms with one dependent only on mole fraction:

$$\boldsymbol{G_m^{\gamma/\gamma'} = G_m^{\gamma}(x_i) + G_m^{\gamma'(O)}\left(y_i^{(s)}\right) - G_m^{\gamma'(O)}\left(y_i^{(s)} = x_i\right)} \quad (2)$$

when $G_m^{\gamma'(O)}(y_i^{(s)})$ and $G_m^{\gamma'(O)}(y_i^{(s)} = x_i)$ are equal, the ordering terms cancel out and the phase is completely disordered. The term $G_m^{\gamma'(O)}(y_i^{(s)})$ takes on the partitioned form, as described by Dupin et al. [6], and is expressed as

$$G_m^{\gamma'(O)}(y_i^{(s)}) = \sum_i \sum_j (y_i' y_j'' {}^{o}G_{i:j}^{\gamma'(O)}) + RT\left[\frac{3}{4}\sum_i y_i' \ln(y_i') + \frac{1}{4}\sum_j y_j'' \ln(y_j'')\right] + \sum_i \sum_j \sum_k \left\{ y_i' y_j' y_k'' \left[\sum_k {}^{v}L_{i,j:k}^{\gamma'(O)}(y_i' - y_j')^v\right]\right\} + \sum_i \sum_j \sum_k \left\{ y_k' y_i'' y_j'' \left[\sum_k {}^{v}L_{k:i,j}^{\gamma'(O)}(y_i'' - y_j'')^v\right]\right\} + \sum_i \sum_j \sum_k \sum_l (y_i' y_j' y_k' y_l'' {}^{v}L_{i,j,k:l}^{\gamma'(O)} + y_i'' y_j'' y_k'' y_l' {}^{v}L_{l:i,j,k}^{\gamma'(O)}) \quad (3)$$

here *i*, *j*, *k*, and *l* represent Al, Co, Cr, or Ni. Ansara et al. [49] proposed a set of constraints for this equation for both end-members and interaction parameters that must fulfilled for the phase to disorder correctly even in the case of a non-partitioned model. This is best illustrated in the mathematically equivalent four sublattice model (4SL) (A,B,…) (A,B,…) (A,B,…) (A,B,…) for the $L1_2$. While not true for the 2SL model, the 4SL model has all sites equivalent, and consequently, two species can be interchanged on sublattices without changing the energy of the system. This can be represented by, for the $L1_2$, as

$$G_{A:A:A:B}^{4SL-\gamma'} = G_{A:A:B:A}^{4SL-\gamma'} = \ldots = G_{A_3B}^{4SL-\gamma'} \quad (4)$$

In addition, interactions between species A and B in any sublattice are equivalent if site occupancy in the other sublattices remains the same. As described by Ansara et al. [11] and Dupin et al. [6], the mathematical equivalence of the 4SL and 2SL models for $L1_2$ (when $y_i^{4SL-(1)} = y_i^{4SL-(2)} = y_i^{4SL-(3)} = y_i'$ and $y_i^{4SL-(4)} = y_i''$) allows 2SL parameters to be represented in terms of 4SL parameters for the binary, ternary, and the quaternary systems. However, the $L1_0$ ordering is lost in the conversion of the 4SL to the 2SL fcc model because the $G_{A:A:B:B}^{4SL-\gamma'}$ end-member in the 4SL model has no equivalent in the 2 SL model. End-members with $L1_2$ ordering, $G_{A_3B}^{4SL-\gamma'}$ and $G_{AB_3}^{4SL-\gamma'}$, can be expressed as G_{A_3B} and G_{AB_3} in the 2SL model, respectively. A detailed descriptions of the constraints and conversions can be found in Ref. [50] in the case that no 4SL reciprocal interactions, or so called approximations to short-range ordering [51], exists ($L_{A,B:A,B:*:*}^{4SL-\gamma'}$). Though this is outside the scope of the present work, Yuan et al. [52] and Franke [53] has presented the conversion from 4SL to 2SL with the inclusion of the reciprocal interactions for the binary case. The 2SL expressions for the binary and ternary cases concerned in the present work are given by Ref. [6] as

$$G_{A:B}^{\gamma'} = G_{AB_3} \quad (5)$$

$$G_{B:A}^{\gamma'} = G_{A_3B} \quad (6)$$

$${}^{0}L_{A,B:A}^{\gamma'} = -\frac{3}{2}G_{AB_3} + \frac{3}{2}G_{A_2B_2} + \frac{3}{2}G_{A_3B} \quad (7)$$

$${}^{0}L_{A,B:B}^{\gamma'} = +\frac{3}{2}G_{AB_3} + \frac{3}{2}G_{A_2B_2} - \frac{3}{2}G_{A_3B} \quad (8)$$

$${}^{1}L_{A,B:A}^{\gamma'} = +\frac{1}{2}G_{AB_3} - \frac{3}{2}G_{A_2B_2} + \frac{3}{2}G_{A_3B} \quad (9)$$

$${}^{1}L_{A,B:B}^{\gamma'} = +\frac{3}{2}G_{AB_3} + \frac{3}{2}G_{A_2B_2} - \frac{1}{2}G_{A_3B} \quad (10)$$

$${}^{0}L_{*:A,B}^{\gamma'} = {}^{0}L_{A,B}^{\gamma'} \quad (11)$$

$${}^{1}L_{*:A,B}^{\gamma'} = {}^{1}L_{A,B}^{\gamma'} \quad (12)$$

$${}^{0}L_{A,B:*}^{\gamma'} = {}^{0}L_{A,B}^{\gamma'} \quad (13)$$

$${}^{1}L_{A,B:*}^{\gamma'} = {}^{1}L_{A,B}^{\gamma'} \quad (14)$$

$${}^{0}L_{A,B:C}^{\gamma'} = -\frac{3}{2}G_{A_3C} - \frac{3}{2}G_{B_3C} + \frac{3}{2}G_{AB_2C} + \frac{3}{2}G_{A_2BC} \quad (15)$$

$${}^{0}L_{A,C:B}^{\gamma'} = -\frac{3}{2}G_{A_3B} - \frac{3}{2}G_{BC_3} + \frac{3}{2}G_{ABC_2} + \frac{3}{2}G_{A_2BC} \quad (16)$$

$${}^{0}L_{B,C:A}^{\gamma'} = -\frac{3}{2}G_{AB_3} - \frac{3}{2}G_{AC_3} + \frac{3}{2}G_{ABC_2} + \frac{3}{2}G_{AB_2C} \quad (17)$$

$${}^{1}L_{A,B:C}^{\gamma'} = -\frac{1}{2}G_{A_3C} + \frac{1}{2}G_{B_3C} - \frac{3}{2}G_{AB_2C} + \frac{3}{2}G_{A_2BC} \quad (18)$$

$${}^{1}L_{A,C:B}^{\gamma'} = -\frac{1}{2}G_{A_3B} + \frac{1}{2}G_{BC_3} - \frac{3}{2}G_{ABC_2} + \frac{3}{2}G_{A_2BC} \quad (19)$$

$${}^{1}L_{B,C:A}^{\gamma'} = -\frac{1}{2}G_{AB_3} + \frac{1}{2}G_{AC_3} - \frac{3}{2}G_{ABC_2} + \frac{3}{2}G_{AB_2C} \quad (20)$$

$${}^{0}L_{A,B,C:A}^{\gamma'} = +G_{AB_3} - \frac{3}{2}G_{A_2B_2} - \frac{3}{2}G_{A_3B} + G_{AC_3} - \frac{3}{2}G_{A_2C_2} - \frac{3}{2}G_{A_3C} - \frac{3}{2}G_{ABC_2} - \frac{3}{2}G_{AB_2C} + 6G_{A_2BC} \quad (21)$$

$${}^{0}L_{A,B,C:B}^{\gamma'} = -\frac{3}{2}G_{AB_3} - \frac{3}{2}G_{A_2B_2} + G_{A_3B} + G_{BC_3} - \frac{3}{2}G_{B_2C_2} - \frac{3}{2}G_{B_3C} - \frac{3}{2}G_{ABC_2} + 6G_{AB_2C} - \frac{3}{2}G_{A_2BC} \quad (22)$$

$${}^{0}L_{A,B,C:C}^{\gamma'} = -\frac{3}{2}G_{AC_3} - \frac{3}{2}G_{A_2C_2} + G_{A_3C} - \frac{3}{2}G_{BC_3} - \frac{3}{2}G_{B_2C_2} + G_{B_3C} + 6G_{ABC_2} - \frac{3}{2}G_{AB_2C} - \frac{3}{2}G_{A_2BC} \quad (23)$$

Furthermore, the Gibbs energy of each stoichiometric compound can be expressed as the sum of the bond energies (U):

$$G_{A:B:C:D} = U_{AB} + U_{AC} + U_{AD} + U_{BC} + U_{BD} + U_{CD} + \alpha_{ABCD} \quad (24)$$

and for binary and ternary compounds, the Gibbs energies are given by

$$G_{AB_3} = 3U_{AB} + 3\alpha_{AB_3} \quad (25)$$

$$G_{A_2B_2} = 3U_{AB} \quad (26)$$

$$G_{A_3B} = 3U_{AB} + 3\alpha_{A_3B} \quad (27)$$

$$G_{A_2BC} = 2U_{AB} + 2U_{AC} + U_{BC} + \alpha_{A_2BC} \quad (28)$$

The correction terms, α_i, are applied for the Gibbs energies when the results $\alpha_{ABCD} = 0$ are not satisfactory, as is shown by Kusoffsky et al. [51]. However, this introduces additional parameters and is preferably not implemented unless first-principles results show strong dissimilarity between G_{AB_3} and G_{A_3B}. Some bond energies are fixed from the binary and ternary assessments including U_{AlNi}, U_{AlCr}, and U_{CrNi} from the Al–Cr–Ni description by Dupin et al. [6]. The bond energies U_{AlCo} and U_{CoNi} are assessed in the present work by utilizing first-principles calculations and experimental results.

Table 2
Calculated DFT elastic stiffness constants and various properties of the end-members of B2 and γ′ compared to experimental data and calculations available in the literature. Stable end-members CoAl, NiAl, and Ni_3Al are bolded while mechanically unstable CoNi and Cr_3Al are italicized.

End-member	Temp (K)	C_{11}	C_{12}	C_{44}	V_0 (Å^3/atom)	B_0 (GPa)	ν	Scaling factor	Θ_D (K)	Ref.
B2										
CoAl	298	305.6	121.1	140.4	11.615	178.2	0.233	0.893	640	This work
CoAl	298	268.8	107.2	139.2						Expt. [71]
CoAl	298	320	108	140		175	0.213			Calc. [76]
AlCr	298	262.4	146.6	126.4	14.031	124.6	0.269	0.822	722	This work
NiAl	298	218.2	141.4	117.6	12.129	157.8	0.301	0.756	523	This work
NiAl	73	210	135	117						Expt. [72]
NiAl	298	211.5	143.2	112.1						Expt. [73]
NiAl	296	197	119	110		145				Expt. [74]
NiAl	295	205	135	117		159				Expt. [75]
NiAl									470–560	Expt. [95]
NiAl		202	129	113						Calc. [77]
NiAl		233	121	114	12.069	159				Calc. [76]
CoCr	298	306.6	179.8	148.6	11.600	214.0	0.294	0.772	537	This work
CoNi	*298*	*119.7*	*239.3*	*142.5*	*11.107*	*190.9*				This work
CrNi	298	185.3	157.5	125.0	12.175	148.5	0.325	0.705	429	This work
γ′-$L1_2$										
Al_3Co	298	196.6	88.1	66.4	13.663	125.5	0.288	0.783	527	This work
Al_3Co					12.932					Calc. [86]
Co_3Al	298	190.6	162.7	97.1	11.472	172.4	0.362	0.622	396	This work
Co_3Al					10.857					Calc. [86]
Al_3Cr	298	190.1	62.5	73.2	14.838	105.3	0.230	0.900	579	This work
Cr_3Al	*298*	*184.3*	*238.9*	*107.9*	*12.431*	*198.7*				This work
Al_3Ni	298	191.8	75.9	32.1	14.222	110.7	0.341	0.670	437	This work
Ni_3Al	298	248.1	158.1	129.0	11.385	178.4	0.302	0.755	503	This work
Ni_3Al	90	227	148	129						Expt. [78]
Ni_3Al	300	224.5	148.6	124.4						Expt. [79]
Ni_3Al									470	Expt. [96]
Ni_3Al		242.2	151.8	125.4	11.365	180				Calc. [80]
Ni_3Al		231	142	124						Calc. [77]
Co_3Cr	298	434.7	213.5	193.9	10.560	258.0	0.271	0.818	627	This work
Cr_3Co	298	272.9	223.1	125.1	11.367	245.9	0.365	0.614	449	This work
Co_3Ni	298	287.8	165.5	143.1	10.927	203.6	0.287	0.786	506	This work
Ni_3Co	298	287.3	164.8	138.5	10.947	196.1	0.290	0.779	501	This work
Cr_3Ni	298	278.2	218.5	152.7	11.440	238.0	0.338	0.676	494	This work
Ni_3Cr	298	281.4	147.6	137.7	11.261	188.1	0.272	0.816	518	This work

Table 3
Calculated DFT elastic stiffness constants and various properties of the end-members of σ.

End-member	C_{11}	C_{12}	C_{13}	C_{33}	C_{44}	C_{66}	V_0 (Å^3/atom)	B_0 (GPa)	ν	Scaling factor	Θ_D (K)
$(Al)_8(Al)_{18}(Cr)_4$	*118.4*	*110.8*	*50.6*	*175.2*	*−18.4*	*27.6*	*15.704*	*86*			
$(Al)_8(Cr)_{18}(Cr)_4$	460.6	156.5	139.2	469.0	108.6	147.9	12.369	199	0.273	0.815	674
$(Co)_8(Co)_{18}(Cr)_4$	354.5	134.7	129.1	342.8	53.9	75.7	11.121	197	0.333	0.689	446
$(Co)_8(Cr)_{18}(Cr)_4$	503.1	211.9	167.1	534.1	103.1	132.7	11.333	249	0.305	0.748	603
$(Ni)_8(Ni)_{18}(Cr)_4$	351.5	155.8	114.2	355.2	35.5	59.6	11.109	198	0.358	0.631	409
$(Ni)_8(Cr)_{18}(Cr)_4$	427.8	159.2	141.0	475.2	92.4	106.5	11.451	240	0.298	0.763	566
$(Al)_8(Co)_{18}(Cr)_4$	301.6	113.6	93.6	365.3	57.6	88.3	11.648	174	0.298	0.764	499
$(Co)_8(Al)_{18}(Cr)_4$	286.0	125.7	73.5	277.2	65.7	63.3	13.072	141	0.289	0.781	553
$(Al)_8(Ni)_{18}(Cr)_4$	297.2	120.5	78.4	332.4	41.9	64.5	11.834	173	0.329	0.696	452
$(Ni)_8(Al)_{18}(Cr)_4$	301.3	135.5	78.5	245.0	75.3	78.1	13.249	135	0.277	0.806	580
$(Co)_8(Ni)_{18}(Cr)_4$	367.0	146.4	106.7	385.9	36.1	81.3	10.974	209	0.342	0.667	432
$(Ni)_8(Co)_{18}(Cr)_4$	361.9	124.8	116.7	387.5	57.3	74.8	10.757	233	0.320	0.717	461

3.2. Sigma (σ)

When adding Ni to the Al–Co–Cr system, the σ phase modeling needs to be modified accordingly. The model for σ is adapted to accommodate Ni in the first and second sublattices: $(Al,Co,Ni)_8(Al,Co,Cr,Ni)_{18}(Cr)_4$, and the ternary end-members that describe σ now include: σ-$(Al)_8(Co)_{18}(Cr)_4$ and σ-$(Co)_8(Al)_{18}(Cr)_4$ in Al–Co–Cr, σ-$(Al)_8(Ni)_{18}(Cr)_4$ and σ-$(Ni)_8(Al)_{18}(Cr)_4$ in Al–Cr–Ni, as well as σ-$(Co)_8(Ni)_{18}(Cr)_4$ and σ-$(Ni)_8(Co)_{18}(Cr)_4$ in Co–Cr–Ni. No σ end-members exist for the Al–Co, Al–Ni, and Co–Ni binary systems in the confines of the present model.

The sublattice model implemented here for σ does not offer the best description of this CoCr-base σ, as discussed in detail by Joubert [54]. In the current model, Cr can take on a maximum composition of 73.3 at% at the end-member (A)8(Cr)18(Cr)4 (where A is Al or Co). A non-simplified σ model would include 5 distinct sublattices relating to Wyckoff positions with all four Al, Co, Cr, and Ni allowed to occupy each sublattice: $(Al,Co,Cr,Ni)_2(Al,Co,Cr,Ni)_4(Al,Co,Cr,Ni)_8(Al,Co,Cr,Ni)_8(Al,Co,Cr,Ni)_8$ [54,55]. Within this model, 1024 end-members would have to be defined. Simplifications made in Refs. [5] by combining certain sites and restricting site occupation, which are commonly made [54], were thus retained here. A model based on a better suited site combination exists [54], which would lead to a maximum Cr

Table 4
Calculated enthalpies, entropies and Gibbs energies of formation of B2 and γ′ end-members at 298 K with respect to the standard reference states from DFT. Experiments and calculations at various temperatures, including 298 K, are included for comparison; experimental temperature information is given in the second column when available. Mechanically unstable end-members have 0 K enthalpies of formation shown in italics. Asterisks denote data from compilations by other authors.

End-member	Temp. (K)	$\Delta_f H^{298}$ (kJ/mol atom)	$\Delta_f S^{298}$ (J/mol atom/K)	$\Delta_f G^{298}$ (kJ/mol atom)	Ref.
B2					
CoAl	298	−57.673	−8.231	−55.220	This work
CoAl	1100	−59.5			Expt. [81]
Co Al	1073	−60.7 ± 0.5			*Expt. [82]
AlCr	298	−2.776	−6.449	−0.854	This work
NiAl	298	−64.211	−4.241	−62.947	This work
NiAl	298	−66.1 ± 1.3			Expt. [83]
NiAl	Various	−66.4 ± 2.0, −67.0 −62.0, −67.4 ± 2.55 −66.0 ± 0.13, −58.3 ± 1.1			*Expt. [83]
NiAl	298	−67.18			Calc. [84]
CoCr	298	16.597	1.031	16.289	This work
CoNi	*298*	*5.66*			This work
CrNi	298	24.262	5.925	22.497	This work
γ′-L1$_2$					
Al_3Co	298	−20.035	−5.627	−18.358	This work
Al_3Co	0	−22.6			Calc. [86]
Co_3Al	298	−17.345	4.043	−18.550	This work
Co_3Al	0	−19.9			Calc. [86]
Al_3Cr	298	−9.197	−6.699	−7.200	This work
Cr_3Al	*298*	*−12.94*			This work
Al_3Ni	298	−21.175	−1.268	−20.798	This work
Al_3Ni	0	−22.9			Calc. [86]
Ni_3Al	298	−42.126	−2.187	−41.474	This work
Ni_3Al	298	−40.6 ± 1.0			Expt. [25]
Ni_3Al	298	−41.3 ± 1.3			Expt. [85]
Ni_3Al	Various	−37.6 ± 4.2, −38.2 ± 5, −40.6 ± 1, −47.0			*Expt. [85]
Ni_3Al	900	−45.6 ± 1.1	−4.05 ± 1.2	−41.9 ± 0.2, −47.5 ± 1.1, −34.2 ± 0.33, −36.2	*Expt. [87]
Ni_3Al	298	−46.39			Calc. [84]
Ni_3Al	0	−42.38			Calc. [86]
Co_3Cr	298	6.475	−2.176	7.123	This work
Cr_3Co	298	18.079	4.662	16.690	This work
Co_3Ni	298	0.390	−0.303	0.480	This work
Ni_3Co	298	1.321	−0.192	1.378	This work
Cr_3Ni	298	14.291	2.291	13.609	This work
Ni_3Cr	298	−0.719	−1.520	−0.266	This work

Table 5
Calculated enthalpies, entropies and Gibbs energies of formation of σ end-members at 298 K from DFT. Energies taken with respect to the standard reference states. Experiments and calculations at various temperatures, including 298 K, are included for comparison. Mechanically unstable end-members have 0 K enthalpies of formation shown in italics.

End-member	$\Delta_f H^{298}$ (kJ/mol atom)	$\Delta_f S^{298}$ (J/mol atom/K)	$\Delta_f G^{298}$ (kJ/mol atom)	Ref.
$(Al)_8(Al)_{18}(Cr)_4$	*10.976*			This work
$(Al)_8(Cr)_{18}(Cr)_4$	1.736	−2.624	2.518	This work
$(Co)_8(Co)_{18}(Cr)_4$	9.615	3.597	8.543	This work
[1]$(Co)_8(Co)_{18}(Cr)_4$	11.65			Calc. [88]
$(Co)_8(Cr)_{18}(Cr)_4$	6.193	0.157	6.146	This work
[1]$(Co)_8(Cr)_{18}(Cr)_4$	8.39			Calc. [88]
[2]$Co_{39.3}Cr_{60.7}$	6.77 ± 0.05			Expt. [14]
$(Ni)_8(Ni)_{18}(Cr)_4$	8.981	5.048	7.476	This work
$(Ni)_8(Cr)_{18}(Cr)_4$	8.339	−2.663	9.133	This work
$(Al)_8(Co)_{18}(Cr)_4$	−13.385	−1.127	−13.049	This work
$(Co)_8(Al)_{18}(Cr)_4$	−24.582	−4.048	−23.375	This work
$(Al)_8(Ni)_{18}(Cr)_4$	−29.500	−0.119	−29.208	This work
$(Ni)_8(Al)_{18}(Cr)_4$	−33.053	−4.952	−31.578	This work
$(Co)_8(Ni)_{18}(Cr)_4$	16.647	3.533	15.594	This work
$(Ni)_8(Co)_{18}(Cr)_4$	23.057	1.456	22.608	This work

Note: [1]0 K, [2]473 K

concentration of 66.7 at% at the end-member $(A)_{10}(Cr)_{16}(Cr)_4$. With similar site occupations, this would yield Cr concentrations closer to experimental results. Changing sublattice models would require remodeling the Co–Cr binary and associated ternaries; this was outside the scope of the current work but will be investigated in the future. The resulting discrepancy is limited (1–5 at%) and the compositional trends are respected, such that the rest of the system is little affected.

4. First-principles methodologies

A detailed description of the first-principles methodology implemented in this work is given in Ref. [5]. The Helmholtz energy $F(V, T)$ of the condensed phases is calculated using the quasiharmonic approach. A four-parameter Birch–Murnaghan (BM4) equation of state (EOS) [56,57] is used in the fitting to obtain the Helmholtz energy. For the calculations of the elastic stiffness constants, the method proposed by Shang et al. [58] is applied. The lattice vibration model utilized is the Debye–Grüneisen model using a scaling factor in order to both increase accuracy and efficiency. Details about this model have been published previously [59,60].

Table 6
Calculated enthalpies of mixing for A2 from DFT. The results are based on binary and ternary SQS calculations at 0 K with reference states taken as bcc-A2 for Al, Co, and Cr, and Ni. B2 end-members with the same reference states are included. Energies for mechanically unstable ordered structures are shown in italics. Values for Al-Co, Al-Cr, Co-Cr, and Al–Co–Cr and adapted from previous work [5] and are indicated with an asterisk *.

System	Al	Co	Cr	Ni	SQS prototype	ΔH_{mix} (kJ/mol -atom)	$\Delta_f H$ B2-β (kJ/mol atom)	ΔH^{order} (kJ/mol atom)
***Al–Co**	0.75	0.25			16	−8.99		
	0.5	0.5			16	−21.58	−67.75	−46.17
	0.25	0.75			16	−18.42		
***Al–Cr**	0.75		0.25		16	0.93		
	0.5		0.5		16	1.41	−7.96	−9.37
	0.25		0.75		16	1.42		
Al–Ni	0.75			0.25	16	−25.52		
	0.5			0.5	16	−39.83	−73.80	−33.97
	0.25			0.75	16	−31.83		
***Co–Cr**		0.75	0.25		16	9.99		
		0.5	0.5		16	11.98	11.99	0.01
		0.25	0.75		16	9.59		
Co–Ni		0.75		0.25	16	0.20		
		0.5		0.5	16	−0.81	***5.66***	***6.47***
		0.25		0.75	16	−0.37		
Cr–Ni			0.75	0.25	16	10.02		
			0.5	0.5	16	9.15	20.12	10.97
			0.25	0.75	16	4.98		
***Al–Co–Cr**	0.5	0.25	0.25		32	−9.42		
	0.25	0.5	0.25		32	−6.69		
	0.25	0.25	0.5		32	−0.86		
	0.33	0.33	0.33		36	−7.46		
Al–Co–Ni	0.5	0.25		0.25	32	−25.81		
	0.25	0.5		0.25	32	−20.43		
	0.25	0.25		0.5	32	−23.59		
	0.33	0.33		0.33	36	−25.82		
Co–Cr–Ni		0.5	0.25	0.25	32	0.86		
		0.25	0.5	0.25	32	11.95		
		0.25	0.25	0.5	32	8.03		
		0.33	0.33	0.33	36	3.83		

Table 7
Calculated enthalpies of mixing for γ from DFT. These calculations are based on binary and ternary SQS calculations at 0 K with references taken as fcc-γ for Al, Co, and Cr, and Ni. γ′ end-members with the same reference states are also shown. Energies for mechanically unstable ordered structures are shown in italics.

System	Al	Co	Cr	Ni	SQS prototype	ΔH_{mix} (kJ/mol atom)	$\Delta_f H$ $L1_2$-γ′ (kJ/mol atom)	ΔH^{order} (kJ/mol atom)
Al–Co	0.75	0.25			16	−9.28	−20.80	−11.51
	0.5	0.5			16	−18.00		
	0.25	0.75			16	−13.54	−18.62	−5.09
Al–Cr	0.75		0.25		16	−2.52	−19.04	−16.52
	0.5		0.5		16	−6.86		
	0.25		0.75		16	−7.08	***−12.94***	***−5.86***
Al–Ni	0.75			0.25	16	−17.05	−21.15	−4.10
	0.5			0.5	16	−30.54		
	0.25			0.75	16	−27.86	−42.22	−14.37
Co–Cr		0.75	0.25		16	−0.90	−5.04	−4.15
		0.5	0.5		16	−5.46		
		0.25	0.75		16	−6.86	−10.48	−3.62
Co–Ni		0.75		0.25	16	−0.48	−0.94	−0.46
		0.5		0.5	16	−0.67		
		0.25		0.75	16	−0.77	0.90	1.67
Cr–Ni			0.75	0.25	16	−12.69	−13.88	−1.19
			0.5	0.5	16	−9.03		
			0.25	0.75	16	−5.79	−10.03	−4.24
Al–Co–Cr	0.5	0.25	0.25		32	−11.66		
	0.25	0.5	0.25		32	−11.39		
	0.25	0.25	0.5		32	−18.06		
	0.33	0.33	0.33		24	−15.33		
Al–Co–Ni	0.5	0.25		0.25	32	−21.66		
	0.25	0.5		0.25	32	−17.13		
	0.25	0.25		0.5	32	−21.68		
	0.33	0.33		0.33	24	−22.62		
Co–Cr–Ni		0.5	0.25	0.25	32	−3.20		
		0.25	0.5	0.25	32	−8.14		
		0.25	0.25	0.5	32	−5.04		
		0.33	0.33	0.33	24	−5.90		

Table 8
Calculated enthalpies of mixing for B2 from DFT. The results are based on ternary SQS calculations at 0 K with reference states taken as bcc-A2 for Al, Co, and Cr, and Ni. Energies for mechanically unstable binary ordered structures are shown in italics. Values for Al–Co, Al–Cr, Co–Cr, and Al–Co–Cr and adapted from previous work [5] and are indicated with an asterisk *.

	Section	Al	Co	Cr	Ni	SQS prototype	ΔH_{mix} (kJ/mol atom)
*Al–Co–Cr	**(Al)(Co,Cr)**	0.5		0.5			−7.96
		0.5	0.25	0.25		8	−32.77
		0.5	0.5				−67.75
	(Co)(Al,Cr)	0.5	0.5				−67.75
		0.25	0.5	0.25		8	−27.20
			0.5	0.5			11.99
	(Cr)(Al,Co)		0.5	0.5			11.99
		0.25	0.25	0.5		8	8.22
		0.5		0.5			−7.96
Al–Co–Ni	**(Al)(Co,Ni)**	0.5			0.5		−73.80
		0.5	0.25		0.25	8	−68.64
		0.5	0.5				−67.75
	(Co)(Al,Ni)	0.5	0.5				−67.75
		0.25	0.5		0.25	8	−26.94
			0.5		0.5		***5.66***
	(Ni)(Al,Co)		0.5		0.5		***5.66***
		0.25	0.25		0.5	8	−33.61
		0.5			0.5		−73.80
Co–Cr–Ni	**(Co)(Cr,Ni)**		0.5		0.5		5.66
			0.5	0.25	0.25	8	10.80
			0.5	0.5			11.99
	(Cr)(Co,Ni)		0.5	0.5			11.99
			0.25	0.5	0.25	8	17.62
				0.5	0.5		20.12
	(Ni)(Co,Cr)			0.5	0.5		20.12
			0.25	0.25	0.5	8	16.02
			0.5		0.5		5.66

Special quasirandom structures calculations (SQS) [61] are performed to predict enthalpies of mixing in the A2, B2, γ and γ′ phases. The calculations for γ utilizes binary 16-atom cells developed by Wolverton [62] and ternary 24/32-atom cells by Shin et al. [63]. The supercell generated by Jiang [64], is used for the B2 ternary calculations of the $A_{0.5}B_{0.5}C$ composition sections, see Fig. 1 (b). To enable the γ′ SQS calculations along certain composition sections, such as Ni_3Al to Co_3Al, a 24-atom ternary SQS supercell (Fig. 1(c)) is generated using the Alloy Theoretic Automated Toolkit (ATAT) [65] together with the Monte Carlo method developed recently by van de Walle et al. [66]. Other cell sizes are tested to ensure that the selected cell size is sufficient. Other SQS settings for these calculations and the relaxation requirements in obtaining a final structure remain the same as in previous work [5]. To obtain the scaling factors to be used in the Debye–Grüneisen model for finite-temperature thermodynamic properties or B2, γ′ and σ end-members, elastic constant calculations are performed. The effectiveness and accuracy of using a scaling factor for the Debye–Grüneisen model has been demonstrated previously [67].

First-principles DFT calculations are performed using the Vienna ab-initio Simulation Package (VASP) [68] with spin-polarization due to the ferromagnetic nature of Co and Ni as well as the antiferromagnetic nature of Cr. The Project augmented-wave (PAW) method is used to describe electron–ion interactions while the Perdew, Burke, and Ernzerhof (PBE) [69] implementation of the generalized gradient approximation (GGA) is used to describe electron exchange and correlation. To ensure that enough basis sets are included in the calculation, a plane-wave cutoff energy of 400 eV is consistently used for all calculations. Reciprocal *k*-meshes used for fcc-Al/Co/Cr/Ni, hcp-Co, and bcc-Al/Co/Cr/Ni are $21 \times 21 \times 21$, $23 \times 23 \times 12$ and $17 \times 17 \times 17$, respectively. For the intermetallic B2, γ′ and σ, the reciprocal k-meshes $15 \times 15 \times 15$, $21 \times 21 \times 21$, and $6 \times 6 \times 11$ are used, respectively.

Table 9
Calculated enthalpies of mixing for γ′ from DFT. The results are based on ternary SQS calculations at 0 K with reference states taken as fcc-γ for Al, Co, and Cr, and Ni. Energies for mechanically unstable binary ordered structures are shown in italics.

	Section	Al	Co	Cr	Ni	SQS prototype	ΔH_{mix} (kJ/mol atom)
Al–Co–Cr	**(Al)(Co,Cr)$_3$**	0.25	0.75				−18.62
		0.25	0.375	0.375		24	−12.37
		0.25		0.75			***−12.94***
	(Co)(Al,Cr)$_3$	0.75	0.25				−20.80
		0.375	0.25	0.375		24	−25.57
			0.25	0.75			−10.48
	(Cr)(Al,Co)$_3$	0.75		0.25			−19.04
		0.375	0.375	0.25		24	−14.04
			0.75	0.25			−5.04
Al–Co–Ni	**(Al)(Co,Ni)$_3$**	0.25	0.75				−18.62
		0.25	0.375		0.375	24	−29.84
		0.25			0.75		−42.22
	(Co)(Al,Ni)$_3$	0.75	0.25				−20.80
		0.375	0.25		0.375	24	−28.12
			0.25		0.75		0.90
	(Ni)(Al,Co)$_3$	0.75			0.25		−21.15
		0.375	0.375		0.25	24	−25.03
			0.75		0.25		−0.94
Co–Cr–Ni	**(Co)(Ni,Cr)$_3$**		0.25		0.75		0.90
			0.25	0.375	0.375	24	−5.64
			0.25	0.75			−10.48
	(Cr)(Ni,Co)$_3$			0.25	0.75		−10.03
			0.375	0.25	0.375	24	−3.87
			0.75	0.25			−5.04
	(Ni)(Co,Cr)$_3$		0.75		0.25		−0.94
			0.375	0.375	0.25	24	−5.61
				0.75	0.25		−13.88

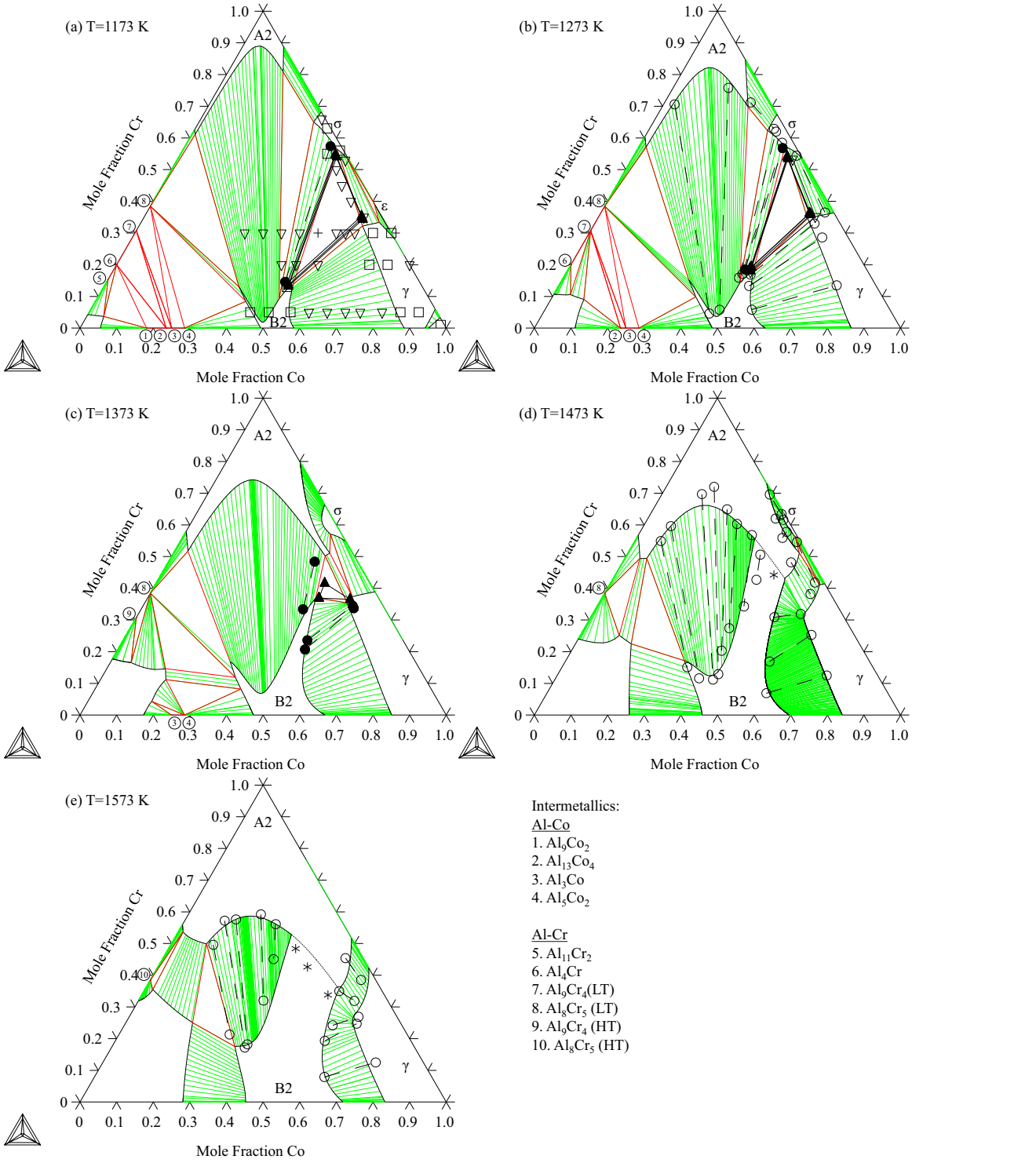

Fig. 2. Calculated Al–Co–Cr isothermal sections (solid lines) at 1173 (a), 1273 (b), 1373 (c), 1473 (d) and 1573 K (e). Experimental phase equilibrium data by Moskvitina et al. [92] is included for comparison: single phase (□), 2-phase (▽), and 3-phase (+).and by Ishikawa et al. [21]: 2-phase (○), order-disorder transition (∗).Phase equilibria data from the Ref. [5]: 2-phase (•), 3-phase (▲).The calculated order-disorder transition is also shown (• • •).

5. Results and discussion

5.1. First-principles results

The results of the first-principles calculations for the B2 and γ′ end-members are shown in Table 2. This includes elastic stiffness constants (C_{ij}), volume/atom (V_0), bulk modulus (B_0), Poisson's ratio (Voigt–Reuss–Hill effective medium), the Debye model scaling factor as well as the Debye temperatures for each end-member. These results are crucial properties necessary for accurate finite temperature predictions. End-members B2-CoNi and γ′-Cr_3Al are shown to be mechanically unstable due to the stability criteria $C_{11} > |C_{12}|$, $C_{44} > 0$, and $C_{11}+2C_{12} > 0$ for cubic structures [70]. B2-CoAl, NiAl and γ′-Ni3Al are the only stable end-members, and experimental results for these are included in Table 2. Present C_{ij} and B_0 results for B2-CoAl and NiAl agree well with

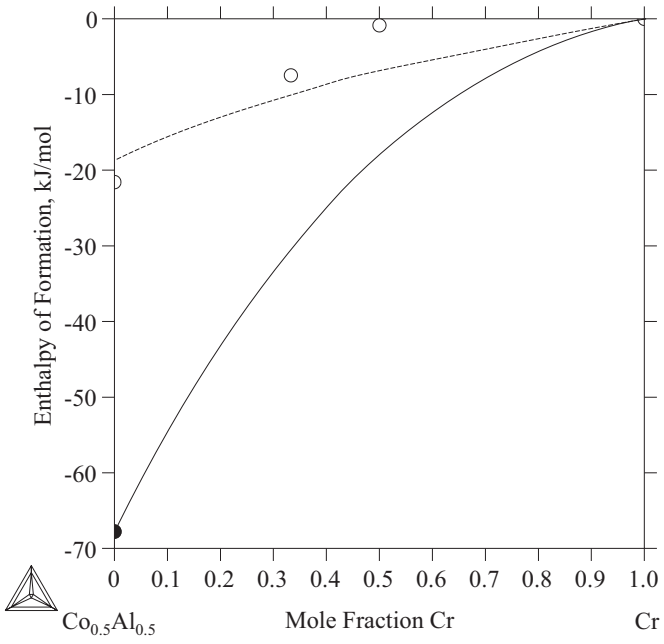

Fig. 3. Calculated CALPHAD A2 (---) and B2 (—) enthalpies of formation of the $Co_{0.5}Al_{0.5}$–Cr vertical section compared to first-principles results for the A2 (○) and B2 phases (●) at 298 K. Reference states are taken as A2 for Al, Co and Cr.

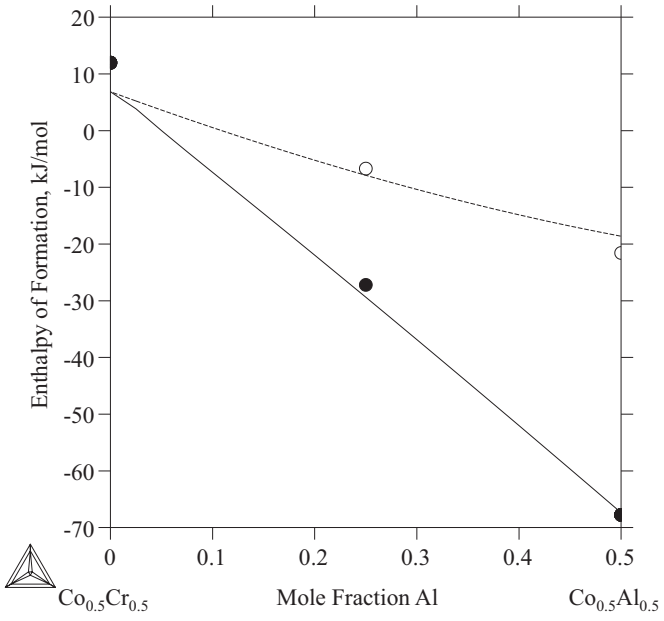

Fig. 4. Calculated CALPHAD A2 (---) and B2 (—) enthalpies of formation of the $Co_{0.5}Cr_{0.5}$–$Co_{0.5}Al_{0.5}$ vertical section compared to first-principles results for the A2 (○) and B2 phases (●) at 298 K. Reference states are taken as A2 for Al, Co and Cr.

experimental findings [71–75] at various temperatures as well as other first-principles calculations [76,77]. It should be noted that C_{ij} decreases as a function of temperature. The C_{ij} and B_0 results for γ′-Ni_3Al [78,79] also are shown to agree with experimental data and other calculations [77,80]. Elastic and equation of state calculations for other end-members are not available in the literature.

In Table 3, the elastic stiffness constants for the end-members of σ are listed. The end-member σ-$(Al)_8(Al)_{18}(Cr)_4$ can be concluded to be mechanically unstable as its $C_{44} < 0$ breaks the necessary elastic stability requirements for a tetragonal (I) crystal class [70].

Table 4 includes the enthalpies ($\Delta_f H^{298}$, kJ/mol atom), entropies

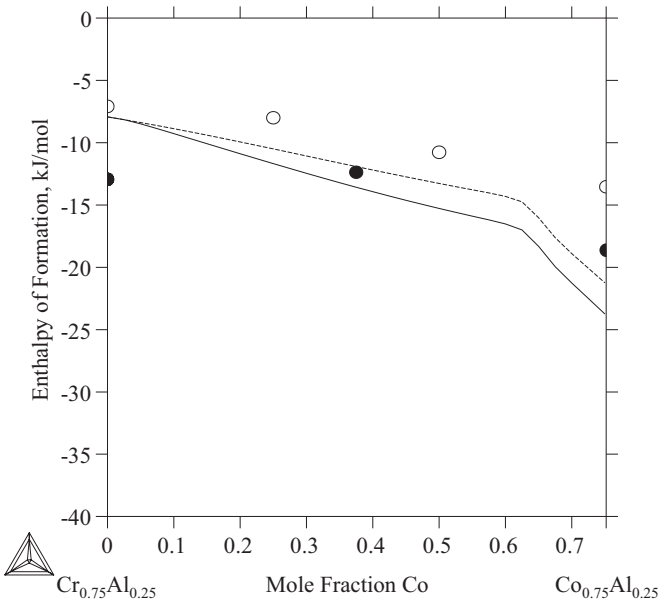

Fig. 5. Calculated CALPHAD γ (---) and γ′ (—) enthalpies of formation for the $(Cr_xCo_{1-x})_{0.75}Al_{0.25}$ vertical section compared at 298 K compared to first-principles SQS results for γ (○) and γ′ (●). Reference states are taken as γ for Al, Co and Cr.

($\Delta_f S^{298}$, J/mol atom/K) and Gibbs energies ($\Delta_f G^{298}$, kJ/mol atom) of formation at 298 K relative to standard reference states for the pure elements. The enthalpies of formation for B2-CoAl and NiAl from fcc-Al, hcp-Co, bcc-Cr and fcc-Ni are in good agreement with experiments at 298 K and other temperatures. The enthalpy of formation of B2-CoAl predicted in the present work at 1100 K is −59.911 kJ/mol atom, between the experimental value of −59.5 by Henig et al. [81] at 1100 K and the compilation value of -60.7 ± 0.5 by Rzyman and Moser [82] at 1073 K. The experimental enthalpy of formation of B2-NiAl varies from −58.3 to −67 kJ/mol atom according to Rzyman et al. [83] while the value at 298 K predicted in the present work is −64.211 kJ/mol atom. Present results also agree with previous DFT predictions by Arroyave et al. [84] at 298 K. In the case of Ni_3Al, the calculated enthalpy of formation ($\Delta_f H^{298}$) of −42.126 kJ/mol atom agrees with the measured values -40.6 ± 1.0 by Kek et al. [25] and -41.3 ± 1.3 by Rzyman et al. [85]. Additional experimental values compiled by Rzyman et al. [85] indicate enthalpies of formation between −47 and −37.6 kJ/mol atom at various temperatures for Ni_3Al. Other first-principles calculations by Ohtani et al. [86] and Arroyave et al. [84] produced values of −42.38 and −46.39 kJ/mol atom. Results for the entropy of formation (−3.252 J/mol atom/K) and Gibbs energy (−39.809 kJ/mol atom) agree with measured values by Róg et al. [87] at 900 K for Ni_3Al. Additionally, the Gibbs energy of formation at 900 K vary between −34.2 to −47.5 kJ/mol atom according to other experiments compiled by Róg et al. [87]. Al_3Co, Al_3Ni, Co_3Al end-member enthalpies of formation calculated by Ohtani et al. [86] at 0 K are also in agreement with the present results. The overall good agreement reported above validates the method of the present work for prediction of finite temperature thermodynamic properties by Shang et al. [56].

As is shown in Table 5, calculated formation enthalpy at 0 K by Pavlů et al. [88] for both σ-CoCr end-members are more positive than the predictions in the present work. This is due to the use of LMTO energies for σ end-members and discrepant DFT energies for the magnetic elements by Pavlů et al. [88]. Unfortunately, calorimetric experiments for σ-CoCr prove to be unreliable as enthalpies of formation range from −3 to +10 kJ/mol atom [14,88,89]. Downie and Arslan [14] studied the formation enthalpy of one σ–CoCr sample close to the composition of the end-

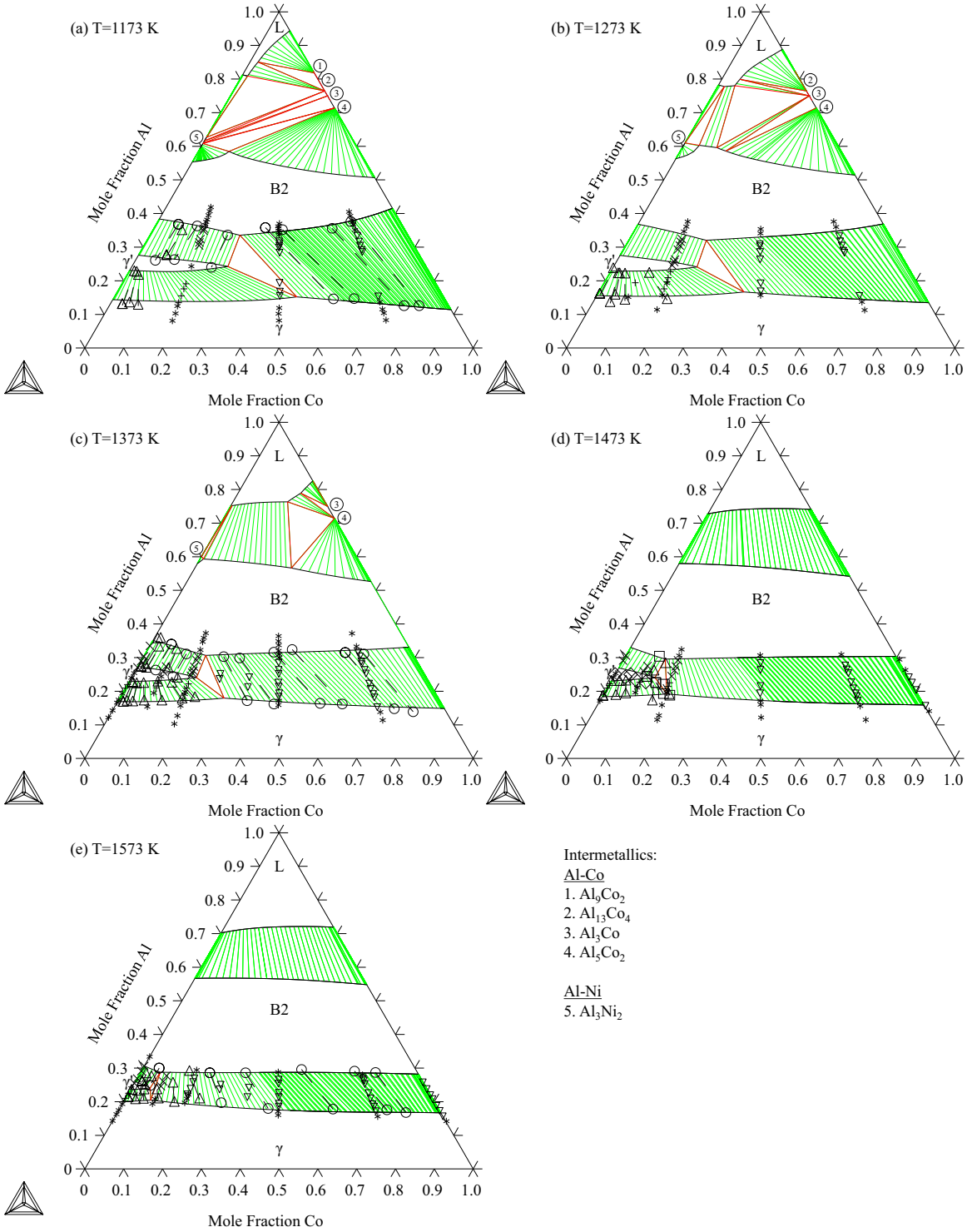

Fig. 6. Calculated Al–Co–Ni isothermal sections (solid lines) at 1173 (a), 1273 (b), 1373 (c), 1473 (d) and 1573 K (e). Experimental data from Jia et al. [24] (Δ), Kainuma et al. [27] (○), and Albers et al. [28] (1-phase ◇, 2-phase □) are included for comparison. Equilibrated alloys from Schramm [23] are also shown: 1-phase (✱), γ′+B2(×), γ+γ′(+), and γ+B2 (▽).

member σ-$(Co)_8(Cr)_{18}(Cr)_4$ at 473 K and measured enthalpies of formation of 6.77 kJ/mol atom. While no direct comparison can be made due to the different compositions, the predicted value of 6.19 kJ/mol atom for σ-$(Co)_8(Cr)_{18}(Cr)_4$ is in good agreement with the measured value for a similar composition. It can be seen that all binary σ end-members have rather positive enthalpies of formation at 298 K with $(Al)_8(Al)_{18}(Cr)_4$ being mechanically unstable. In the Co-Cr case, positive entropies of formation can be seen for both end-members indicating potential stabilization of σ at higher temperatures as it is not stable on the convex hull at 0 K [88].

SQS calculations from A2, γ, B2 and γ′ are shown in Tables 6, 7, 8, and 9, respectively. In the case of Cr-containing systems, the huge difference in Cr lattice stability between DFT and CALPHAD makes SQS calculations for γ difficult to interpret. Wolverton and Ozolins have noted similar problems for calculations involving Cr in fcc structures [90]. By and large, taking the fcc reference state

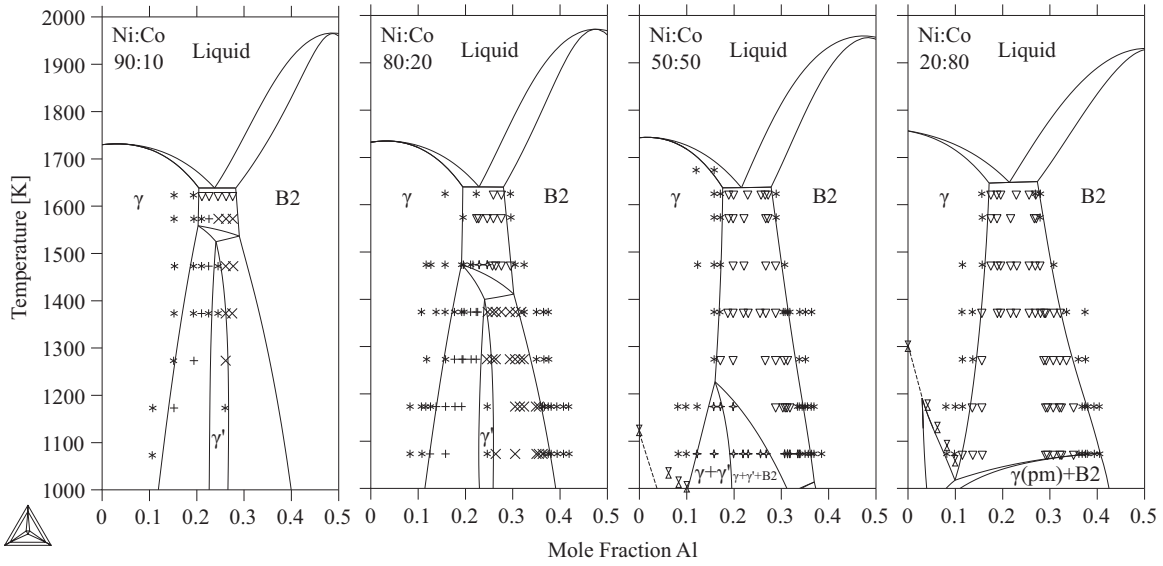

Fig. 7. Calculated Al–Co–Ni vertical sections at Ni:Co ratios of 90:10, 80:20, 50:50, and 20:80 compared to equilibrated alloys from Schramm [23]: 1-phase (*), γ′+B2(×), γ+γ′(+), γ+B2 (▽), 3-phase (☆), and Curie temperature (⧖). The γ ferromagnetic-paramagnetic transition is also shown with (• • •).

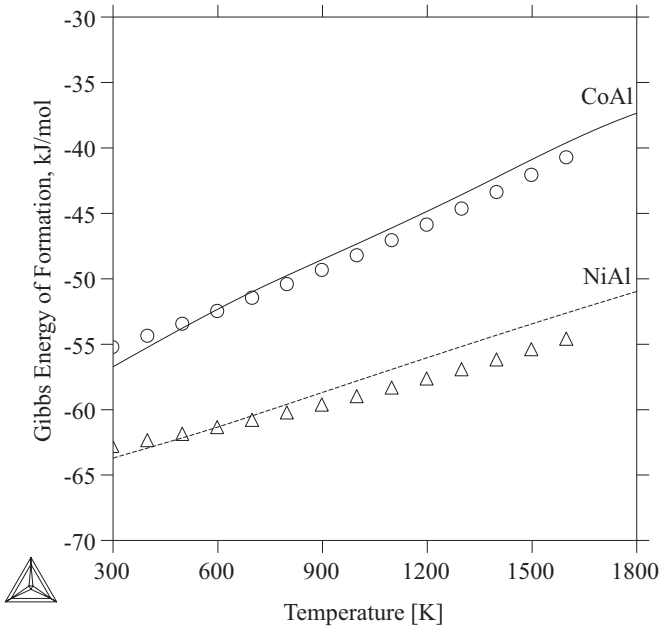

Fig. 8. CALPHAD Gibbs energies of formation for B2-CoAl (—) and B2-NiAl (– – –) from the CALPHAD modeling compared to their respective results from the Debye–Grüneisen model (○ and △).

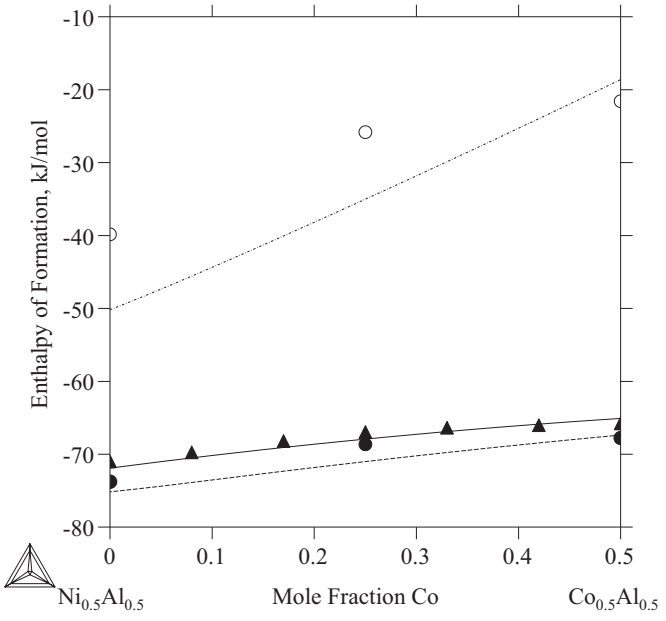

Fig. 9. Calculated CALPHAD B2 (—) enthalpies of formation for the $(Ni_xCo_{1-x})_{0.5}Al_{0.5}$ vertical section compared to measurements from Grun et al. (▲) [29] at 1073 K (error bars approximately size of symbols). Experimental reference states are liquid Al, solid γ-Co, and solid γ-Ni. CALPHAD Enthalpies of formation for A2 (- ● -) and B2 (– – –) with all A2 reference states at 298 K are shown in comparison to first-principles SQS results for A2 (○) and B2 (●).

for Cr will produce enthalpies of mixing that are too negative near the Cr-rich portion of the phase diagram as any addition to fcc-Cr produces great stability.

Ternary SQS calculations provide guidance towards modeling of the energetics in the systems shown here and are therefore weighted accordingly during optimization. It is often the case that binary SQS calculations differ in energies compared to adopted binary models. In this case, strictly fitting to the coupled ternary SQS calculations can produce ill results and poor descriptions. This is akin, then, to the adopting of SQS calculations when DFT and CALPHAD lattice stabilities are very different [55]. Therefore, the trends, rather than absolute energies, provide more meaning in this context.

It can be seen in Table 6 that Al-rich B2-CoAl and NiAl, have the largest ordering and enthalpies of formation relative to their respective A2 disordered states. This is unexpected given the high melting points and large composition ranges of B2 in both the Al–Co and Al–Ni systems. It can also be concluded that B2-CrAl has a much lower ordering energy compared to CoAl and NiAl. Furthermore, B2-CoNi and CrNi all have positive ordering energies relative to their disordered states with CoNi being mechanically unstable which can be attributed to the almost ideal mixing behavior in the A2 for Co–Ni; between −0.81 and 0.2 kJ/mol atom. B2-CoCr also presents an interesting case as its ordering energy is nearly 0. Much like with B2, in the γ/γ′ case, γ′-Al_3Co, Co_3Al, Al_3Ni, and Ni_3Al have the largest ordering tendencies, see Table 7. In the Al–Cr system, γ′-Al_3Cr has a large ordering energy while Cr_3Al is mechanically unstable based on its elastic stiffness constants. For Co–Cr and Cr–Ni, small ordering energies are seen for γ′-Co_3Cr, Cr_3Co, Cr_3Ni, and Ni_3Cr end-members. Interestingly, the present

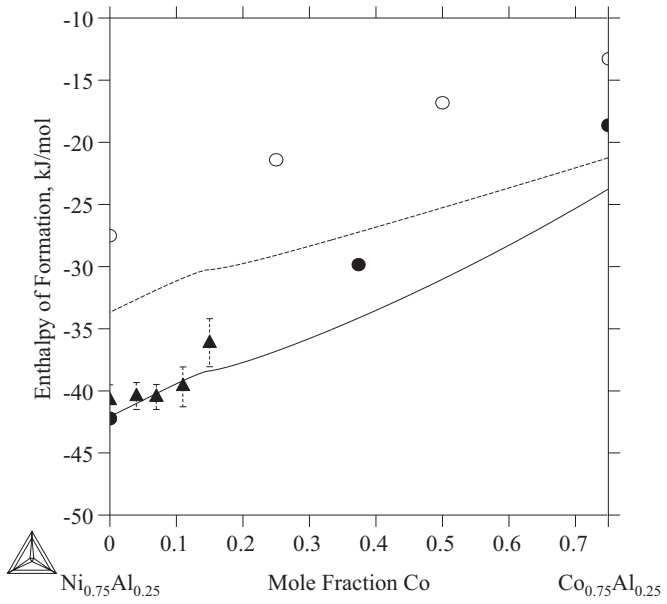

Fig. 10. Calculated CALPHAD γ′ (—) enthalpies of formation for the $(Ni_xCo_{1-x})_{0.75}Al_{0.25}$ vertical section compared to measurements from Kek et al. (▲) [25] at 298 K. Experimental reference states are solid γ for Al, Co, and Ni. The CALPHAD enthalpy of formation for the γ (– – –) with all γ reference states at 298 K are shown in comparison to first-principles SQS results for γ (○) and γ′ (●).

results for ordering in the Cr–Ni binary is in agreement with the bond energy assessed by Dupin et al. [6]. The calculations for γ Co–Ni demonstrate its similarity with A2 of which mixing behavior almost is ideal. Ordering energies in the Co–Ni binary are negligible from the present results.

5.1.1. CALPHAD modeling results

5.1.1.1. Al–Co–Cr. The previous modeling of the Al–Co–Cr system included the Co–Cr binary by Oikawa et al. [12]. While a satisfactory phase diagram was obtained, the enthalpy of formation of one σ end-member, σ-$(Co)_8(Cr)_{18}(Cr)_4$, was −6.27 kJ/mol atom. This corresponds to enthalpies of formation much lower than those measured by Downie et al. at 473 K [14], which range between +2 and +7 kJ/mol atom around the composition range where σ is present. Present DFT calculations indicate that the enthalpies of formation of the end-members σ-$(Co)_8(Co)_{18}(Cr)_4$ and σ-$(Co)_8(Cr)_{18}(Cr)_4$ are 9.62 and 6.29 kJ/mol atom at 298 K, respectively. The modeling by Kusoffsky et al. [51] resulted in end-member enthalpies of 9.83 and 0.003 kJ/mol-atom at 298 K for σ-$(Co)_8(Co)_{18}(Cr)_4$ and σ-$(Co)_8(Cr)_{18}(Cr)_4$, which are both positive and in agreement with findings by Downie et al. [14]. Using the model by Oikawa et al. [12], the same end-member enthalpies are 8.70 and −6.27 kJ/mol atom. While this produces correct phase boundaries, its disagreement with the current DFT calculations and measurements by Downie et al. [14] could extrapolate poorly in higher order systems. This justifies the selection of the Co–Cr description by Kusoffsky et al. [51] in the present work.

The A2/B2 partitioned model is still retained in the present work for B2 but with fewer, decoupled A2/B2 interaction parameters, such as in the modeling of Al–Fe–Ni by Zhang et al. [91]. As seen in Fig. 2(a) and (b), the 1173 and 1273 K isotherms remain nearly identical to previous work. The important A2+B2, B2+γ, and B2+γ+σ regions are described well with the new models when compared to measurements from Liu et al. [5], Mosktivina et al. [92] and Ishikawa et al. [21].

At 1373 K (Fig. 2(c)) the new assessment reproduces B2+γ, and A2+B2+γ regions better than previous calculations. It should be noted that Gómez-Acebo et al. also performed diffusion couple studies of Al–Co–Cr alloys at 1373 K [93] but used relatively short heat treatment times and their results are thus not included in the current assessment. Results at 1473 K for the A2+γ and B2+γ regions are also improved (Fig. 2(d)). These improvements will prove crucial in the quaternary system as most MCrAlY alloys are of the B2+γ variety. Previous modeling efforts also attempted to capture the complex A2+B2 phase boundary curvature seen especially at 1473 K (Fig. 2(d)), and it has been determined that additional asymmetrical B2 interaction parameters were needed to reproduce the curvature. This is omitted in the present model as more experiments are needed to confirm these phase boundaries, and over-fitting may produce unreliable results in the quaternary extrapolation. Even without the asymmetrical parameters, the A2+B2 regions are reproduced well at 1373, 1473, and 1573 K, respectively (Fig. 2(c), (d), and (e)). Fig. 3 shows the $Co_{0.5}Al_{0.5}$–Cr vertical section at 298 K with predicted SQS solution enthalpies of mixing for A2 and the enthalpy of formation for B2-CoAl. Fig. 4 depicts a similar calculated $Co_{0.5}Cr_{0.5}$–$Co_{0.5}Al_{0.5}$ vertical section in comparison to SQS results (Tables 6 and 8). It can be seen that in both cases the present, calculated CALPHAD results coordinate well with first-principles predicted results. In Fig. 5 the calculated γ and γ′ enthalpies of formation for the $(Cr_xCo_{1-x})_{0.75}Al_{0.25}$ vertical section at 298 K are compared to their respective SQS calculations (Tables 7 and 9). The Cr_3Al end-member (Fig. 5) is not mechanical stable, as shown by present elastic constant calculations, indicating that its true enthalpy of formation is not well-defined. Given the instability, the ordered state has the same energy as a disordered γ at this composition since any ordering energy contribution is not to be expected. The bond energy term U_{CoCr} is not assessed in the present ternary modeling as it is metastable in all ternaries. It will be modeled using quaternary data alongside with the present DFT calculations.

5.1.1.2. Al–Co–Ni. The binary subsystems adopted in the present work produces a ternary extrapolation of the Al–Co–Ni system that agrees quite well with B2+γ, B2+γ′, and γ+γ′ phase boundaries as well as enthalpies [23–25,27–29]. Bond energies U_{AlCo} and U_{CoNi} are modeled using experimental information as well as first-principles calculation results, including SQS enthalpies of mixing. Al–Co–Ni isotherms at 1173 up to 1573 K are shown in Fig. 6(a) through (e). The important phase regions of B2, γ and γ′ appear at all temperatures. Good agreement with measurements from Jia et al. [24], Kainuma et al. [27] and Schramm [23] (Fig. 6 (a)–(e)) is seen at all temperatures. Data on single-phase γ′ and two-phase γ′+B2 and γ+γ′ alloys equilibriated at 1473 K by Albers et al. [28] also match the present results (Fig. 6(d)). No composition measurements in the γ+γ′+B2 phase region have been performed at any temperatures for comparison. However, given the good agreement for the single and two-phase regions around the ternary region, it is expected to be accurate. Fig. 7 shows calculated Co_xNi_y–Al vertical sections at Ni:Co ratios of 90:10, 80:20, 50:50, and 20:80 in comparison to experimental data by Schramm [23]. Good agreement is seen at all Ni:Co ratios for single-, two- and three-phase regions.

Fig. 8 shows the Gibbs energies of formation for B2-CoAl, initially modeled by Dupin and Ansara [9] but modified in the present work, and for B2-NiAl modeled by Dupin et al. [6]. First-principles predictions using the Debye–Grüneisen model are also included and good agreement is seen for both B2 end-members. Fig. 9 shows the calculated A2 and B2 enthalpies of formation compared to enthalpy measurements by Grun et al. [29] at 1073 K as well as first-principles SQS results (Tables 6 and 8). Satisfactory agreement is obtained although the metastable A2 enthalpy of mixing at $Ni_{0.5}Al_{0.5}$ deviate slightly from the present SQS results. This can be attributed to the sublattice model conversion of the Al–Ni system by Dupin et al. [6] which was performed without the

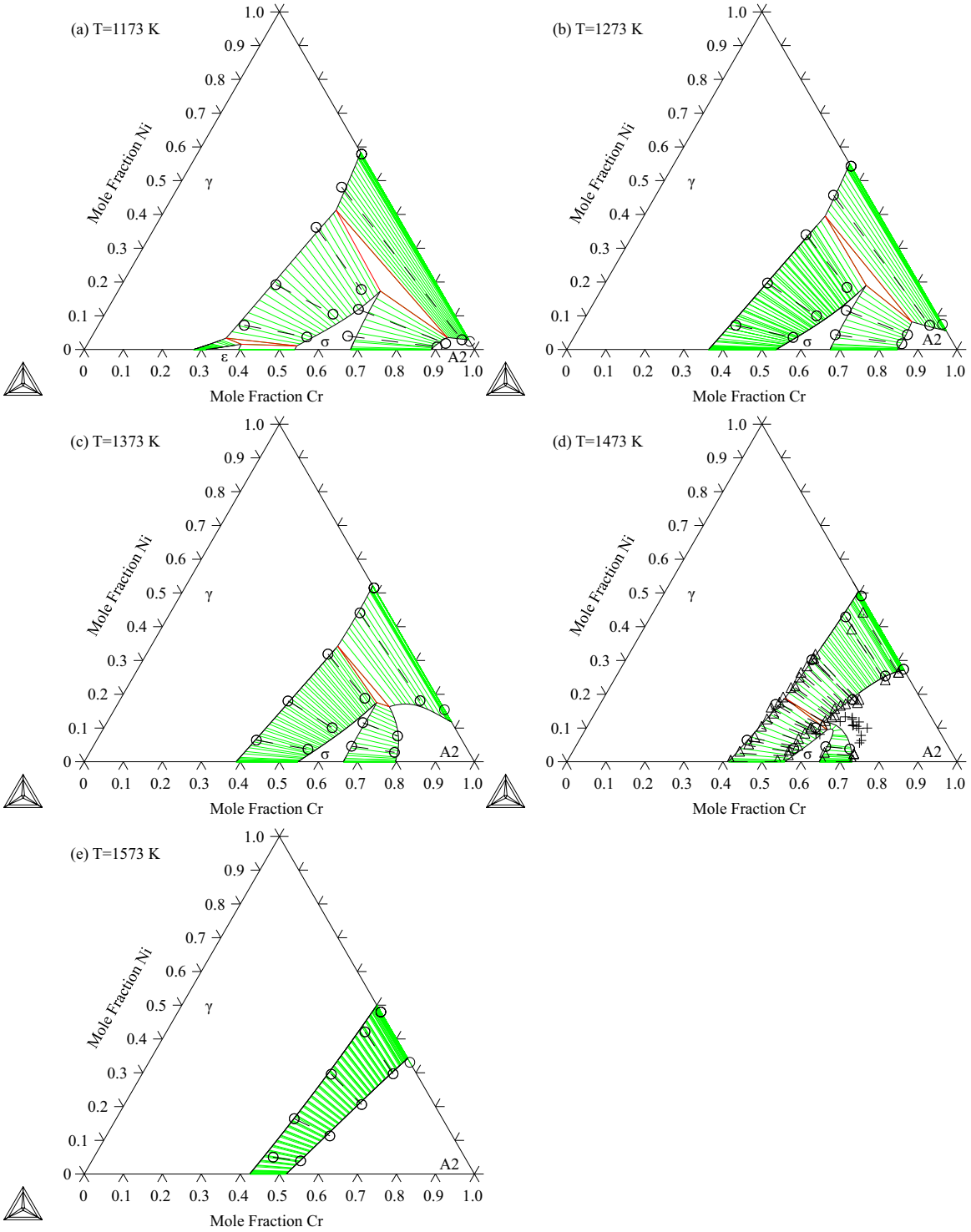

Fig. 11. Calculated Co–Cr–Ni isothermal sections (solid lines) at 1173 (a), 1273 (b), 1373 (c), 1473 (d) and 1573 K (e). Experimental results of investigations of the 2-phase equilibria by Omori et al. [40] (○) and Zhanpeng J. [41](▵) are included as comparison. A2/σ phase boundaries measured by Zhanpeng [41] are also shown (+).

availability of these new SQS calculations. Due to the metastable nature of the A2, such a deviation does not prompt the re-assessment of Al–Ni binary.

Fig. 10 shows γ and γ′ enthalpies of formation compared with measurements by Kek et al. [25] at 298 K and present SQS results (Tables 7 and 9). Similar to A2 in Al–Ni, good agreement is seen for γ′ at $Ni_{0.75}Al_{0.25}$ but not for the metastable γ at this composition. Lack of information on the mixing behavior of γ in the Al–Co description by Dupin and Ansara [9] also creates an uncertainty in energy compared to present SQS results for $Co_{0.75}Al_{0.25}$. Calculations in the present work give a Co_3Al ordering energy of −5.09 kJ/mol atom, which is different than that produced by Dupin [22] due to differences in bond energy parameters U_{AlCo} and U_{CoNi}. Dupin assessed values of $U_{AlCo} = -9870+3.068\times T$ and $U_{CoNi} = 4000$. Using these bond energies, the enthalpy of formation for Co_3Al at 298 K is −28.64 kJ/mol relative to the disordered solution, which is −21.24 kJ/mol (order energy of −7.4 kJ/mol). Present DFT calculations yield values of −18.62 kJ/mol for the

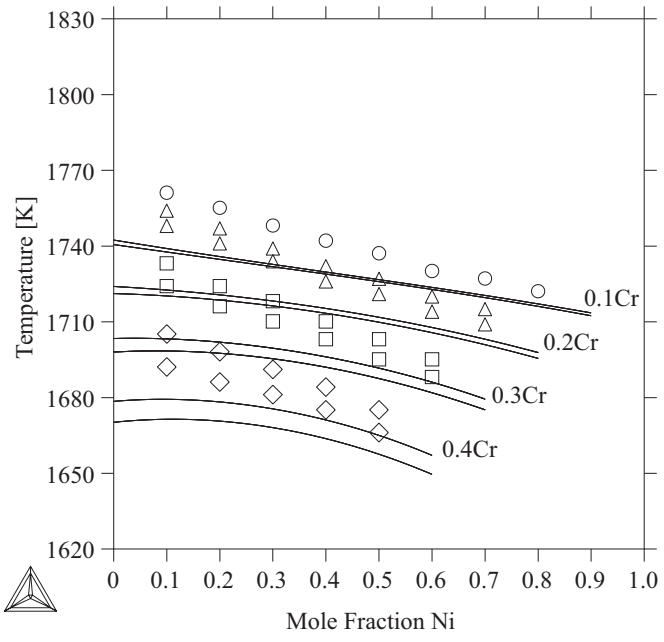

Fig. 12. Calculated CALPHAD liquidus and solidus temperatures (—) in the Co–Cr–Ni ternary compared to measurements from Omori et al. [40] at various Cr concentration levels: 0.1Cr (○), 0.2Cr (△), 0.3Cr (□), 0.4 (◇).

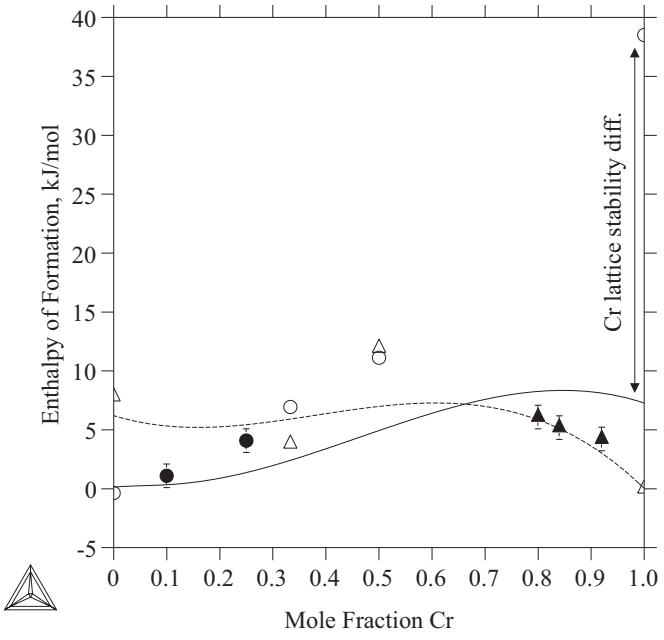

Fig. 13. Calculated CALPHAD γ (—) and A2 (– – –) enthalpies of formation of the $Co_{0.5}Ni_{0.5}$–Cr vertical section compared to measured γ (●) and A2 (▲) enthalpies from Kubachewski and Hack [42] at 1523 K. Experimental reference states are solid γ-Co, A2-Cr and γ-Ni. First-principles SQS results for the γ (○) and A2 phases (Δ) at 298 K with the same reference states as the experimental measurements are also included.

ordered Co_3Al relative to the SQS disordered solution (energy of −13.54 kJ/mol), as seen in Table 4. It can be seen that the calculated DFT values are smaller in magnitude compared to the CALPHAD energies. Our results also agree with first-principles results in Ref. [86], where the enthalpy of formation of Co_3Al was found to be −19.9 kJ/mol.

Therefore, the updated value for U_{AlCo} = −4872 is smaller in magnitude and omits the temperature dependence by the addition of a $U4_{AlCo}$=3023 term, similar to that in the Al–Ni system [6,11]. Using this new value, the enthalpy of formation of Co_3Al at 298 K is calculated to be −23.77 kJ/mol. Additionally, U_{CoNi} is set to 0 due to small differences in energies between the ordered and disordered states of Co_3Ni and Ni_3Co calculated in the present work, as is shown in Tables 4 and 7.

5.1.1.3. Co–Cr–Ni. The ternary extrapolation produced with the Co–Cr binary by Kusoffsky et al. [13] is better than that produced with that by Oikawa et al. [12]. If the description by Oikawa et al. [12] is used, ^{0}L, ^{1}L and ^{2}L interaction parameters are required for the A2 and γ phases in order to reproduce the enthalpies of formation measured by Kubaschewski and Hack [42] as well as first-principles predictions. Additional excess entropy terms and ternary σ end-members are then required to reproduce phase boundary data from Zhmurko et al. [39], Omori et al. [40], and Zhanpeng [41]. On the other hand, with the binary description by Kusoffsky et al. [13], enthalpies of formation [42] and phase boundaries [39–41] are well produced at 1073–1373 K without the introduction of any ternary interaction parameters. Symmetrical ternary interaction parameters are simply used to improve the phase boundary agreement at 1473–1573 K.

As seen in Fig. 11 (a) and (b), the present description agrees well with EPMA measurements by Omori et al. [40] at 1173 and 1273 K. Tie-line compositions and directions match measured values well for the A2+ σ, γ+σ, and A2+γ regions. Fig. 11(c) and (d) shows the rapid decomposition of σ in accordance with data by Omori et al. [40] and Zhanpeng [41] at 1373 to 1473 K. The agreement is good between the calculated phase boundaries and EPMA measurements from both experiments, especially at 1473 K where the calculated A2+σ boundary is similar to the loop measured by Zhanpeng [41]. Attempts at fitting this phase boundary resulted in σ becoming too stable at 1573 K which disagrees with results from the more self-consistent data set by Omori et al. [40]. At 1573 K (Fig. 11(e)), only the A2+γ region remains as σ has decomposed at this temperature. Calculated tie-lines in this region are in good agreement with measurements by Omori et al. [40]. Fig. 12 shows the calculated liquidus and solidus temperatures at 10–40% Cr compared with DSC measurements by Omori et al. [40]. Disagreement arises primarily from the Co–Cr binary where melting temperatures suggested by Omori et al. [40] are consistently about 20 K higher than the model by Kusoffsky et al. [13]. It should be noted that liquidus and solidus measurements by Omori et al. [40] disagree slightly with the binary model by Kusoffsky et al. [13]. Given the small amount of melting data in the Co-rich region of the Co–Cr phase diagram, more experiments need to be performed in order to adjust the parameters in the Co–Cr model by Kusoffsky et al. [13].

In Fig. 13, the calculated enthalpies of formation for the A2 and γ at 1523 K are compared to measured enthalpies by Kubachewski and Hack [42] and to SQS calculations for the solution phases (Tables 6 and 7). Reference states are taken to be γ-Co, A2-Cr and γ-Ni in order to enable direct comparison with calorimetric values. Enthalpies of formation values for A2 agree with experiments as well as the "s" shape predicted by first-principles which reaches a maximum at 50% Cr. Agreement for γ compared to the measured values are also good. However, first-principles results show some deviation. This can be attributed to the large difference in lattice stability for γ-Cr between CALPHAD and DFT, which is 31 kJ/mol atom. Overall, this work has produced a thermodynamic description of the Co–Cr–Ni system that agrees well with measured and first-principles predicted energies in addition to experimental phase equilibria.

6. Conclusions

The Al–Co–Cr, Al–Co–Ni, and Co–Cr–Ni ternary systems are reviewed and investigated thoroughly in the present work. Due to

the lack of thermochemical data and the metastability of phases in the ternary systems, first-principles calculations are performed. SQS calculations and Debye–Grüneisen predictions are used to predict energies for the important A2, B2, γ, and γ′ phases. These results are used to produce CALPHAD models that agree well with experimental results in the literature including a number of isotherms at temperatures ranging from 1173 to 1573 K. The ternary systems modeled in this work are to be combined into a Al–Co–Cr–Ni quaternary description for use in predicting the thermodynamics of MCrAl coatings.

Acknowledgments

This work was supported by the U.S. Department of Energy through Grant DE-FE0024056. Computing resources on Cyberstar are provided by the Materials Simulation Center and the Research Computing and Cyberinfrastructure Group at the Pennsylvania State University. Additionally, this work used the Extreme Science and Engineering Discovery Environment (XSEDE), which is supported by National Science Foundation Grant number ACI-1053575 [94]. The authors would like to thank Dr. Brian Gleeson and Austin Ross for stimulating discussions. The authors would also like to thank Elizabeth K. Rebhun for translating the German articles found in *Zeitschrift für Metallkunde* as well as editing the manuscript.

Appendix A. Supplementary material

Supplementary data associated with this article can be found in the online version at http://dx.doi.org/10.1016/j.calphad.2015.12.007.

Appendix A

See Table A1

Table A1
Parameters for the binary systems not shown except for where modifications are made.

Phase	Model	Parameter	System	References
Liquid	$(Al,Co,Cr,Ni)_1$	${}^0L^{Liq}_{Al,Co,Cr}= +30000$	Al–Co–Cr	Liu et al. [5]
		${}^0L^{Liq}_{Al,Co,Ni}= +20000$	Al–Co–Ni	This work
		${}^0L^{Liq}_{Co,Cr,Ni}= -16000$	Co–Cr–Ni	This work
fcc-A1	$(Al,Co,Cr,Ni)_1$	${}^0L^{fcc-A1}_{Al,Co,Cr}= +990+8.278\times T$	Al–Co–Cr	This work
		${}^0L^{fcc-A1}_{Al,Co,Ni}=0$	Al–Co–Ni	This work
		${}^0L^{fcc-A1}_{Co,Cr,Ni}= -40710+13.533\times T$	Co–Cr–Ni	This work
$\gamma'/L1_2$	$(Al,Co,Cr,Ni)_{0.75}(Al,Co,Cr,Ni)_{0.25}$Ordered part of fcc-A1	$G^{\gamma'}_{Al:Co}=G^{\gamma'}_{Co:Al}=AL3CO=ALCO3=3U1ALCO$	Al–Co	This work
		$U1ALCO= -4872$	Al–Co	This work
		${}^0L^{\gamma'}_{Al,Co:*}=3U3ALCO$, ${}^0L^{\gamma'}_{*:Al,Co}=U3ALCO$	Al–Co	This work
		$U3ALCO=0$	Al–Co	This work
		${}^1L^{\gamma'}_{Al,Co:*}=3U4ALCO$, ${}^1L^{\gamma'}_{*:Al,Co}=U4ALCO$	Al–Co	This work
		$U4ALCO= +3023$	Al–Co	This work
		$G^{\gamma'}_{Co:Ni}=G^{\gamma'}_{Ni:Co}=CO3NI=CONI3=3U1CONI$	Co–Ni	This work
		$U1CONI=0$	Co–Ni	This work
		Other interactions shown in Eq. 1.5-1.28		
bcc-A2	$(Al,Co,Cr,Ni,Va)_1$	${}^0L^{bcc-A2}_{Al,Co,Cr}= -28128$	Al–Co–Cr	This work
		${}^1L^{bcc-A2}_{Al,Co,Cr}= +123468-61.879\times T$	Al–Co–Cr	This work
		${}^2L^{bcc-A2}_{Al,Co,Cr}= -12107-32.267\times T$	Al–Co–Cr	This work
		${}^0L^{bcc-A2}_{Al,Co,Ni}= -15483$	Al–Co–Ni	This work
		${}^0L^{bcc-A2}_{Co,Cr,Ni}= -60134+17.700\times T$	Co–Cr–Ni	This work
B2	$(Al,Co,Cr,Ni,Va)_{0.5}(Al,Co,Cr,Ni,Va)_{0.5}$Ordered part of bcc-A2	$G^{B2}_{Al:Co}=G^{B2}_{Co:Al}=0.5GB2ALCO-0.5LB2ALCO$	Al–Co	Liu et al. [5]
		$GB2ALCO= -138500+34.620\times T$	Al–Co	Dupin and Ansara [9]
		$LB2ALCO= +56531-37.040\times T$	Al–Co	Liu et al. [5]
		$G^{B2}_{Co:Cr}=G^{B2}_{Cr:Co}= -3.074\times T$	Co–Cr	This work
		$G^{B2}_{Co:Ni}=G^{B2}_{Ni:Co}= +3864-1.664\times T$	Co–Ni	This work
		${}^0L^{B2}_{Al:Co,Cr}={}^0L^{B2}_{Co,Cr:Al}= -11069$	Al–Co–Cr	This work
		${}^0L^{B2}_{Cr:Al,Co}={}^0L^{B2}_{Al,Co:Cr}= -30895$	Al–Co–Cr	This work
		${}^0L^{B2}_{Ni:Al,Co}={}^0L^{B2}_{Al,Co:Ni}= -21769$	Al–Co–Ni	This work
σ	$(Al,Co,Ni)_8(Al,Co,Cr,Ni)_{18}(Cr)_4$	$G^{\sigma}_{Al:Ni:Cr}-8G^{fcc}_{Al}-18G^{bcc}_{Ni}-4G^{bcc}_{Cr}= -1045169$	Al–Cr–Ni	This work
		$G^{\sigma}_{Ni:Al:Cr}-8G^{fcc}_{Ni}-18G^{bcc}_{Al}-4G^{bcc}_{Cr}= -1169367$	Al–Cr–Ni	This work
		$G^{\sigma}_{Ni:Co:Cr}-8G^{fcc}_{Ni}-18G^{bcc}_{Co}-4G^{bcc}_{Cr}=0$	Co–Cr–Ni	This work
		$G^{\sigma}_{Co:Ni:Cr}-8G^{fcc}_{Co}-18G^{bcc}_{Ni}-4G^{bcc}_{Cr}=0$	Co–Cr–Ni	This work
		Al–Co–Cr σ parameters remain same as Liu et al. [5]		

References

[1] G.W. Goward, Progress in coatings for gas turbine airfoils, Surf. Coat. Technol. 108–109 (1998) 73–79.
[2] D.R. Clarke, C.G. Levi, Materials design for the next generation thermal barrier coatings, Annu. Rev. Mater. Res. 33 (2003) 383–417, http://dx.doi.org/10.1146/annurev.matsci.33.011403.113718.
[3] R. Darolia, Thermal barrier coatings technology: critical review, progress update, remaining challenges and prospects, Int. Mater. Rev. 58 (2013) 315–348.
[4] A.G. Evans, D.R. Mumm, J.W. Hutchinson, G.H. Meier, F.S. Pettit, Mechanisms controlling the durability of thermal barrier coatings, Prog. Mater. Sci. 46 (2001) 505–553.
[5] X.L. Liu, T. Gheno, B.B. Lindahl, G. Lindwall, B. Gleeson, Z.-K. Liu, First-principles calculations experimental study, and thermodynamic modeling of the Al–Co–Cr system, PLoS One 10 (2015) e0121386.
[6] N. Dupin, I. Ansara, B. Sundman, Thermodynamic re-assessment of the ternary system Al–Cr–Ni, Calphad 25 (2001) 279–298.
[7] U.R. Kattner, Construction of a thermodynamic database for Ni-base superalloys: a case study, in: P.E.A. Turchi, A. Gonis, R.D. Shull (Eds.), TMS CALPHAD Alloy Thermodyn., 2002, pp. 147–164.
[8] T. Gheno, X.L. Liu, G. Lindwall, Z.-K. Liu, B. Gleeson, Experimental study and thermodynamic modeling of the Al–Co–Cr–Ni system, Sci. Technol. Adv. Mater. 16 (2015) 055001, http://dx.doi.org/10.1088/1468-6996/16/5/055001.
[9] N. Dupin, I. Ansara, Thermodynamic assessment of the system Al–Co, Rev. Métall. 95 (1998) 1121–1129.
[10] I. Ansara, A.T. Dinsdale, M.H. Rand, COST 507: Definition of Thermochemical and Thermophysical Properties to Provide a Database for the Development of New Light Alloys-Thermochemical Database for Light Metal Alloys, Office for Official Publications of the European Communities, Luxembourg, 1998.
[11] I. Ansara, N. Dupin, H.L. Lukas, B. Sundman, Thermodynamic assessment of the Al–Ni system, J. Alloy. Compd. 247 (1997) 20–30, http://dx.doi.org/10.1016/S0925-8388(96)02652-7.
[12] K. Oikawa, G.-W. Qin, T. Ikeshoji, R. Kainuma, K. Ishida, Direct evidence of magnetically induced phase separation in the fcc phase and thermodynamic calculations of phase equilibria of the Co–Cr system, Acta Mater. 50 (2002) 2223–2232.
[13] A. Kusoffsky, B. Jansson, A thermodynamic evaluation of the Co–Cr and the C–Co–Cr systems, Calphad 21 (1997) 321–333.
[14] D.B. Downie, F. Arslan, Enthalpies of formation of (cobalt + chromium) alloys at 473 K, J. Chem. Thermodyn. 15 (1983) 645–649.
[15] I. Ansara, B. Sundman, The Scientific Group Thermodata Europe, in: P. S. Glaeser (Ed.), Comput. Handl. Dissem. Data, 1987, pp. 154–158.
[16] A.F. Guillermet, Assessment of the tzxhermodynamic properties of the Ni–Co system, Z. Met. 78 (1987) 639.
[17] B.-J. Lee, On the stability of Cr carbides, Calphad 16 (1992) 121–149, http://dx.doi.org/10.1016/0364-5916(92)90002-F.
[18] P. Gustafson, A thermodynamic evaluation of the Cr–Ni–W system, Calphad 12 (1988) 277–292, http://dx.doi.org/10.1016/0364-5916(88)90008-9.
[19] F. Stein, C. He, N. Dupin, Melting behaviour and homogeneity range of B2 CoAl and updated thermodynamic description of the Al–Co system, Intermetallics 39 (2013) 58–68.
[20] H.L. Chen, E. Doernberg, P. Svoboda, R. Schmid-Fetzer, Thermodynamics of the Al_3Ni phase and revision of the Al–Ni system, Thermochim. Acta 512 (2011) 189–195, http://dx.doi.org/10.1016/j.tca.2010.10.005.
[21] K. Ishikawa, M. Ise, I. Ohnuma, R. Kainuma, K. Ishida, Phase equilibria and stability of the BCC aluminide in the Co–Cr–Al system, Ber. Bunsenges. Phys. Chem. 102 (1998) 1206–1210.
[22] N. Dupin, Contribution A L'Evaluation Thermodynamique Des Alliages Polyconstitues A Base De Nickel (Ph.D. thesis), Grenoble Institute of Technology, France, 1992.
[23] J. Schramm, Das dreistoffsystem nickel-kobalt-aluminium, Z. Met. 33 (1941) 403–412.
[24] C.C. Jia, K. Ishida, T. Nishizawa, Partition of alloying elements between gamma (A), gamma prime (L12), and beta (B2) phases in Ni-Al base systems, Metall. Mater. Trans. A 25A (1994) 473–485.
[25] S. Kek, C. Rzyman, F. Sommer, Determination of the enthalpy of formation of ternary Ni_3Al-Based Alloys, An. Fiss. Ser. B 86 (1990) 31–38.
[26] J. Zhu, M.S. Titus, T.M. Pollock, Experimental investigation and thermodynamic modeling of the co-rich region in the Co–Al–Ni–W quaternary system, J. Ph. Equilib. Diffus. 35 (2014) 595–611, http://dx.doi.org/10.1007/s11669-014-0327-5.
[27] R. Kainuma, M. Ise, C.-C. Jia, H. Ohtani, K. Ishida, Phase equilibria and microstructural control in the Ni–Co–Al system, Intermetallics 4 (1996) S151–S158, http://dx.doi.org/10.1016/0966-9795(96)00034-9.
[28] M. Albers, D. Kath, K. Hilpert, Thermodynamic activities and phase boundaries for the alloys of the solid solution of Co in Ni_3Al, Metall. Mater. Trans. A 28 (1997) 2183–2188.
[29] A. Grün, E.-T.E.-T. Henig, F. Sommer, A. Grun, Calorimetric determination of the enthalpy of formation and the description of the constitutional defects of the ordered (Ni, Co)1-yAly phase, Z. Met. 89 (1998) 591–597.
[30] T. Gödecke, M. Scheffer, R. Luck, S. Ritsch, C. Beeli, Isothermal sections of phase equilibria in the Al–AlCo–AlNi system, Z. Met. 89 (1998) 687–698.
[31] T. Gödecke, M. Ellner, Phase equilibria in the Al-rich portion of the ternary system Co–Ni–Al at 75 and 78 at% Al, Z. Met. 88 (1997) 382–389.
[32] T. Gödecke, Liquidus projection surface and phase equilibria with liquid of the Al–AlCo–AlNi ternary subsystem, Z. Met. 88 (1997) 557–569.
[33] T. Gödecke, M. Scheffer, R. Luck, S. Ritsch, C. Beeli, Formation and phase boundaries of $(Co,Ni)_3Al_4$ and the ternary X phase in the Al–AlCo–AlNi system, Z. Met. 88 (1997) 687–697.
[34] T. Velikanova, K. Korniyenko, V. Sidorko, Al–Co–Ni Phase Ternary Diagram Evaluation, Springer Materials, Stuttgart, Germany, 2004 http://materials.springer.com/msi/docs/sm_;msi_r_10_011478_02.
[35] N.C. Oforka, B.B. Argent, Thermodynamics of Ni–Cr–Al Alloys, J. Less-Common Met. 114 (1985) 97–109.
[36] R.W. Cutler, The 1200 C Isothermal Sections of the Ni–Al–Cr and the Ni–Al–Mo Ternary Phase Diagrams, The Ohio State University, Columbus, OH, 2011.
[37] W. Huang, Y.A. Chang, Thermodynamic properties of the Ni–Al–Cr system, Intermetallics 7 (1999) 863–874, http://dx.doi.org/10.1016/S0966-9795(98)00138-1.
[38] S. Yang, M. Jiang, H. Li, Y. Liu, L. Wang, Assessment of Co–Cr–Ni ternary system by CALPHAD technique, Rare Met. 31 (2012) 75–80.
[39] G.P. Zhmurko, E.G. Kabanova, V.N. Kuznetsov, A.V. Leonov, Phase equilibria in the Co–Cr–Ni system, Mosc. Univ. Chem. Bull. 63 (2008) 234–235, http://dx.doi.org/10.3103/S0027131408040135.
[40] T. Omori, J. Sato, K. Shinagawa, I. Ohnuma, K. Oikawa, R. Kainuma, et al., Experimental determination of phase equilibria in the Co–Cr–Ni system, J. Ph. Equilib. Diffus. 35 (2014) 178–185, http://dx.doi.org/10.1007/s11669-014-0292-z.
[41] J. Zhanpeng, A study of the range of stability of sigma phase in some ternary systems, Scand. J. Met. 10 (1981) 279–287.
[42] O. Kubachewski, K. Hack, Heats of formation and of transformation in the system nickel-cobalt-chromium, Z. Met. 70 (1979) 789–791.
[43] N. Dupin, I. Ansara, On the sublattice formalism applied to the B2 phase, Z. Met. 90 (1999) 76–85.
[44] B. Sundman, I. Ohnuma, N. Dupin, U.R. Kattner, S.G. Fries, An assessment of the entire Al–Fe system including D03 ordering, Acta Mater. 57 (2009) 2896–2908.
[45] B. Jansson, Evaluation of parameters in thermochemical models using different types of experimental data simultaneously, Technical Report TRITAMAC-0234, Stockholm, Sweden, 1984.
[46] B. Sundman, B. Jansson, J.-O. Andersson, The Thermo-Calc databank system, Calphad 9 (1985) 153–190, http://dx.doi.org/10.1016/0364-5916(85)90021-5.
[47] J.-O. Andersson, T. Helander, L. Höglund, P. Shi, B. Sundman, Thermo-Calc & DICTRA, computational tools for materials science, Calphad 26 (2002) 273–312.
[48] H.L. Lukas, S.G. Fries, B. Sundman, Computational Thermodynamics: The Calphad Method, 1st ed., New York, NY, 2007.
[49] I. Ansara, B. Sundman, P. Willemin, Thermodynamic modeling of ordered phases in the Ni–Al system, Acta Met. 36 (1988) 977–982, http://dx.doi.org/10.1016/0001-6160(88)90152-6.
[50] N. Dupin, B. Sundman, A thermodynamic database for Ni-base superalloys, Scand. J. Met. 30 (2001) 184–192.
[51] A. Kusoffsky, N. Dupin, B. Sundman, On the compound energy formalism applied to FCC ordering, Calphad 25 (2001) 549–565.
[52] X. Yuan, L. Zhang, Y. Du, W. Xiong, Y. Tang, A. Wang, et al., A new approach to establish both stable and metastable phase equilibria for fcc ordered/disordered phase transition: application to the Al–Ni and Ni–Si systems, Mater. Chem. Phys. 135 (2012) 94–105, http://dx.doi.org/10.1016/j.matchemphys.2012.04.028.
[53] P. Franke, An assessment of the ordered phases in Mn–Ni using two- and four-sublattice models, Z. Met. 98 (2007) 954–960.
[54] J.-M. Joubert, Crystal chemistry and Calphad modeling of the [sigma] phase, Prog. Mater. Sci. 53 (2008) 528–583.
[55] R. Mathieu, N. Dupin, J.-C. Crivello, K. Yaqoob, A. Breidi, J.-M. Fiorani, et al., CALPHAD description of the Mo–Re system focused on the sigma phase modeling, Calphad 43 (2013) 18–31, http://dx.doi.org/10.1016/j.calphad.2013.08.002.
[56] S.L. Shang, Y. Wang, D. Kim, Z.-K. Liu, First-principles thermodynamics from phonon and Debye model: application to Ni and Ni_3Al, Comput. Mater. Sci. 47 (2010) 1040–1048.
[57] F. Birch, Finite elastic strain of cubic crystals, Phys. Rev. 71 (1947) 809–824.
[58] S.L. Shang, Y. Wang, Z.-K. Liu, First-principles elastic constants of α- and θ-Al_2O_3, Appl. Phys. Lett. 90 (2007) 101909.
[59] C.L. Zacherl, S.-L. Shang, A. Saengdeejing, Z.-K. Liu, Phase stability and thermodynamic modeling of the Re–Ti system supplemented by first-principles calculations, Calphad 38 (2012) 71–80.
[60] X.L. Liu, C.Z. Hargather, Z.-K. Liu, First-principles aided thermodynamic modeling of the Nb–Re system, Calphad 41 (2013) 119–127.
[61] A. Zunger, S.-H. Wei, L.G. Ferreira, J.E. Bernard, Special quasirandom structures, Phys. Rev. Lett. 65 (1990) 353–356.
[62] C. Wolverton, Crystal structure and stability of complex precipitate phases in Al–Cu–Mg–(Si) and Al–Zn–Mg alloys, Acta Mater. 49 (2001) 3129–3142, http://dx.doi.org/10.1016/S1359-6454(01)00229-4.
[63] D. Shin, A. van de Walle, Y. Wang, Z.-K. Liu, First-principles study of ternary fcc solution phases from special quasirandom structures, Phys. Rev. B 76 (2007) 144204, http://dx.doi.org/10.1103/PhysRevB.76.144204.
[64] C. Jiang, L.-Q. Chen, Z.-K. Liu, First-principles study of constitutional point defects in B2 NiAl using special quasirandom structures, Acta Mater. 53 (2005) 2643–2652.
[65] A. van de Walle, M. Asta, G. Ceder, The alloy theoretic automated toolkit: a user guide, Calphad 26 (2002) 539–553, http://dx.doi.org/10.1016/S0364-5916

(02)80006-2.
[66] A. van de Walle, P. Tiwary, M. de Jong, D.L. Olmsted, M. Asta, A. Dick, et al., Efficient stochastic generation of special quasirandom structures, Calphad 42 (2013) 13–18, http://dx.doi.org/10.1016/j.calphad.2013.06.006.
[67] X.L. Liu, B.K. VanLeeuwen, S.S.-L. Shang, Y. Du, Z.-K. Liu, On the scaling factor in Debye–Grüneisen model: a case study of the Mg–Zn binary system, Comput. Mater. Sci. 98 (2015) 34–41.
[68] G. Kresse, J. Furthmüller, Efficient iterative schemes for ab initio total-energy calculations using a plane-wave basis set, Phys. Rev. B 54 (1996) 11169–11186.
[69] J. Perdew, K. Burke, M. Ernzerhof, Generalized gradient approximation made simple, Phys. Rev. Lett. 77 (1996) 3865–3868.
[70] F. Mouhat, F.-X. Coudert, Necessary and sufficient elastic stability conditions in various crystal systems, Phys. Rev. B 90 (2014) 224104, http://dx.doi.org/10.1103/PhysRevB.90.224104.
[71] S.P. Bafuk, Master's Thesis, Michigan Technological University, 1981.
[72] N. Rusović, H. Warlimont, The elastic behaviour of β2-NiAl alloys, Phys. Status Solidi 44 (1977) 609–619, http://dx.doi.org/10.1002/pssa.2210440225.
[73] R.J. Wasilewski, Elastic Constants and Young's Modulus of NiAl, Trans. Met. Soc. AIME 236 (1966) 2–4.
[74] M. Mostoller, R. Nicklow, D. Zehner, S.-C. Lui, J. Mundenar, E. Plummer, Bulk and surface vibrational modes in NiAl, Phys. Rev. B 40 (1989) 2856–2872, http://dx.doi.org/10.1103/PhysRevB.40.2856.
[75] T. Davenport, L. Zhou, J. Trivisonno, Ultrasonic and atomic force studies of the martensitic transformation induced by temperature and uniaxial stress in NiAl alloys, Phys. Rev. B 59 (1999) 3421–3426, http://dx.doi.org/10.1103/PhysRevB.59.3421.
[76] A.V. Ponomareva, Y.K. Vekilov, I.A. Abrikosov, Effect of Re content on elastic properties of B2 NiAl from ab initio calculations, J. Alloy. Compd. 586 (2014) S274–S278, http://dx.doi.org/10.1016/j.jallcom.2012.12.103.
[77] Y. Wang, J.J. Wang, H. Zhang, V.R. Manga, S.L. Shang, L.-Q. Chen, et al., A first-principles approach to finite temperature elastic constants, J. Phys. Condens. Matter 22 (2010) 225404, http://dx.doi.org/10.1088/0953-8984/22/22/225404.
[78] K. Tanaka, M. Koiwa, Single-crystal elastic constants of intermetallic compounds, Intermetallics 4 (1996) S29–S39, http://dx.doi.org/10.1016/0966-9795(96)00014-3.
[79] S.V. Prikhodko, J.D. Carnes, D.G. Isaak, H. Yang, A.J. Ardell, Temperature and composition dependence of the elastic constants of Ni_3Al, Metall. Mater. Trans. A 30 (1999) 2403–2408.
[80] D.E. Kim, S.L. Shang, Z.K. Liu, Effects of alloying elements on elastic properties of Ni_3Al by first-principles calculations, Intermetallics 18 (2010) 1163–1171, http://dx.doi.org/10.1016/j.intermet.2010.02.024.
[81] E.T. Henig, H.L. Lukas, G. Petzow, Enthalpy of formation and description of the defect structure of the ordered beta-phase in Co–Al, Z. Met. 71 (1980) 398–402.
[82] K. Rzyman, Z. Moser, Calorimetric studies of the enthalpies of formation of Al_3Ni_2, AlNi and $AlNi_3$, Prog. Mater. Sci. 49 (2004) 581–606, http://dx.doi.org/10.1016/j.pmatsci.2003.08.001.
[83] K. Rzyman, Z. Moser, R.E. Watson, M. Weinert, Enthalpies of formation of AlNi: experiment versus theory, J. Ph. Equilib. 19 (1998) 106–111.
[84] R. Arroyave, D. Shin, Z.-K. Liu, Ab initio thermodynamic properties of stoichiometric phases in the Ni–Al system, Acta Mater. 53 (2005) 1809–1819, http://dx.doi.org/10.1016/j.actamat.2004.12.030.
[85] K. Rzyman, Z. Moser, R.E. Watson, M. Weinert, Enthalpies of formation of Ni_3Al: experiment versus theory, J. Ph. Equilib. 17 (1996) 173–178.
[86] H. Ohtani, M. Yamano, M. Hasebe, Thermodynamic analysis of the Co–Al–C and Ni–Al–C systems by incorporating ab initio energetic calculations into the CALPHAD approach, Calphad 28 (2004) 177–190, http://dx.doi.org/10.1016/j.calphad.2004.08.003.
[87] G. Róg, A. Kozłowska-Róg, G. Borchardt, L. Dörrer, W. Löser, Determination of the standard Gibbs free energy of the intermetallic compound Ni_3Al in the temperature range (820–920) K by a solid-state galvanic cell method, J. Chem. Thermodyn. 37 (2005) 97–100, http://dx.doi.org/10.1016/j.jct.2004.07.033.
[88] J. Pavlů, J. Vřešťál, M. Šob, Ab initio study of formation energy and magnetism of sigma phase in Cr–Fe and Cr–Co systems, Intermetallics 18 (2010) 212–220.
[89] H.B. Bell, J.P. Hajra, F.H. Putland, P.J. Spencer, The determination of the thermodynamic properties of cobalt–chromium alloys using solid-electrolyte EMF and high-temperature calorimetric, Tech. Met. Sci. 7 (1973) 185–190.
[90] C. Wolverton, V. Ozoliņš, First-principles aluminum database: energetics of binary Al alloys and compounds, Phys. Rev. B 73 (2006) 144104, http://dx.doi.org/10.1103/PhysRevB.73.144104.
[91] L. Zhang, J. Wang, Y. Du, R. Hu, P. Nash, X.-G. Lu, et al., Thermodynamic properties of the Al–Fe–Ni system acquired via a hybrid approach combining calorimetry, first-principles and CALPHAD, Acta Mater. 57 (2009) 5324–5341, http://dx.doi.org/10.1016/j.actamat.2009.07.031.
[92] E.S. Moskvitina, V.N. Kuznetsov, L.S. Guzei, Refinement of the Co–Cr–Al Phase-Diagram, Vestn. Mosk. Univ. Seriya 2 Khimiya (Moscow Univ. Chem. Bull.), vol. 33, 1992, pp. 373–374.
[93] T. Gómez-Acebo, B. Navarcorena, F. Castro, Interdiffusion in multiphase, Al–Co–Cr–Ni–Ti diffusion couples, J. Ph. Equilib. Diffus. 25 (2004) 237–251, http://dx.doi.org/10.1361/15477030419496.
[94] J. Towns, T. Cockerill, M. Dahan, I. Foster, K. Gaither, A. Grimshaw, et al., XSEDE: accelerating scientific discovery, Comput. Sci. Eng. 16 (2014) 62–74, http://dx.doi.org/10.1109/MCSE.2014.80.
[95] D.B. Miracle, The physical and mechanical properties of NiAl, Acta Met. Mater. 41 (1993) 649–684.
[96] C. Stassis, F. Kayser, C. Loong, D. Arch, Lattice dynamics of Ni_3Al, Phys. Rev. B 24 (1981) 3048–3053, http://dx.doi.org/10.1103/PhysRevB.24.3048.

CALPHAD: Computer Coupling of Phase Diagrams and Thermochemistry 51 (2015) 178–192

Contents lists available at ScienceDirect

CALPHAD: Computer Coupling of Phase Diagrams and Thermochemistry

journal homepage: www.elsevier.com/locate/calphad

Thermodynamic modeling of the aluminum–iron–oxygen system

Greta Lindwall *, Xuan L. Liu, Austin Ross, Huazhi Fang, Bi-Cheng Zhou, Zi-Kui Liu

Department of Materials Science and Engineering 111 Research Unit A, The Pennsylvania State University, University Park, PA 16801, USA

ARTICLE INFO

Article history:
Received 5 November 2014
Received in revised form
8 September 2015
Accepted 9 September 2015
Available online 1 October 2015

ABSTRACT

The aluminum–iron–oxygen (Al–Fe–O) system is an important subsystem within several material classes, especially when considering oxidation of high-performance structural materials or deoxidation of steels during steelmaking. Despite its industrial importance as well as the large amount of experimental information available in literature, no complete phase diagram has been reported for this system. Therefore, a thermodynamic description, by means of the CALPHAD method, is developed in this study. To account for the complexity of the solid oxides including non-stoichiometry, solid solution in the phases and cation distribution between different lattice sites, the compound energy formalism is applied for the modeling. The liquid phase is modeled utilizing the ionic two-sublattice model. The sublattice models are selected with the aim to achieve compatibility with the Al–Ni–O and Fe–Ni–O systems to facility development of a quaternary thermodynamic description. The evaluated model is validated by comparison to available experimental data. Satisfactory agreement with both thermochemical and phase equilibrium data is concluded.

1. Introduction

The aluminum–iron–oxygen (Al–Fe–O) system is an important system for several applications. In steelmaking, for example, Al is extensively used to remove O from the slag. Aluminum has a strong affinity to O and quickly reacts with dissolved O to form the corundum oxide ($(Al,Fe)_2O_3$) when added to the liquid melt, which easily floats up and absorbs into the top slag for removal. Often, undesired spinel oxides ($(Al,Fe)_3O_4$) are formed together with corundum. Therefore, for greater control of the steelmaking process, knowledge about slag properties is needed, in particular about the metal-slag reactions. This requires a better understanding of equilibrium phase relations in this ternary system.

Understanding of thermodynamic properties of the Al–Fe–O system is also a necessity when developing materials aimed for high temperature applications in corrosive environments. In the 1930's, iron aluminides attracted great attention when their excellent oxidation resistance first was observed [1,2]. Along with a number of advantageous properties such as low cost, abundancy and relatively low density, these alloys were considered for a wide range of applications [3] including piping and tubing for fossil energy applications, jet engine compressors blades and housings as well as food handling equipment only to mention a few. The corrosion resistance derives from the thermodynamic stability and relatively slow growth of the alumina surface layer that forms upon exposure to an oxidizing environment. For the same reason, Ni-base alloys, aimed for applications at high temperatures in harsh environments, are alloyed with Al, and their resulting corrosion will predominately depend on the stability and growth behavior of this protective oxide layer.

Additionally, color enhancement of natural and synthetic sapphires often require high temperature heat treatments (in excess of 1000 °C) in O_2 environments [4,5]. Optimal conditions under which Fe^{+3} ions can be reduced to Fe^{+2} for color augmentation can lead to formation of undesired phases. Traditionally, these conditions have been determined using numerous gem samples [4]. A thermodynamic model can aid in the determination of these optimal conditions by predicting Fe^{+2} concentrations and unwanted phase formations.

Motivated by the development materials by computational design, the thermodynamic description of the Al–Fe–O system is modeled in the current work by means of the CALPHAD method (CALculations of PHAse Diagrams). In this method each phase in a system is modeled separately by establishing a description that represents the Gibbs free energy and its dependence of temperature, composition and pressure. Thermodynamic phase equilibria can then be predicted by finding the phase constitution that minimizes the total free energy of the system under given

* Corresponding author.
E-mail addresses: gretalindwall@gmail.com (G. Lindwall), xul119@psu.edu (X.L. Liu), austinross42@gmail.com (A. Ross), huf12@psu.edu (H. Fang), zhoubicheng@gmail.com (B.-C. Zhou), prof.zikui.liu@gmail.com (Z.-K. Liu).

http://dx.doi.org/10.1016/j.calphad.2015.09.004
0364-5916/

conditions. A thermodynamic model of the Al–Fe–O system is included in the FactSage database [6], but to the authors' knowledge, no details or model parameters for the system are available in the literature. Furthermore, the phase models applied in the present work are carefully selected in order to facilitate construction of a consistent description of the Al–Fe–Ni–O system by making use of the available description of Fe–Ni–O [7,8] and the description of Al–Ni–O under development [9].

2. Thermodynamic models

Thermodynamic modeling of oxides represents an area for which the CALPHAD approach is particularly powerful. Since experimental information for thermodynamic properties of oxides is often limited due to experimental difficulties, details of recommended assessment procedures for CALPHAD modeling of oxides using the compound energy formalism have been discussed extensively over the years [10–12]. In this work the recommended strategy suggested by Hillert et al. [12] is followed for the spinel phase. In addition to the spinel phase, liquid, corundum, halite and the orthorhombic $AlFeO_3$ oxide are modeled. The remaining phases, relevant for the Al–Fe–O system (solid solution and intermetallic phases), are adopted as modeled in the binary systems Al–O [13,14], Fe–O [7,15,16] and Al–Fe [17].

2.1. Liquid

The selected model for the liquid phase is the ionic two-sublattice liquid model [18,19] with the formula $(Al^{+3},Fe^{+2})_P(O^{-2},Va^{-Q},AlO_{1.5},FeO_{1.5})_Q$ where P and Q are the number of sites on the two sublattices, respectively, and vary in order to sustain electroneutrality. This model formula is consistent with the liquid model for the Fe–C – Cr–Mn–Ni–O by Kjellqvist [20] where the $FeO_{1.5}$ species also was included. The neutral species, $AlO_{1.5}$, stems from the assessment of the binary Al–O system by Hallstedt [21]. It should be mentioned that a newer model for Al-containing systems has been suggested [22] where the $AlO_{1.5}$ was replaced by the specie AlO_2^{-1} to better describe the $CaO–Al_2O_3–SiO_2$ and $MgO–Al_2O_3–SiO_2$ systems. In this work the neutral $AlO_{1.5}$ is kept for consistency with an electroslag remelting database under development [23].

The liquid model for the metallic binary, Al–Fe [17], is adopted as it can be converted to the ionic two-sublattice liquid model; it is identical to the substitutional solution model at sufficient low oxygen contents. The Gibbs energy for the liquid phase in the system is then given by

$$\begin{aligned}
G_m^{liquid} &= y_{Al^{+3}}y_{O^{-2}}{}^0G_{Al^{+3}:O^{-2}} + y_{Fe^{+2}}y_{O^{-2}}{}^0G_{Fe^{+2}:O^{-2}} \\
&+Qy_{Va^{-Q}}(y_{Al^{+3}}{}^0G_{Al^{+3}:Va^{-Q}} + y_{Fe^{+2}}{}^0G_{Fe^{+2}:Va^{-Q}}) \\
&+Q(y_{AlO_{1.5}}{}^0G_{AlO_{1.5}} + y_{FeO_{1.5}}{}^0G_{FeO_{1.5}}) \\
&+RTP(y_{Al^{+3}}\ln(y_{Al^{+3}}) + y_{Fe^{+2}}\ln(y_{Fe^{+2}})) \\
&+RTQ(y_{O^{-2}}\ln(y_{O^{-2}}) + y_{Va^{-Q}}\ln(y_{Va^{-Q}}) + y_{AlO_{1.5}}\ln(y_{AlO_{1.5}}) \\
&+ y_{FeO_{1.5}}\ln(y_{FeO_{1.5}})) + {}^E G_m
\end{aligned} \tag{1}$$

where the y:s are the site-fractions, and the ${}^EG_m$ is the excess Gibbs energy accounting for the interactions between the species within the sublattices expressed as

$$\begin{aligned}
{}^EG_m &= Qy_{Va}^2y_{Al^{+3}}y_{Fe^{+2}} \\
&\quad ({}^0L_{Al^{+3},Fe^{+2}:Va} + {}^1L_{Al^{+3},Fe^{+2}:Va}(y_{Al^{+3}} - y_{Fe^{+2}}) \\
&\quad + {}^2L_{Al^{+3},Fe^{+2}:Va}(y_{Al^{+3}} - y_{Fe^{+2}})^2) \\
&+y_{Va}y_{Al^{+3}}y_{O^{-2}}{}^0L_{Al^{+3}:O^{-2},Va} + y_{Va}y_{Al^{+3}}y_{AlO_{1.5}}{}^0L_{Al^{+3}:AlO_{1.5},Va} \\
&+y_{Va}y_{Fe^{+2}}y_{O^{-2}}({}^0L_{Fe^{+2}:O^{-2},Va} + {}^1L_{Fe^{+2}:O^{-2},Va}(y_{O^{-2}} - y_{Va})) \\
&+Qy_{Va}y_{Fe^{+2}}y_{AlO_{1.5}}{}^0L_{Fe^{+2}:AlO_{1.5},Va} + Qy_{Va}y_{Fe^{+2}}y_{FeO_{1.5}} \\
&\quad {}^0L_{Fe^{+2}:FeO_{1.5},Va} \\
&+Qy_{Va}y_{Al^{+3}}y_{AlO_{1.5}}{}^0L_{Al^{+3}:AlO_{1.5},Va} + Qy_{Va}y_{Al^{+3}}y_{FeO_{1.5}} \\
&\quad {}^0L_{Al^{+3}:FeO_{1.5},Va} \\
&+y_{Fe^{+2}}y_{FeO_{1.5}}y_{O^{-2}}({}^0L_{Fe^{+2}:FeO_{1.5},O^{-2}} \\
&\quad + {}^1L_{Fe^{+2}:FeO_{1.5},O^{-2}}(y_{FeO_{1.5}} - y_{O^{-2}})) \\
&+y_{Fe^{+2}}y_{AlO_{1.5}}y_{O^{-2}}{}^0L_{Fe^{+2}:AlO_{1.5},O^{-2}} + y_{Va}y_{Al^{+3}}y_{Fe^{+2}}y_{O^{-2}} \\
&\quad {}^0L_{Al^{+3},Fe^{+2}:O^{-2},Va}
\end{aligned} \tag{2}$$

here, the comma is used to differentiate between species on the same sublattices, whereas a colon is used to differentiate between species on different sublattices. A large number of interaction parameters are possible but in Eq. 2 only the interaction parameters used for the present modeling are included.

2.2. Spinel

Spinel is the generic name for a mineral group of oxides where the oxide anions are arranged in a cubic close-packed lattice and where the cations occupy octahedral and tetrahedral sites within this lattice. In the Al–Fe–O system, the spinel is an important phase in the middle of the $FeO–Fe_2O_3–Al_2O_3$ system. The stable spinels in the system are hercynite ($FeAl_2O_4$) and magnetite (Fe_3O_4). In this work, the description for the magnetite sub-system is adopted from the Fe–O assessment by Sundman [15] and modified subsequently by Kjellqvist et al. [24]. The hercynite subspinel can be represented using the formula $(Al^{+3},Fe^{+2})_1(Al^{+3},Fe^{+2})_2(O^{-2})_4$ with the Gibbs energy given as

$$\begin{aligned}
G_m^{spinel} &= y'_{Fe^{+2}}y''_{Fe^{+2}}{}^0G^{spinel}_{Fe^{+2}:Fe^{+2}} + y'_{Fe^{+2}}y''_{Al^{+3}}{}^0G^{spinel}_{Fe^{+2}:Al^{+3}} \\
&+ y'_{Al^{+3}}y''_{Fe^{+2}}{}^0G^{spinel}_{Al^{+3}:Fe^{+2}} + y'_{Al^{+3}}y''_{Al^{+3}}{}^0G^{spinel}_{Al^{+3}:Al^{+3}} - TS_m^{spinel} \\
&+ {}^EG_m^{spinel}
\end{aligned} \tag{3}$$

here, y' and y'' represent the site fraction of ions on the first sublattice (tetrahedral sites) and second (octahedral sites) sublattice, respectively. ${}^EG_m^{spinel}$ describes the interaction between the ions within a sublattice. By applying the strategy suggested by Hillert et al. [12], the order parameter $\xi = y'_{Al^{+3}} = 1 - y'_{Fe^{+2}}$ is introduced to represent the degree of inversion of the spinel. If $\xi = 0$, the spinel is normal; i.e. divalent cations are occupying the tetrahedral sites whereas trivalent cations occupy octahedral sites, and if $\xi = 1$, the spinel is inverse. In this case the tetrahedral sites are occupied by trivalent ions, and both trivalent and divalent ions consequently need to enter the octahedral sites due to the condition of electroneutrality. Using these relations the Gibbs energy of hercynite becomes

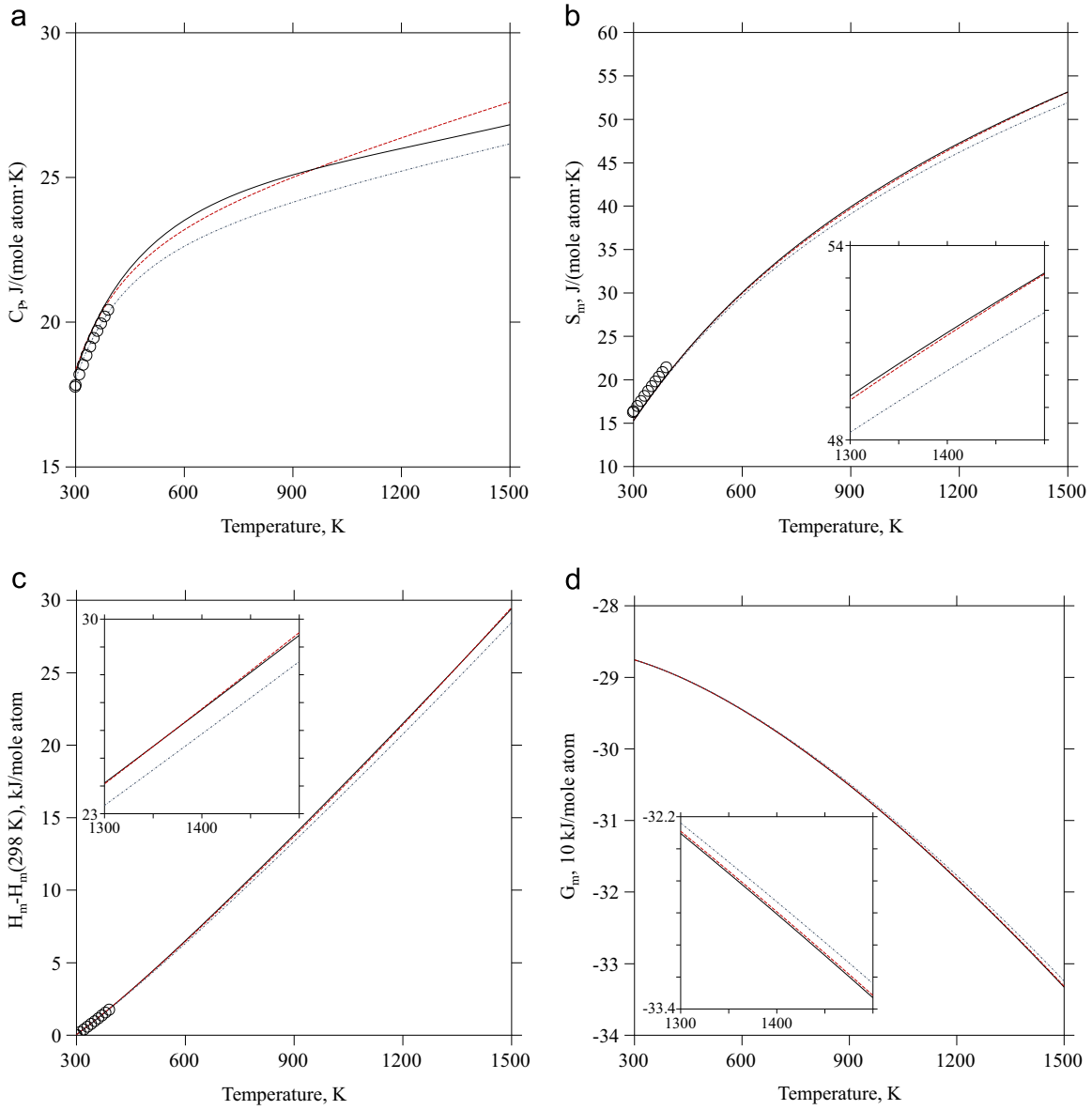

Fig. 1. Calculated heat capacity (a), entropy (b), heat content (c) and Gibbs energy (d) of hercynite compared to the normal ${}^{0}G^{spinel}_{Fe^{+2}:Al^{+3}}$ end-member (dash-dotted line), SGTE data [31] (dashed line) and measured heat capacity of polycrystalline hercynite [58] (represented by ○).

Table 1
Standard entropy at 298.15 K for hercynite ($FeAl_2O_4$).

$S_{298.15}$, J/(mole atom· K)	Reference
15.2	This work
16.3 ± 0.2	Klemme and Miltenburg[58]
15.2	King[59]
16.6 ± 0.8	Holland and Powell[73]
15.3	Berman[74]
16.9	Sack and Ghiorso[75]
17.6	Berman and Aranovich[76]
16.7 ± 0.1	Gottschalk[77]
17.6	Chatterjee et al.[78]
15.4	Holland and Powell[79]

$$G_m^{spinel} + T{\cdot}S_m^{spinel}(\xi) - {}^{E}G_m^{spinel} = {}^{0}G^{spinel}_{Fe^{+2}:Al^{+3}} + \xi{\cdot}J + 0.5{\cdot}\xi^2{:}\ G_{Fe^{+2}Al^{+3}:Fe^{+2}Al^{+3}} \quad (4)$$

where

$$J = 0.5{\cdot}({}^{0}G^{spinel}_{Fe^{+2}:Fe^{+2}} - 3{\cdot}{}^{0}G^{spinel}_{Fe^{+2}:Al^{+3}} + 2{\cdot}{}^{0}G^{spinel}_{Al^{+3}:Al^{+3}}) \quad (5)$$

and

$$\Delta G_{Fe^{+2}Al^{+3}:Fe^{+2}Al^{+3}} = {}^{0}G^{spinel}_{Fe^{+2}:Al^{+3}} + {}^{0}G^{spinel}_{Al^{+3}:Fe^{+2}} - {}^{0}G^{spinel}_{Fe^{+2}:Fe^{+2}} - {}^{0}G^{spinel}_{Al^{+3}:Al^{+3}} \quad (6)$$

the function J is hence related to the degree of inversion of the spinel and can be evaluated if the preferred site occupancy has been measured experimentally. $\Delta G_{Fe^{+2}Al^{+3}:Fe^{+2}Al^{+3}}$ represents the reciprocal reaction energy and is normally, but not exclusively, approximated to be zero. Assuming $\Delta G_{Fe^{+2}Al^{+3}:Fe^{+2}Al^{+3}} = 0$ means that the energy for the exchange from an Fe^{+2} ion to an Al^{+3} ion on the tetrahedral site is the same regardless of the ion type occupying the octahedral sites. The end-member, ${}^{0}G^{spinel}_{Fe^{+2}:Al^{+3}}$, represents the normal spinel at the hercynite composition. Since

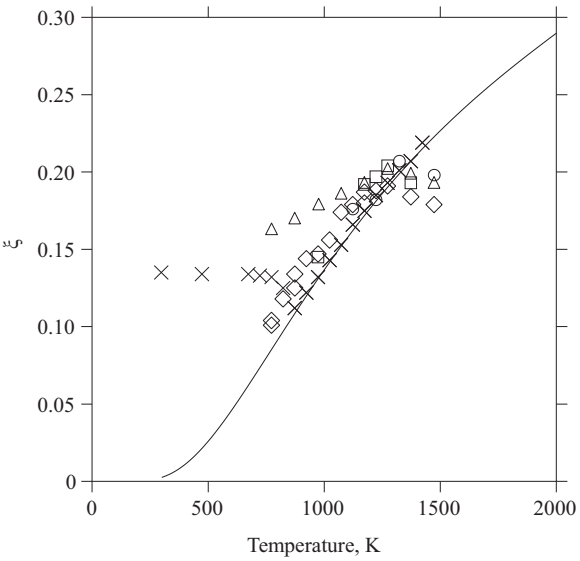

Fig. 2. Calculated degree of inversion, ξ ($Fe_{1-\xi}$ $Al_{\xi}(Fe_{\xi/2}Al_{1-(\xi/2)})O_4$), for hercynite as a function of temperature compared to experimental measurements by Harrison et al. [30] (represented by ×) using Neutron diffraction, by Larsson et al. [28] (represented by ○ and △) using Mossbauer spectroscopy and by Larsson et al. [28] (represented by □ and ◇) using XRD analysis.

hercynite shows a low degree of inversion at low temperatures [25–30], the properties of this end-member can be expected to be close to the properties measured experimentally for hercynite for which an expression has been assessed and is available in the SGTE database for substances, SSUB4 [31]. However, with increased temperature, the degree of inversion of hercynite increases and this assumption is not justified. Fortunately, the thermodynamics of cation disorder in spinels have been the subjects of several studies. One model by O'Neill and Navrotsky [32] suggests that the difference between the enthalpy of a spinel with an intermediate degree of inversion and a normal spinel can be represented by a quadratic function of the inversion parameter, ξ;

$$\Delta H_{disorder} = \alpha\cdot\xi + \beta\cdot\xi^2 \tag{7}$$

where α and β are constants. The change in Gibbs free energy relative a normal spinel can then be obtained by combining this enthalpy expression with the configurational entropy of the cation disorder;

$$\Delta G_{disorder} = \alpha\cdot\xi + \beta\cdot\xi^2 + RT\sum_{i,j} N_j y_i^j \ln(y_i^j) \tag{8}$$

here, y_i^j is the site fraction of cation i on sublattice j and N_j is the number of sites on sublattice j per formula unit. This formula has been shown to be applicable to a number of spinels with different disordering of divalent and trivalent cations [32]. In the case of hercynite, Harrison et al. [30] evaluated the α and β constants in the temperature range 873–1423 K resulting in $\alpha = 31.3 \pm 1.1$ kJ/mole-formula and $\beta = 19.7 \pm 3.4$ kJ/mole-formula. Their results are used here as guidance when modifying the Gibbs energy expression obtained experimentally to describe the perfectly normal spinel end-member ($^0G^{spinel}_{Fe^{+2}:Al^{+3}} = {}^0G_{SGTE-hercynite} - \Delta G_{disorder}$). This is discussed further in Section 4.

In the case of ionic phase models, such as for spinel, it is necessary to designate a charged reference state. Here, the Fe–O end-members for the Al–Fe spinel are fixed from the Fe–O assessment [15] and consequently, the same charged reference state as for magnetite is selected; i.e. $^0G^{spinel}_{Fe^{+2}:Fe^{+3}} = {}^0G^{spinel}_{Fe^{+3}:Fe^{+2}}$. The reciprocal reaction, $\Delta G_{Fe^{+2}Al^{+3}:Fe^{+2}Al^{+3}}$, is approximated to be zero, leading to the following expressions of the remaining end-members of this spinel sub-system

$$^0G^{spinel}_{Al^{+3}:Al^{+3}} = 1.5\cdot{}^0G^{spinel}_{Fe^{+2}:Al^{+3}} + J - 0.5\cdot{}^0G^{spinel}_{Fe^{+2}:Fe^{+2}}$$

$$^0G^{spinel}_{Al^{+3}:Fe^{+2}} = 0.5\,{}^0G^{spinel}_{Fe^{+2}:Fe^{+2}} + 0.5\cdot{}^0G^{spinel}_{Fe^{+2}:Al^{+3}} + J \tag{9}$$

Alumina in the form of metastable γ-Al_2O_3 can exist in the spinel structure with its Gibbs energy given by $^0G_{s-Al2O3}$. In order to account for this excess oxygen, vacancies are introduced on the second sublattice: i.e. $(Al^{+3},Fe^{+2})_1(Al^{+3},Fe^{+2},Va)_2(O^{-2})_4$. A neutral combination for its Gibbs energy can be expressed as

$$8\cdot{}^0G_{s-Al2O3} = 5\cdot\ {}^0G^{spinel}_{Al^{+3}:Al^{+3}} + {}^0G^{spinel}_{Al^{+3}:Va} - 2 \cdot RT(6\cdot\ln(6) - 5\ \cdot\ln(5)) \tag{10}$$

where the end-member $^0G^{spinel}_{Al^{+3}:Va}$ describes the extension of spinel from $FeAl_2O_4$ towards Al_2O_3.

Furthermore in the Fe-O binary [15,33], the spinel phase includes both divalent and trivalent Fe ions, and for compatibility, Fe^{+3} is introduced and allowed to occupy both tetrahedral and octahedral sites. The full formula for the spinel in the Al–Fe–O system then becomes

$$(Fe^{+2}, Fe^{+3}, Al^{+3})(Fe^{+2}, Fe^{+3}, Al^{+3},Va)_2(Fe^{+2},Va)_2(O^{-2})_4 \tag{11}$$

Here, an additional sublattice with Fe^{+2} and vacancies has also been introduced to enable compatibility with the spinel description by Kjellqvist [20].

Again, the pure Fe end-members are fixed from the Fe–O assessment. The end-members $^0G^{spinel}_{Al^{+3}:Fe^{+3}:Va}$ and $^0G^{spinel}_{Fe^{+3}:Al^{+3}:Va}$ are obtained by setting the reciprocal reactions $\Delta G_{Fe^{+2}Al^{+3}:Fe^{+3}Al^{+3}} = 0$ and $\Delta G_{Fe^{+3}Al^{+3}:Fe^{+3}Al^{+3}} = DG3P3$ where $DG3P3 \neq 0$. The remaining six end-members with Fe^{+2} on the third sublattice are obtained by assuming a series of reciprocal reactions to be zero.

2.3. Corundum and halite

Both the Al–O and the Fe–O binaries include phases with the generic name corundum: Fe_2O_3 and Al_2O_3. In the current work, the oxide with the corundum structure is modeled using three sublattices,

$$(Fe^{+2}, Fe^{+3}, Al^{+3})_2(Fe^{+3},Va)_1(O^{-2})_3. \tag{12}$$

Since this phase is present in both binaries, the majority of the end-members are fixed from the Al–O [13] and Fe–O [15,33] modeling, respectively. One end-member, $^0G^{corundum}_{Al^{+3}:Fe^{+3}}$, remains to be defined and is obtained by assuming that the reciprocal reaction energy, $\Delta G_{Fe^{+3}Al^{+3}:Fe^{+3}Va}$, is zero. This results in

$$^0G^{corundum}_{Al^{+3}:Fe^{+3}} = {}^0G^{corundum}_{Al^{+3}:Va} + 85\,000. \tag{13}$$

The halite phase has a NaCl-type of structures and is modeled using one sublattice for metal ions and one for oxygen ions as follows

$$(Fe^{+2}, Fe^{+3}, Al^{+3},Va)_1(O^{-2})_1. \tag{14}$$

The FeO end-members are adopted from the binary Fe–O assessment [15] and the AlO end-member is from the Al–Mg–O assessment by Mozaffari-Jovein [14]. This expression for the AlO end-member is also adopted by Saltykov et al. [34] when modeling the oxidation behavior of Al–Cr–Ni alloys. Here, $^0G^{halite}_{Va:O^{-2}} = 0$, is the charged reference point.

Table 2
Parameters for the thermodynamic descriptions of the phases in the Al–Fe–O system in units: Joule–mole formula and Kelvin.

LIQUID: $(Al^{+3},Fe^{+2})_P(O^{-2},Va,AlO_{1.5},FeO_{1.5})_Q$	
${}^0G_{Al^{+3}:O^{-2}} - 2H^{SER}_{Al} - 3H^{SER}_O$	+GLIQAL2O3+1 000 000
${}^0G_{Fe^{+2}:O^{-2}} - 2H^{SER}_{Fe} - 2H^{SER}_O$	+4·GFEOLIQ
${}^0G_{Al^{+3}:Va} - H^{SER}_{Al}$	+GLIQAL
${}^0G_{Fe^{+2}:Va} - H^{SER}_{Fe}$	+GLIQFE
${}^0G_{AlO_{1.5}} - H^{SER}_{Al} - 1.5H^{SER}_O$	+0.5·GLIQAL2O3
${}^0G_{FeO_{1.5}} - H^{SER}_{Fe} - 1.5H^{SER}_O$	−89 819+39.962·T+2.5·GFEOLIQ
${}^0L_{Al^{+3},Fe^{+2}:Va}$	−91 976.5+22.1314·T
${}^1L_{Al^{+3},Fe^{+2}:Va}$	−5672.58+4.8728·T
${}^2L_{Al^{+3},Fe^{+2}:Va}$	+121.9
${}^0L_{Al^{+3}:O^{-2},Va}$	−829 000+106·T
${}^0L_{Fe^{+2}:O^{-2},Va}$	+176 681−16.368·T
${}^1L_{Fe^{+2}:O^{-2},Va}$	−65 655+30.869·T
${}^0L_{Fe^{+2}:O^{-2},FeO_{1.5}}$	−26 362
${}^1L_{Fe^{+2}:O^{-2},FeO_{1.5}}$	+13 353
${}^0L_{Fe^{+2}:O^{-2},AlO_{1.5}}$	− 40 000+25·T*
${}^0L_{Al^{+3}:Va,AlO_{1.5}}$	+110 000+46·T
${}^0L_{Al^{+3}:Va,FeO_{1.5}}$	+110 000*
${}^0L_{Fe^{+2}:Va,AlO_{1.5}}$	+178 992*
${}^0L_{Fe^{+2}:Va,FeO_{1.5}}$	+110 000
${}^0L_{Al^{+3},Fe^{+2}:Va,O^{-2}}$	−740 767*
CORUNDUM: $(Al^{+3},Fe^{+2},Fe^{+3})_2(Fe^{+3},Va)_1(O^{-2})_3$	
${}^0G_{Al^{+3}:Fe^{+3}:O^{-2}} - 2H^{SER}_{Al} - H^{SER}_{Fe} - 3H^{SER}_O$	+ GCORUND+85 000*
${}^0G_{Al^{+3}:Va:O^{-2}} - 2H^{SER}_{Al} - 3H^{SER}_O$	+GCORUND
${}^0G_{Fe^{+2}:Fe^{+3}:O^{-2}} - 3H^{SER}_{Fe} - 3H^{SER}_O$	+GFE2O3+85 000
${}^0G_{Fe^{+2}:Va:O^{-2}} - 2H^{SER}_{Fe} - 3H^{SER}_O$	+GFE2O3
${}^0G_{Fe^{+3}:Fe^{+3}:O^{-2}} - 3H^{SER}_{Fe} - 3H^{SER}_O$	+GFE2O3+85 000
${}^0G_{Fe^{+3}:Va:O^{-2}} - 2H^{SER}_{Fe} - 3H^{SER}_O$	+GFE2O3
${}^0L_{Al^{+3},Fe^{+3}:Va:O^{-2}}$	+110 010−31.781·T*
${}^1L_{Al^{+3},Fe^{+3}:Va:O^{-2}}$	+25 408*
${}^2L_{Al^{+3},Fe^{+3}:Va:O^{-2}}$	−65 489*
Magnetic properties:for compounds containing only Fe cations $T_C=-2867$ and $\beta=-25.1$for compounds containing Al cations $T_C=0$ and $\beta=0$	
SPINEL: $(Al^{+3},Fe^{+2},Fe^{+3})_1(Al^{+3},Fe^{+2},Fe^{+3},Va)_2(Fe^{+2},Va)_2(O^{-2})_4$	
${}^0G_{Al^{+3}:Al^{+3}:Va:O^{-2}} - 3H^{SER}_{Al} - 4H^{SER}_O$	+GPP*
${}^0G_{Al^{+3}:Fe^{+2}:Va:O^{-2}} - H^{SER}_{Al} - 2H^{SER}_{Fe} - 4H^{SER}_O$	+GP2*
${}^0G_{Al^{+3}:Fe^{+3}:Va:O^{-2}} - H^{SER}_{Al} - 2H^{SER}_{Fe} - 4H^{SER}_O$	+GP3*
${}^0G_{Al^{+3}:Va:Va:O^{-2}} - H^{SER}_{Al} - 4H^{SER}_O$	+GPV*
${}^0G_{Fe^{+2}:Al^{+3}:Va:O^{-2}} - 2H^{SER}_{Fe} - H^{SER}_{Al} - 4H^{SER}_O$	+GFEAL2O4*
${}^0G_{Fe^{+2}:Fe^{+2}:Va:O^{-2}} - 3H^{SER}_{Fe} - 4H^{SER}_O$	+7·GFE3O4+JFF
${}^0G_{Fe^{+2}:Fe^{+3}:Va:O^{-2}} - 3H^{SER}_{Fe} - 4H^{SER}_O$	+7·GFE3O4
${}^0G_{Fe^{+2}:Va:Va:O^{-2}} - H^{SER}_{Fe} - 4H^{SER}_O$	+5·GFE3O4 +CFE3O4
${}^0G_{Fe^{+3}:Al^{+3}:Va:O^{-2}} - H^{SER}_{Fe} - 2H^{SER}_{Al} - 4H^{SER}_O$	+G3P*
${}^0G_{Fe^{+3}:Fe^{+2}:Va:O^{-2}} - 3H^{SER}_{Fe} - 4H^{SER}_O$	+7·GFE3O4
${}^0G_{Fe^{+3}:Fe^{+3}:Va:O^{-2}} - 3H^{SER}_{Fe} - 4H^{SER}_O$	+7·GFE3O4−JFF
${}^0G_{Fe^{+3}:Va:Va:O^{-2}} - H^{SER}_{Fe} - 4H^{SER}_O$	+5·GFE3O4−JFF+CFE3O4

Table 2 (*continued*)

${}^0G_{*:*:Fe^{+2}:O^{-2}} - H^{SER}_{*} - 2H^{SER}_{*} - 2H^{SER}_{Fe} - 4H^{SER}_{O}$	$+G_{*:*:Va:O^{-2}}$ + GF2F3F2B-GF2F3VAB
${}^0L_{Fe^{+2}:Al^{+3},Fe^{+3}:Va:O^{-2}}$	$+16\ 427 - 6.4653 \cdot T^*$
${}^0L_{Fe^{+3}:Al^{+3},Fe^{+3}:Va:O^{-2}}$	$-132\ 425 - 39.326 \cdot T^*$
${}^1L_{Fe^{+3}:Al^{+3},Fe^{+3}:Va:O^{-2}}$	$-91\ 226 + 80.135 \cdot T^*$
${}^2L_{Fe^{+3}:Al^{+3},Fe^{+3}:Va:O^{-2}}$	$-91.\ 20798 \cdot T^*$
Magnetic properties: for compounds containing only Fe cations $T_C = 848$ and $\beta = 44.54$ for compounds containing Al cations $T_C = 0$ and $\beta = 0$	
HALITE: $(Al^{+3},Fe^{+2},Fe^{+3},Va)_1(O^{-2})_1$	
${}^0G_{Al^{+3}:O^{-2}} - H^{SER}_{Al} - H^{SER}_{O}$	$+50\ 000 + 0.5 \cdot$ GCORUND
${}^0G_{Fe^{+2}:O^{-2}} - H^{SER}_{Fe} - H^{SER}_{O}$	+ GWUSTITE
${}^0G_{Fe^{+3}:O^{-2}} - H^{SER}_{Fe} - H^{SER}_{O}$	$+1.25 \cdot$ AWUSTITE $+1.25 \cdot$ GWUSTITE
${}^0G_{Va:O^{-2}} - H^{SER}_{O}$	0
${}^0L_{Fe^{+2},Fe^{+3}:O^{-2}}$	$-12\ 324.4$
${}^1L_{Fe^{+2},Fe^{+3}:O^{-2}}$	$+20\ 070$
$AlFeO_3$: $(Al^{+3})_1(Fe^{+3})_1(O^{-2})_3$	
${}^0G_{Al^{+3}:Fe^{+3}:O^{-2}} - H^{SER}_{Al} - H^{SER}_{Fe} - 3H^{SER}_{O}$	+ GALFEO3*
BCC_A2: $(Al,Fe)_1(O,Va)_3$	
${}^0G_{Al:Va} - H^{SER}_{Al}$	+ GBCCAL
${}^0G_{Fe:Va} - H^{SER}_{Fe}$	+ GHSERFE
${}^0TC_{Fe:Va}$	+ 1043
${}^0\beta_{Fe:Va}$	+ 2.22
${}^0G_{Al:O} - H^{SER}_{Al} - H^{SER}_{O}$	+ GHSERAL + 1.5 · GO2GAS + 195 · T
${}^0G_{Fe:O} - H^{SER}_{Fe} - H^{SER}_{O}$	+ GHSERFE + 1.5 · GO2GAS + 195 · T
${}^0L_{Fe:O,Va}$	$-517\ 548 + 71.83 \cdot T$
${}^0L_{Al,Fe:Va}$	$+4 \cdot$ L0BCC $- 4 \cdot$ W1
${}^1L_{Al,Fe:Va}$	$+8 \cdot$ L1BCC
${}^1T_{CAl,Fe:Va}$	504
BCC_B2: $(Al,Fe)_{0.5}(Al,Fe)_{0.5}(O,Va)_3$	
${}^0G_{Al:Al:Va} = {}^0G_{Fe:Fe:Va}$	0
${}^0G_{Fe:Al:Va} = {}^0G_{Al:Fe:Va}$	$-2 \cdot$ W1
${}^0G_{Al:Al:O} = {}^0G_{Fe:Fe:O}$	0
${}^0G_{Fe:Al:O} = {}^0G_{Al:Fe:O}$	$-2 \cdot$ W1
FCC: $(Al,Fe)_1(O,Va)_1$	
${}^0G_{Al:Va} - H^{SER}_{Al}$	+ GHSERAL
${}^0G_{Fe:Va} - H^{SER}_{Fe}$	+ GHFEFCC
${}^0TC_{Fe:Va}$	+ 67
${}^0\beta_{Fe:Va}$	+ 0.7
${}^0G_{Al:O} - H^{SER}_{Al} - H^{SER}_{O}$	+ GHSERAL + 0.5 · GO2GAS − 236 446.62
${}^0G_{Fe:O} - H^{SER}_{Fe} - H^{SER}_{O}$	+ GFEFCC + 0.5 · GO2GAS + 65 · T
${}^0L_{Al,Fe:Va}$	$-76\ 066.1 + 18.6758 \cdot T$
${}^1L_{Al,Fe:Va}$	$+21\ 167.4 + 1.3398 \cdot T$
${}^0L_{Al,Fe:O}$	$-76\ 066.1 + 18.6758 \cdot T$
${}^1L_{Al,Fe:O}$	$+21\ 167.4 + 1.3398 \cdot T$
${}^0L_{Al:O,Va}$	$-90\ 252.23$
${}^0L_{Fe:O,Va}$	$-168\ 758 + 19.17 \cdot T$
Al_2Fe: $(Al)_2(Fe)_1$	
${}^0G_{Al:Fe} - 2H^{SER}_{Al} - H^{SER}_{Fe}$	$+2 \cdot$ GHSERAL + GHSERFE $- 98\ 096.9 + 18.7503 \cdot T$
Al_2Fe_2: $(Al)_2(Fe)_2$	
${}^0G_{Al:Fe} - 2H^{SER}_{Al} - 2H^{SER}_{Fe}$	$+2 \cdot$ GHSERAL + GHSERFE $- 99\ 526 + 19.811 \cdot T$
Al_5Fe_2: $(Al)_5(Fe)_2$	
${}^0G_{Al:Fe} - 5H^{SER}_{Al} - 2H^{SER}_{Fe}$	$+5 \cdot$ GHSERAL $+2 \cdot$ GHSERFE $- 228\ 250 + 48.\ 99503 \cdot T$
Al_5Fe_4: $(Al,Fe)_1$	
${}^0G_{Al} - H^{SER}_{Al}$	+ GHSERAL + 12 178.9 $- 4.813 \cdot T$
${}^0G_{Fe} - H^{SER}_{Fe}$	+ GHSERFE + 5009.03
${}^0L_{Al,Fe}$	$-131\ 649 + 29.4833 \cdot T$
${}^1L_{Al,Fe}$	$-18\ 619.5$
$Al_{13}Fe_4$: $(Al)_{251}(Fe)_{94}(Al,Va)_{55}$	

Table 2 (*continued*)

${}^0G_{Al:Fe:Al} - 306H_{Al}^{SER} - 94H_{Fe}^{SER}$	$+17.978 \cdot GHSERAL + 5.523 \cdot GHSERFE$ $-724\ 138.4 + 174.840 \cdot T$
${}^0G_{Al:Fe:Va} - 251H_{Al}^{SER} - 94H_{Fe}^{SER}$	$+14.746 \cdot GHSERAL + 5.523 \cdot GHSERFE$ $-652\ 860.6 + 170.530 \cdot T$
Functions	
GHSERAL ($298.15 < T < 700$)	$-7976.15 + 137.093038 \cdot T - 24.3671976 \cdot T \cdot \ln(T) - 0.001884662 \cdot T^2 - 8.77664 \cdot 10^{-7} \cdot T^3 + 74092 \cdot T^{-1}$
GHSERAL ($700 < T < 933.47$)	$-11276.24 + 223.048446 \cdot T - 38.5844296 \cdot T \cdot \ln(T) + 0.018531982 \cdot T^2 - 5.764227 \cdot 10^{-6} \cdot T^3 + 74092 \cdot T^{-1}$
GHSERAL ($933.47 < T < 2900$)	$-11278.378 + 188.684153 \cdot T - 31.748192 \cdot T \cdot \ln(T) - 0.230524 \cdot 10^{28} \cdot T^{-9}$
GHSERFE ($298.15 < T < 1811$)	$+1225.7 + 124.134 \cdot T - 23.5143 \cdot T \cdot \ln(T)$ $-0.00439752 \cdot T^2$ $-5.8927 \cdot 10^{-8} \cdot T^3 + 77359 \cdot T^{-1}$
GHSERFE ($1811 < T < 6000$)	$-25383.581 + 299.31255 \cdot T - 46 \cdot T \cdot \ln(T) + 2.29603 \cdot 10^{31} \cdot T^{-9}$
GBCCAL ($298.15 < T < 6000$)	$+GHSERAL + 10083 - 4.813 \cdot T$
GFEFCC ($298.15 < T < 1811$)	$+GHSERFE - 1462.4 + 8.282 \cdot T - 1.15 \cdot T \cdot \ln(T)$ $+6.4 \cdot 10^{-4} \cdot T^2$
GFEFCC ($1811 < T < 6000$)	$+GHSERFE - 1713.815 + 0.94001 \cdot T + 4.9251 \cdot 10^{30} \cdot T^{-9}$
GLIQAL2O3 ($298.15 < T < 600$)	$+1\ 607\ 850.8 + 405.559491 \cdot T - 67.4804 \cdot T \cdot \ln(T) - 0.06747 \cdot T^2 + 1.4205433 \cdot 10^{-5} \cdot T^3 + 938780 \cdot T^{-1}$
GLIQAL2O3 ($600 < T < 1500$)	$-1\ 625\ 385.57 + 712.394972 \cdot T - 116.258 \cdot T \cdot \ln(T) - 0.0072257T^2 + 2.78532 \cdot 10^{-7} \cdot T^3 + 2\ 120\ 700 \cdot T^{-1}$
GLIQAL2O3 ($1500 < T < 1912$)	$-1672662.69 + 1010.9932 \cdot T - 156.058 \cdot T \cdot \ln(T) + 0.00709105 \cdot T^2 - 6.29402 \cdot 10^{-7} \cdot T^3 + 12\ 366\ 650 \cdot T^{-1}$
GLIQAL2O3 ($1912 < T < 2327$)	$+29178041.6 - 168360.926 \cdot T + 21987.1791 \cdot T \cdot \ln(T) - 6.99552951 \cdot T^2 + 4.10226192 \cdot 10^{-4} \cdot T^3 - 7.98843618 \cdot 10^{+9} \cdot T^{-1}$
GLIQAL2O3 ($2327 < T < 4000$)	$-1\ 757\ 702.05 + 1344.84833 \cdot T - 192.464 \cdot T \cdot \ln(T)$
GLIQFEO	$-137\ 252 + 224.641 \cdot T - 37.1815 \cdot T \cdot \ln(T)$
GLIQAL ($298.15 < T < 933.47$)	$+11\ 005.029 - 11.841867 \cdot T + 7.934 \cdot 10^{-20} \cdot T^7 + GHSERAL$
GLIQAL ($933.47 < T < 6000$)	$+10\ 482.382 - 11.253974 \cdot T + 1.231 \cdot 10^{28} \cdot T^{-9} + GHSERAL$
GLIQFE ($298.15 < T < 1811$)	$+12\ 040.17 - 6.55843 \cdot T - 3.67516 \cdot 10^{-21} \cdot T^7 + GHSERFE$
GLIQFE ($1811 < T < 6000$)	$+14\ 544.751 - 8.01055 \cdot T - 2.29603 \cdot 10^{+31} \cdot T^{-9} + GHSERFE$
GO2GAS ($298.15 < T < 1000$)	$-6961.74451 - 76729.7484 \cdot T^{-1} - 51.0057202 \cdot T - 22.2710136 \cdot T \cdot \ln(T) - 0.0101977469 \cdot T^2 + 1.32369208 \cdot 10^{-6} \cdot T^3$
GO2GAS ($1000 < T < 3000$)	$-13137.5203 + 525809.556 \cdot T^{-1} + 25.3200332 \cdot T - 33.627603 \cdot T \cdot \ln(T) - 0.00119159274 \cdot T^2 + 1.35611111 \cdot 10^{-8} \cdot T^3$
GO2GAS ($3000 < T < 6000$)	$-27973.4908 + 8766421.4 \cdot T^{-1} + 62.5195726 \cdot T - 37.9072074 \cdot T \cdot \ln(T) - 8.50483772 \cdot 10^{-4} \cdot T^2 + 2.14409777 \cdot 10^{-8} \cdot T^3$
L0BCC	$-30740 + 7.9972 \cdot T$
L1BCC	$+386.15$
W1	$+860 \cdot R$
GCORUND ($298.15 < T < 600$)	$-1\ 707\ 351.3 + 448.021092 \cdot T - 67.4804 \cdot T \cdot \ln(T) - 0.06747 \cdot T^2 + 1.4205433 \cdot 10^{-5} \cdot T^3 + 938\ 780 \cdot T^{-1}$
GCORUND ($600 < T < 1500$)	$-1\ 724\ 886.06 + 754.856573 \cdot T - 116.258 \cdot T \cdot \ln(T) - 0.0072257 \cdot T^2 + 2.78532 \cdot 10^{-7} \cdot T^3 + 2\ 120\ 700 \cdot T^{-1}$
GCORUND ($1500 < T < 3000$)	$-1\ 772\ 163.19 + 1053.4548 \cdot T - 156.058 \cdot T \cdot \ln(T) + 0.00709105 \cdot T^2 - 6.29402 \cdot 10^{-7} \cdot T^3 + 12\ 366\ 650 \cdot T^{-1}$
GGAMMA ($298.15 < T < 600$)	$-1\ 689\ 977.34 + 469.458181 \cdot T - 70.5452 \cdot T \cdot \ln(T) - 0.070794 \cdot T^2 + 1.491345 \cdot 10^{-5} \cdot T^3 + 981\ 165 \cdot T^{-1}$
GGAMMA ($600 < T < 1500$)	$-1\ 708\ 389.72 + 791.591946 \cdot T - 121.754 \cdot T \cdot \ln(T) - 0.0075467 \cdot T^2 + 2.89573 \cdot 10^{-7} \cdot T^3 + 2\ 222\ 750 \cdot T^{-1}$
GGAMMA $1500 < T < 3000$)	$-1\ 758\ 861.74 + 1110.41976 \cdot T - 164.253 \cdot T \cdot \ln(T) + 0.00775305 \cdot T^2 - 6.8247 \cdot 10^{-7} \cdot T^3 + 13162750 \cdot T^{-1}$
GFE2O3	$-858\ 683 + 827.946 \cdot T - 137.0089 \cdot T \cdot \ln(T) + 1\ 453\ 810 \cdot T^{-1}$
GWUSTITE	$+279318 + 252.848 \cdot T - 46.12826 \cdot T \cdot \ln(T) - 0.0057402984 \cdot T^2$
AWUSTITE	$-55384 + 27.888 \cdot T$
GPP*	$+1.5 \cdot GFEAL24 - 0.5 \cdot GF2F2VAB + J$
GFEAL2O4*	$-2\ 038\ 654.70 + 958.16741 \cdot T - 155.3938 \cdot T \cdot \ln(T)$ $-0.0097141 \cdot T^2 + 1\ 566\ 908 \cdot T^{-1}$
G3P*	$-GF2F3VAB + GF3F3VAB + GFEAL2O4 + DG3P3P$
GP2*	$+J + 0.5 \cdot GFEAL24 + 0.5 \cdot GF2F2VAB$
GFE3O4	$-161\ 731 + 144.873 \cdot T - 24.9879 \cdot T \cdot \ln(T) - 0.0011952256 \cdot T^2 + 206\ 520 \cdot T^{-1}$ $+402520 - 30.529 \cdot T$
JFF	$+46\ 826 - 27.266 \cdot T$
GP3*	$+GF2F3VAB + 0.5 \cdot GFEAL2O4 + J - 0.5 \cdot GF2F2VAB$
GPV*	$+8 \cdot GGAMMA - 7.5 \cdot GFEAL2O4 + 2.5 \cdot GF2F2VAB - 5 \cdot J + 44.9543481 \cdot T$
CFE3O4	$+120730 - 20.102 \cdot T$
GF2F3F2B	$+GF2F3VAB + GSPDF2VB$
GF2F3VAB	$+7 \cdot GFFB$
GF2F2VAB	$+7 \cdot GFFB + JFF$
GF3F3VAB	$+7 \cdot GFFB - JFF$
GSPDF2VB	$+2 \cdot GFFB - JFF + D$
GFFB	$-161\ 731 + 144.873 \cdot T - 24.9879 \cdot T \cdot \ln(T) - 0.0011952256 \cdot T^2 + 206\ 520 \cdot T^{-1}$
*J**	$+29163.95 + 7.88 \cdot T$
DG3P3P*	$+133\ 833.21 - 52.276862 \cdot T$
GALFEO3*	$-1284485.36 + 795.2115 \cdot T - 126.28 \cdot T \cdot \ln(T) - 0.013681 \cdot T^2 + 1512700 \cdot T^{-1} + 1.1664 \cdot 10^{-7} \cdot T^3$
R	8.3144621

Parameters that have been assessed in the present work are designated with "*". The parameter from the SGTE database SSUB4 [24] is designated with "a". Included parameters not assessed in this work stem from the binary assessments Al–O[13, 14], Fe–O[7, 15, 16] and Al–Fe[17].

Orthorhombic $AlFeO_3$

The ternary oxide, $AlFeO_3$, is orthorhombic with a $FeGaO_3$ structure [35]. It is believed to be stable only at higher temperatures and the stability range is dependent on the O partial pressure. The tetrahedral sites and the regular octahedral sites have preference for Al whereas Fe prefers the two irregular six-fold sites. Although non-stoichiometric compositions have been observed [36,37], it is modeled as a stoichiometric compound in the current work for the sake of simplicity. Its Gibbs energy function is hence given by

$$G_m^{AlFeO_3} - H^{SER} = a_0 + a_1 \cdot T + a_2 \cdot T \cdot l\,n(T) + a_3 \cdot T^2 + a_4 \cdot T^{-1} + a_5 \cdot T^3 \quad (15)$$

where a_0–a_5 are the parameters to be optimized by accounting for thermochemical data from literature.

3. The Al–Fe–O system in the literature

A comprehensive review of data on the Al–Fe–O system

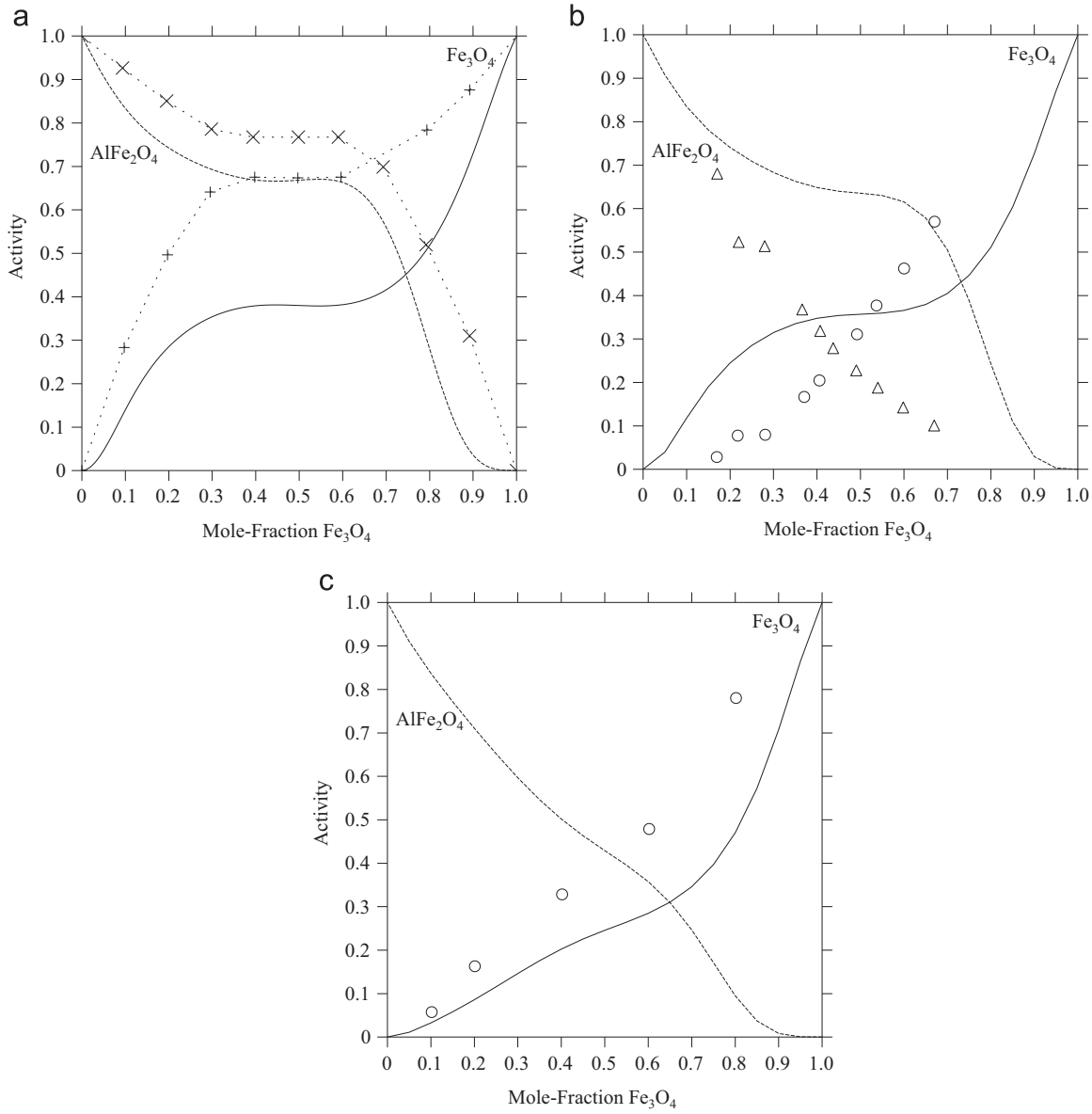

Fig. 3. Calculated activities of Fe_3O_4 and $FeAl_2O_4$ in the Fe_3O_4–$FeAl_2O_4$ system at (a) 1133, (b) 1173 and (c) 1573 K in comparison with experimental data by (b) Schmahl and Dillenburg [60] at 1173 K (represented by ○ and △) and (c) Petric et al. [61] at 1573 K (represented by ○) and estimated data by (a) Petric et al. [61] at 1133 K (represented by + · · · + · · · + and × · · · × · · · ×).

published up until 2006 is provided by the Landolt-Börnstein New Series IV/IIDI [38] and is hence, not repeated here. Some additional works, however, are accounted for in the current modeling and require some attention. In 2009 Rhamdhani et al. [37] studied phase equilibria of Fe–Ni–X–O (X=Mg, Al) systems in air, including the lower-order system, Al–Fe–O, at temperatures between 1473 and 1873 K and constructed the Fe_2O_3-Al_2O_3 vertical section. They applied equilibration and quenching techniques, followed by measurements of the phase composition using EPMA (electron probe X-ray microanalysis). They found differences in their results compared to previously published data and attributed this to the enhanced accuracy and reliability that the EPMA technique provides compared to other commonly applied techniques such as XRD (X-Ray Diffraction) [39]. The most distinctive difference being the higher solubility of Al in the Fe-rich corundum (hematite).

Another work that includes this Fe_2O_3–Al_2O_3 vertical section, which also was not included in the Landolt-Börnstein review, is the study by Hansson et al. [40] in 2004. The exclusion of this work in the review is probably due to the fact that the investigations concerned the Al–Fe–Zn–O system in air and not the ternary Al–Fe–O system. However, none of the ternary oxides showed to dissolve any significant concentrations of ZnO and the compositions could therefore be regarded as very close to the Fe_2O_3–Al_2O_3 section. Hansson et al. [40] also used EPMA for their phase composition determinations and notably concluded similar discrepancies compared to previous data as Rhamdhani et al. [37] would do some years later.

In addition to the experiments, the study by Rhamdhani et al. [37] included thermodynamic calculations using the FactSage [6] software. The method to develop the thermodynamic descriptions utilized by FactSage is similar as the current approach, and it should be noted that the modeling work in the Al–Fe–O system for the FactSage database has been mentioned in the literature [10,41]. However, any detailed descriptions of the applied phase models or model parameters have not been published.

Another recent experiment not included in the Landolt-Börnstein review concerns the equilibrium solubility of Al and O in liquid Fe and was performed by Kang et al. [42] in 2009. They equilibrated molten

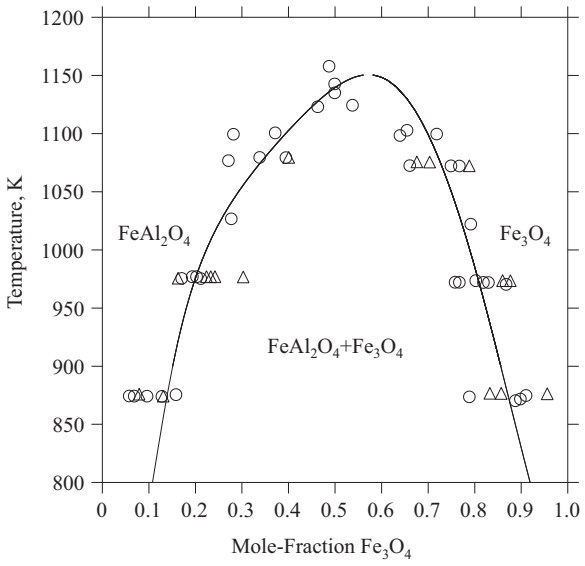

Fig. 4. Calculated miscibility gap in the spinel phase in the $FeAl_2O_4$–Fe_3O_4 section in comparison with experimental data by Turnock and Eugster [52]. Experiments were performed from both directions; both exsolution experiments where spinel solid solutions grown at temperatures above the solvus were used as starting materials and then held at temperatures below solvus for the two phases to exsolve (represented by ▵) and solid solution experiments where equal amounts of synthetic end-members were mixed together by grinding and then held at a chosen temperature to induce solid solution (represented by ○).

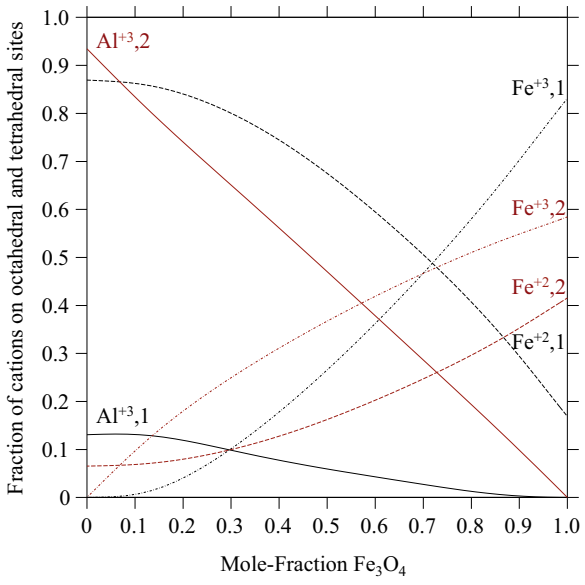

Fig. 5. Calculated cation distributions in spinel at 973 K in the Al_2O_3–Fe_2O_3 and $FeAl_2O4$-Fe_3O_4 sections. The black lines represent the first spinel sublattice (tetrahedral sites, 1) and the red lines represent the second spinel sublattice (octahedral sites, 2). (For interpretation of the references to color in this figure legend, the reader is referred to the web version of this article.)

steels with varying Al content with pure Al_2O_3 crucibles at 1873 K and measured the Al and O contents using inductively couples plasma atomic emission spectroscopy (ICP-AES) and inert gas fusion infrared absorption spectroscopy (IGFA), respectively. Compared to earlier work [43–51], including the recommended equilibrium curve by the Japan Society for the Promotion of Science (JSPS) [43], the results by Kang et al. [42] showed lower O solubility in Fe alloys with Al contents higher than 1 wt%, while the O solubility in Fe alloys with Al contents less than 1 wt% was found to be slightly higher.

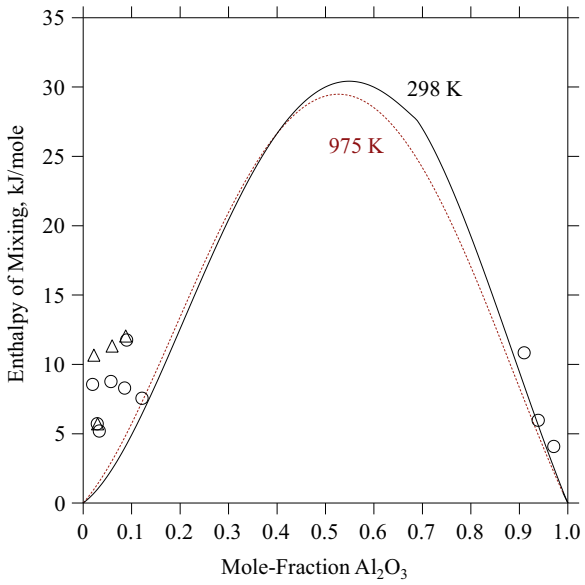

Fig. 6. (color online): Calculated enthalpy of mixing in the Fe_2O_3–Al_2O_3 solid solution at 298 (dashed line) and 975 K (solid line) in comparison with experimentally determined mixing enthalpies by Majzlan et al. [35] at 298 K (represented by ○) and at 975 K (represented by ▵).

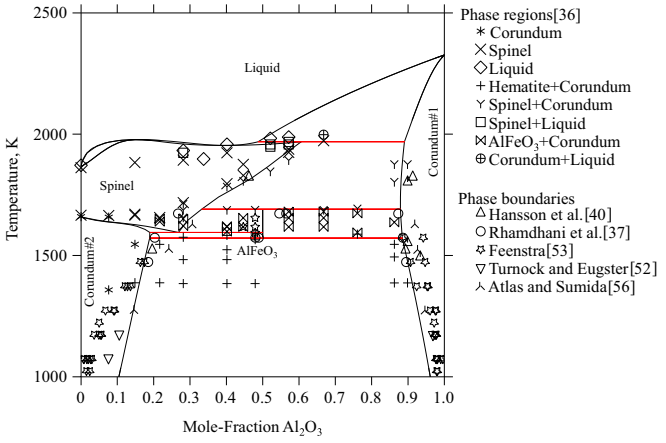

Fig. 7. (color online): Calculated phase diagram (solid lines) in the Fe_2O_3–Al_2O_3 section in air. Total pressure is 1 atm. According to Rhamdhani et al. [37] and Hansson et al. [40] (represented by ○ and ▵, respectively), the solubility of Al in corundum#2 is higher than measured by Muan and Gee [36] (represented by ✳ and +). Experimental results by Feenstra et al. [53] (represented by ☆ at the pressure 0.001, 8, 17, 24, 30, 35 and 40 kbar), by Turnock and Eugster [52] (represented by ▿) and by Atlas and Sumida [56] (represented by ⅄). Other measurements by Muan and Gee[36] show different phase regions; one-phase spinel (represented by ×), one-phase liquid (represented by ◇), two-phase region $AlFeO_3$/corundum (represented by ⋈), two-phase region spinel/liquid (represented by □) and two-phase region corundum/liquid (represented by ⊕).

4. Procedure of model parameter evaluation

First the spinel phase is investigated. As described in the previous section, the charged reference compound stemming from the Fe–O system is adopted; i.e. all the end-member shared with the Fe–O system are taken from Refs. [15,33]. To assess an expression for the normal spinel end-member, ${}^{0}G^{spinel}_{Fe^{+2}:Al^{+3}:Va}$, the Gibbs energy function for hercynite in the SGTE solution database, SSUB4 [31], is used as a starting point together with the results by Harrison et al. [30]. Their evaluation of the constants α and β (Eq. 7) together with the measured degree of inversion gives the difference of the Gibbs free energy with respect to the perfectly normal hercynite, $\Delta G_{disorder}$, as a function of temperature (Eq. 8). This

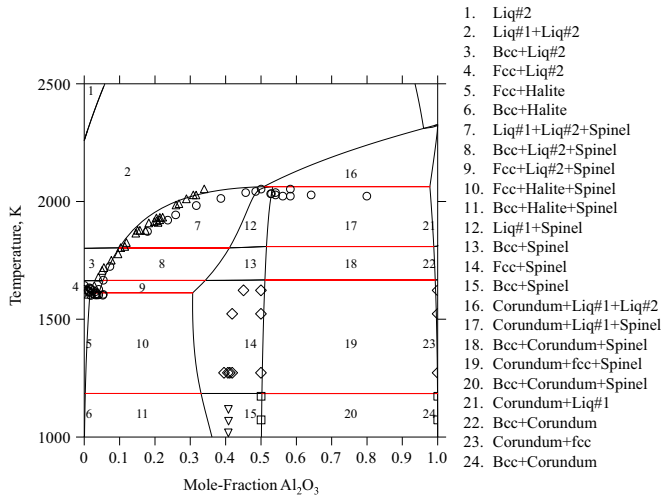

Fig. 8. Calculated phase equilibria (solid lines) in the FeO–Al_2O_3 system in contact with Fe. The calculations for the liquids are in good agreement with the experimental results on the Fe-rich side (represented by ▵ [54] and ○ [55]). The calculated phase boundaries between "halite+spinel+Fe(bcc/fcc)" and "spinel+Fe(bcc/f" show some discrepancy compared to the results by Turnock and Eugster [52] (represented by ▿) and by Atlas and Sumida [56] (represented by ⋄). The calculated phase boundary between "spinel+Fe(bcc/fcc)" and "corundum+spinel+Fe(bcc/fcc)" show agreement with the results by Atlas and Sumida [56] (represented by ⋄) as well as the results by Elrefaie and Smeltzer [57] (represented by □).

disordered contribution is then subtracted from the SGTE expression and the resulting expression is used for the end-member ${}^{0}G^{spinel}_{Fe^{+2}:Al^{+3}:Va}$. The measured degree of inversion by Harrison et al. [30] is also used to evaluate the function J (Eq. 5) which gives an expression of the ${}^{0}G^{spinel}_{Al^{+3}:Al^{+3}:Va}$ end-member. The remaining end-members, specifically for the Al–Fe–O system, are obtained by using the reciprocal relations shown in the previous section. The selected reciprocal relations are assumed to be zero with the exception of $\Delta G_{Fe^{+3}Al^{+3}:Fe^{+3}Al^{+3}} = DG3P3$ which is used as one of the optimization variables. In addition, two interaction parameters, $L_{Fe^{+2}:Al^{+3},Fe^{+3}:Va}$ and $L_{Fe^{+3}:Al^{+3},Fe^{+3}:Va}$, are introduced. This is necessary in order to reproduce the measured miscibility gap for the spinel phase in the $FeAl_2O_4$–Fe_3O_4 section and also enables reproduction of the vertical Fe_2O_3–Al_2O_3 sections.

Interaction parameters for the corundum phase are evaluated by accounting for the experimental information on the phase equilibria in the Al_2O_3–Fe_2O_3 section [37,52] and thermochemical data by Majzlan et al. [35]. The most recent experimental investigation by Rhamdhani et al. [37] is given a high weight in the evaluation. Their results agree with the miscibility gap studied by Turnock and Eugster [52] which also concluded a larger solubility of Al in corundum on the Fe-rich compared to the studies by Feenstra et al. [53], Majzlan et al. [35] and Muan and Gee [36].

The temperature dependence of Gibbs energy of the orthorhombic $AlFeO_3$ oxide is evaluated by accounting for the thermochemical data reported on by Majzlan et al. [35] and phase equilibria data in the Al_2O_3–Fe_2O_3 section in air. The phase boundary data is used in conjunction with thermochemical data to make $AlFeO_3$ stable with respect to the other oxides at the temperatures where it has been observed experimentally.

The interaction parameters for the liquid phase are evaluated by accounting for the Al and O solubility data in the Fe-rich corner, by Kang et al. [42], and phase equilibria data from the vertical sections FeO–Al_2O_3 [52,54–57] and Fe_2O_3–Al_2O_3 [36]. The model parameters for all phases are listed in Table 2.

5. Results and discussion

In Figs 1–5, the calculated properties of the spinel phase are shown in comparison to experiments. Fig 1 includes the heat capacity (Fig 1(a)), the molar entropy (Fig 1(b)), heat content (Fig 1(c)) and Gibbs free energy (Fig 1(d)) at the $FeAl_2O_4$ composition as a function of temperature. In the figure, properties calculated with the SGTE substances database, SSUB4 [31] as well as experimental results by Klemme and Miltenburg [58] are also shown. In addition, the properties for the normal spinel end-member (${}^{0}G^{spinel}_{Fe^{+2}:Al^{+3}}$) as modeled in the present work are included. The three energies (SGTE, the end-member and the final modeling result) are close at lower temperature. As the temperature increases, the difference between the final energy and the end-member energy increases. This is expected due to the enhanced degree of inversion.

The experimental results by Klemme and Miltenburg [58] are the most recent measurements for hercynite and focus on the lower temperature range (3–400 K). They used adiabatic calorimetry and reported a standard entropy of 16.3 J/(mole atom K) for hercynite at 298.15 K. In Table 1, standard entropy values reported in literature are listed along with the calculated result. It can be concluded that the reported values are scattered and that the present result is the same as the value reported by King [59]. The inconsistencies in these data sets were discussed by Klemme and Miltenburg [58], who suggested that further work is needed to investigate the magnetic structure of hercynite at low temperature which they suggested was the reason for the scattering. They also noted that the thermodynamics of hercynite are also not yet fully understood at higher temperatures since there are no measured high-temperature heat capacity or heat content data published; i.e. only estimated high-temperature heat capacity functions are available. It should also be mentioned that the magnetic properties of hercynite is not accounted for in this work and only properties from room temperature and above are assessed.

In Fig. 2, the calculated degree of inversion for hercynite ($FeAl_2O_4$) is shown in comparison with experimental data [28,30]; i.e. the fraction of Al^{+3} ions occupying the tetrahedral sites. The increase in the degree of inversion with temperature from 873 to 1423 K by Harrison et al. [30] is exactly reproduced by present calculations. The decrease in the measured degree of inversion seen at about 873 K is regarded to be due to a kinetic phenomenon caused by the system moving towards its equilibrium degree of order from the relatively disordered state maintained after quenching from the synthesis temperature and is, hence, not expected to agree with the calculated equilibrium fraction Fig. 2.

Fig. 3(a), (b) and (c) shows the activity of $FeAl_2O_4$ and Fe_3O_4 in the spinel solid solution in the $FeAl_2O_4$–Fe_3O_4 section at 1133, 1173 and 1573 K, respectively. The activities for Fe_3O_4 and $FeAl_2O_4$ at 1173 K by Schmahl and Dillenburg [60] are included in Fig. 3(b) and for Fe_3O_4 at 1573 K by Petric et al. [61] in Fig. 3(c). In Fig. 3(a) the activities for Fe_3O_4 and $FeAl_2O_4$ at 1133 K as suggested by Petric et al. [61] are included. These activities were derived by applying an empirical analysis using the occurrence of the miscibility gap in the Fe_3O_4–$FeAl_2O_4$ system, which shows a critical temperature around 1133 K [52].

The calculated activities do not reproduce the results by Schmahl and Dillenburg [60] at 1173 K (Fig. 3(b)) whereas better agreement with the results by Petric et al. [61] is concluded at 1133 (Fig. 3(a)) and 1573 K (Fig. 3(c)). In particular, the trends calculated at 1133 K compare well with the reported activities by Petric et al. [61]. Petric et al. also commented on the results by Schmahl and Dillenburg [60] saying that those activities were inconsistent with miscibility gap formation. Similarly, if the spinel phase is modeled to reproduce the activities by Schmahl and Dillenburg [60] at 1173 K, agreement with the experimentally

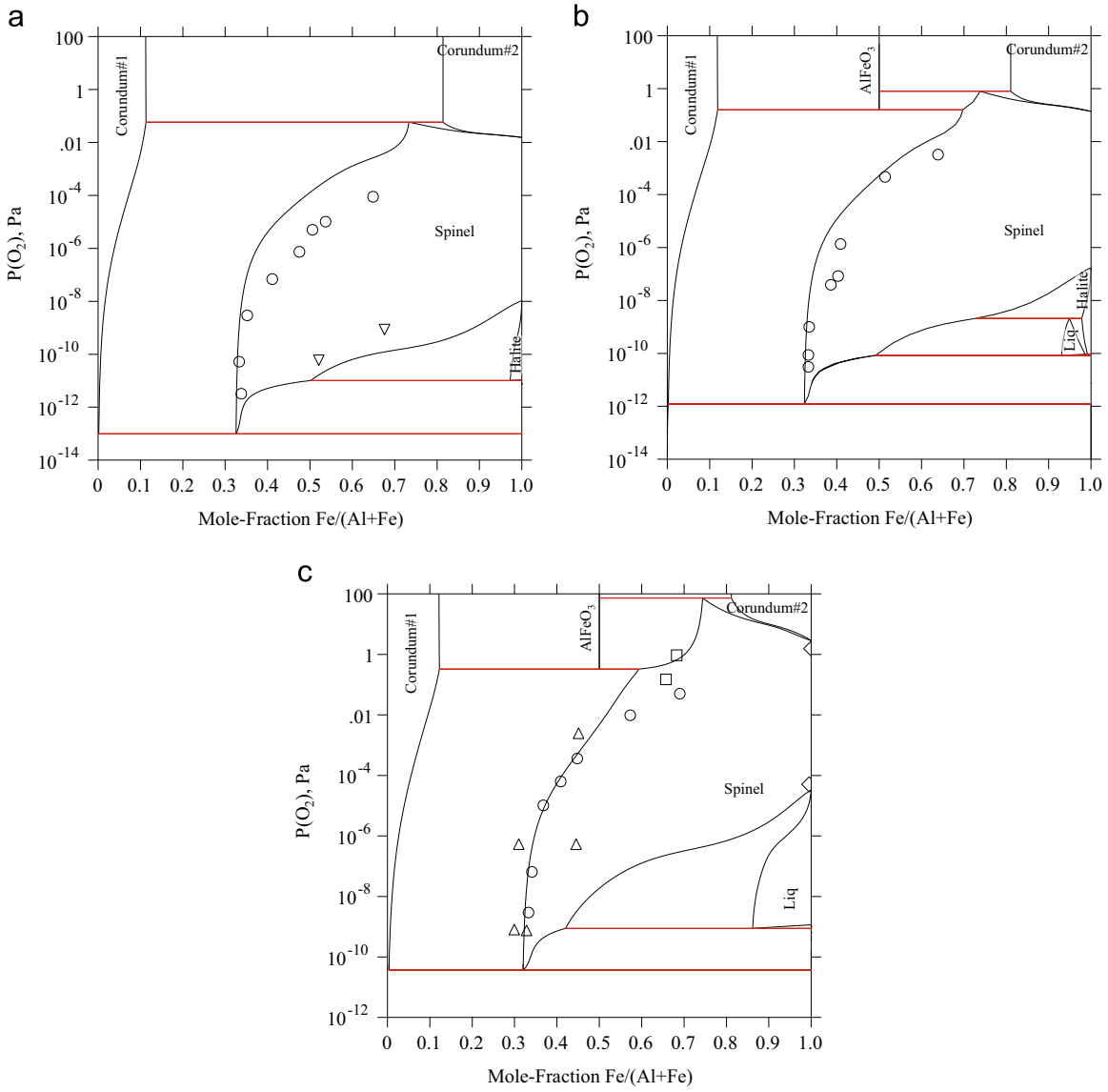

Fig. 9. Calculated composition-oxygen activity phase diagram at 1553 (a), 1641 (b) and 1773 K (c) in comparison with experiments by Meyers et al. [68] (represented by ○ and ▽), by Muan and Gee [36] (represented by △) and by Roiter [69] (represented by □). Total pressure is $1 \cdot 10^5$ Pa.

observed miscibility gap becomes unattainable. The calculated miscibility gap in the Fe_3O_4–$FeAl_2O_4$ system is shown in Fig. 4, in comparison with the measurements reported by Turnock and Eugster [52].

Fig. 5 concerns the cation distribution in the spinel phase at 973 K showing the change in cation fractions on the different sublattice sites when going from magnetite (Fe_3O_4) to hercynite ($FeAl_2O_4$).

Further properties for the modeled corundum phase are shown in Fig. 6 where the calculated enthalpies of formation for the corundum solid solution along Al_2O_3–Fe_2O_3 at 298 and 975 K are compared to the drop-solution calorimetry measurements by Majzlan et al. [35]. Taking into account the experimental uncertainties, the present results can be regarded as satisfactory. In addition to accounting for this enthalpy data, the interaction parameters for the corundum phase are evaluated with respect to $Al_2O_3-Fe_2O_3$ vertical section. The calculated $Al_2O_3-Fe_2O_3$ diagram in equilibrium with air at 1 bar is shown in Fig. 7 compared with experimental. At 1473 K, only the two corundum phases are predicted to be stable and the solubilities of Al in Fe-rich corundum#2 and of Fe in Al-rich corundum#1 increase with increasing temperature. These predictions agree with the results by Rhamdhani et al. [37] (represented by ○ in Fig. 7), which also show the same trend as reported by Hansson et al. [40] (represented by △ in Fig. 7) at lower temperatures (1473, 1523 and 1573 K). At higher temperatures, good agreement with Hansson et al. [40] is concluded (1823 K) whereas the agreement with Rhamdhani et al. [37] has decreased somewhat (1673 K). Compared to the results by Muan and Gee [36] (represented by ✳ and + in Fig. 7), it can be seen that the calculated solubility of Al in Fe-rich corundum#2 is predicted to be higher.

The calculated Al solubility in corundum#2 is also notably larger than reported by earlier works [35, 53] with the exception of the results by Atlas and Sumida [56] (represented by ⅄ in Fig. 7) and by Turnock and Eugster [52] (represented by ▽ in Fig. 7) that on the contrary, are closer to the predicted Al-solubility.

As mentioned in previous section, using the thermochemical data by Majzlan et al. [35] alone is not enough to obtain the behavior of the $AlFeO_3$ as observed experimentally, and the stability ranges for this phase in air suggested by Rhamdhani et al. [37] was allowed to influence the final expression of its Gibbs energy (Eq. 15). The calculated enthalpy of formation from oxides at 298 K of

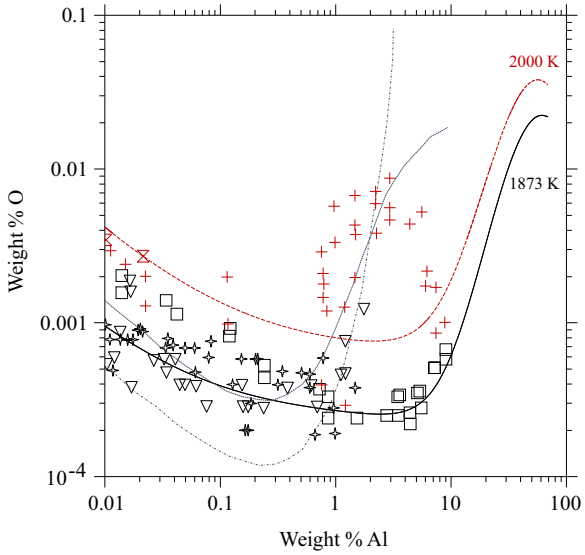

Fig. 10. Calculated Al–O equilibria in liquid Fe alloys at 1873 (black solid line) and 2000 K (red dashed line) in comparison with experiments [42, 45, 47–50, 80] (symbols in respective colors), compiled experiments by Itoh et al. [44] (blue dotted line) and the JSPS recommended curve [43] (blue dot dashed line). The calculated results reproduces the results by Kang et al. [42] (represented by □) well at higher Al contents. (For interpretation of the references to color in this figure legend, the reader is referred to the web version of this article.)

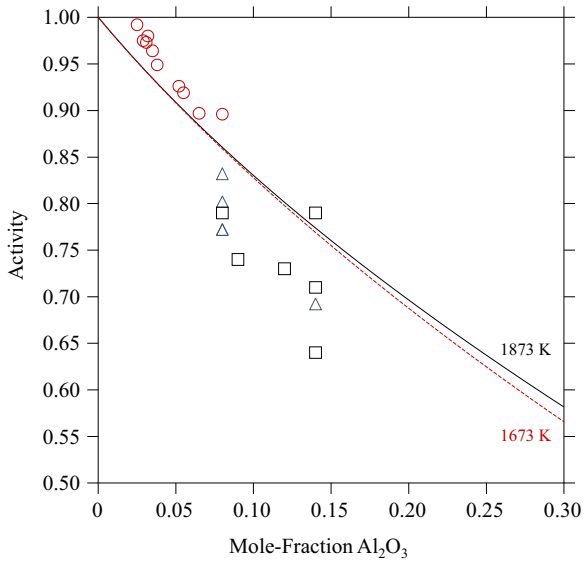

Fig. 11. Calculated activity of FeO in the FeO–Al_2O_3 liquid phase at 1673 and 1873 K compared to experimental measurements by Ban-Ya et al. [70] at 1673 K (represented by ○) and by Fredriksson and Seetharaman [71] at 1823 and 1873 K (represented by ▵ and □).

2.8 kJ/mole atom is hence altered compared to the experimentally determined energy; 5.6 ± 0.4 kJ/mole atom [35]. This difference of ~3 kJ is acceptable. The same is concluded for the standard entropy which was estimated to 19.8 J/(mole atom K) by Majzlan et al. [35] at 298 K and is calculated to 15.1 J/(mole atom K) using the current description.

Another issue associated with the ternary $AlFeO_3$ oxide needs to be addressed. Whereas Rhamdhani et al. [37] observed the $AlFeO_3$ to be stable together with two corundum phases and the spinel phase at 1573 K, Muan [62] and Muan and Gee [36] were not able to either synthesize or decompose $AlFeO_3$ at temperatures lower than 1591 K which calls into question their suggestion of 1591 K as the lower equilibrium limit. Additional contradictory experimental results in the literature complicates the matter further; e.g. the oxide has been synthesized at ~1073 K [63], and there are evidence of stability in the range 1223–1473 K [64] as well as in the range 1273–1673 K [65]. The investigations by Majzlan et al. [35] led them to conclude that $AlFeO_3$ is not stable with respect to Fe-rich and Al-rich corundum at 298 K and that it is entropically stabilized at higher temperatures. They predict it to be stable at temperatures above around 1730 ± 70K. The stability range of the $AlFeO_3$ oxide is also suggested to be dependent on the oxygen partial pressure. Muan [62] and Muan and Gee [36] proposed the stability range 1591 to 1683 K in air and 1591 to 1768 K at an O partial pressure of 1 bar. The investigations by Rhamdhani et al. [37] and Hansson et al. [40] were both in air and the three-phase region (corundum, spinel and $AlFeO_3$) was observed to exist from about 1573 up to somewhere around 1673 K. The calculated stability range for this phase in air, using the present developed description, goes from 1572 up to 1691 K, see Fig. 7, and is comparable with experiments by Rhamdhani et al. [37] as a consequence of the weighting during the parameter optimization. The calculated stability range at the partial pressure of 1 bar is, on the other hand, less comparable to experiments. It is predicted to 1571–1951 K which is a temperature interval about 200 K wider than suggested by Muan and Gee [36] and Muan [62]. If the oxide instead is modeled to reproduce this stability range, at 1 bar, it is not stable at any temperatures in air. The simplified model, only accounting for a temperature dependence, applied for this oxide in the current work, is apparently not sufficient to mimic the complex properties of this phase. However, as this oxide is regarded to be of negligible importance for the intended application of this work and since convincing and precise experimental information obviously is lacking, this simplification is currently accepted.

Another phase equilibrium that have been studied extensively is the FeO–Al_2O_3 section in contact with Fe. The calculated vertical section along FeO–Al_2O_3 is shown in Fig. 8 together with experimental data [52,54–57]. The experiments show consistency with regard to the liquidus on the Fe-rich side [54,55,57] and are well reproduced by the present model. The calculated melting of spinel is at 2058 K which can be compared to the reported melting temperatures of 2073 [66] and 2093 K [55,67]. In Fig. 8 it can also be concluded that the calculated phase boundary between "spinel + halite + Fe(fcc)" and "spinel + Fe(fcc)" as well as between "spinel + halite + Fe(bcc)" and "spinel + Fe(bcc)" show discrepancy compared to the data set by Atlas and Sumuda [56] (represented by ◇ in Fig. 8) and Turnock and Eugster [52] (represented by ▽ in Fig. 8). In particular in comparison with Atlas and Sumida's results (represented by ⅄ in Fig. 7). Their measurement of a higher Al content than calculated in Fe_2O_3–Al_2O_3 section (Fig. 7) is similar to what is concluded for the FeO–Al_2O_3 section (Fig. 8). The disagreement is apparent but less in the case of the data by Turnock and Eugster [52].

In Fig. 9, calculated O activity at 1553, 1641 and 1773 K, in the spinel stability area is shown as a function of metallic element ratios and in comparison with experimental data by Meyers et al. [68], Roiter [69] and Muan and Gee [36]. The agreement between calculations and experiments is satisfactory at all temperature although the agreement is better for the two higher temperatures.

In Fig. 10, the calculated Al and O solubilities in the liquid phase at 1873 and 2000 K are shown in comparison with various experimental datasets. At 1873 K, the calculated solubility (solid black line in Fig. 10) agrees with the most recent study by Kang et al. [42] (represented by □ in Fig. 10) at higher Al contents, above 1 wt%. At lower Al contents, the calculated O solubility is somewhat lower than measured by Kang et al. [42] but agrees with the data by Rohde et al. [48] (represented by ▽ in Fig. 10) and Janke et al. [49] (represented by ✦ in Fig. 10) as well as with the equilibrium curve compiled by Itoh et al. [44] (dotted grey line in

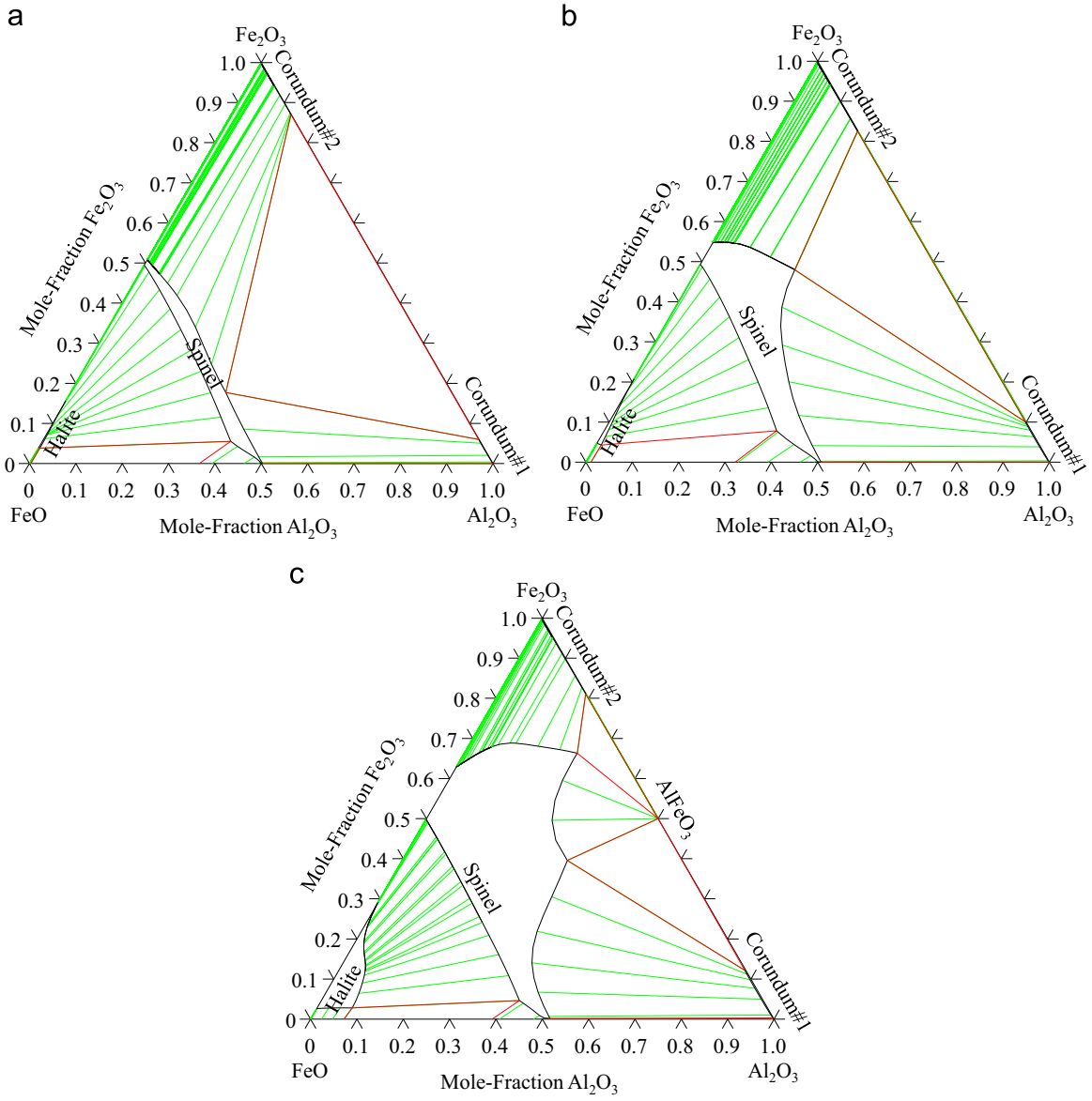

Fig. 12. Calculated Al_2O_3–FeO–Fe_2O_3 isothermal sections at 1173 (a), 1473 (b), and 1773 K (c).

Fig. 10). It is interesting to note that until the study by Kang et al. [42], the JSPS curve (dashed-dotted grey line in Fig. 10) has been considered as the most reliable. Due to the discrepancy between their data and the commonly accepted JSPS data, Kang et al. [42] performed additional examinations for alloy containing higher Al contents in order to eliminate possible sources of error. Furthermore, they reviewed the data accounted for by JSPS and came to the conclusion that the JSPS curve was not as reliable as previously understood. The data measured at 2013 K by D'Entremont et al. [51] (represented by + in Fig. 10) show some scatter but is in the same range as the calculated solubility at 2000 K (dashed red line). In addition, the calculated solubility at 2000 K exactly reproduces the measurements by McLean et al. [50] at 1996 K (represented by ⧖ in Fig. 10) at lower Al contents.

The calculated FeO activities in the liquid phase the FeO–Al_2O_3 system at 1673 and 1873 K are shown in Fig. 11 in comparison to measurements at 1673 K by Ban-Ya et al. [70] and by Fredriksson and Seetharaman [71] at 1823 and 1873 K, respectively. As can be seen the calculated FeO activity does not change much with temperature. Furthermore, it is noted that experimental results scatter considerable and that relative large error bars are expected.

Finally, three isothermal sections in the FeO–Fe_2O_3–Al_2O_3 system at 1173, 1473 and 1773 K are calculated (Fig. 12), to demonstrate how the phase relations change with increasing temperature. The low temperature Section, 1173 K, compare well with the conclusion drawn in the review by Raghavan [72].

6. Conclusion

The current work involves thermodynamic modeling of the Al–Fe–O system by means of the CALPHAD method. Model parameters within CEF for the solid solution oxides including, spinel, corundum and halite, and the ionic liquid, have been evaluated and critically validated in respect to available experimental information. Most of the experimental data sets are well reproduced by the developed description although considerable scatter in different sets of experimental data available in the literature can be concluded.

Phase models have been carefully selected in order to facilitate construction of a multicomponent thermodynamic description of the Al–Fe–Ni–O system which requires not only the same

sublattice models for all included phases but also consistency regarding the choice of the charged reference points for the different oxides. Here, the Al–Fe–O description is made compatible with Fe–Ni–O description available in literature [7,8] and the Al–Ni–O system under development [9].

Acknowledgment

This work was financially supported at the The Pennsylvania State University by the National Energy Technology Laboratory through the RES Contract No. DE-FE00400 and DE-FE0024056. This report was prepared as an account of work sponsored by an agency of the United States Government. Neither the United States Government nor any agency thereof, nor any of their employees, makes any warranty, express or implied, or assumes any legal liability or responsibility for the accuracy, completeness, or usefulness of any information, apparatus, product, or process disclosed, or represents that its use would not infringe privately owned rights. Reference herein to any specific commercial product, process, or service by trade name, trademark, manufacturer, or otherwise does not necessarily constitute or imply its endorsement, recommendation, or favoring by the United States Government or any agency thereof. The views and opinions of authors expressed herein do not necessarily state or reflect those of the United States Government or any agency thereof.

The authors would also like to acknowledge David Alman at NETL for supportive and valuable input.

Appendix A. Supplementary material

Supplementary material associated with this article can be found in the online version at doi:10.1016/j.calphad.2015.09.004.

References

[1] N. A. Ziegler, Resistance of iron-aluminum alloys to oxidation at high temperatures, Inst. Min. Met. Engr., Inst. Met. Div. Tech. Pub., 6, 1932.
[2] C. Sykes, J.W. Bampfylde, The physical properties of iron-aluminum alloys, J. Iron Steel Inst. 130 (1934) 389–410.
[3] C.G. McKamey, J.H. DeVan, P.F. Tortorelli, V.K. Sikka, A review of recent developments in Fe3Al-based alloys, J. Mater. Res. 6 (2011) 1779–1805, http://dx.doi.org/10.1557/JMR.1991.1779.
[4] T.V. Bgasheva, E.A. Ahmetshin, E.V. Zharikov, Heat treatment enhancement of natural orange-red sapphires, Adv. Mater. Sci 12 (2012) 31–44, http://dx.doi.org/10.2478/v10077-012-0006-3.
[5] P. Winotai, S. Saiseng, T. Sudyoadsuk, Optimization of heat treatments of African green sapphires, Mod. Phys. Lett. B. 15 (2001) 873–882, http://dx.doi.org/10.1142/S0217984901002646.
[6] C.W. Bale, P. Chartrand, S.A. Degterov, G. Erikson, K. Hack, R. Ben Mahfoud, et al., FactSage thermochemical software and databases, Calphad 26 (2002) 189–228.
[7] L. Kjellqvist, M. Selleby, B. Sundman, Thermodynamic modelling of the Cr-Fe-Ni-O system, Calphad Comput. Coupling Ph. Diagr. Thermochem. 32 (2008) 577–592, http://dx.doi.org/10.1016/j.calphad.2008.04.005.
[8] R. Luoma, A Thermodynamic Analysis of the System Fe-Cr-Ni-C-O, Acta Polytech. Scand. (2002) 1–91.
[9] G. Lindwall, A. Ross, W. Zhao, L.X. Liu, H. Fang, B. Gleeson, et al., Development of a thermodynamic basis for prediction of oxide scale formation in nickel-base alloys aimed for advanced energy systems, 2015, submitted for publication.
[10] T.I. Barry, A.T. Dinsdale, J.A. Gisby, B. Hallstedt, M. Hillert, B. Jansson, et al., The compound energy model for ionic solutions with applications to solid oxides, J. Phase Equilib. 13 (1992) 459–475, http://dx.doi.org/10.1007/BF02665760.
[11] S.A. Degterov, A.D. Pelton, H.-J. Seifert, O. Fabrichnaya, J.P. Hajra, A. Navrotsky, et al., Thermodynamic Modelling of oxide and oxynitride phases, Z. Für Met 92 (2001) 533–549.
[12] M. Hillert, L. Kjellqvist, H. Mao, M. Selleby, B. Sundman, Parameters in the compound energy formalism for ionic systems, Calphad 33 (2009) 227–232, http://dx.doi.org/10.1016/j.calphad.2008.05.006.
[13] J.R. Taylor, A.T. Dinsdale, M. Hilleit, M. Selleby, A Critical assessment of tnermodynamic and phase diagram data for the Al–O system, Calphad 16 (1992) 173–179, http://dx.doi.org/10.1016/0364-5916(92)90005-I.
[14] H. Mozaffarie-Jovein, Enwincklung und Einsatz von keramischen Materialien als Wärmedammschicht fur Ni-Basis-legierungen für Temperaturen gösser als 1350 C, 2002, PhD thesis, Universität Stuttgart, Stuttgart, 2003.
[15] B. Sundman, An assessment of the Fe-O System, J. Ph. Equilib. 12 (1991) 127–140.
[16] M. Kowalski, P.J. Spencer, Thermodynamic reevaluation of the Cr-O, Fe-O and Ni-O systems, Calphad 19 (1995) 229–243.
[17] I. Ansara, A.T. Dinsdale, M.H. Rand, Thermochemical Datanase Light Metal Alloy, Cost 507 2 (1998) 20–22.
[18] M. Hillert, B. Jansson, B. Sundman, J. Ågren, A two-sublattice model for molten solutions with different tendency for ionization, Metall. Trans. A. 16 (1985) 261–266, http://dx.doi.org/10.1007/BF02815307.
[19] B. Sundman, Modification of the two-sublattice model for liquids, Calphad 15 (1991) 109–119, http://dx.doi.org/10.1016/0364-5916(91)90010-H.
[20] L. Kjellqvist, Thermodynamic description of the Fe-C-Cr-Mn-Ni-O system, PhD thesis, KTH, Royal Institute of Technology, Stockholm, 2009.
[21] B. Hallstedt, Thermodynamic Assessment of the System MgO-Al203, J. Am. Ceram. Soc. 75 (1992) 1497–1507.
[22] H. Mao, M. Selleby, B. Sundman, A re-evaluation of the liquid phases in the CaO–Al2O3 and MgO–Al2O3 systems, Calphad 28 (2004) 307–312, http://dx.doi.org/10.1016/j.calphad.2004.09.001.
[23] C. Guo, S.-L. Shang, Z. Du, P.D. Jablonski, M.C. Gao and Z.-K. Liu,Thermodynamic modeling of the CaO–CaF2-Al2O3 system, 2015, submitted for publication.
[24] L. Kjellqvist, M. Selleby, Adding C to the thermodynamic description of the Cr–Fe–Ni–O system, Calphad 33 (2009) 393–397, http://dx.doi.org/10.1016/j.calphad.2008.12.002.
[25] S.R. Bohlen, W.A. Dollase, V.J. Wall, Calibration and Applications of Spinel Equilibria in the System FeO–$Al2O_3$–SiO2, J. Pet. 27 (1986) 1143–1156, http://dx.doi.org/10.1093/petrology/27.5.1143.
[26] F. Chassagneux, A. Rousset, Preparation et etude structurale des spinelles (FeAl2 – 2z'Cr2z)O4, J. Solid State Chem. 16 (1976) 161–166, http://dx.doi.org/10.1016/0022-4596(76)90018-9.
[27] R.J. Hill, X-ray powder diffraction profile refinement of synthetic hercynite, Am. Mineral. 69 (1984) 937–942.
[28] L. Larsson, H.S.C. O'Neill, H. Annersten, Crystal chemistry of synthetic hercynite (FeAl2O4) from XRD structural refinements and Mössbauer spectroscopy, Eur. J. Miner. 6 (1994) 39–51.
[29] C.M. Yagnik, H.B. Mathur, A. Mossbauer, and X-ray diffraction study on the cation distribution in FeAl2O4, J. Phys. C Solid State Phys. 1 (1968) 469–472, http://dx.doi.org/10.1088/0022-3719/1/2/320.
[30] R.J. Harrison, S.A.T. Redfern, H.S.C. O'Neill, The temperature dependence of the cation distribution in synthetic hercynite ($FeAl_2O_4$) from in-situ neutron structure refinements, Am. Mineral. 83 (1998) 1092–1099.
[31] SGTE Substances Database version 4, 2008.
[32] H.S.C. O'Neill, A. Navrotsky, Simple spinels: crystallographic parameters, cation radii, lattice energies, and cation distribution, Am. Mineral. 68 (1983) 181–194.
[33] L. Kjellqvist, M. Selleby, B. Sundman, Thermodynamic modelling of the Cr–Fe–Ni–O system, Calphad 32 (2008) 577–592, http://dx.doi.org/10.1016/j.calphad.2008.04.005.
[34] P. Saltykov, O. Fabrichnaya, J. Golczewski, F. Aldinger, Thermodynamic modeling of oxidation of Al–Cr–Ni alloys, J. Alloys Compd. 381 (2004) 99–113, http://dx.doi.org/10.1016/j.jallcom.2004.02.053.
[35] J. Majzlan, A. Navrotsky, B.J. Evans, Thermodynamics and crystal chemistry of the hematite-corundum solid solution and the $FeAlO_3$ phase, Phys. Chem. Miner. 29 (2002) 515–526, http://dx.doi.org/10.1007/s00269-002-0261-7.
[36] A. Muan, C.L. Gee, Phase equilibrium studies in the system iron oxide-Al2O3 in air and at 1 atm. O2 pressure, J. Am. Ceram. Soc 39 (1956) 207–214.
[37] M.A. Rhamdhani, T. Hidayat, P.C. Hayes, E. Jak, Subsolidus phase equilibria of Fe-Ni-X-O (X=Mg, Al) systems in air, Metall. Mater. Trans. B 40 (2009) 25–38 10.1007/s11663-008-9213-z.
[38] O. Kubaschewski, R. Schmid-fetzer, L. Rokhlin, L. Cornish, Aluminim-iron-oxygen, in: G. Effenberg, S. Ilyenko (Eds.), Landolt-Börnstein Gr. IV Phys. Chem., Springer, 2008, pp. 1–48, http://dx.doi.org/10.1007/978-3-540-69761-9.
[39] E. Jak, P.C. Hayesa, H.G. Lee, Improved methodologies for the determination of high temperature phase equilibria, Met. Mater. 1 (1995) 1–8.
[40] R. Hansson, P.C. Hayes, E. Jak, Experimental Study Of Phase Equilibria in the Al-Fe-Zn-O system in air, Metall. Mater. Trans. B. 35 (2004).
[41] T.I. Barry, A.T. Dinsdale, J.A. Gisby, Predict. Thermochem. Ph. Equilib. Slags (1993).
[42] Y. Kang, M. Thunman, D. Sichen, T. Morohoshi, K. Mizukami, K. Morita, Aluminum deoxidation equilibrium of molten iron–aluminum alloy with wide aluminum composition range at 1 873 K, ISIJ Int. 49 (2009) 1483–1489, http://dx.doi.org/10.2355/isijinternational.49.1483.
[43] Japan Society for the Promotion of Science, Recommended Values of Equilibrium Constants for the Reactions in Steelmaking, 1984.
[44] H. Itoh, M. Hino, S. Ban-Ya, Assessment of Al Deoxidation Equilibrium in Liquid Iron, J. Iron Steel Inst. Japan 83 (1997) 773–778.
[45] D.C. Hilty, W. Crafts, The solubility of oxygen in liquid iron containing aluminum, Trans. AIME 188 (1950) 181–204.
[46] R. J. Fruehan, Activities in liquid Fe – Al – O and Fe – Ti – O alloys, Metall. Trans. 1 (n.d.), 3403–3410. http://dx.doi.org/10.1007/BF03037871.
[47] H. Schenk, E. Steinmetz, K.K. Mehta, Equilibria and Kinetics of the Separation

of Alumina from Fe-O-Al System at 1600 C, Arch. Für Das Eisenhüttenwes 41 (1970) 131–138.
[48] L.E. Rohde, A. Choudhury, M. Wahlster, New Investigations on the Al-O Equilibrium in Iron Melts, Arch. Für Das Eisenhüttenwes 42 (1971) 165–174.
[49] D. Janke, W. Fischer, Deoxidation Equilibria of Ti, Al and Zr in Fe Melts at 1600 C, Arch. Für Das Eisenhüttenwes 47 (1976) 195–198.
[50] A. McLean, B. H.B., Experimental study of reaction Al2O3 + 3H2 = 3H2O + 2Al, J. Iron Steel Inst. Japan 203 (1965) 123.
[51] J.C. D'Entremont, D.L. Guernsey, J. Chipman, No Title, Trans. Met. Soc. AIME 227 (1963) 14.
[52] A.C. Turnock, H.P. Eugster, Fe-Al Oxides: Phase Relationships, J. Petrol 3 (1962) 533–565.
[53] A. Feenstra, An Experimental Study of Fe-Al Solubility in the System Corundum-Hematite up to 40 kbar and 1300 C, J. Petrol 46 (2005) 1881–1892, http://dx.doi.org/10.1093/petrology/egi038.
[54] V.W. Oelsen, G. Heynert, Die Reaktionen zwischen Eisen-Mangan-Schmelzen und den Schmelzen ihrer Aluminate, Arch. Für Das Eisenhüttenwes (1955) 567–575.
[55] V.W.A. Fischer, A. Hoffmann, Das Zustandsschaubild Eisenoxydul-Aluminiumoxyd, Arch, Für Das Eisenhüttenwes (1956) 3–346.
[56] L.M. Atlas, W.K. Sumida, Solidus, Subsolidus, and Subdissociation Phase Equilibria in the System Fe-Al-O, J. Am. Chem. Soc. 41 (1958) 150–160.
[57] F.A. Elrefaie, W.W. Smeltzer, Thermodynamics of the System Iron- Aluminum-Oxygen between 1073 K and 1573 K, Metall. Mater. Trans. A: Phys. Metall. Mater. Sci. 14 (1983) 85–93.
[58] S. Klemme, J.C. van Miltenburg, Thermodynamic properties of hercynite (FeAl2O4) based on adiabatic calorimetry at low, Am. Mineral. 88 (2003) 68–72.
[59] B.G. King, Heat capacities at low temperatures and entropies of five spinel minerals, J. Phys. Chem. 60 (1955) 410–412.
[60] N.G. Schmahl, H. Dillenburg, Gleichgewichtsuntersuchungen an eisenoxidhaltigen Mischphasen innerhalb der Dreistoffsysteme Fe-Al-O, Fe-Cr-0 und Fe-V-O, Zeitschrift Für Phys. Chemie 65 (1969) 119–138.
[61] A. Petric, K.T. Jacob, C.B. Alcock, Thermodynamic Properties of Fe304-FeA1204 Spinel Solid Solutions, J. Am. Ceram. Soc. 64 (1981) 632–639.
[62] A. Muan, On the stability of the phase Fe2O3.Al2O3, Am. J. Sci. 256 (1958) 413–422.
[63] A.D. Polli, F.R. Lange, C.G. Levi, Crystallization behavior and microstructural evolution of (Al,Fe)2O3 synthesized from liquid precursors, J. Am. Ceram. Soc. (1996).
[64] K.J.D. Mackenzie, R.M. Berezowski, Thermal and Mössbauer studies of iron-containing hydrous silicates, V. Berthierine, Thermochim. Acta. 74 (1984) 291–312, http://dx.doi.org/10.1016/0040-6031(84)80030-1.
[65] C. Donnet, Microstructure and thermochemistry sintered alumina of ion-implanted, Appl. Surf. Sci. 68 (1993) 19–33.
[66] F.Y. Galakhov, Alumina regions of ternary aluminosilicate systems communication 1. The systems FeO-Al2O3-SiO2 and MnO-Al2O3-SiO2, Bull. Acad. Sci. USSR Div. Chem. Sci. 6 (1958) 539–545, http://dx.doi.org/10.1007/BF01169268.
[67] I.A. Novokhatskii, B.F. Belov, A.V. Gorokh, A.A. Savinskaya, The Phase Diagram for the System Ferrous Oxide-Alumina, Russ. J. Phys. Chem. 39 (1965) 1498–1499.
[68] C.E. Meyers, T.O. Mason, W.T. Petuskey, J.W. Halloran, H.K. Bowen, Phase Equilibria in the System Fe-Al-O, J. Am. Ceram. Soc. 63 (1980) 659–663, http://dx.doi.org/10.1111/j.1151-2916.1980.tb09856.x.
[69] B.D. Roiter, Phase Equilibria in the Spinel Region of the System FeO-Fe2O3-Al2O3, J. Am. Ceram. Soc. 47 (1964) 509–511, http://dx.doi.org/10.1111/j.1151-2916.1964.tb13799.x.
[70] S. Ban-Ya, K. Chiba, Y. Hikosaka, Thermodynamics of FeO-MxOy(MxOy= CaO, SiO2, TiO2 and Al2O3) binary melts in equilibrium with solid iron, J. Iron Steel Inst. Japan 66 (1980) 1484–1493.
[71] P. Fredriksson, S. Seetharaman, Thermodynamic studies of FeO-containing slags and their impact on ladle refining process, in: Int. Conf. Molten Slags Fluxes Salts. South African Inst. Min. Metall., 2004: pp. 285–292.
[72] V. Raghavan, The Al-Fe-O (Aluminum-Iron-Oxygen) System, Phase Diagrams of Ternary Iron Alloys. Part 5: Ternary Systems Containing Iron and Oxygen, Indian Inst. Met (1989) 10–28.
[73] T.J.B. Holland, R. Powell, An enlarged and updated internally consistent thermodynamic dataset with uncertainties and correlations: the system K2O-Na2O-CaO-MgO-MnO-FeO-Fe2O3-Al2O3-TiO2-SiO2-C-H2-O2, J. Metamorph. Geol. 8 (1990) 89–124, http://dx.doi.org/10.1111/j.1525-1314.1985.tb00325.x.
[74] R.G. Berman, Thermobarometry using multi-equilibrium calculations: a new technique, with petrological applications, Can. Mineral. 29 (1991) 833–855.
[75] R.O. Sack, M.S. Ghiorso, An internally consistent model for the thermodynamic properties of Fe-Mg-titanomagnetite-aluminate spinels, Contrib. Mineral. Petrol. 106 (1991) 474–505, http://dx.doi.org/10.1007/BF00321989.
[76] R.G. Berman, L.Y. Aranovich, Optimized standard state and solution properties of minerals, Contrib. Mineral. Petrol. 126 (1996) 1–24, http://dx.doi.org/10.1007/s004100050232.
[77] M. Gottschalk, Internally consistent thermodynamic data for rock-forming minerals in the system SiO2-TiO2-Al2O3-Fe2O3-CaO-MgO-FeO-K2O-Na2O-H2O-CO2, Eur. J. Mineral. 9 (1996) 175–223, http://dx.doi.org/10.1127/ejm/9/1/0175.
[78] N.D. Chatterjee, R. Krüger, G. Haller, W. Olbricht, The Bayesian approach to an internally consistent thermodynamic database: theory, database, and generation of phase diagrams, Contrib. Mineral. Petrol. 133 (1998) 149–168, http://dx.doi.org/10.1007/s004100050444.
[79] T.J.B. Holland, R. Powell, An internally consistent thermodynamic data set for phases of petrological interest, J. Metamorph. Geol. 16 (1998) 309–343, http://dx.doi.org/10.1111/j.1525-1314.1998.00140.x.
[80] R.J. Fruehan, M. Lean, Activities in Liquid Fe-AI-O and Fe-Ti-O Alloys 1 (1970) 3403–3410.

OPEN ACCESS
IOP Publishing | National Institute for Materials Science
Science and Technology of Advanced Materials
Sci. Technol. Adv. Mater. **16** (2015) 055001 (12pp)
doi:10.1088/1468-6996/16/5/055001

Experimental study and thermodynamic modeling of the Al–Co–Cr–Ni system

Thomas Gheno[1], Xuan L Liu[2], Greta Lindwall[2], Zi-Kui Liu[2] and Brian Gleeson[1]

[1] Department of Mechanical Engineering and Materials Science, University of Pittsburgh, Pittsburgh, PA 15261, USA
[2] Department of Materials Science and Engineering, The Pennsylvania State University, University Park, PA 16802, USA

E-mail: thg14@pitt.edu

Received 14 May 2015, revised 23 July 2015
Accepted for publication 5 August 2015
Published 21 September 2015

Abstract

A thermodynamic database for the Al–Co–Cr–Ni system is built via the Calphad method by extrapolating re-assessed ternary subsystems. A minimum number of quaternary parameters are included, which are optimized using experimental phase equilibrium data obtained by electron probe micro-analysis and x-ray diffraction analysis of NiCoCrAlY alloys spanning a wide compositional range, after annealing at 900 °C, 1100 °C and 1200 °C, and water quenching. These temperatures are relevant to oxidation and corrosion resistant MCrAlY coatings, where M corresponds to some combination of nickel and cobalt. Comparisons of calculated and measured phase compositions show excellent agreement for the β–γ equilibrium, and good agreement for three-phase β–γ–σ and β–γ–α equilibria. An extensive comparison with existing Ni-base databases (TCNI6, TTNI8, NIST) is presented in terms of phase compositions.

S Online supplementary data available from stacks.iop.org/STAM/16/055001/mmedia

Keywords: bondcoat, phase compositions, phase equilibrium, Calphad, MCrAlY

1. Introduction

Nickel- and cobalt-base alloys are widely used in high temperature structural applications, such as aero, marine and land-based gas turbines. Coherent precipitation of geometrically close-packed γ' ($L1_2$, ordered cubic based on Ni_3Al) in the γ (A1, fcc solid solution based on Ni) matrix provides outstanding high temperature strength to Ni-base superalloys, which are found in high pressure turbine disks and blades, where the thermo-mechanical load is most demanding [1, 2]. However, the continuous increase in operating temperatures and in the chemically aggressive character of combustion environments has prompted the development of oxidation and corrosion resistant coatings [3–5]. Two main types of materials are currently in use: diffusion coatings based on β-NiAl (B2, ordered cubic), and overlay MCrAlY (M = Ni, Co or both) coatings based on a β–γ microstructure.

Conventional Co-base superalloys rely on carbide and solid-solution strengthening and have been confined to moderately high temperature components (700 °C–900 °C) such as turbine vanes [6]. The recent discovery of a stable γ' Co_3(Al, W) compound [7] has inspired the development of novel high strength Co-base alloys [8–12]. Their high melting point makes them promising candidates for higher service temperatures and, ultimately, increased efficiencies. However, their poor oxidation resistance [13, 14] requires the use of coatings, and MCrAlYs are considered for this purpose [15].

As modern MCrAlYs often contain significant amounts of both nickel and cobalt, a sound description of the Al–Co–Cr–Ni system's thermodynamic properties is desired to ensure an optimal design of these coatings and control of their microstructural evolutions. Yet, while thermodynamic models and databases exist which cover this quaternary system in principle, evaluations against experimental data are scarce,

mostly qualitative and partial at best; no thorough assessment has been openly reported.

Common MCrAlY coatings have a primary β–γ microstructure at high temperatures, above about 1100 °C. At temperatures typical of service conditions (800 °C–1000 °C), the coatings may also form γ', σ or α, depending on their specific composition (σ: Frank–Kasper based on CoCr; α: A2, bcc solid solution based on Cr). Achar *et al* [16] used the TTNI database from Thermotech (version not specified) to calculate phase equilibria for a large number of NiCoCrAl alloys in the temperature range 950 °C–1050 °C. However, the comparison with experimental data was limited to the identification of the phases formed, and phase compositions were not reported. The authors concluded on a good agreement between experimental and predicted phase constitutions, except for cobalt contents in excess of 20 wt.%. Similarly, Ma and Schoenung [17] reviewed published reports of experimental phase constitutions and discussed phase equilibria in the quaternary system predicted by the TTNI7 database, but they did not evaluate the database against experimental data quantitatively. Brož *et al* [18, 19] reported experimental phase compositions together with phase equilibria calculated using a developmental database, with a focus on the γ–γ' equilibrium. However, they did not publish the details of their thermodynamic modeling.

Several multi-component phase equilibrium calculations including Al, Co, Cr and Ni have been recently published in relation with the development of 'high entropy alloys' [20] based on AlCoCrCuFeNi compositions. Again these studies (see for example [21, 22]) report qualitative comparisons of experimental versus calculated phase constitutions using commercial databases, which does not allow these databases to be evaluated with a satisfactory accuracy. Furthermore, the thermodynamic models and parameters underlying these databases are not openly available, and cannot therefore be examined.

The present paper reports a new, developmental Al–Co–Cr–Ni database built by the Calphad method from re-assessed ternary subsystems [23]. The database is provided in a non-encrypted format. A quantitative evaluation of this and existing databases is provided, based on new experimental data obtained from NiCoCrAlY alloys in the temperature range 900 °C–1200 °C. A variety of compositions were used to cover a large part of the quaternary system. In the future, our database will be updated to include reactive elements such as yttrium or hafnium.

2. Experimental procedures

Ingots of nominal compositions given in table 1 were prepared by argon arc melting, drop cast into 10 mm diameter rods, and homogeneized for 6 h at 1200 °C and 48 h at 1150 °C in vacuum at the Materials Preparation Center of Ames Laboratory[3]. Specimens approximately 1 mm thick were vacuum-encapsulated in quartz capsules, further homogenized 48 h at 1150 °C in a tube furnace, and slowly brought to equilibration temperature. Equilibration treatments were conducted at 900 °C, 1100 °C and 1200 °C for 525, 100 and 50 h, respectively, followed by water quenching to retain the equilibrium microstructures. Phase constitutions were studied by x-ray diffraction (XRD) with a PANalytical Empyrean instrument, using a Co radiation source ($K\alpha_1 = 1.789$ Å).

Polished sections of the heat-treated alloys were prepared by standard metallographic procedures. Phase compositions were determined by electron probe micro-analysis (EPMA) using a JEOL JXA-8530F field emission gun instrument. For each element, measured intensities were converted to concentrations by interpolation via a calibration curve built using a series of standards of known compositions (chemical analysis by inductively coupled plasma mass spectrometry). The probe size used during measurements was about 1 μm, and the alloy microstructures were sufficiently coarse for each phase to be analyzed individually.

[3] Materials Preparation Center, Ames Laboratory USDOE, Ames, IA, USA.

Table 1. Nominal compositions (at.%) of the NiCoCrAlY alloys used for experimental study. All alloys contained an additional 0.1 at. % Y.

#	Al	Cr	Co	Ni
A1	24	15	19	42
A2	26	20	18	36
A3	18	28	18	36
A4	12	30	30	28
A5	16	33	30	21
A6	24	10	19	47
A7	14	16	26	44

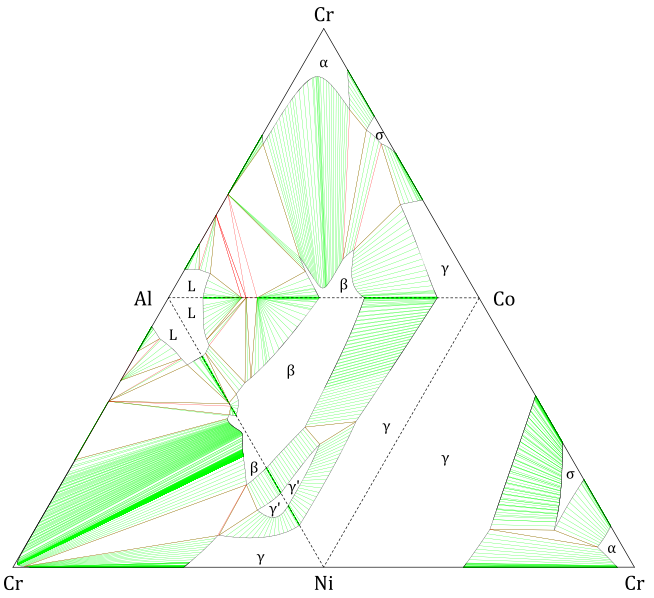

Figure 1. Isothermal sections (1000 °C) of the four ternary subsystems [23] used in the present work, combined to represent the four faces of the isothermal Al–Co–Cr–Ni quaternary tetrahedron.

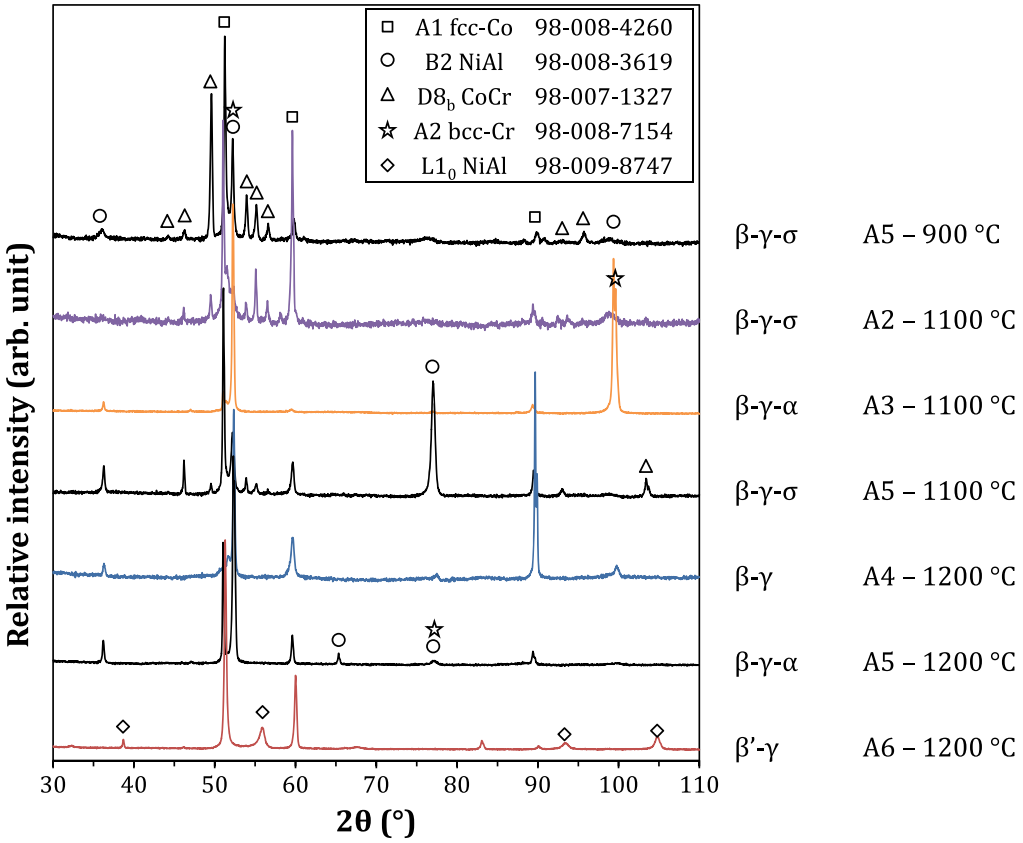

Figure 2. XRD analysis of phase constitution of selected alloys. The insert indicates ICSD card numbers.

Table 2. Phase compositions of the NiCoCrAlY alloys measured by EPMA (at.%). Yttride compositions are not included. γ' was formed in A6 and A7 at 900 °C but was too finely dispersed to be analyzed. Alloy A5 at 1100 °C was mainly β–γ–σ, but σ was locally replaced by α (see text); both compositions are included here.

T (°C)	#	β				γ				σ				α			
		Al	Cr	Co	Ni	Al	Cr	Co	Ni	Al	Cr	Co	Ni	Al	Cr	Co	Ni
900	A1	35.1	5.1	11.2	48.5	7.2	30.5	29.2	33.2								
	A2	36.1	6.0	12.8	45.1	6.1	34.2	32.3	27.5	1.4	59.7	28.2	10.8				
	A3	34.9	6.2	9.1	49.9	7.0	32.7	25.2	35.1	1.2	61.2	23.4	14.2				
	A4	35.9	6.5	14.0	43.6	6.1	33.5	34.0	26.3	1.4	59.0	28.9	10.7				
	A5	36.6	7.0	19.0	37.5	5.9	33.7	40.5	20.0	1.7	57.8	32.6	7.9				
	A6	33.6	3.4	11.6	51.4	9.8	20.3	29.6	40.3								
	A7	33.4	3.9	11.6	51.0	9.8	20.6	29.4	40.2								
1100	A1	32.9	8.1	13.9	45.1	9.8	28.0	27.3	34.9								
	A2	33.6	11.4	14.6	40.4	8.3	36.4	27.2	28.1	3.3	58.2	24.5	13.9				
	A3	33.0	11.6	11.5	43.9	8.7	35.9	22.4	33.0					4.6	62.1	17.8	15.5
	A4	32.7	9.8	17.7	39.7	9.2	31.0	31.9	27.9								
	A5	32.7	13.0	22.5	31.8	8.2	36.5	35.7	19.6	3.6	56.9	29.8	9.7	7.0	53.5	28.0	11.4
	A6	31.2	5.1	13.9	49.9	12.8	17.3	26.2	43.8								
	A7	31.2	5.5	14.0	49.4	12.8	17.5	26.2	43.5								
1200	A1	30.4	9.7	15.0	44.9	11.7	26.0	25.2	37.1								
	A3	29.4	15.7	13.1	41.9	10.1	35.7	21.0	33.2					9.0	49.3	18.6	23.1
	A4	30.5	12.2	19.6	37.7	10.8	29.6	30.9	28.7								
	A5	27.7	19.1	24.8	28.4	9.8	35.1	34.1	21.0					11.3	43.0	29.5	16.2
	A6	29.9	6.0	15.0	49.1	14.0	16.3	25.0	44.8								
	A7	30.0	6.6	15.3	48.2	13.8	16.8	25.4	44.0								

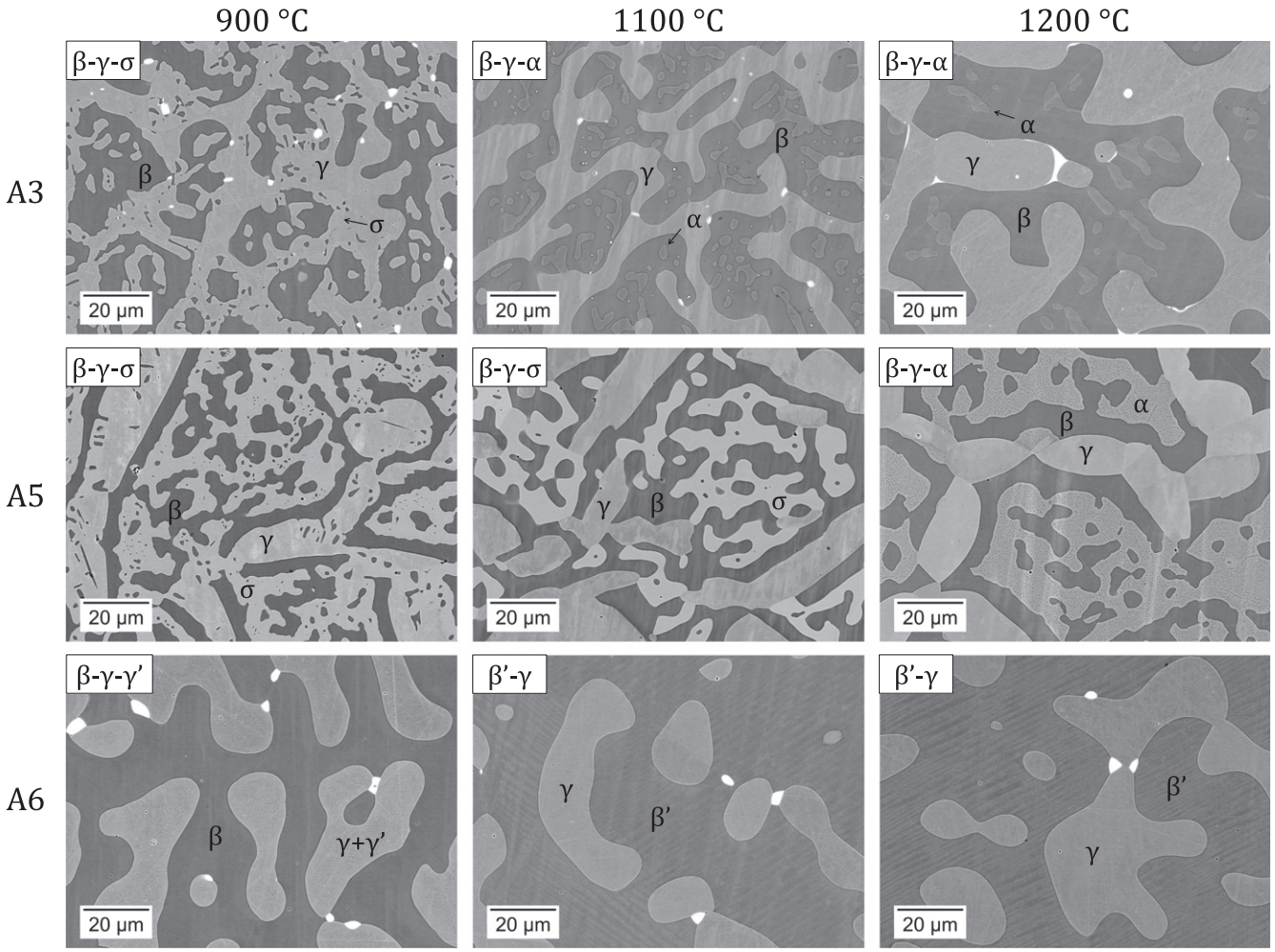

Figure 3. Microstructure of alloys A3, A5 and A6 equilibrated at 900 °C, 1100 °C and 1200 °C. Bright precipitates are yttrium-rich compounds.

3. Calphad thermodynamic models

The Al–Co–Cr, Al–Co–Ni and Co–Cr–Ni ternary systems remodeled in [23] were combined with the Al–Cr–Ni description by Dupin *et al* [24] to produce a quaternary Al–Co–Cr–Ni extrapolation. Discrepancies in higher order systems often stem from inappropriate parameter choices in lower order systems [25]. Indeed, two distinct sets of optimized parameters may appear to describe a system equally well, but give different results when extrapolated to a higher order system. Therefore the ternary models of [23] were developed using both thermochemical data predicted from first-principles calculations [26] and quaternary experimental data from the present paper, i.e., the optimized ternary parameters were systematically extrapolated to the quaternary system to ensure consistency. This was done using the PARROT module [27] within Thermo-Calc [28, 29].

Isothermal sections of the four ternary subsystems (1000 °C) are combined in figure 1 to represent the four faces of the isothermal quaternary tetrahedron. To extrapolate γ' from Al–Cr–Ni and Al–Co–Ni into the quaternary system, interaction parameters in the quaternary system based on bond energies U for γ'-$L1_2$ were introduced: ${}^0L^{\gamma'}_{\mathrm{Al,Co,Cr:Ni}}$, ${}^0L^{\gamma'}_{\mathrm{Al,Co,Ni:Cr}}$, ${}^0L^{\gamma'}_{\mathrm{Al,Cr,Ni:Co}}$, ${}^0L^{\gamma'}_{\mathrm{Co,Cr,Ni:Al}}$. Details on the implementation of such parameters are given in [30, 31]. A quaternary model first obtained on this basis reproduced experimental phase stabilities and compositions well. However, calculated σ compositions had an excess of Co and Cr at the expense of Al and Ni, especially at 900 °C. Given the good agreement seen in the ternary systems containing σ, Al–Co–Cr and Co–Cr–Ni [23], the discrepancy was attributed to the lack of a metastable σ in the adopted Al–Cr–Ni model. However, alteration of binary and ternary parameters in Al–Cr–Ni for σ would make this phase stable, which is in fact not observed in either Cr–Ni or Al–Cr–Ni [24, 32]. A reciprocal interaction parameter (${}^0L^{\sigma}_{\mathrm{Co,Ni:Al,Cr:Cr}}$) was therefore introduced to yield greater Al and Ni contents in σ without stabilizing it in Al–Cr–Ni. An additional metastable binary β interaction parameter (${}^0L^{\beta}_{\mathrm{Co,Ni:Cr}}$) in the Co–Cr–Ni ternary was included to improve phase compositions for Co and Cr in β. Due to the metastability of γ' in ternaries containing Co–Cr (Al–Co–Cr and Co–Cr–Ni), the ordering contribution from Co–Cr, U_{CoCr}, was optimized using quaternary data where γ' is stable, and DFT results from [23]. With these two excess parameters and one ordering parameter, a satisfactory description of the quaternary

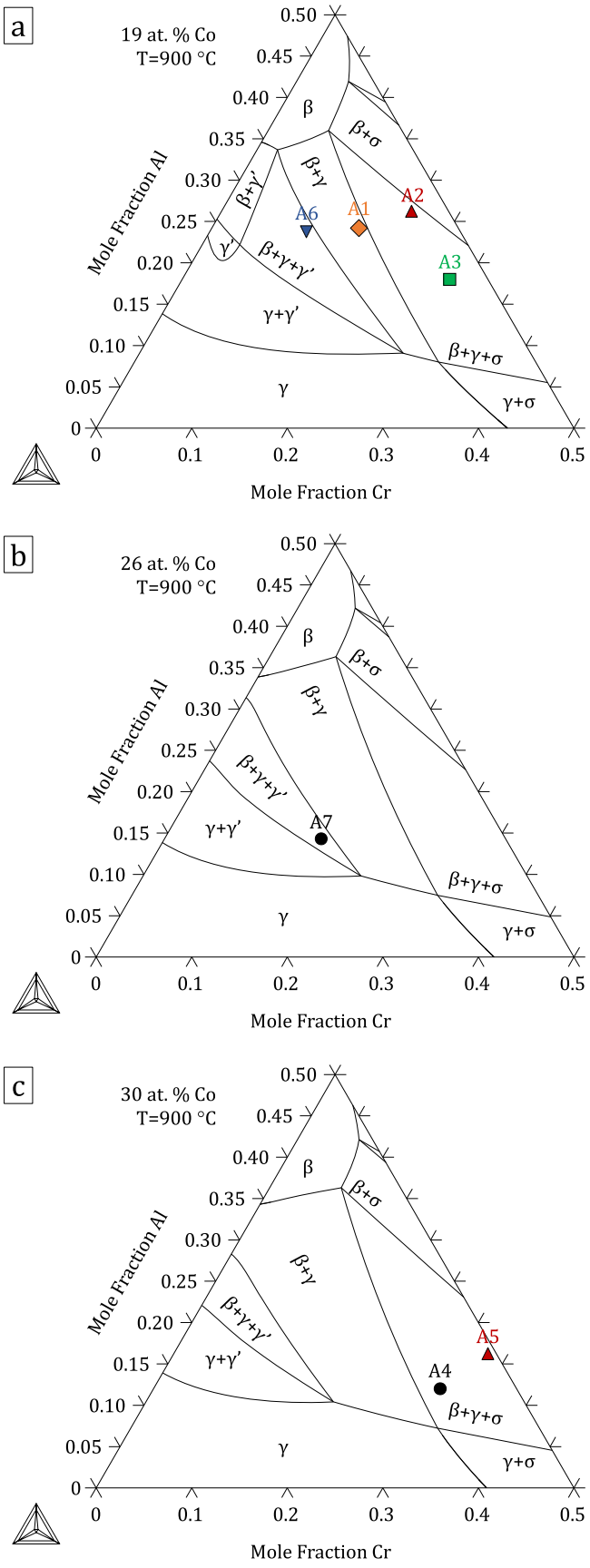

Figure 4. Isothermal (900 °C), isoplethal Al–Co–Cr–Ni sections at (a) 19, (b) 26 and (c) 30 at.% Co. Nominal compositions of the alloys used in this study are indicated. Note that some alloys shown in (a) are not strictly in the plane of the calculation as their Co contents are slightly different from 19 at.%.

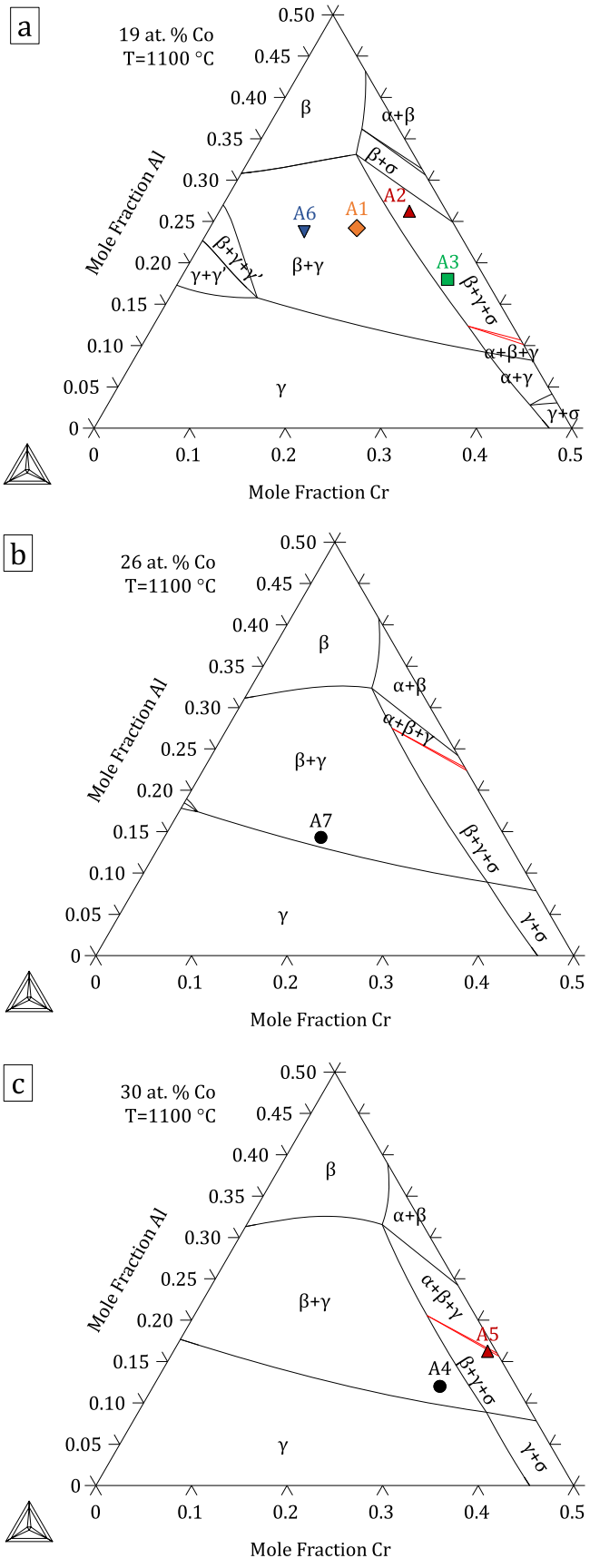

Figure 5. Isothermal (1100 °C), isoplethal Al–Co–Cr–Ni sections at (a) 19, (b) 26 and (c) 30 at.% Co. Nominal compositions of the alloys used in this study are indicated. Note that some alloys shown in (a) are not strictly in the plane of the calculation as their Co contents are slightly different from 19 at.%.

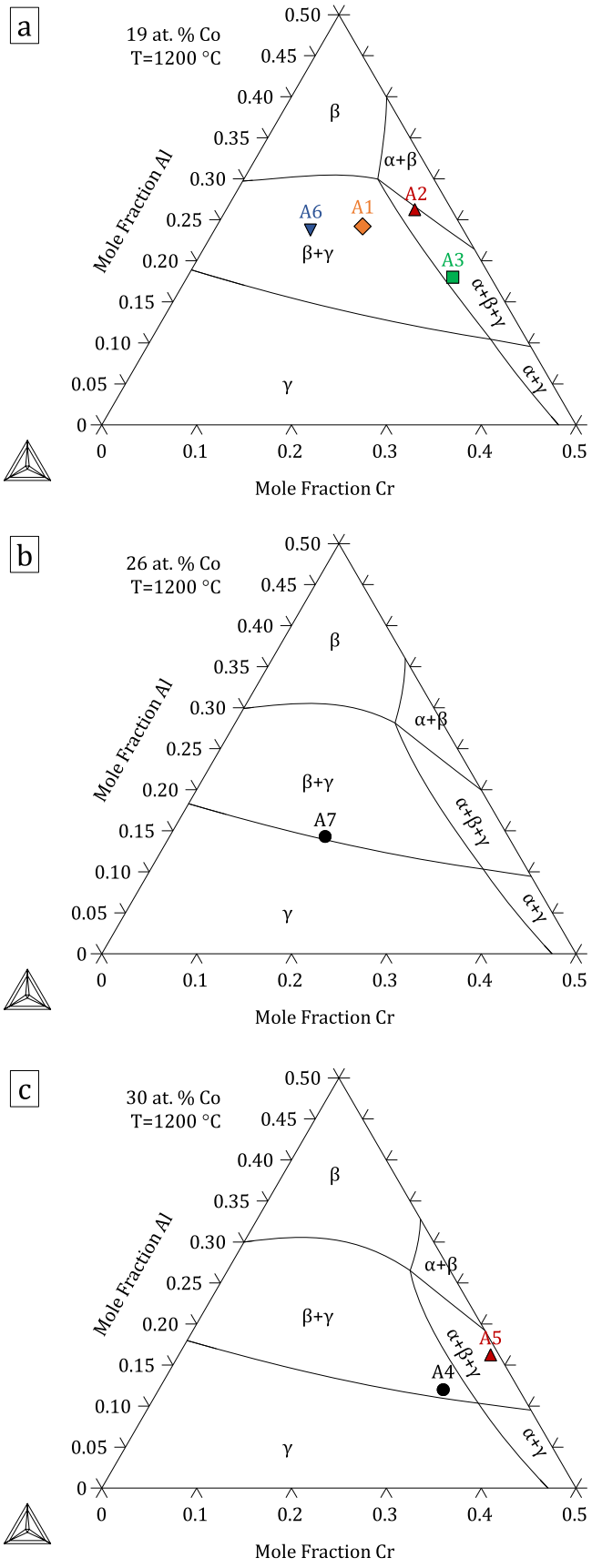

Figure 6. Isothermal (1200 °C), isoplethal Al–Co–Cr–Ni sections at (a) 19, (b) 26 and (c) 30 at.% Co. Nominal compositions of the alloys used in this study are indicated. Note that some alloys shown in (a) are not strictly in the plane of the calculation as their Co contents are slightly different from 19 at.%.

system was obtained. The PARROT module within Thermo-Calc was used to assess these parameters using phase equilibrium data from the present paper, with additional data from [19, 33] for the γ–γ' equilibrium.

4. Results and discussion

4.1. Experimental results

Alloy phase constitutions were determined through a combination of XRD (selected spectra shown in figure 2), phase composition analysis (EPMA results given in table 2), and examination of the microstructures (selected micrographs shown in figure 3). In figure 3, the dark matrix is β, the gray phases are α, γ and σ (by increasing brightness), and the bright precipitates are Y-containing intermetallics. All alloys exhibit a primary β–γ microstructure typical of MCrAlY materials.

At 1200 °C, alloys with high chromium contents (A3, A5) produce α in addition to β and γ. The α and β phases both have a cubic structure, and their XRD signals could not be resolved with the instrument available. However, the phases exhibit very distinct compositions (table 2). In Cr-lean alloys (A6, A7), NiAl martensite, noted β', is found instead of β. Martensite is identified by XRD from its $L1_0$ tetragonal structure (see alloy A6 in figure 2), and presents a typical [34] twinned microstructure (figure 3). Its presence does not affect phase equilibrium since it is formed by a diffusionless transformation during cooling. At 1100 °C, the Cr-rich phase is either α or σ, depending on alloy composition. The two phases differ in their composition, with σ dissolving more Co and slightly less Al than α. Further, XRD clearly identifies the $D8_b$ tetragonal structure of σ (see alloys A2 and A5 versus A3 in figure 2). The σ phase is stabilized at the expense of α in alloys with higher Co (A4, A5 versus A3) or lower Cr contents (A2 versus A3). In the case of alloy A5, the σ phase is locally replaced by α (i.e., there existed regions with a β–γ–α equilibrium); this is due to the fact that the $\sigma \rightarrow \alpha$ transition temperature is very close to 1100 °C, as discussed in section 4.2. The $\beta \rightarrow \beta'$ transformation is observed for Cr-lean alloys equilibrated at 1100 °C, but not at 900 °C (see alloy A6 in figure 3). At 900 °C, the Cr-rich alloys precipitate σ, and no α is found. Precipitation of γ' in γ is observed for the Cr-lean alloys (A6, A7). The presence of γ' could not be confirmed by XRD because its diffraction pattern was not resolved from that of γ with the instrument available, and γ' precipitates were too small for their composition to be measured accurately by EPMA. Qualitatively, the precipitates were found to have less Cr and more Al than the matrix, and the cuboidal microstructure is typical of γ–γ' equilibria.

If yttrium is disregarded and we consider the quaternary Al–Co–Cr–Ni system, three-phase equilibria are univariant, which explains the slight variations of the γ–β–α or γ–β–σ equilibria in the different alloys. At 1200 °C, the difference between the compositions of α and β reflects a significant miscibility gap. This is to be compared with our previous work [35], which showed that in the Al–Co–Cr system the α–β (A2–B2) miscibility gap was suppressed and replaced by an

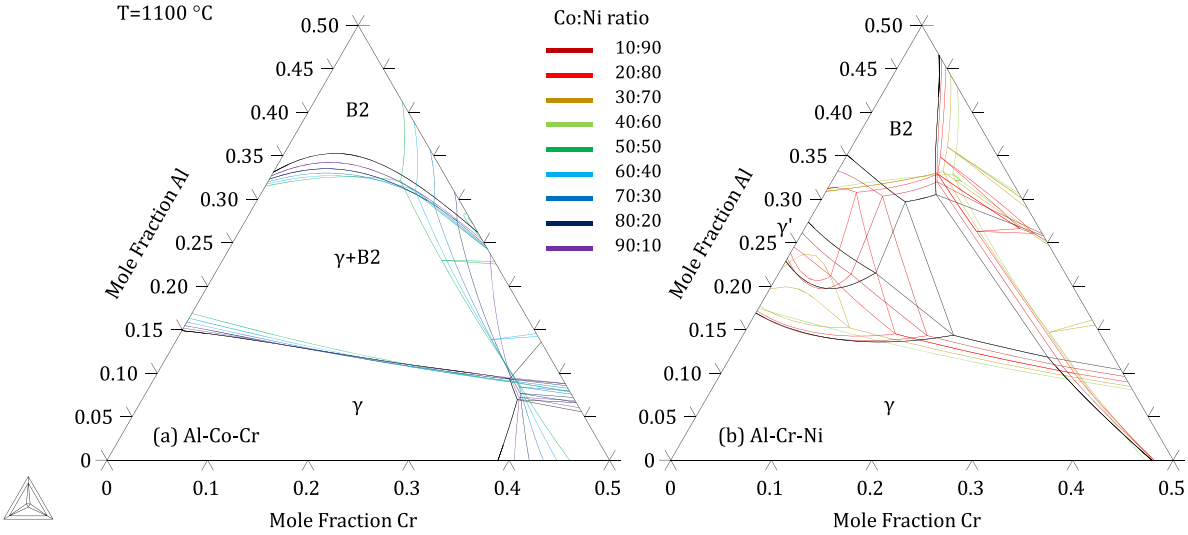

Figure 7. Isothermal (1100 °C) sections of the Al–Co–Cr–Ni system plotted for constant Co:Ni ratios (see color scale inserted). Cobalt-rich and Ni-rich sections are superimposed on the (a) Al–Co–Cr and (b) Al–Cr–Ni diagram, respectively. A combination of the two plots describes the full quaternary system as a function of the Co:Ni ratio.

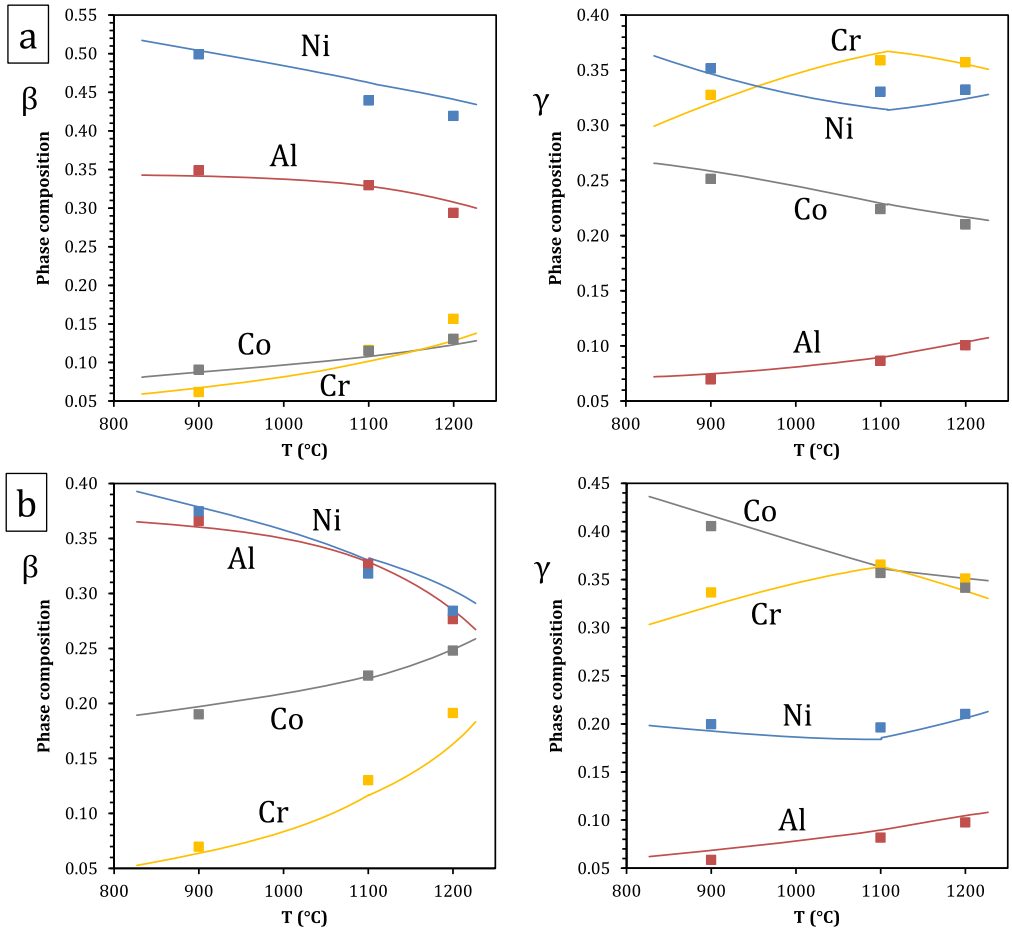

Figure 8. Composition of the β and γ phases of alloys (a) A3 and (b) A5, calculated and measured by EPMA.

order–disorder transition between 1100 °C and 1200 °C. In contrast, Dupin *et al* [24] showed that the mutual solubilities of α and β remained very limited up to melting in the NiAl–Cr pseudo-binary system. Thus in terms of the α–β phase relationship, the Al–Co–Cr–Ni system exhibits an intermediate behavior between those of Al–Co–Cr and Al–Cr–Ni. The tendency to a disordering of the β structure with increasing temperature is observed here as the Al and Cr

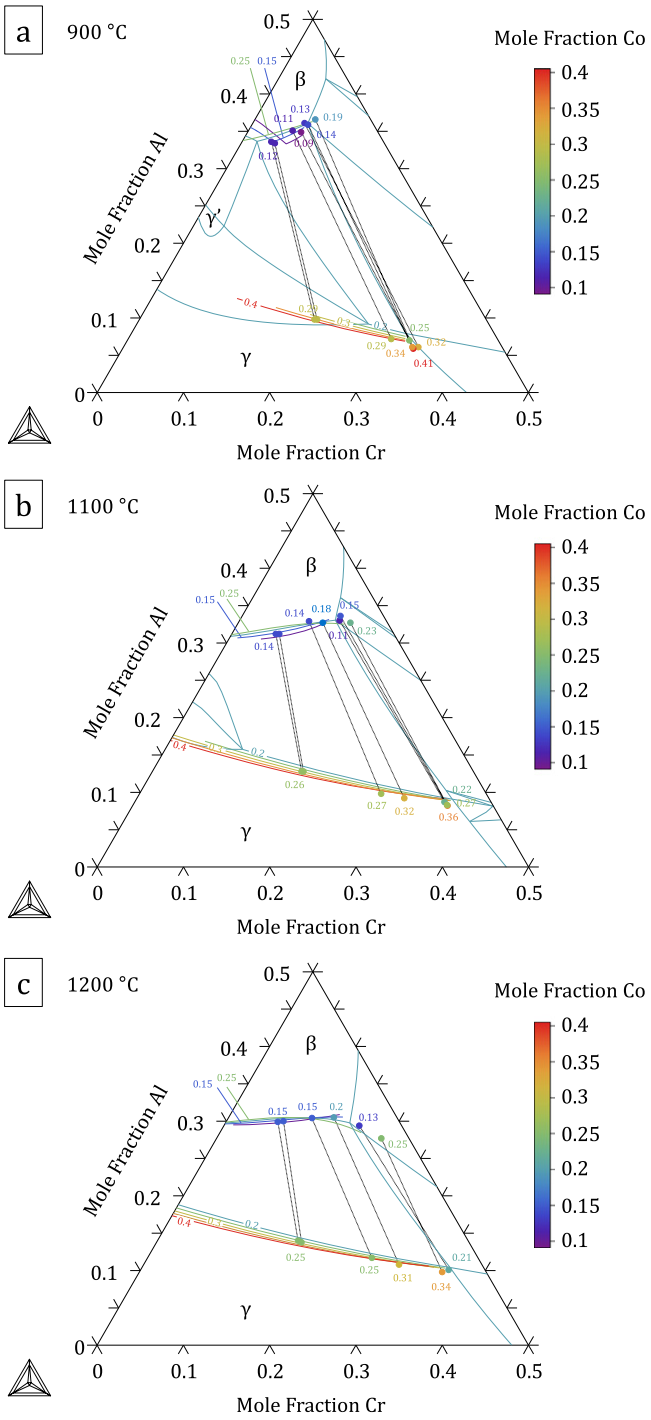

Figure 9. Isothermal, Co-isoplethal sections of the Al–Co–Cr–Ni system at (a) 900 °C, (b) 1100 °C and (c) 1200 °C. The $\beta/\beta+\gamma$ and $\beta+\gamma/\gamma$ phase boundaries are represented for various Co contents using the indicated color code, forming a Co contour map. Experimental β and γ compositions are given, where the same color code has been applied to the end points, and measured Co concentrations are also indicated. Tie-lines projected on a plane of constant Co are also added to indicate the compositions in equilibrium.

contents of the β phase show large variations at 1200 °C (table 2). Higher Co contents favor an increase of Cr solubility and decrease of Al content in β, as could be expected from the behavior of the Al–Cr–Ni and Al–Co–Cr systems. As the temperature decreases to 1100 and 900 °C, the range of Al and Cr concentrations in β is restricted.

In terms of alloy microstructures, α precipitation mainly occurred within β, as expected considering the similar crystal structure of these two cubic phases. Precipitation of σ is seen in figure 3 to have occurred both from α, reflecting the replacement of α by σ in the three-phase equilibrium as the temperature decreases, and at the expense of γ at the β–γ interface, driven by the decrease of Cr solubility in γ. In the latter case, heterogeneous nucleation reflects the lack of compatibility between the tetragonal σ and the other phases of the system. In contrast, γ' is exclusively found within γ. Coherent precipitation is typically observed for these two cubic phases.

4.2. Calphad modeling results

The thermodynamic parameters resulting from the present assessment, given in the supplementary material: File S1, were built into a database included in File S2. Figures 4–6 show calculated quaternary isoplethal, isothermal sections at three cobalt contents (19, 26, and 30 at.%) and temperatures (900 °C, 1100 °C, and 1200 °C) with nominal alloy compositions overlaid. Correct phase constitutions are predicted for all alloys based on their nominal compositions, except in one case: at 1100 °C, alloy A3 is predicted to be in a β–γ–σ field, while it was found to form α and not σ (figure 2). For this particular composition, the $\alpha \rightarrow \sigma$ transition temperature is calculated to be 1109 °C, quite close to 1100 °C. In the case of alloys A6 and A7 at 900 °C, γ' was predicted to form, in agreement with our observations (see A6 in figure 3). Figure 7 shows isothermal (1100 °C) sections at constant Co:Ni ratios from 10:90 to 90:10, superimposed on the Al–Co–Cr and Al–Cr–Ni diagrams. The destabilizing effect of cobalt on γ' is clearly illustrated in figure 7(b), where the γ' region is seen to shrink with increasing Co:Ni ratio.

A comparison of predicted and measured phase compositions is provided in figures 8–10. The calculated β–γ equilibria are in very good agreement with the experimental data. This is illustrated in figure 8 where phase compositions calculated on the basis of nominal alloy compositions are plotted as a function of temperature for alloys A3 and A5, together with experimental data. In figure 9, isothermal $\beta/\beta+\gamma$ and $\beta+\gamma/\gamma$ phase boundaries from isopleths are plotted with colors corresponding to constant cobalt contents, thus forming a contour map. Experimental β–γ tie-lines are superimposed, where the same color code has been applied to the end-points, and measured x_{Co} values are also indicated. All alloys are represented, but the α and σ phases were omitted. The database is evaluated by comparing the color (i.e., cobalt content) of a datapoint with that of the surrounding phase boundaries. Again a very good agreement is observed: even though the Al and Cr solubilities in β and γ show relatively limited variations with cobalt content in the compositional space studied, the trends observed experimentally are well reproduced by the calculation.

In the case of σ and α, the agreement is slightly less good, as shown in figure 10, where phase compositions are

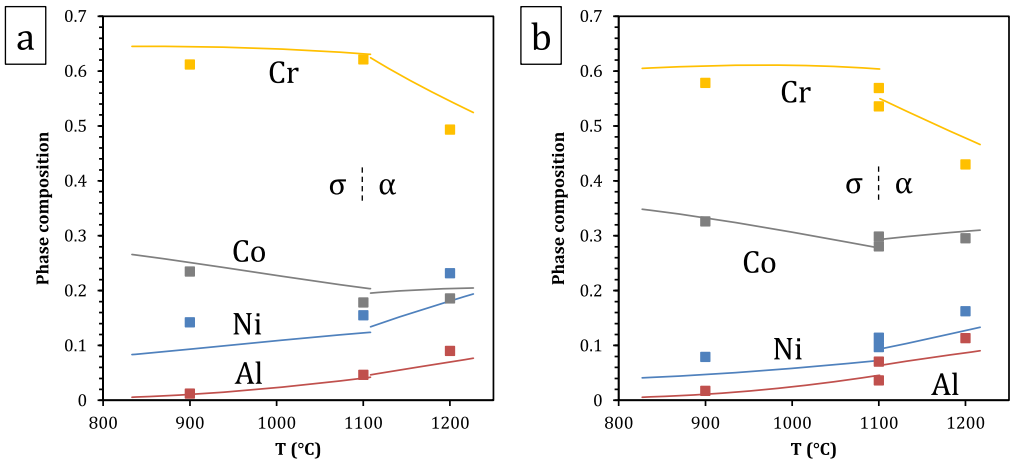

Figure 10. Composition of the σ and α phases of alloys (a) A3 and (b) A5, calculated and measured by EPMA.

plotted as a function of temperature for alloys A3 and A5. The $\sigma \rightarrow \alpha$ transition temperature for alloy A5 is calculated to be 1101 °C. Experimentally, both regions of β–γ–σ and of β–γ–α equilibrium were observed at 1100 °C. Accuracy in the annealing temperature or the calculated transition temperature is not expected to be better than one degree; whether the actual temperature was slightly above or slightly below the transition temperature, equilibrium over macroscopic distances would require remarkable compositional uniformity, and excessively long annealing time: here small heterogeneities locally stabilize either σ or α. This is also illustrated in figure 5(c), where the nominal composition of alloy A5 is seen to be close to the β–γ–σ–α and β–γ–α fields at this temperature. Both σ and α compositions are plotted in figure 10, and the database is seen to predict the trend observed upon the phase transformation reasonably well. The small discrepancy can be attributed to the sublattice model implemented here for σ, which does not offer the best description of this CoCr-base σ, as discussed in detail by Joubert [36]. In the current model, Cr can take on a maximum composition of 73.3 at.% at the end-member $(A)_8(Cr)_{18}(Cr)_4$ (where A is Al or Co). A non-simplified σ model would include five distinct sublattices relating to Wyckoff positions with all four Al, Co, Cr, and Ni allowed to occupy each sublattice: $(Al, Co, Cr, Ni)_2(Al, Co, Cr, Ni)_4(Al, Co, Cr, Ni)_8(Al, Co, Cr, Ni)_8(Al, Co, Cr, Ni)_8$ [36, 37]. Within this model, 1024 end-members would have to be defined. Simplifications made in [23, 35] by combining certain sites and restricting site occupation, which are commonly made [36], were thus retained here. A model based on a better suited site combination exists [36], which would lead to a maximum Cr concentration of 66.7 at.% at the end-member $(A)_{10}(Cr)_{16}(Cr)_4$. With similar site occupations, this would yield Cr concentrations closer to experimental results. Changing sublattice models would require remodeling the Co–Cr binary and associated ternaries; this was outside the scope of the current work but will be investigated in the future. The resulting discrepancy is limited (1–5 at.%) and the compositional trends are respected, such that the rest of the system is little affected. Overall, the present quaternary modeling provides a very good description of all phase compositions.

4.3. Comparison with existing databases

Figure 11 shows phase compositions calculated on the basis of nominal alloy compositions using our developmental database (CRALDAD1 for chromium and aluminium DFT-augmented database 1), and three existing databases (TCNI6 [38], TTNI8 [39], NIST Ni-base superalloy [40]), compared with the present experimental results. Four alloys (A3, A4, A5, A6) were selected so as to cover a large compositional region of the system. All calculations were conducted using Thermo-Calc, with the same conditions. The newer TCNI7 was later verified to produce the same results as the TCNI6 results included here.

As a general observation, CRALDAD offers the best fit to the experimental results. This could be expected since it was built using these results. The important criterion in evaluating a database is its consistency over a large range of temperatures and compositions, ideally assessed with a number of independent experimental datasets. Reliable experimental data in the quaternary system are lacking, thus in the following the four databases are simply evaluated against the present dataset.

The CRALDAD, TCNI6 and TTNI8 databases provide a relatively good depiction of the γ phase, while that given by NIST presents a number of issues. For example, the solubility of Cr in γ is overestimated at 1200 °C and 1100 °C, especially for Co-rich alloys (A4, A5), but underestimated at 900 °C. Inconsistencies are also noted in the Ni/Co ratio in γ: NIST tends to overestimate Co and underestimate Ni at 1200 °C and 1100 °C and in the case of alloy A5 at 900 °C, but at the lower temperature, the contrary is observed for the Co-lean alloy A3. Only CRALDAD and TTNI8 provide a very accurate representation of Al solubility in γ at all three temperatures, although the variance obtained with TCNI6 is small (<2 at.% difference compared to the experimental data).

Modeling of the β phase is subject to more discrepancy. Only CRALDAD provides a consistently good description,

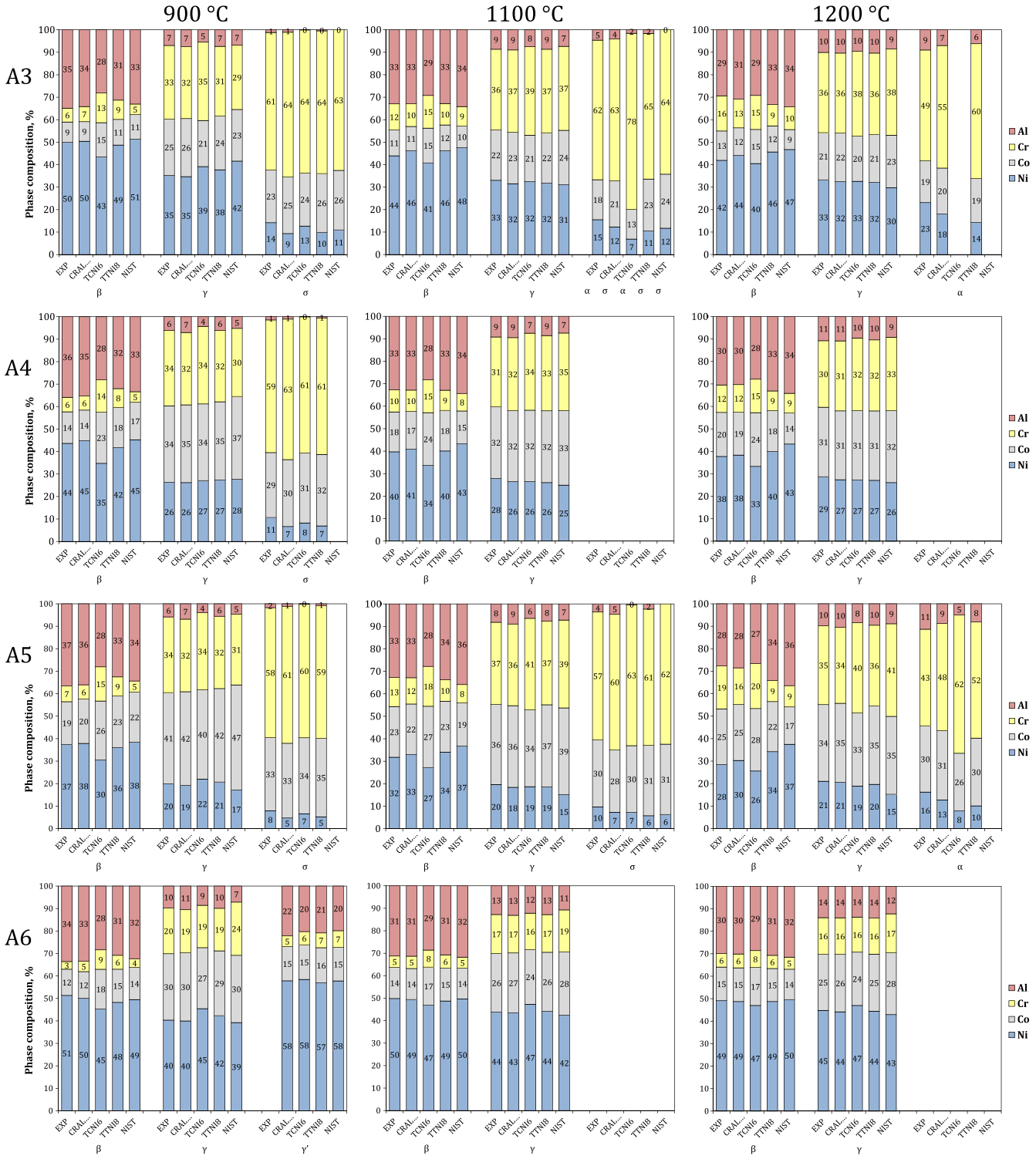

Figure 11. Comparison of experimental (EXP) and calculated phase compositions for alloys A3, A4, A5 and A6 at 900 °C, 1100 °C and 1200 °C. Calculations based on the present developmental database (CRALDAD), and existing databases (TCNI6, TTNI8, NIST).

while the quality of that obtained with the other databases shows significant variations with temperature. TCNI6, for instance, offers a relatively good fit at 1200 °C, but proves inadequate at 1100 °C and 900 °C, as it underestimates Al and Ni, and overestimates Cr and Co, with rather large errors (up to 9 at.% versus the experimental data). On the contrary, the compositions calculated from NIST show large differences with experimental data at 1200 °C (up to 10 at.%), but the spread is reduced at the lower temperatures. Finally, TTNI8 is at significant variance at 1200 and 900 °C, but proves excellent at 1100 °C.

Significant discrepancies also emerge in the case of the Cr-rich phase, which is either α or σ depending on temperature and alloy composition. The NIST database fails to

account for α formation at 1200 °C, predicts σ instead of α in alloy A3 at 1100 °C, and does not always predict σ formation at 900 °C, depending on alloy composition. Furthermore, it does not account for any Al solubility in σ when it successfully predicts its formation. CRALDAD offers the best representation of α at 1200 °C: it overestimates Cr and underestimates Ni and Al, but less so than TTNI8 and TCNI6. All databases tend to overestimate Cr, and underestimate Ni, in σ. CRALDAD provides the best description of σ at 1100 °C—in particular, it accounts for the relatively high Al solubility–but it tends to overestimate the Cr content slightly more than TTNI8 or TCNI6 do at 900 °C. As mentioned earlier, the σ model implemented in CRALDAD is not the best adapted. TCNI6 uses a model better suited to CoCr-base σ, which should produce a lower Cr content; however, the composition given by TCNI6 is only slightly better than that of CRALDAD at 900 °C, and TCNI6 actually yields a higher Cr content at 1100 °C. The absence of a clear advantage for TCNI6 illustrates the complexity of modeling a quaternary system.

The descriptions of γ' could not be evaluated due to the absence of experimental data. Compositions calculated for alloy A6 at 900 °C are all similar. More experimental input is required to correctly assess this part of the quaternary system, but the fact that CRALDAD successfully predicted γ' formation is encouraging, since it was built more specifically toward the description of the equilibrium of β and γ with either α or σ.

The NIST, TCNI6 and TTNI8 databases were built with the aim of modeling nickel base superalloys, which have a γ–γ' microstructure and significantly less Al, Cr and Co than the NiCoCrAlY alloys considered here. While the compositions of phases in equilibrium are evidently related via a mass balance, this rationalizes the fact that all three databases provided better representations of γ than they did for the Al-rich β or the Cr-rich α and σ. This also explains why these databases best represented the β–γ equilibrium in alloy A6, which has less Cr than the other alloys. In the case of the NIST database, the Al–Co–Cr subsystem is not assessed, and σ is modeled as a binary CoCr compound, with no Al solubility. This in turns affects the composition of the γ and β phases, and partly explains the discrepancies observed here between experimental and calculated compositions. The Al solubility in σ also tends to be underestimated by TCNI6. Despite the σ model used in CRALDAD being less well adapted than that of TCNI6, the parameter optimization in CRALDAD allows the high Al solubility to be accounted for. Outside of the σ phase, the good consistency of CRALDAD over the 900 °C–1200 °C temperature range reflects the effort to include, as much as possible, physically correct descriptions of all phases in the underlying ternary subsystems.

5. Conclusions

Extrapolation of the re-assessed ternary subsystems into the Al–Co–Cr–Ni system led to a description in very good agreement with experimental data, using a minimum number of quaternary interaction parameters. This assessment was based on a set of EPMA and XRD data obtained over a relatively wide range of compositions and temperatures. Primarily designed toward MCrAlY coatings, our database allows excellent representation of phase boundaries in β–γ equilibria at 900 °C–1200 °C, and correctly accounts for three-phase β–γ–σ and β–γ–α equilibria in alloys rich and Co and Cr. The $\sigma \rightarrow \alpha$ transition temperature, as well as compositional trends in the Cr-rich phases, are well described. Leads for an improved description of σ are identified. Precipitation of γ' at 900 °C in Cr-lean alloys was successfully predicted, although a finer assessment will require more experimental data. Comparison with existing databases on the basis of a set of measured phase compositions is favorable to our developmental database.

Acknowledgments

This work was supported by the Department of Energy through grant DE-FE0024056. The authors thank Ursula Kattner at NIST for providing the NIST database, and Michael Gao at NETL for providing phase compositions calculated with the TCNI6 and TTNI8 databases.

References

[1] Sims C T, Stoloff N S and Hagel W C 1987 *Superalloys* 2nd edn (New York: Wiley)
[2] Reed R C 2006 *The Superalloys* (Cambridge: Cambridge University Press)
[3] Goward G W 1998 *Surf. Coat. Technol.* **108** 73
[4] Nicholls J 2000 *JOM* **52** 28
[5] Evans A G, Mumm D, Hutchinson J W, Meier G H and Pettit F S 2001 *Prog. Mater. Sci.* **46** 505
[6] Beltran A M 1987 *Superalloys* 2nd edn ed C T Sims, N S Stoloff and W C Hagel (New York: Wiley)
[7] Sato J, Omori T, Oikawa K, Ohnuma I, Kainuma R and Ishida K 2006 *Science* **312** 90
[8] Miura S, Ohkubo K and Mohri T 2007 *Mater. Trans.* **48** 2403
[9] Suzuki A and Pollock T M 2008 *Acta Mater.* **56** 1288
[10] Shinagawa K, Omori T, Oikawa K, Kainuma R and Ishida K 2009 *Scripta Mater.* **61** 612
[11] Pollock T M, Dibbern J, Tsunekane M, Zhu J and Suzuki A 2010 *JOM* **62** 58
[12] Bauer A, Neumeier S, Pyczak F, Singer R F and Goeken M 2012 *Mater. Sci. Eng.* A **550** 333
[13] Klein L, Bauer A, Neumeier S, Goeken M and Virtanen S 2011 *Corros. Sci.* **53** 2027
[14] Klein L, von Bartenwerffer B, Killian M S, Schmuki P and Virtanen S 2014 *Corros. Sci.* **79** 29
[15] Vermaak N, Mottura A and Pollock T M 2013 *Corros. Sci.* **75** 300
[16] Achar D R G, Munoz-Arroyo R, Singheiser L and Quadakkers W J 2004 *Surf. Coat. Technol.* **187** 272
[17] Ma K and Schoenung J M 2010 *Surf. Coat. Technol.* **205** 2273
[18] Brož P, Buršík J, Svoboda M and Kroupa A 2002 *Mater. Sci. Eng.* A **324** 28
[19] Brož P, Buršík J and Picha R 2002 *Intermetallics* **10** 635
[20] Tsai M-H and Yeh J-W 2014 *Mater. Res. Lett.* **2** 107

[21] Zhang C, Zhang F, Chen S L and Cao W S 2012 *JOM* **64** 839
[22] Manzoni A, Daoud H, Mondal S, van Smaalen S, Völkl R, Glatzel U and Wanderka N 2013 *J. Alloy. Compd.* **552** 430
[23] Liu X L, Lindwall G, Gheno T and Liu Z K 2015 *Calphad* accepted
[24] Dupin N, Ansara I and Sundman B 2001 *Calphad* **25** 279
[25] Lukas H L, Fries S G and Sundman B 2007 *Computational Thermodynamics: The Calphad Method* 1st edn (Cambridge: Cambridge University Press)
[26] Liu Z-K 2009 *J. Phase Equilib. Diff.* **30** 517
[27] Jansson B 1984 Evaluation of parameters in thermochemical models using different types of experimental data simultaneously *Technical Report* TRITAMAC-0234 Stockholm, Sweden
[28] Sundman B, Jansson B and Andersson J-O 1985 *Calphad* **9** 153
[29] Andersson J-O, Helander T, Höglund L, Shi P and Sundman B 2002 *Calphad* **26** 273
[30] Dupin N 1995 Contribution à l'évaluation thermodynamique des alliages polyconstitués à base de nickel *PhD Thesis* INP Grenoble
[31] Dupin N and Sundman B 2001 *Scand. J. Metall.* **30** 184
[32] Lee B-J 1992 *Calphad* **16** 121
[33] Buršík J, Brož P and Popovič J 2006 *Intermetallics* **14** 1257
[34] Boullay P, Schryvers D and Ball J M 2003 *Acta Mater.* **51** 1421
[35] Liu X L, Gheno T, Lindahl B B, Lindwall G, Gleeson B and Liu Z K 2015 *PLOS One* **10** e0121386
[36] Joubert J-M 2008 *Prog. Mater. Sci.* **53** 528
[37] Mathieu R, Dupin N, Crivello J-C, Yaqoob K, Breidi A, Fiorani J-M, David N and Joubert J-M 2013 *Calphad* **43** 18
[38] http://thermocalc.com/media/5979/2013-05-31-tcni6_extended_info.pdf: accessed 13 March 2015
[39] http://thermocalc.com/media/5980/dbd_ttni8.pdf: acessed 20 February 2015
[40] Kattner U R 2002 Construction of a thermodynamic database for Ni-base superalloys: a case study *TMS: Calphad and Alloy Thermodynamics* (Warrendale, PA: TMS)

PLOS | ONE

RESEARCH ARTICLE

First-Principles Calculations, Experimental Study, and Thermodynamic Modeling of the Al-Co-Cr System

Xuan L. Liu[1]*, Thomas Gheno[2], Bonnie B. Lindahl[3], Greta Lindwall[1], Brian Gleeson[2], Zi-Kui Liu[1]

1 Department of Materials Science and Engineering, The Pennsylvania State University, University Park, Pennsylvania, 16802, United States of America, **2** Department of Mechanical Engineering and Materials Science, University of Pittsburgh, Pittsburgh, Pennsylvania, 15261, United States of America, **3** Department of Materials Science and Engineering, KTH Royal Institute of Technology, SE-100 44, Stockholm, Sweden

* xul119@psu.edu

Citation: Liu XL, Gheno T, Lindahl BB, Lindwall G, Gleeson B, Liu Z-K (2015) First-Principles Calculations, Experimental Study, and Thermodynamic Modeling of the Al-Co-Cr System. PLoS ONE 10(4): e0121386. doi:10.1371/journal.pone.0121386

Academic Editor: Dennis Salahub, University of Calgary, CANADA

Received: December 3, 2014

Accepted: January 31, 2015

Published: April 13, 2015

Data Availability Statement: All relevant data are within the paper and its Supporting Information files.

Funding: XLL, GL, and ZKL acknowledges that the computational aspects of this work were financially supported by the NSF Industry/University Cooperative Research Center for Computational Materials Design (CCMD, http://www.ccmd.psu.edu/), including dues contributions of CCMD members, through grants IIP-1034965 (Penn State) and IIP-1034968 (Georgia Tech) and the Office of Naval Research (ONR, http://www.onr.navy.mil/) with the contract number N0014-07-1-0638 managed by

Abstract

The phase relations and thermodynamic properties of the condensed Al-Co-Cr ternary alloy system are investigated using first-principles calculations based on density functional theory (DFT) and phase-equilibria experiments that led to X-ray diffraction (XRD) and electron probe micro-analysis (EPMA) measurements. A thermodynamic description is developed by means of the calculations of phase diagrams (CALPHAD) method using experimental and computational data from the present work and the literature. Emphasis is placed on modeling the bcc-A2, B2, fcc-γ, and tetragonal-σ phases in the temperature range of 1173 to 1623 K. Liquid, bcc-A2 and fcc-γ phases are modeled using substitutional solution descriptions. First-principles special quasirandom structures (SQS) calculations predict a large bcc-A2 (disordered)/B2 (ordered) miscibility gap, in agreement with experiments. A partitioning model is then used for the A2/B2 phase to effectively describe the order-disorder transitions. The critically assessed thermodynamic description describes all phase equilibria data well. A2/B2 transitions are also shown to agree well with previous experimental findings.

Introduction

Nickel-base superalloys used in the hot sections of gas turbines require corrosion-resistant coatings to withstand the harsh thermo-chemical conditions prevailing in these combustion environments [1,2]. Overlay MCrAlY (M = Ni, Co or NiCo) coatings are widely used for this purpose, either solely or in conjunction with a thermally insulating ceramic topcoat, most commonly yttria-stabilized zirconia, to comprise a thermal barrier coating (TBC) system [3–6]. During service, microstructural evolution of the MCrAlY layer arises as a result of temperature variations, reactions with the environment such as selective oxidation removing Al from the subsurface, or interdiffusion with the substrate material, driven by differences in chemical

David Shifler. TG and BG acknowledges that the experimental aspects of this work were partly supported by the Department of Energy under grant number DE-FE0007271 through the University Turbine Systems Research (UTSR) Program run by the National Energy Technology Laboratory (NTEL, http://www.netl.doe.gov/), with Dr. Seth Lawson being the Project Manager. One of the authors, BL, acknowledges funding from the European Research Fund for Coal and Steel (RFCS, http://cordis.europa.eu/coal-steel-rtd/) project "Precipitation in High Manganese Steels" under the grant agreement no. RFSR-CT-2010-00018. The funders had no role in study design, data collection and analysis, decision to publish, or preparation of the manuscript.

Competing Interests: The authors have declared that no competing interests exist.

potentials. A good knowledge of the alloy thermodynamics is critical to understanding and predicting these evolutionary processes, which in turn affect the corrosion resistance and mechanical properties of the system.

Computational design of effective MCrAl-based coating compositions necessitates a thermodynamic description methodology which can predict phase compositions and fractions at the temperatures of interest. One such method is CALPHAD, which has been used extensively and successfully in the thermodynamic modeling of many multi-component systems including Ni-base superalloys [7,8]. The CALPHAD approach parameterizes the Gibbs energy functions of all phases in unary, binary and ternary systems using computational and experimental data on phase equilibria and thermochemistry. The parameters are entered in a database and extrapolations to multi-component systems can be made. Limitations are known to exist in the current description of the quaternary Al-Co-Cr-Ni system for Co contents in excess of 20 wt. % [9,10] which are common in practice [2,11,12]. While assessment of the Al-Cr-Ni system has been well documented [7], the thermodynamic properties of the Al-Co-Cr system have not been adequately assessed.

Phases important to coating systems are B2 (β, $Pm\bar{3}m$, simple cubic type) and fcc-A1 (γ, $Fm\bar{3}m$, disordered f.c.c.). However, bcc-A2 (α, $Im\bar{3}m$, disordered b.c.c.), hcp-A3 (ε, $P6_3/mmc$, disordered h.c.p.) and sigma (σ, $P4_2/mnm$, Frank-Kasper) must also be modeled to allow for a complete description. One important feature of the Al-Co-Cr system is the A2/B2 second-order transformation at temperatures above 1373 K [13]. The present study aims to construct a thermodynamic model accounting for the A2/B2 ordering phenomenon, where atoms take on distinct lattice sites in B2. The two phases have vastly different compositions at low temperatures, but merge to similar compositions at higher temperatures which has to be accounted for in the thermodynamic model.

As phase equilibrium data are scarce, especially in the important B2+γ+σ region, experiments are conducted in this study at 1173, 1273, and 1373 K to aid the thermodynamic modeling. Additionally, first-principles calculations based on density functional (DFT) theory are incorporated to supplement the lack of experimentally measured thermochemical data in the ternary system [14] as well as to study the A2+B2 miscibility gap that is prevalent over the entire phase diagram. Ultimately, this system will be used in the construction of a multicomponent Al-Co-Cr-Ni-Y database. As a result, this database needs to be compatible with previously modeled Al-Co-Ni [15] and Al-Cr-Ni [7] systems.

The Al-Co thermodynamic model assessed by Dupin and Ansara [16] is adopted in the present work. This will allow compatibility with Dupin's [15] model of the Al-Co-Ni system. The Co-Cr system modeled by Oikawa et al. [17] is found to successfully capture experimental activity [18], enthalpy [18] and phase boundary data [17], which are crucial toward the extension to the Al-Co-Cr ternary, and is therefore adopted here. It also allows compatibility with the modeling of the Co-Cr-Ni system by Yang et al. [19], which would enable modeling of the quaternary Al-Co-Cr-Ni system. In Oikawa et al.'s [17] treatment of the Co-Cr system, no indication of B2 ordering was reported, hence the B2 phase will be modeled as a metastable phase with data from first-principles calculations. Saunders' [20] assessment of the Al-Cr system, used in COST507, is used here. Its description of the composition range of some intermetallics is not complete, but this will be shown to have no impact on the Al-Co-Cr system at the temperatures of interest in this study. Although XRD data from Helander and Tolochko [21] indicate a possible B2 ordering, no A2 to B2 second-order transition has been conclusively established in the Al-Cr system. Following Dupin et al. [7] who noted that a A2/B2 transition would modify the A2-$AlCr_2$ phase boundary and require additional experimental data for proper assessment, the B2-AlCr phase is not included here.

Ishikawa et al. [13] investigated the Al-Co-Cr system in the temperature range 1273–1623 K using multi-phase alloys and diffusion couples. Isotherms at 1573 and 1623 K showed complete dissolution of σ and a particularly large composition range for the B2 phase. The experimental work also provided compositions for the A2/B2 order-disorder transition at 1473 K and above, which are important to the present modeling. Previous models are combined with ternary data from the literature and this work to produce the overall thermodynamic description.

Materials and Methods

Experimental procedures

Ingots of nominal compositions (at. %) Co-20Cr-20Al-0.4Y (# A4), Co-26Cr-11Al-0.1Y (A5), Co-35Cr-6Al-0.1Y (A6) and Co-35Cr-11Al-0.1Y (A7) were prepared by arc-melting and drop-cast in a chamber evacuated and back-filled with 0.5 atm of argon. Specimens were cut to approximate dimensions of 10 x 10 x 1 mm, vacuum-encapsulated in quartz capsules, homogenized for 48 h at 1423 K in a tube furnace, and slowly brought to equilibration temperature. Equilibration treatments were conducted at 1173, 1273 and 1373 K for 500, 200 and 100 h, respectively, followed by water quenching to retain the equilibrated microstructures. Phase constitutions were studied by X-ray diffraction (XRD) with a PANalytical Empyrean instrument, using a Co radiation source ($K_{\alpha 1}$ = 1.789 Å).

Polished sections of the heat-treated alloys were prepared by standard metallographic procedures. Phase compositions were determined by electron probe micro-analysis (EPMA) using a JEOL JXA-8530F field emission gun instrument. For each element, measured intensities were converted to concentrations by interpolation via a calibration curve built using a series of standards of known compositions (chemical analysis by inductively coupled plasma mass spectrometry). The probe size used during measurements was about 1 μm, and the alloy microstructures were sufficiently coarse for each phase to be analyzed individually.

CALPHAD thermodynamic models

Solution phases: bcc, fcc (γ), hcp (ε), and liquid. In the present work, the Gibbs energies of γ, ε, and liquid solution phases are modeled using the following equation based on a single sublattice,

$$G_m^{\Phi} = \sum x_i {}^{o}G_i^{\Phi} + RT\sum x_i ln x_i + {}^{XS}G_m^{\Phi} + RT\,{}^{Magnetic}G_m^{\Phi} \qquad \text{Eq.1}$$

where ${}^{o}G_i^{\Phi}$ represents the molar Gibbs energy of the pure elements, i = Al, Co, Cr, with structure Φ taken from the SGTE Unary PURE4 database [22], and the other symbols have their usual meanings. In Eq. 1, the first term represents the physical mixing of the elements and the second term is the contribution from the ideal entropy of mixing. The excess term, ${}^{XS}G_m^{\Phi}$, is modeled using a Redlich-Kister polynomial [23] to represent the non-ideal interactions between Al, Co and Cr, as shown below:

$$\begin{aligned} {}^{XS}G_m^{\Phi} &= \sum_i \sum_{j>i} x_i x_j \sum_{v=0} {}^{v}L_{i,j}^{\Phi}(x_i - x_j) \\ &+ \sum_i \sum_{j>i} \sum_{k>j} x_i x_j x_k \left[{}^{1}L_{i,j,k}^{\Phi}(x_i + \delta_{i,j,k}) + {}^{2}L_{i,j,k}^{\Phi}(x_j + \delta_{i,j,k}) + {}^{3}L_{i,j,k}^{\Phi}(x_k + \delta_{i,j,k}) \right] \end{aligned} \qquad \text{Eq.2}$$

Where $\delta_{i,j,k} = (1 - x_i - x_j - x_k) / 3$. The binary and ternary interaction terms, ${}^{v}L_{i,j}^{\Phi}$ and ${}^{v}L_{i,j,k}^{\Phi}$, are expressed in the form $A + B \times T$ where A and B are the model parameters to be evaluated. Due to the ferromagnetic nature of Co and the antiferromagnetic nature of Cr, ${}^{Magnetic}G_m^{\Phi}$ is included to capture magnetic contributions to the Gibbs energy [24,25]. Hillert and Jarl [24] expressed the

magnetic contribution as:

$$^{Magnetic}G_m^{\Phi} = RTln(\beta+1)f(\tau) \quad \text{Eq.3}$$

where β represents the average magnetic moment and the function $f(\tau)$ is related to the Curie temperature (T_C):

$$\begin{aligned} f(\tau) &= 1 - \frac{1}{A}\left[\frac{79\tau^{-1}}{140p} + \frac{474}{497}\left(\frac{1}{p}-1\right)\left(\frac{\tau^3}{6}+\frac{\tau^9}{135}+\frac{\tau^{15}}{600}\right)\right], if\ \tau = \frac{T}{T_C} \le 1 \\ f(\tau) &= -\frac{1}{A}\left(\frac{\tau^{-5}}{10}+\frac{\tau^{-15}}{315}+\frac{\tau^{-25}}{1500}\right), if\ \tau = \frac{T}{T_C} \ge 1 \\ A &= \frac{518}{1125}+\frac{11,692}{15,975}\left(\frac{1}{p}-1\right) \end{aligned} \quad \text{Eq.4}$$

The constant p takes on values of 0.28 for fcc and hcp metals and 0.4 for bcc metals.

To account for the A2/B2 order-disorder transition, the bcc phase is modeled using the partitioning model, which treats the ordered and disordered components separately [26]. The disordered component of A2 is described using Eq. 1, and the model for the ordered component is described in the next section. Additionally, triple-defect mechanisms are especially important when considering site ordering in B2-aluminide-containing systems such as Al-Co [16], Al-Fe [27] or Al-Ni [7]. To account for this phenomenon [29] when the A2 phase is combined with the B2 phase, vacancies have been introduced in the substitutional sublattice of the A2 phase model as in Ref. [26]. Ordering of the bcc phase will be described in the following section.

Intermetallic phases: B2 and σ

The two ordered phases, B2 and σ, are described using sublattice models based on the compound energy formalism (CEF) [28]. In order to describe the A2/B2 ordering for the bcc phase, both A2 and B2 are modeled using a single Gibbs energy function where the ordered part (B2) is described by a sublattice formula $(Al,Co,Cr,Va)_1(Al,Co,Cr,Va)_1$ and the disordered part (A2) by $(Al,Co,Cr,Va)_1$. Specifically, B2 is appended to the already existing A2 model. Then, as implemented in Thermo-Calc, free energy minimization determines whether A2 and/or B2 are stable depending on the input conditions. In addition, a set of parameterization constraints derived by Dupin and Ansara [26] are used to partition the ordered and disordered parts of the A2/B2 Gibbs energy to allow independent evaluations. The B2 phase contains six stoichiometric compounds, or "end-members" (excluding vacancies) which represent the reference states generated when pure components fully occupy a sublattice; i.e. B2-(Al)(Al), B2-(Al)(Co), B2-(Al)(Cr), B2-(Co)(Cr), B2-(Co)(Co), and B2-(Cr)(Cr). The end-members of the B2 phase in the present system all come from binary systems and as a result, their formation energies are fixed by the previous Al-Co and Al-Cr binary assessments in this model; B2 is not included in the Co-Cr assessment by Oikawa et al. [17] and is therefore modeled in the present work.

The partitioning model describes the A2 and B2 with one single Gibbs energy function and the same sublattice model, $(Al,Co,Cr,Va)_1(Al,Co,Cr,Va)_1$. As a result, the Gibbs energy of A2 combined with B2 is described as:

$$G_m^{\alpha/\beta} = G_m^{\beta}(x_i) + \Delta G_m^{order}(y_i^{(s)}) \quad \text{Eq.5}$$

to include contributions from the disordered solution, $G_m^{\beta}(x_i)$, in A2 as well as from the ordered B2 itself, $\Delta G_m^{order}(y_i^{(s)})$. Here, $\Delta G_m^{order}(y_i^{(s)})$ can be separated into two terms, and the total Gibbs

energy of A2 and B2 becomes:

$$G_m^{\alpha/\beta} = G_m^{\alpha}(x_i) + G_m^{\beta(O)}(y_i^{(s)}) - G_m^{\beta(O)}(y_i^{(s)} = x_i) \quad \text{Eq.6}$$

where $y_i^{(s)}$ denotes the site fraction of element i on sublattice s. It can be seen that the ordering independent term, $G_m^{\alpha}(x_i)$, and the ordering dependent terms $G_m^{\beta(O)}(y_i^{(s)})$ and $G_m^{\beta(O)}(y_i^{(s)} = x_i)$ are separated in a way to allow each to be modeled independently. The term $G_m^{\beta(O)}(y_i^{(s)})$ takes on the partitioned form, as described by Dupin and Ansara [26]:

$$\begin{aligned} G_m^{\beta(O)}(y_i^{(s)}) &= \sum_i \sum_j (y_i' y_j'' {}^{o}G_{i:j}^{\beta(O)} + y_j' y_i'' {}^{o}G_{j:i}^{\beta(O)}) + RT[\sum_i y_i' ln(y_i') + \sum_j y_j'' ln(y_j'')] \\ &+ \sum_i \sum_j \sum_k \{y_i' y_j' y_k'' [\sum_k {}^{v}L_{i,j:k}^{\beta(O)} (y_i' - y_j')^v]\} + \sum_i \sum_j \sum_k \{y_k' y_i'' y_j'' [\sum_k {}^{v}L_{k:i,j}^{\beta(O)} (y_i'' - y_j'')^v]\} \\ &+ \sum_i \sum_j \sum_k \sum_l y_i' y_j' y_k'' y_l'' {}^{v}L_{i,j:k,l}^{\beta(O)} + \sum_i \sum_j \sum_k \sum_l (y_i' y_j' y_k' y_l'' {}^{v}L_{i,j,k:l}^{\beta(O)} + y_i'' y_j'' y_k'' y_l' {}^{v}L_{l:i,j,k}^{\beta(O)}) \end{aligned} \quad \text{Eq.7}$$

When the phase becomes disordered, i.e. $y_i' = y_i'' = x_i$, $G_m^{\beta(O)}(y_i^{(s)}) - G_m^{\beta(O)}(y_i^{(s)} = x_i)$ equals zero and eliminates the ordering energy contribution. The equivalence of the CEF and partitioned models is obtained using $2G_m^{Partition}(y_i^{(s)}) = G_m^{CEF}(y_i^{(s)})$. In Eq. 7, ${}^{o}G_{i:j}^{\beta(O)}$ represents the Gibbs energy of a B2 end-member expressed by Eq. 10 with i and j in the first and second sublattices, respectively. $L_{i:j,k}^{\beta(O)}$ is the interaction term between end-members of *i*:*j* and *i*:*k* that takes the form of $A + B{\times}T$ where A and B are the model parameters to be evaluated in modeling process. Relationships between the interaction parameters used in the CEF and partitioned models exist and are derived by Dupin and Ansara [26]. B2 end-members have both sites equivalent to one another so A2 disordering is possible when those sites have the same disordered occupancy. This crystallographic site equivalency is taken into account with the following expressions [26]:

$${}^{o}G_{i:j}^{\beta} = {}^{o}G_{j:i}^{\beta},\ {}^{v}L_{i,j:k}^{\beta} = {}^{v}L_{k:i,j}^{\beta},\ {}^{v}L_{i,j:k,l}^{\beta} = {}^{v}L_{k,l:i,j}^{\beta},\ \text{and}\ {}^{v}L_{i,j,k:l}^{\beta} = {}^{v}L_{l:i,j,k}^{\beta} \quad \text{Eq.8}$$

As adopted from the Co-Cr binary [17], σ is modeled with the sublattice formulation $(Al, Co)_8(Al,Co,Cr)_{18}(Cr)_4$. The phase σ contains σ-$(Al)_8(Al)_{18}(Cr)_4$, σ-$(Al)_8(Cr)_{18}(Cr)_4$, σ-$(Co)_8(Co)_{18}(Cr)_4$, σ-$(Co)_8(Cr)_{18}(Cr)_4$ binary and σ-$(Al)_8(Co)_{18}(Cr)_4$, σ-$(Co)_8(Al)_{18}(Cr)_4$ ternary end-members. To extend the solubility of σ from the binary Co-Cr system, Al must be introduced while keeping consistency with the original model for σ. Joubert [29] suggested that Al should only be allowed to mix in the first and second sublattices given its size and electronic characteristics. In accordance with this, a model described as $(Al,Co)_8(Al,Co,Cr)_{18}(Cr)_4$ is established. The Gibbs energy of σ in per mole of formula has the form,

$$\begin{aligned} G_m^{\sigma} &= \sum_i \sum_j y_i' y_j'' {}^{o}G_{i:j:Cr}^{\sigma} + RT[8\sum_i y_i' ln(y_i') + 18\sum_j y_j'' ln(y_j'')] \\ &+ \sum_{i_1} \sum_{i_2} \sum_j \{y_{i_1}' y_{i_2}' y_j'' [\sum_k {}^{k}L_{i_1,i_2:j:Cr}^{\sigma} (y_{i_1}' - y_{i_2}')^k]\} \\ &+ \sum_i \sum_{j_1} \sum_{j_2} \{y_i' y_{j_1}'' y_{j_2}'' [\sum_k {}^{k}L_{i:j_1,j_2:Cr}^{\sigma} (y_{j_1}'' - y_{j_2}'')^k]\} \end{aligned} \quad \text{Eq.9}$$

where y_i' and y_i'' represent the site fractions of i in the first and second sublattices, ${}^{o}G_{i:j:Cr}^{\sigma}$ represents the Gibbs energy of particular σ end-members as shown by Eq. 10, and $L_{i:j,k:Cr}^{\sigma}$ is the interaction term between end-members of *i*:*j*:Cr and *i*:*k*:Cr.

The described binary and ternary end-members for B2 and σ are modeled as follows,

$$G_m^{Al_xCo_yCr_z} = x^o G_{Al}^{fcc} + y^o G_{Co}^{hcp} + z^o G_{Cr}^{bcc} + \Delta_f G^{Al_xCo_yCr_z} \quad \text{Eq.10}$$

where $\Delta_f G^{Al_xCo_yCr_z} = \Delta_f H^{Al_xCo_yCr_z} - T\Delta_f S^{Al_xCo_yCr_z}$ and represents the Gibbs energy of formation of a particular B2 or σ end-member with the composition $Al_xCo_yCr_z$. The Debye-Grüneisen model is used to predict the enthalpy and entropy of the compounds as a function of temperature from 0 K properties obtained by the DFT calculations. Details for these calculations are presented in the following section. The PARROT module within Thermo-Calc [30] is used to assess all model parameters for each phase in the system using the phase equilibrium data from our experimental measurements and the results by Ishikawa et al. [13] as well as first-principles thermochemical data calculated in the present work. PARROT is a thermodynamic data assessment module which has been developed to fit model parameters to experimental data by a least mean square method [31].

First-principles methodologies

The Helmholtz energy, $F(V,T)$, of a condensed phase, in terms of the quasiharmonic approach, from first-principles calculations based on DFT is expressed as follows [32,33]:

$$F(V,T) = E_{0K}(V) + F_{Vib}(V,T) + F_{T-el}(V,T) \quad \text{Eq.11}$$

In the above expression, $F_{Vib}(V,T)$ and $F_{T\text{-}el}(V,T)$ represent the temperature-dependent vibrational and thermal-electronic contributions, respectively. In the present work, the Helmholtz energy is taken approximately as the Gibbs energy due to the negligible ambient pressure used in the modeling. The thermal electronic contribution to the Helmholtz energy is estimated based on the electronic density of states and calculated using Fermi-Dirac statistics for metallic systems [32]. $E_{0K}(V)$ is the static contribution at 0 K without the zero-point vibrational energy. It is obtained using a four-parameter Birch-Murnaghan (BM4) equation of state (EOS) [32,34]:

$$E_{0K}(V) = a + bV^{-2/3} + cV^{-4/3} + dV^{-2} \quad \text{Eq.12}$$

where a, b, c, and d are fitting parameters. Energy versus volume (E-V) data used in the fitting are relaxed with respect to ionic positions and cell shape at the given volumes.

Lattice vibrations are modeled with the Debye-Grüneisen model with the benefit of both accuracy and efficiency; the relevant equations have been described in detail in previous publications [35,36]. The scaling factor is implemented to scale the Debye temperature as a consequence of the differences in transverse and longitudinal phonon modes [37]. It has been shown that the scaling factor is highly dependent on the crystal structure [38,39]. This factor can be estimated from elastic constant calculations using DFT and then averaged as an isotropic medium. Elastic constant calculations are implemented in this work for fcc-Al, hcp-Co, bcc-Co, B2, and σ using the method proposed by Shang et al. [40].

In order to predict A2 solution mixing, calculations of the enthalpy of mixing based on special quasirandom structures calculations (SQS) [41] are performed using the 16-atom binary A2 model developed by Jiang et al. [42] and the 32- or 36-atom ternary A2 model developed by Jiang [43]. Additionally, ternary B2 solution mixing calculations are also performed using 8- and 16-atom supercells generated for the isostructural B2-AlNi system by Jiang et al. [44]. SQS calculation procedures for the present work are performed with the method recently implemented by Lieser et al. [45]. The SQS supercells are first relaxed with respect to cell volume only, and then to only cell volume and shape, and finally to cell volume, shape as well as ion positions simultaneously. Radial distribution functions (RDF) of relaxed supercells are compared

with the ideal bcc structure after each relaxation step [45]. The structures with the lowest energy that retain the required structural symmetry are used in the present work.

The Vienna *ab-initio* Simulation Package (VASP) [46] is used for spin-polarized DFT calculations due to the ferro- and antiferromagnetic natures of Co and Cr, respectively. Electron-ion interactions are described by the accurate projector augmented-wave (PAW) method [47,48]. The generalized gradient approximation (GGA) as implemented by Perdew, Burke, and Ernzerhof (PBE) [49] is used to describe the electron exchange and correlation. A plane-wave cut-off energy of 400 eV is consistently used to ensure enough basis sets are included, as recommended by the VASP manual [50]. Reciprocal *k*-meshes used for fcc-Al/Co, hcp-Co, bcc-Al/Co/Cr, B2 and σ are 21×21×21, 23×23×12, 17×17×17, 15×15×15, and 6×6×11, respectively. The structures are relaxed by implementing the Methfessel-Paxton method [51] to minimize the forces acting on the atoms. After relaxations, a final calculation using the tetrahedron with Blöchl corrections [52] is applied to ensure an accurate total energy calculation.

Results and Discussion

Experimental results

Alloy phase constitutions were determined through a combination of XRD (selected spectra shown in Fig 1) and phase composition analyses (EPMA results given in Table 1). At 1173 and 1273 K, the alloys A4, A5 and A7 are within the B2-γ-σ three-phase triangle, which is an invariant equilibrium in a three-component system. Small differences measured between the phase compositions are larger than the experimental standard deviation, and may reflect the slight influence of Y on phase equilibria. Selected microstructures observed after equilibration at 1273 and 1373 K are shown in Fig 2. In Fig 2A and 2B, the dark matrix is B2, the two light phases are γ and σ, and the bright precipitates are Y-containing intermetallics (denoted MY). These phases are identified based on their measured compositions and associated XRD results. This phase constitution is typical for equilibrium at 1173 and 1273 K. At 1373 K, the B2 phase exhibits compositions that vary widely between the four alloys studied. These are substantially different from those measured at 1173 and 1273 K, with Al contents as low as 16.2 at.% and Cr contents as high as 36.9 at.%. Nevertheless, XRD confirmed that the ordered B2 structure is maintained at 1373 K. In the absence of σ reflections, it is concluded that σ has been replaced by A2, which dissolves significantly more Al (Table 1). The A2 and B2 phases each have a cubic structure, and their peaks cannot be resolved with the instrument available. Analysis by EPMA (not shown here) indicated that two types of Co-rich yttrides were present, containing ~ 7 at.% and ~ 9 at.% Y, with 18–25 at.% Cr and 9–14 at.% Al. Due to the low volume fraction of these phases, their structures could not be determined by XRD.

The present experimental results confirm and refine the phase relationships originally documented by Ishikawa et al. [13]. Between 1273 and 1373 K, the B2+γ+σ three-phase region is replaced by an A2+B2+γ triangle, and the solubility of Cr in B2 drastically increases. Both are due to the shrinkage of the A2/B2 miscibility gap as the temperature increases, and to the associated dissolution of σ into A2. Ishikawa et al. [13] observed the A2/B2 order-disorder transition at 1473 K. The present measurements show very close compositions for B2 and A2 in equilibrium with γ at 1373 K and therefore, indicate that the miscibility gap is closed slightly above 1373 K.

First-principles results

To provide a benchmark for the first-principles methodology used in the present work, fundamental properties of Al, Co, Cr and relevant phases, shown in Table 2, are compared with previous first-principles calculations [53,54] and data from various experiments [55–59]. Good

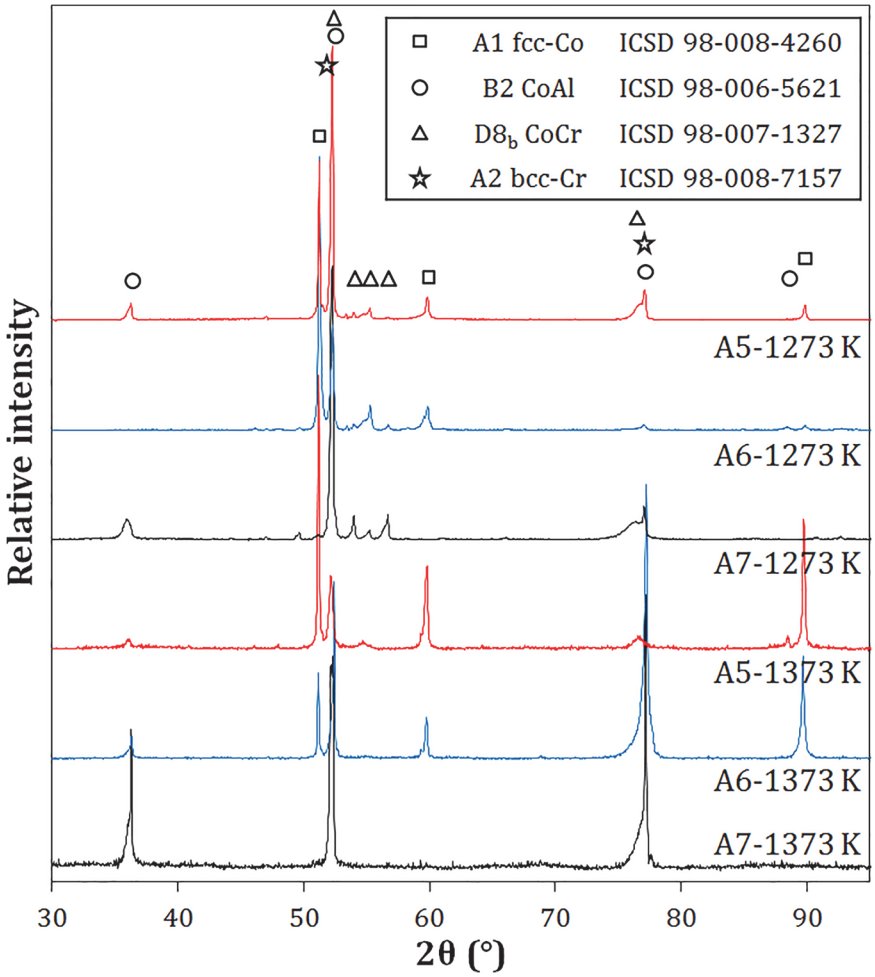

Fig 1. XRD analysis of selected alloy phase constitutions at 1273 K and 1373 K. Note that preferential orientations inherent to cast microstructures were still present after annealing. Specimens were rotated in-plane to ensure that all phases were detected.

doi:10.1371/journal.pone.0121386.g001

agreement is seen for these properties for all three elements in their standard element reference (SER) state (pure, most stable at 298 K and 1 bar) [22]. It should be noted that Cr takes on an anti-ferromagnetic state at 0 K. The results agree with previous calculations and experiments [56,59,60] for anti-ferromagnetic Cr. The lattice parameters and bulk modulus of B2-(Al)(Co) agree with previous results [61,62] and hence, the predicted values for B2-(Co)(Cr) and B2-(Cr)(Al) can be adopted with confidence. No measured bulk moduli for σ-CoCr could be found in the literature and hence, only experimental lattice parameters are compared. The calculated values for the end-members σ-$(Co)_8(Co)_{18}(Cr)_4$ and σ-$(Co)_8(Cr)_{18}(Cr)_4$ are compared to the lattice parameter of a σ-$Co_{13}Cr_{17}$ alloy and are in good agreement with measurements by Dickins et al. [55].

Results from our recent study on the Debye-Grüneisen model [63] indicate that using a calculated scaling factor for the Debye temperature is an accurate and efficient method to predict thermodynamic properties of pure elements and intermetallic phases in comparison with the more computationally demanding phonon supercell approach. Table 2 shows that the pure-element properties derived from the EOS fitting match experiments [56–58] and the DFT predictions [54,60]. Therefore, the Debye approximation is used to estimate the thermodynamic

Table 1. Phase compositions of the CoCrAlY alloys measured by EPMA (at.%).

T (K)	Ref.	B2			γ			σ			A2		
		Al	Cr	Co	Al	Cr	Co	Al	Cr	Co	Al	Cr	Co
1173	A4	36.6	13.2	50.3	5.6	34.3	60.1	2.9	54.0	43.1			
	A5	36.3	*13.6*	50.1	5.5	34.8	59.7	2.9	54.5	42.6			
	A6	36.3	14.2	49.5	5.5	35.3	59.2	2.9	54.8	42.3			
	A7	36.8	14.6	48.7				2.9	57.4	39.7			
1273	A4	32.0	18.1	49.9	6.6	35.8	57.6	4.0	53.5	42.5			
	A5	31.2	19.2	49.7	6.8	36.2	57.0	4.0	53.8	42.2			
	A6	31.7	18.9	49.5	6.7	36.2	57.1	3.9	54.1	42.0			
	A7	33.1	18.5	48.3				3.8	56.8	39.4			
1373	A4	28.2	20.7	51.1	8.4	33.7	57.9						
	A5	26.0	23.6	50.3	8.4	34.5	57.2						
	A6	16.2	36.9	46.8	8.0	36.5	55.5				12.4	41.6	46.0
	A7	22.3	33.4	44.2							11.7	48.4	39.9

doi:10.1371/journal.pone.0121386.t001

properties for all end-members of B2 and σ. Predicted enthalpies of formation ($\Delta_f H$) for each end-member of B2 and σ are calculated at 298 K and are shown in Table 3. Note that the non-SER reference B2 formation energies are calculated with respect to the bcc phase of the pure elements and that σ energies are taken with respect to the fcc phase in the first sublattice, bcc in the second and bcc in the third following Ref. [7,17]. Experimental thermochemical data for B2 and σ end-members are unavailable at 298 K and consequently, only previous CALPHAD assessments and DFT results are compared in Table 3. Stein et al. [64] determined values of $\Delta_f H_{298}$ = -64.45 kJ/mol-atom and $\Delta_f S_{298}$ = -11.43 J/mol-atom of B2 based on modeling of experimental enthalpy data at 1100 K. The present DFT predictions using the scaling factor Debye-Grüneisen model are in excellent agreement with these values.

Unfortunately, calorimetric measurements for σ-CoCr have proven unreliable, as reported measured and calculated enthalpies of formation range from -3 to +10 kJ/mol-atom, shown in Ref. [65–67]. Also, the stability of σ in the Co-Cr system was suggested to range from 30 to 45 at.% Co, which is quite different from the calculated end-member compositions of 26.6 and 86.6% at.% Co. However, Downie and Arslan [67] measured the formation enthalpy of one σ–CoCr sample close to the composition of the end-member σ-$(Co)_8(Cr)_{18}(Cr)_4$ at 473 K and found $\Delta_f H$ = 6.77 kJ/mol-atom. While no direct comparison can be made due to the composition and site fractions, the predicted value of $\Delta_f H_{298}$ = 6.19 kJ/mol-atom for σ-$(Co)_8(Cr)_{18}(Cr)_4$ is in good agreement with the measured value. Table 3 shows the final values (non-SER columns) for B2 and σ that are used as input for the thermodynamic modeling in the present work.

For all binary and ternary bcc SQS calculations, RDFs indicate that the simultaneous relaxation of cell volume, shape and ion positions reduce the symmetry of the SQS cell environment. Additionally, ternary SQS calculations show symmetry reduction when only cell volume and shape are allowed to relax. Therefore, SQS supercells with the lowest energy and a coordination environment sufficiently close to the ideal bcc structure are used in the analysis. Calculated binary and ternary enthalpies of mixing are shown in Table 4 and Fig 3 for A2 and B2. Along with the symmetry, the magnetism of the SQS supercells is checked. Cobalt is ferromagnetic at 0 K with an average μB/atom of 2.2 while Al is non-magnetic. At 0 K, Cr is antiferromagnetic with no net average magnetic moment. Our calculations show that Al and Cr additions, both with no net magnetic moment, decrease the μB/atom of Co as a function of composition.

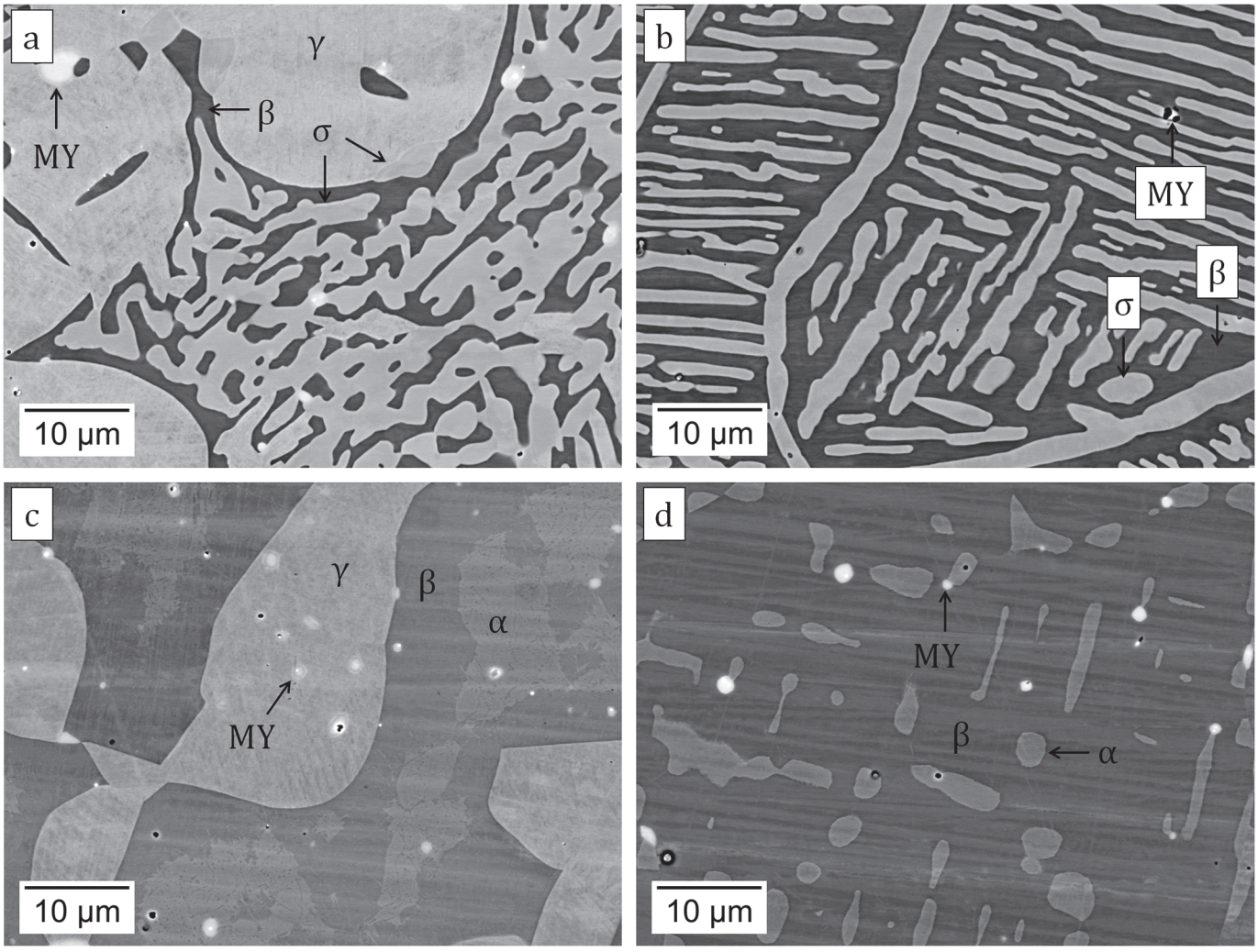

Fig 2. Microstructure of alloys (a,c) A6 and (b,d) A7 equilibrated at (a,b) 1273 K and (c,d) 1373 K. The bright precipitates are Y-containing intermetallics (noted MY).

doi:10.1371/journal.pone.0121386.g002

The SQS calculations, shown in Fig 3 and Table 4, predict the formation of a low-temperature miscibility gap in both Co-Cr and Al-Cr while strong negative mixing is seen in Al-Co. These predictions agree well with experimental observations as well as previous models of the Al-Co [16,64] and Co-Cr [17] binary systems currently adopted for the thermodynamic modeling. In the Co-Cr binary modeled by Oikawa et al. [17], a low temperature A2 miscibility gap is seen at 298 K. Furthermore, the predicted A2 $Al_{0.5}Co_{0.5}$ mixing enthalpy (Table 3) is in good agreement with the Al-Co assessment [16]. However, the Al-Cr model [20] does not produce a low-temperature A2 miscibility gap and hence, disagrees with our current predictions. This is due to a lack of low-temperature themochemical data available in the literature at the time when Al-Cr was originally modeled. Ternary A2 miscibility gaps are also predicted (Fig 3A), especially along the $Al_{0.5}Co_{0.5}$-Cr cross-section where the composition $Al_{0.5}Co_{0.5}$ shows the lowest mixing enthalpy on the whole energy surface. A convex energy surface would produce a tangent from $Al_{0.5}Co_{0.5}$ to pure Cr that generates a large miscibility gap across the entire $Al_{0.5}Co_{0.5}$-Cr cross-section. When B2 mixing is also taken into account, as shown in Fig 3B, this A2 and B2 miscibility gap becomes more prominent across the $Al_{0.5}Co_{0.5}$-Cr cross-section

Table 2. Various properties of the Al, Co, Cr, and the end-members of B2 and σ.

Phase	V_o (Å^3/atom)	B_o (GPa)	Scaling factor	Source
Al (fcc)	16.50	78	0.63	Present work
	17.08	65		DFT[54]
		72		Experiment[56]
		79 (0 K)		Experiment[57]
Co (hcp)	10.88	210	0.78	Present work
	11.07	204		DFT[54]
		191		Experiment[56]
		196 (0 K)		Experiment[58]
Cr (bcc)	11.59	176	0.88	Present work
	11.56	189		DFT[60]
	11.58	258		DFT[54]
		190		Experiment[56]
		192 (0 K)		Experiment [59]
B2 Phase				
(Al)(Co)	11.61	178	0.87	Present work
		157		DFT[61]
		162±5		Experiment[61]
(Co)(Cr)	11.60	214	0.77	Present work
(Cr)(Al)	14.03	125	0.82	Present work
σ Phase				
$(Al)_8(Al)_{18}(Cr)_4$	15.70	86	0.78	Present work
$(Al)_8(Cr)_{18}(Cr)_4$	12.36	199	0.82	Present work
$(Co)_8(Al)_{18}(Cr)_4$	13.07	141	0.78	Present work
$(Al)_8(Co)_{18}(Cr)_4$	11.65	174	0.78	Present work
$(Co)_8(Co)_{18}(Cr)_4$	11.12	197	0.69	Present work
$(Co)_8(Cr)_{18}(Cr)_4$	11.33	249	0.75	Present work

These properties are derived from the energy vs. volume curves using the 4-parameter Birch-Murnaghan EOS. B_0 denotes the bulk modulus. The bulk modulus at room temperature of Al, Co, and Cr are also presented, as reported by Kittel [56]. Other experimental temperatures are shown if known; reported 0 K values are extrapolated from low temperature data.

doi:10.1371/journal.pone.0121386.t002

in accordance with the experiments by Ishikawa et al. [13]. The extremely high formation energy of the end-member (Al)(Co) is responsible for this behavior. Additionally, the SQS results show that A2 is more stable than B2 near Cr because ΔH_{mix} = -1.17 kJ/atom for A2 at the composition $Al_{0.25}Co_{0.25}Cr_{0.5}$ while ΔH_{mix} = 8.22 kJ/atom for B2 at the same composition. These SQS results are in good agreement with measured phase compositions by Ishikawa et al. [13] as well as the present experimental findings. As shown later in Fig 4, this A2/B2 miscibility gap is still observed at 1173 K.

CALPHAD modeling results

The three binary models, Al-Co [16], Co-Cr [17], and Al-Cr [20], are extrapolated to the ternary system using the partitioning model [26]. In addition, thermodynamic parameters from DFT, listed in Table 3, are used as input. The binary B2-(Al)(Co), B2-(Cr)(Al), σ-$(Co)_8(Co)_{18}(Cr)_4$ and σ-$(Co)_8(Cr)_{18}(Cr)_4$ end-members are fixed by previous models and cannot be modified without reassessment of those systems. The initial ternary extrapolation produces a phase diagram with satisfactory phase boundaries for fcc, A2, and B2 at 1173 K compared to experiments,

Table 3. Predicted enthalpies and entropies of formation of B2 and σ end-members at 298 K.

Phase	End-member	$\Delta_f H$(kJ/mol-atom)	$\Delta_f H$ *(SER)*(kJ/mol-atom)	$\Delta_f S$ (J/mol-a)	$\Delta_f S$ *(SER)* (J/mol-a)	Source
(B2)	**(Al)(Co)**	**-66.89**	**-57.67**	-13.73	**-8.23**	Present work
Binary		-64.45		-11.43		CALPHAD[64]
	(Co)(Cr)	11.98	16.60	-1.73	1.03	Present work
	(Cr)(Al)	**-7.37**	**-2.78**	**-9.18**	**-6.45**	Present work
(σ)	**$(Co)_8(Al)_{18}(Cr)_4$**	**-30.56**	**-24.58**	**-7.33**	**-4.05**	Present work
Ternary	**$(Al)_8(Co)_{18}(Cr)_4$**	**-18.93**	**-13.39**	**-4.44**	**-1.13**	Present work
(σ)	$(Co)_8(Co)_{18}(Cr)_4$	3.60	9.62	0.28	3.60	Present work
Binary	0 K		9.84			Present work
	0 K		11.65			DFT[65]
	$(Co)_8(Cr)_{18}(Cr)_4$	5.72	6.19	0.16	0.16	Present work
	0 K		6.20			Present work
	0 K		8.39			DFT[65]
	$(Al)_8(Al)_{18}(Cr)_4$	5.73	11.24	-6.02	-2.74	Present work
	$(Al)_8(Cr)_{18}(Cr)_4$	1.84	1.84	-3.32	-3.32	Present work

Energies are shown in units of J/mol-formula and atom with the most stable end-members shown in bold text. Also, energies taken with respect to standard states are denoted with SER. Energies used for CALPHAD modeling are taken with different reference states depending on the sublattice models used. B2 formation energies are calculated with respect to the bcc phase of the pure elements. For σ, energies are taken with respect to the fcc phase in the first sublattice, bcc in the second and bcc in the third; same as the sublattice model implemented in the current work.

doi:10.1371/journal.pone.0121386.t003

but is at variance with the experimental isothermal sections at all other temperatures [13,68]. A2/B2 regions do not separate at the order/disorder compositions even at temperatures as high as 1623 K, which is at significant variance with experiments (see experimental Section 6.1 for discussion). The poor extrapolation is a result of fixing the B2-(Cr)(Al) end-member to the value proposed by Dupin et al. [7] in their modeling of the Al-Cr-Ni ternary system. Dupin et al. [7] assessed $\Delta_f H$ of B2-(Cr)(Al) to be -13.719 kJ/mol-atom, which is much more stable than the value of -7.37 kJ/mol-atom predicted by DFT in the present work. However, modifying this energy will require significant reassessment of Al-Cr-Ni ternary description and is outside the scope of this work. As a consequence of this fixed B2 end-member, additional interaction parameters for the B2 phase are needed to correctly reproduce its miscibility gap.

The binary B2-(Co)(Cr) end-member and the Co-Cr interaction parameters are evaluated by fitting to the present EPMA results at 1173, 1273, and 1373 K (Table 1) data from Ishikawa et al. [13] as well as first-principles thermochemical data. Given the complexity of the A2/B2 miscibility gap region, as seen in Figs 4–8, ternary, temperature dependent interaction parameters are needed to describe the B2-(Al)(Co) extension into the ternary as well as the A2/B2 transition temperatures. Interaction parameters for the A2 are also needed to capture the Al and Co solubility. The evaluated parameters are shown in Table 5 and built into a thermodynamic database, which can be found in S1 Dataset.

Fig 4 shows the calculated isothermal section at 1173 K compared with the present EPMA results as well as experimental data from Moskvitina et al. [68]. A good agreement between calculations and experiments is reached. Fig 5 shows the calculated isothermal section at 1273 K, which agrees very well with the present experiments as well as measurements by Ishikawa et al. [13]. Fig 6 shows a calculated isothermal section at 1373 K, which agrees well with our experiments, except for the B2 composition in the A2+B2+γ three phase tie-triangle and the A2-B2 tie-line. This is attributed to the fact that the A2/B2 miscibility gap disappears very rapidly with increasing temperature, and as a consequence the morphology of this region of the

Table 4. Calculated enthalpies of mixing for solution A2 and B2.

Al	Co	Cr	SQS prototype	ΔH_{mix} (kJ/mol-atom)
			A2	
			Al-Co	
0.75	0.25		16	-8.71
0.5	0.5		16	-21.69
0.25	0.75		16	-18.57
			Co-Cr	
	0.75	0.25	16	9.99
	0.5	0.5	16	11.98
	0.25	0.75	16	9.59
			Al-Cr	
0.75		0.25	16	2.45
0.5		0.5	16	1.44
0.25		0.75	16	1.01
			Al-Co-Cr	
0.5	0.25	0.25	32	-9.36
0.25	0.5	0.25	32	-6.86
0.25	0.25	0.5	32	-1.17
0.33	0.33	0.33	36	-7.86
Al	**Co**	**Cr**	**SQS prototype**	ΔH_{mix} (kJ/mol-atom)
			B2	
			(Al)(Co)-(Co)(Cr) section	
0.5	0.5	0		-67.75
0.375	0.5	0.125	32	-47.66
0.25	0.5	0.25	8	-27.20
0.125	0.5	0.375	32	-9.96
0	0.5	0.5		11.99
			(Co)(Cr)-(Cr)(Al) section	
0	0.5	0.5		11.99
0.25	0.25	0.5	8	8.22
0.5	0	0.5		-7.96
			(Cr)(Al)-(Al)(Co) section	
0.5	0	0.5		-7.96
0.5	0.125	0.375	32	-18.49
0.5	0.25	0.25	8	-32.77
0.5	0.375	0.125	32	-49.54
0.5	0.5	0		-67.75

These calculations are based on binary and ternary SQS calculations at 0 K with references taken as bcc-A2 for Al, Co, and Cr.

doi:10.1371/journal.pone.0121386.t004

diagram is extremely sensitive to temperature variations around 1373 K. The A2+B2+γ three phase triangle is predicted to disappear at 1423 K measurements by Ishikawa et al. [13] at 1473 K. Fig 7 plots the 1473 K isothermal section, which fits experimental measurements from Ishikawa et al. [13] quite well. At this temperature, the A2/B2 miscibility gap is replaced by a second-order transition represented by a dotted line. The calculation near the transition region shows that the B2 ordering gravitates towards the disordered composition with more Cr additions on the Co-Cr rich side of the phase diagram. This is in good agreement with the

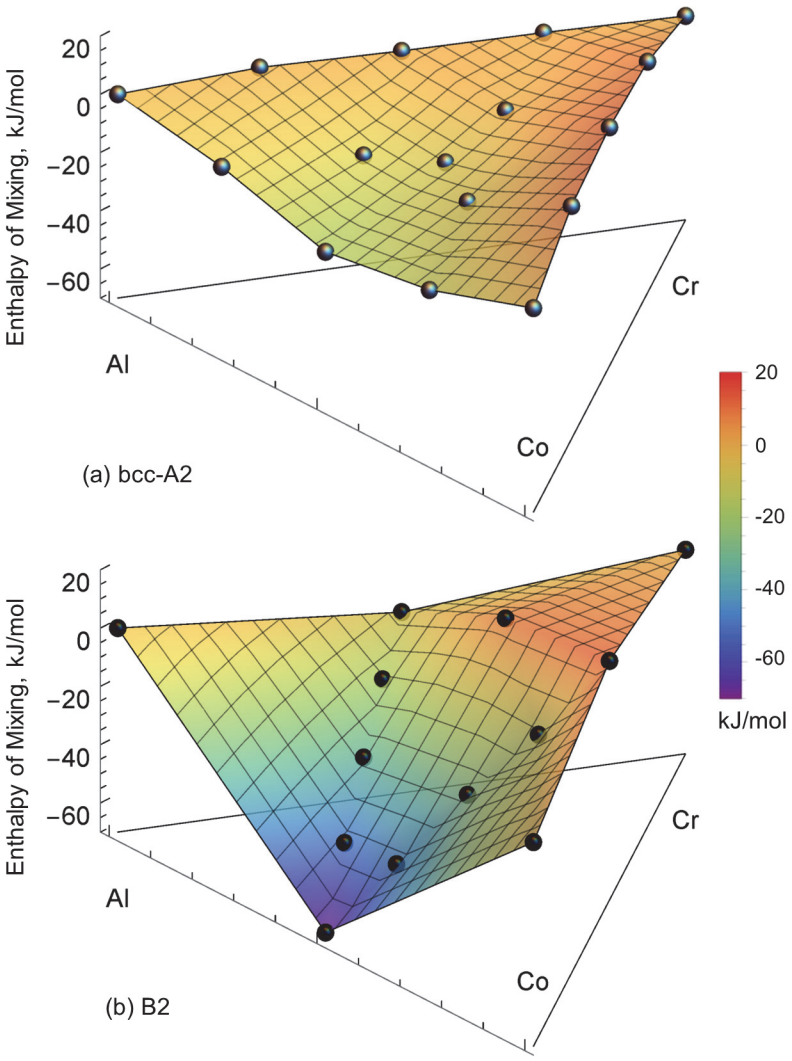

Fig 3. Predicted A2 (a) and B2 (b) enthalpies of mixing. These calculations are based on 16-atom binary and 32/36-atom ternary SQS supercells at 0 K. Grey points in (a) represent distinct A2 SQS compositions and black points in (b) represent B2 SQS compositions. A color map is added to guide the reader in viewing the energy surface.

doi:10.1371/journal.pone.0121386.g003

experimental results on the order/disorder alloys found by Ishikawa et al. [13]. Fig 8 shows the 1573 K isothermal sections. Furthermore, the A2/B2 and B2/γ tie-lines as well as A2/B2 transition points show good agreement at 1573 and 1623 K compared with data from Ishikawa et al. [13] (not included here). An overall good thermodynamic description of Al-Co-Cr, which takes into account predicted first-principles thermochemical data, is produced in this work. We have demonstrated a model that is able to reproduce the rapid replacement of one three-phase σ+B2+γ tie-triangle by another and the sharp increase in the solubility of Cr in B2 from 1273 to 1373 K, as observed experimentally (see Section 6.1).

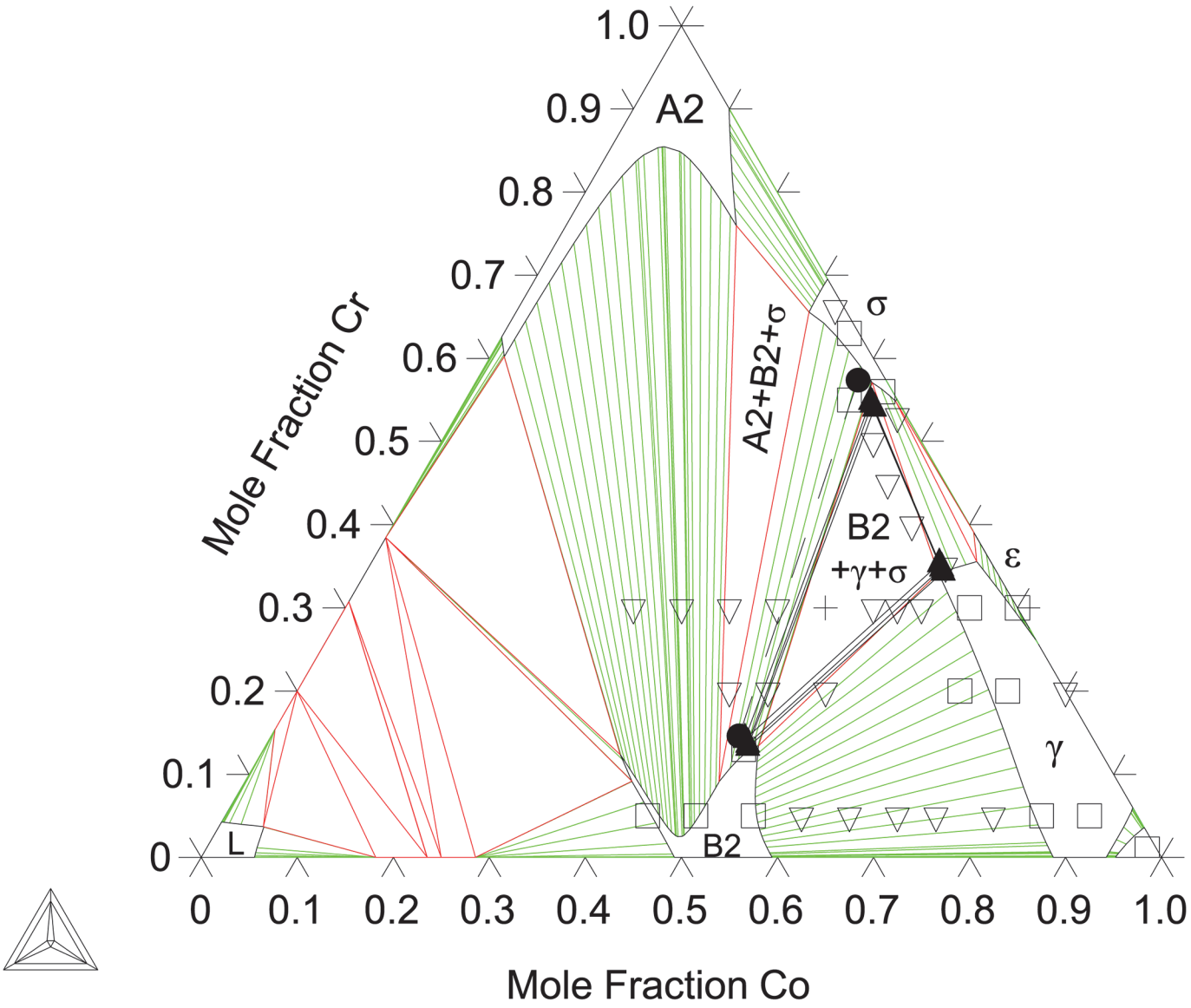

Fig 4. Al-Co-Cr Isothermal section at 1173 K. Shown with phase equilibria data from Moskvitina et al. [68]: single phase (□), 2-phase (▽), and 3-phase (+). Phase equilibria data from the present work: 2-phase (•), 3-phase (▲).

doi:10.1371/journal.pone.0121386.g004

Conclusions

The Al-Co-Cr system is investigated thoroughly using first-principles calculations, XRD, and EPMA measurements to produce a complete CALPHAD thermodynamic description. First-principles DFT calculations predict a large A2/B2 miscibility gap in the ternary system, which is demonstrated experimentally using phase composition measurements from 1173 to 1373 K. In addition, the experimentally-measured phase compositions for A2, B2, γ and σ are in good agreement with previous experimental results [13]. To aid in the modeling of the ternary system, the Debye-Grüneisen model is used to predict finite-temperature data of B2 and σ such as heat capacities, entropies, and enthalpies. It is found that the complex A2/B2 phase region, which includes an order-disorder transition, can be accurately described with a partitioned bcc model. The calculated B2 ordering compositions are also shown to be in agreement with

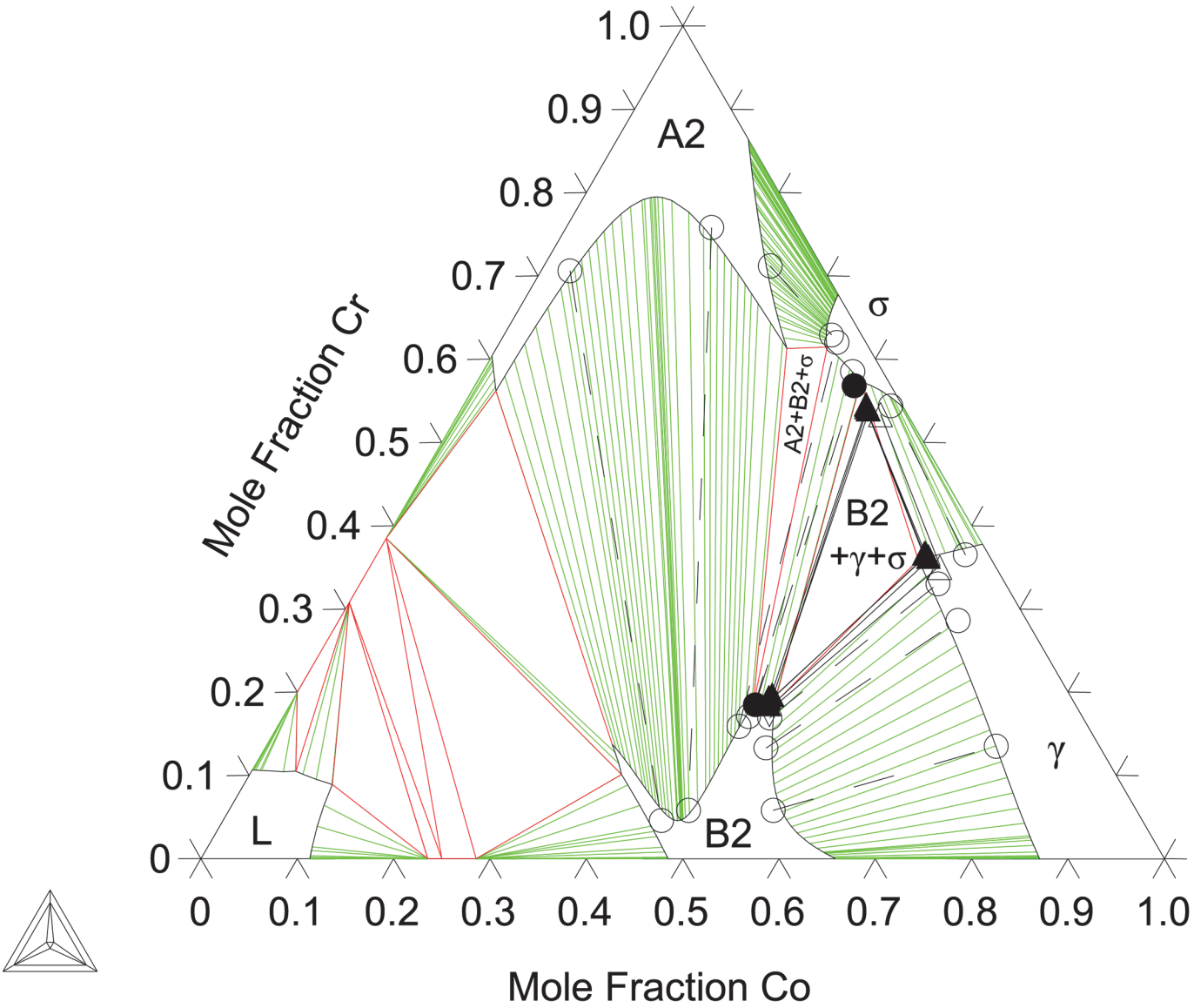

Fig 5. Al-Co-Cr Isothermal section at 1273 K. Shown with phase equilibria data from Ishikawa et al. [13]: 2-phase (⊖), and 3-phase (▽). Experimental phase equilibria data from the present work: 2-phase (●), 3-phase (▲).

doi:10.1371/journal.pone.0121386.g005

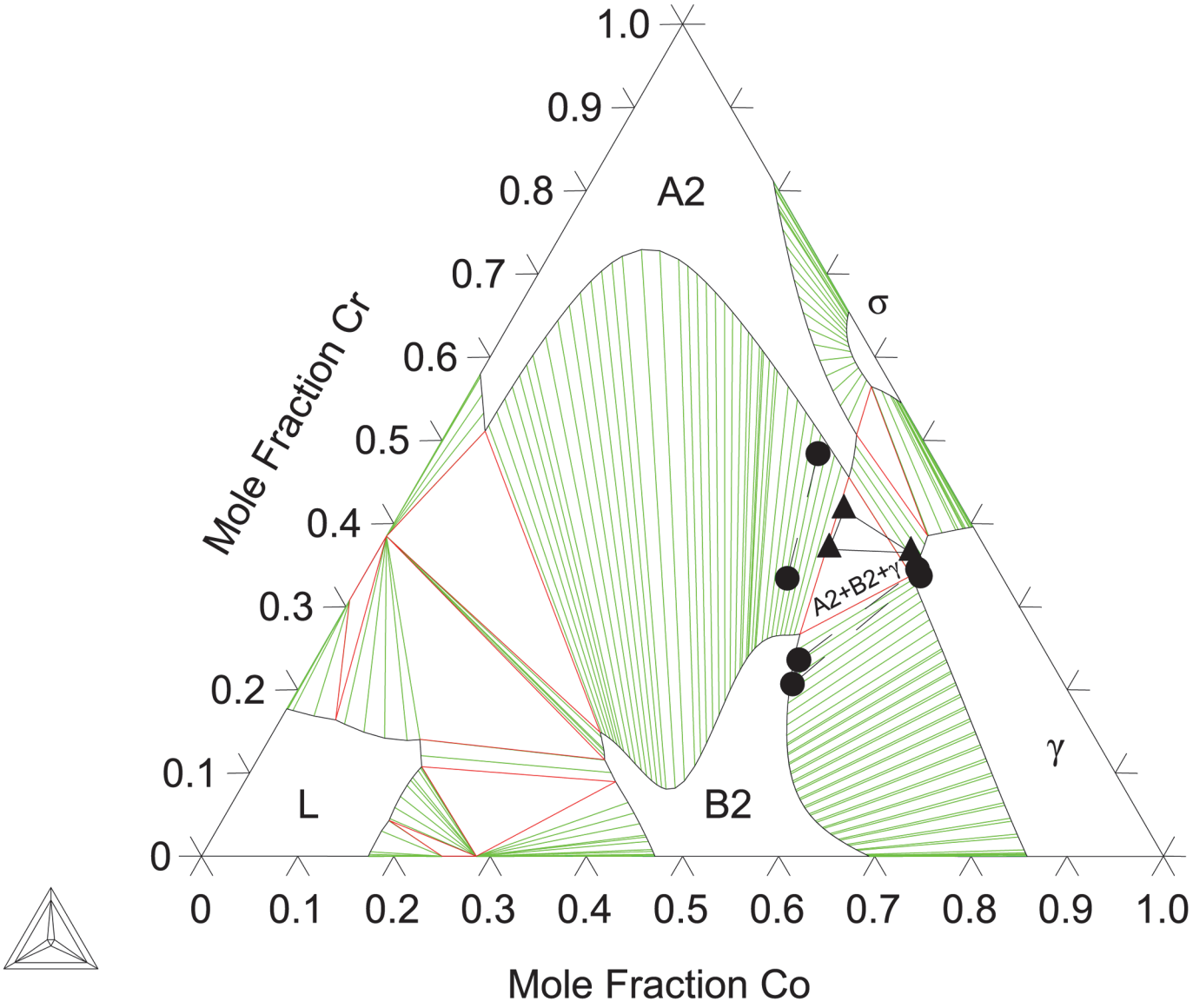

Fig 6. Al-Co-Cr Isothermal section at 1373 K. Shown with phase equilibria data from the present work: 2-phase (•), 3-phase (▲).

doi:10.1371/journal.pone.0121386.g006

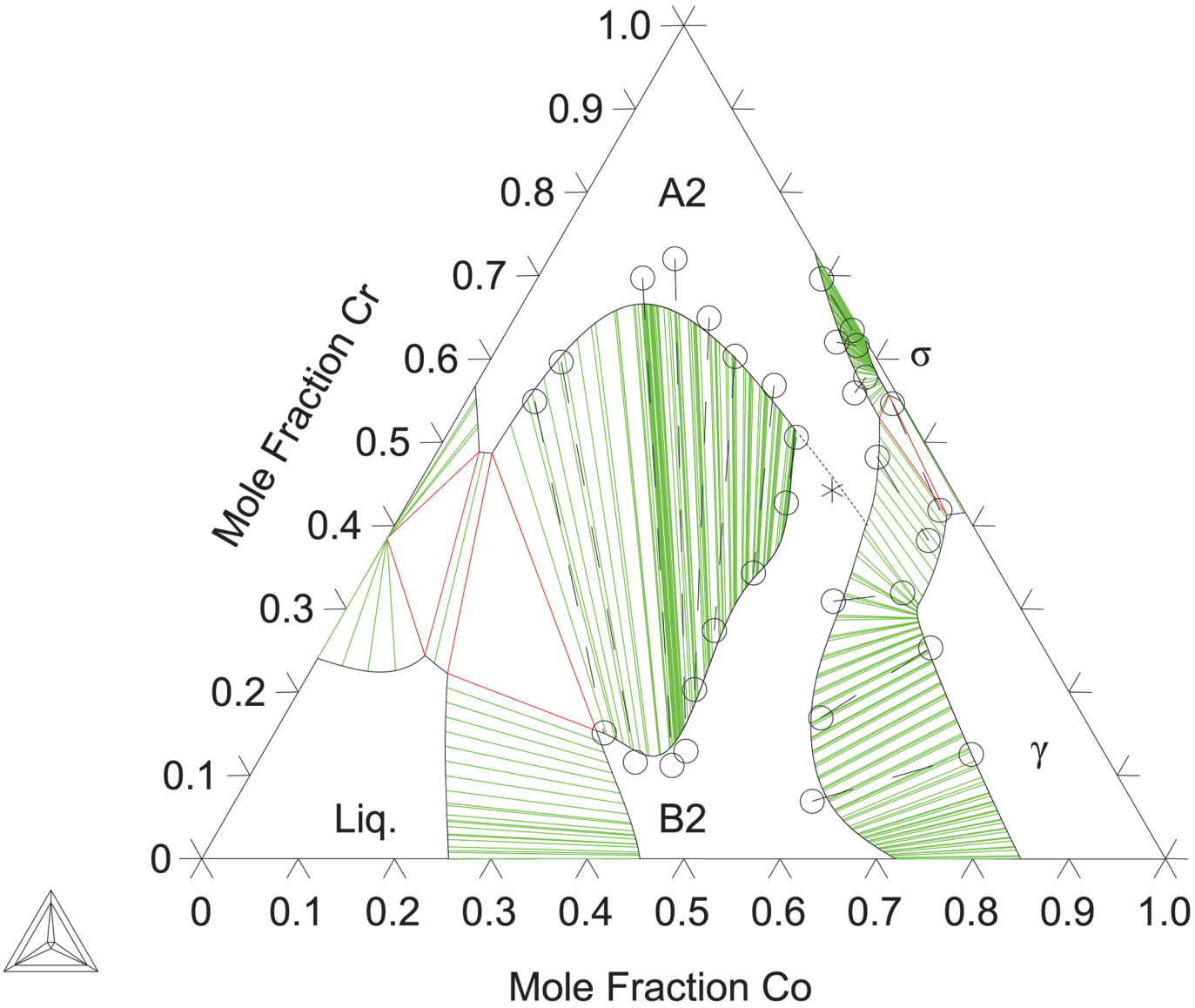

Fig 7. Al-Co-Cr isothermal section at 1473 K. Phase equilibria data from Ishikawa et al. [13]: 2-phase (), order-disorder transition (*). The calculated order-disorder transition is shown with (· · ·).

doi:10.1371/journal.pone.0121386.g007

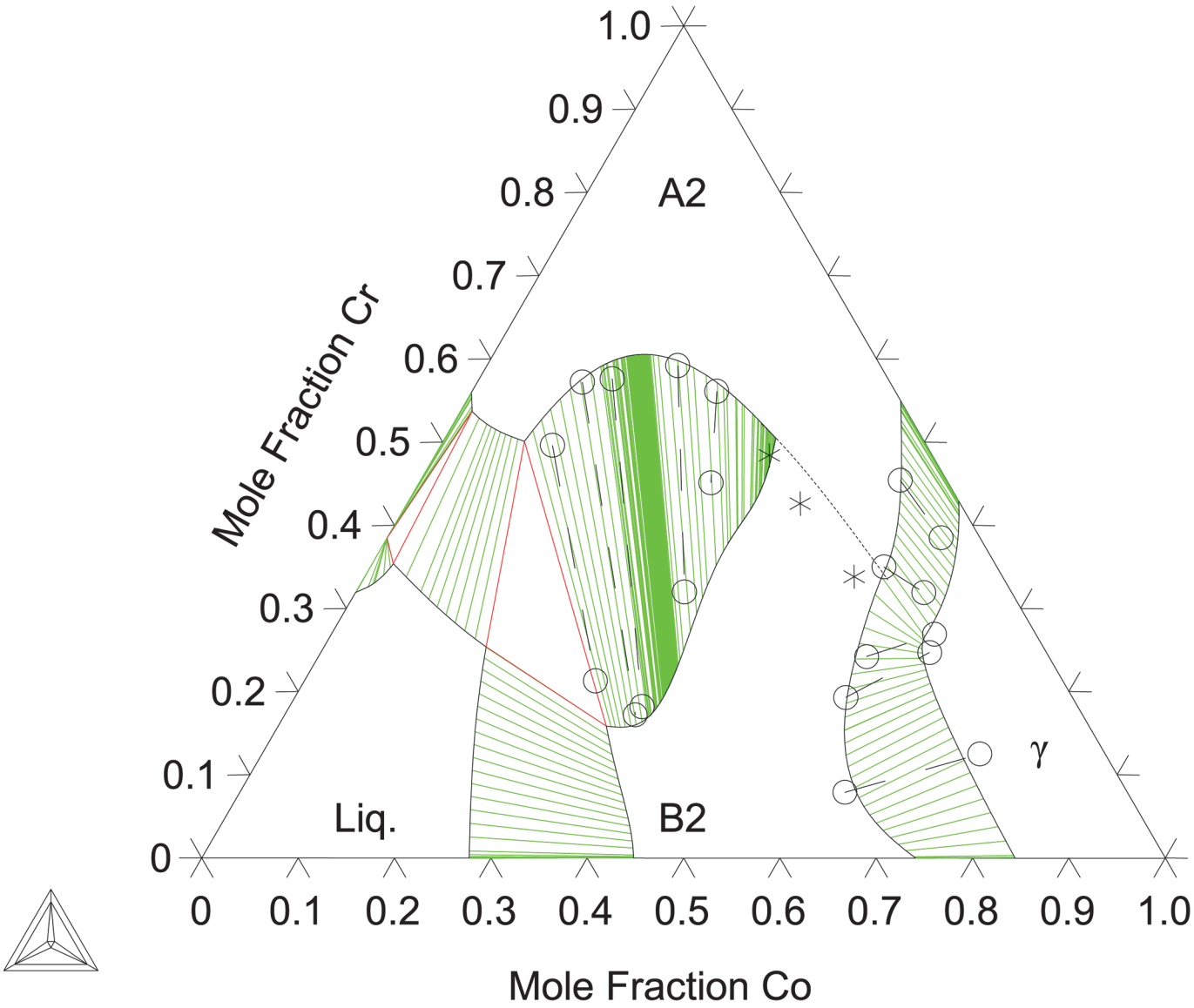

Fig 8. Al-Co-Cr Isothermal section at 1573 K. Phase equilibria data from Ishikawa et al. [13]: 2-phase (○), order-disorder transition (*). The calculated order-disorder transition is shown with (· · ·).

doi:10.1371/journal.pone.0121386.g008

Table 5. Model parameters and functions for the ternary Al-Co-Cr system.

Phase	Parameters	Values	References
liquid (L) phase: $(Al,Co,Cr)_1$	${}^0L^{Liq}_{Al,Co,Cr}$	+30000	Present work
fcc (γ) phase: $(Al,Co,Cr)_1$	${}^0L^{fcc}_{Al,Co,Cr}$	+17295	Present work
hcp (ε) phase: $(Al,Co,Cr)_1$	${}^0L^{hcp}_{Al,Co,Cr}$	+25000	Present work
bcc (A2) phase: $(Al,Co,Cr,Va)_1$	${}^0L^{A2}_{Al,Co}$	+*GB2ALCO*–*LB2ALCO*	Present work
	${}^0L^{A2}_{Al,Cr}$	–54900 + 10 ×*T*	*COST 507*[20]
	${}^0L^{A2}_{Co,Cr}$	+1033–1.481 × *T*	*Oikawa et al*.[17]
	${}^1L^{A2}_{Co,Cr}$	+11972–13.374 × *T*	*Oikawa et al*.[17]
	${}^0L^{A2}_{Al,Va}$	+*GB2ALVA*–*LB2ALVA*	*Dupin et al*.[7]
	${}^0L^{A2}_{Co,Va}$	+*GB2COVA*–*LB2COVA*	Present work
	${}^0L^{A2}_{Cr,Va}$	+100000	*Dupin et al*.[7]
	${}^0L^{A2}_{Al,Co,Cr}$	–*LB2ALCO* + *LBALCOMCR* +*LBCOCRMAL* +*L1BCRALMCO*	Present work
	${}^1L^{A2}_{Al,Co,Cr}$	+*LALCO2CR*–*LB2ALCO* +*LBALCOMCR* + *LBCOCRMAL*	Present work
	${}^2L^{A2}_{Al,Co,Cr}$	–*LB2ALCO* + *LBALCOMCR* +*LBCOCRMAL* –*L1BCRALMCO*	Present work
beta (B2) phase: $(Al,Co,Cr,Va)_{0.5}$ $(Al,Co,Cr,Va)_{0.5}$	${}^0G^{B2}_{Al:Co} = {}^0G^{B2}_{Co:Al}$	+0.5 × *GB2ALCO*–0.5 × *LB2ALCO*	Present work
	$TC^{B2}_{Al:Co} = TC^{B2}_{Co:Al}$	-1450	Present work
	$BMAG^{B2}_{Al:Co} = BMAG^{B2}_{Co:Al}$	-1.35	Present work
	${}^0G^{B2}_{Co:Cr} = {}^0G^{B2}_{Cr:Co}$	+0.5 × *GB2COCR*	Present work
	${}^0G^{B2}_{Cr:Al} = {}^0G^{B2}_{Al:Cr}$	+0.5 × *GB2CRAL*	Present work
	${}^0G^{B2}_{Al:Va} = {}^0G^{B2}_{Va:Al}$	+0.5 × *GB2ALVA*–0.5 × *LB2ALVA*	Present work
	${}^0G^{B2}_{Co:Va} = {}^0G^{B2}_{Va:Co}$	+0.5 × *GB2COVA*–0.5 × *LB2COVA*	Present work
	${}^0G^{B2}_{Cr:Va} = {}^0G^{B2}_{Va:Cr}$	0	Present work
	${}^0L^{B2}_{Co,Cr:Al} = {}^0L^{B2}_{Al:Co,Cr}$	+0.5 × *LBCOCRMAL*	Present work
	${}^0L^{B2}_{Al,Cr:Co} = {}^0L^{B2}_{Co:Al,Cr}$	+0.5 × *LBCRALMCO*	Present work
	${}^0L^{B2}_{Al,Co:Cr} = {}^0L^{B2}_{Cr:Al,Co}$	+0.5 × *LBALCOMCR* + *BU1ALCO*	Present work
	${}^1L^{B2}_{Co,Cr:Al} = {}^1L^{B2}_{Al:Co,Cr}$	+0.5 × *L1BCOCRMAL*	Present work
	${}^1L^{B2}_{Al,Cr:Co} = {}^1L^{B2}_{Co:Al,Cr}$	+0.5 × *L1BCRALMCO*	Present work
	${}^1L^{B2}_{Al,Co:Cr} = {}^1L^{B2}_{Cr:Al,Co}$	+0.5 × *L1BALCOMCR*	Present work
	${}^0L^{B2}_{Al,Co,Cr:Al} = {}^0L^{B2}_{Al:Al,Co,Cr}$	+0.5 × *LAL2COCR*	Present work
	${}^0L^{B2}_{Al,Co,Cr:Co} = {}^0L^{B2}_{Co:Al,Co,Cr}$	+0.5 × *LALCO2CR*	Present work
	${}^0L^{B2}_{Al,Co,Cr:Cr} = {}^0L^{B2}_{Cr:Al,Co,Cr}$	+0.5 × *LALCOCR2*	Present work
sigma (σ) phase: $(Al,Co)_8$ $(Al,Co,Cr)_{18}$ $(Cr)_4$	${}^0G^{\sigma}_{Al:Al:Cr}$	+161148	Present work
	${}^0G^{\sigma}_{Al:Cr:Cr}$	+47886	Present work
	${}^0G^{\sigma}_{Co:Co:Cr}$	–16899–29.814 × *T*	*Oikawa et al*.[17]
	${}^0G^{\sigma}_{Co:Cr:Cr}$	–259935 + 85.097 × *T*	*Oikawa et al*.[17]
	${}^0G^{\sigma}_{Al:Co:Cr}$	–617537	Present work
	${}^0G^{\sigma}_{Co:Al:Cr}$	–931862	Present work
	${}^0L^{\sigma}_{Co:Al,Cr:Cr}$	–195992	Present work
Function	**Value**		
LAL2COCR	0		Present work
LALCO2CR	–78970 + 89.123 × *T*		Present work
LALCOCR2	0		Present work

(*Continued*)

Table 5. (*Continued*)

Phase	Parameters	Values	References
LBCOCRMAL	28320–16.474 × *T*		Present work
LBCRALMCO	0		Present work
LBALCOMCR	–46432		Present work
L1BCOCRMAL	0		Present work
L1BCRALMCO	13276		Present work
L1BALCOMCR	0		Present work
GB2ALCO	–138500 + 34.620 × *T*		Dupin and Ansara [16]
LB2ALCO	54531–37.04 × *T*		Present work
GB2COCR	35909–16.474 × *T*		Present work
GB2CRAL	–4000		*Dupin et al*.[7]
BU1XY (X,Y = Al,Co,Cr)	–0.5 × *LB2XY*		Present work

Only A2, B2, and σ binary parameters are listed in full for their importance, all other binary parameters can be found in the respective binary Al-Co[16], Co-Cr[17], and Al-Cr[20] references as well as the attached database file. Parameters are in units of J/mol-formula.

doi:10.1371/journal.pone.0121386.t005

previous as well as present experimental studies. Overall, a consistent thermodynamic description of the Al-Co-Cr system is produced and its accuracy for predicting thermodynamic properties of all phases relevant for MCrAl-base coatings is confirmed.

Supporting Information

S1 Dataset. Thermodynamic database for the Al-Co-Cr system. This dataset contains the models and parameters built using Thermo-Calc for the Al-Co-Cr alloy system in text format. (TXT)

Acknowledgments

Computing clusters LION and Cyberstar are provided by the Materials Simulation Center and the Research Computing and Cyberinfrastructure Group at the Pennsylvania State University. Additionally, this work used the Extreme Science and Engineering Discovery Environment (XSEDE), which is supported by National Science Foundation grant number ACI-1053575. We would like to also thank Dr. Yi Wang and Richard Otis for stimulating discussions about the computational aspects of this work.

Author Contributions

Conceived and designed the experiments: XLL TG BG ZKL. Performed the experiments: XLL TG. Analyzed the data: XLL TG BL GL BG ZKL. Contributed reagents/materials/analysis tools: TG BG ZKL. Wrote the paper: XLL TG BL GL BG ZKL. Implementing the thermodynamic model: BL.

References

1. Wood JH, Goldman E, in Sims CT, Stoloff NSWCH. Superalloys II. 2nd ed. New York, NY: Wiley-Interscience; 1987.
2. Reed RC. The Superalloys. 1st ed. Cambridge, UK: Cambridge University Press; 2006.
3. Goward GW. Progress in coatings for gas turbine airfoils. Surf Coatings Technol. 1998 Oct; 108–109:73–9.

4. Clarke DR, Levi CG. Materials Design for the Next Generation Thermal Barrier Coatings. Annu Rev Mater Res. 2003; 33:383–417.
5. Darolia R. Thermal barrier coatings technology: critical review, progress update, remaining challenges and prospects. Int Mater Rev. 2013 Aug 18; 58(6):315–48.
6. Evans AG, Mumm DR, Hutchinson JW, Meier GH, Pettit FS. Mechanisms controlling the durability of thermal barrier coatings. Prog Mater Sci. 2001 Jan; 46(5):505–53.
7. Dupin N, Ansara I, Sundman B. Thermodynamic Re-Assessment of the Ternary System Al-Cr-Ni. Calphad. 2001; 25(2):279–98.
8. Kattner UR. Construction of a Thermodynamic Database for Ni-Base Superalloys: A Case Study. TMS: CALPHAD and Alloy Thermodynamics. 2002.
9. Achar DRG, Munoz-Arroyo R, Singheiser L, Quadakkers WJ. Modelling of phase equilibria in MCrAlY coating systems. Surf Coatings Technol. 2004 Oct; 187(2–3):272–83.
10. Toscano J, Gil A, Hüttel T, Wessel E, Naumenko D, Singheiser L, et al. Temperature dependence of phase relationships in different types of MCrAlY-coatings. Surf Coatings Technol. 2007 Dec; 202(4–7):603–7.
11. Nicholls JR. Designing oxidation-resistant coatings. JOM. 2000 Jan; 52(1):28–35.
12. Wright IG, Gibbons TB. Recent developments in gas turbine materials and technology and their implications for syngas firing. Int J Hydrogen Energy. 2007 Nov; 32(16):3610–21.
13. Ishikawa K, Ise M, Ohnuma I, Kainuma R, Ishida K. Phase Equilibria and Stability of the BCC Aluminide in the Co-Cr-Al System. Ber Bunsenges Phys Chem. 1998; 102:1206–10.
14. Liu Z-K. First-Principles Calculations and CALPHAD Modeling of Thermodynamics. J Phase Equilibria Diffus. 2009 Sep 3; 30(5):517–34.
15. Dupin N. Contribution à l'évaluation thermodynamique des alliages polyconstitués à base de nickel (Ph.D. Thesis). INP Grenoble; 1995.
16. Dupin N, Ansara I. Thermodynamic Assessment of the System Al-Co. Rev Métallurgie. 1998; 95 (9):1121–9. PMID: 21267112
17. Oikawa K, Qin G-W, Ikeshoji T, Kainuma R, Ishida K. Direct evidence of magnetically induced phase separation in the fcc phase and thermodynamic calculations of phase equilibria of the Co–Cr system. Acta Mater. 2002 May; 50(9):2223–32.
18. Havrankova J, Vrestal J, Tomiska J. Mass-spectrometric determination of thermodynamic properties of liquid Co-Cr alloys. Kov Mater. 1999; 37:34–41.
19. Yang S, Jiang M, Li H, Liu Y, Wang L. Assessment of Co-Cr-Ni ternary system by CALPHAD technique. Rare Met. 2012 Jan 26; 31(1):75–80.
20. Ansara I, Dinsdale AT, Rand MH. COST 507: Definition of Thermochemical and Thermophysical Properties to Provide a Database for the Development of New Light Alloys—Thermochemical Database for Light Metal Alloys—Volume 2. Luxembourg: Office for Official Publications of the European Communities; 1998.
21. Helander T, Tolochko O. An Experimental Investigation of Possible B 2-Ordering in the Al-Cr System. J Phase Equilibria. 1999; 20(March 1998):57–60.
22. Dinsdale AT. SGTE data for pure elements. Calphad. 1991 Oct; 15(4):317–425.
23. Redlich O, Kister AT. Algebraic Representation of Thermodynamic Properties and the Classification of Solutions. Ind Eng Chem. American Chemical Society; 1948 Feb 1; 40(2):345–8.
24. Hillert M, Jarl M. A Model for Alloying Effects in Ferromagnetic Metals. Calphad. 1978 Jan; 2(3):227–38.
25. Inden G. The role of magnetism in the calculation of phase diagrams. Phys B+C. 1981 Jan; 103(1):82–100.
26. Dupin N, Ansara I. On the sublattice formalism applied to the B2 phase. Zeitschrift für Met. 1999; 90:76–85. doi: 10.1107/S0108767309007235 PMID: 19349661
27. Sundman B, Ohnuma I, Dupin N, Kattner UR, Fries SG. An assessment of the entire Al–Fe system including D03 ordering. Acta Mater. 2009 Jun; 57(10):2896–908.
28. Hillert M. The compound energy formalism. J Alloys Compd. 2001 May; 320(2):161–76.
29. Joubert J-M. Crystal chemistry and Calphad modeling of the [sigma] phase. Prog Mater Sci. 2008 Mar; 53(3):528–83.
30. Andersson J-O, Helander T, Höglund L, Shi P, Sundman B. Thermo-Calc & DICTRA, computational tools for materials science. Calphad. 2002 Jun; 26(2):273–312.

31. Jansson B. Evaluation of parameters in thermochemical models using different types of experimental data simultaneously. Technical Report TRITAMAC-0234. Stockholm, Sweden; 1984.
32. Shang SL, Wang Y, Kim D, Liu Z-K. First-principles thermodynamics from phonon and Debye model: Application to Ni and Ni3Al. Comput Mater Sci. 2010 Feb; 47(4):1040–8.
33. Wang Y, Liu Z-K, Chen L-Q. Thermodynamic properties of Al, Ni, NiAl, and Ni3Al from first-principles calculations. Acta Mater. 2004 May; 52(9):2665–71.
34. Birch F. Finite Elastic Strain of Cubic Crystals. Phys Rev. American Physical Society; 1947 Jun 1; 71 (11):809–24.
35. Zacherl CL, Shang S-L, Saengdeejing A, Liu Z-K. Phase stability and thermodynamic modeling of the Re-Ti system supplemented by first-principles calculations. Calphad. 2012 Sep; 38:71–80.
36. Liu XL, Hargather CZ, Liu Z-K. First-principles aided thermodynamic modeling of the Nb–Re system. Calphad. Elsevier; 2013 Jun; 41:119–27.
37. Alers GA. Use of Sound Velocity Measurements in Determining the Debye Temperature of Solids. Physical Acoustics: Volume 3 Part B. 1965. p. 1–42.
38. Chen Q, Sundman B. Calculation of Debye Temperature for Crystalline Structures—A Case Study on Ti, Zr, and Hf. Acta Mater. 2001; 49:947–61.
39. Lu X-G, Selleby M, Sundman B. Calculations of thermophysical properties of cubic carbides and nitrides using the Debye–Grüneisen model. Acta Mater. 2007 Feb; 55(4):1215–26.
40. Shang SL, Wang Y, Liu Z-K. First-principles elastic constants of α- and θ-Al2O3. Appl Phys Lett. 2007 Mar 7; 90(10):101909.
41. Zunger A, Wei S-H, Ferreira LG, Bernard JE. Special quasirandom structures. Phys Rev Lett. 1990 Jul 16; 65(3):353–6. PMID: 10042897
42. Jiang C, Wolverton C, Sofo J, Chen L-Q, Liu Z-K. First-principles study of binary bcc alloys using special quasirandom structures. Phys Rev B. 2004 Jun 28; 69(21):214202.
43. Jiang C. First-principles study of ternary bcc alloys using special quasi-random structures. Acta Mater. 2009 Sep; 57(16):4716–26.
44. Jiang C, Chen L-Q, Liu Z-K. First-principles study of constitutional point defects in B2 NiAl using special quasirandom structures. Acta Mater. 2005 May; 53(9):2643–52.
45. Lieser AC, Zacherl CL, Saengdeejing A, Liu Z-K, Kecskes LJ. First-principles calculations and thermodynamic re-modeling of the Hf-W system. Calphad. 2012 Sep; 38:92–9.
46. Kresse G, Furthmüller J. Efficient iterative schemes for ab initio total-energy calculations using a plane-wave basis set. Phys Rev B. 1996 Oct 15; 54(16):11169–86. PMID: 9984901
47. Blöchl PE. Projector augmented-wave method. Phys Rev B. 1994 Dec 15; 50(24):17953–79. PMID: 9976227
48. Kresse G, Joubert D. From ultrasoft pseudopotentials to the projector augmented-wave method. Phys Rev B. 1999 Jan 15; 59(3):1758–75.
49. Perdew J, Burke K, Ernzerhof M. Generalized Gradient Approximation Made Simple. Phys Rev Lett. 1996 Oct 28; 77(18):3865–8. PMID: 10062328
50. Kresse G, Marsman M, Furthmüller J. VASP: The Guide. Wein, Austria; 2013.
51. Methfessel M, Paxton AT. High-precision sampling for Brillouin-zone integration in metals. Phys Rev B. American Physical Society; 1989 Aug 15; 40(6):3616–21. PMID: 9992329
52. Blöchl PE, Jepsen O, Andersen OK. Improved tetrahedron method for Brillouin-zone integrations. Phys Rev B. 1994 Jun 15; 49(23):16223–33. PMID: 10010769
53. Wang Y, Curtarolo S, Jiang C, Arroyave R, Wang T, Ceder G, Chen LQ, Liu ZK. Ab initio lattice stability in comparison with CALPHAD lattice stability. Calphad. 2004 Mar; 28(1):79–90.
54. Shang SL, Saengdeejing A, Mei ZG, Kim DE, Zhang H, Ganeshan S, et al. First-principles calculations of pure elements: Equations of state and elastic stiffness constants. Comput Mater Sci. 2010 Jun; 48 (4):813–26.
55. Dickins GJ, Douglas a. MB, Taylor WH. The crystal structure of the Co–Cr σ phase. Acta Crystallogr. 1956 Mar 1; 9(3):297–303.
56. Kittel C. Introduction to Solid State Physics. Wiley; 1995.
57. Kamm GN, Alers G a. Low-Temperature Elastic Moduli of Aluminum. J Appl Phys. 1964; 35(2):327.
58. Mori N. Magnetic Contribution to the Bulk Modulus of 3d Transition Metals and Alloys. Phys B. 1988; 149:226–31.
59. Moruzzi VL, Marcus PM. Antiferromagnetism in 3d Transition Metals. Phys Rev B. 1990; 42(13):8361–6. PMID: 9995009

60. Hafner R, Spišák D, Lorenz R, Hafner J. Magnetic ground state of Cr in density-functional theory. Phys Rev B. 2002 May; 65(18):184432.

61. Mehl MJ, Osburn JE, Papaconstantopoulos DA, Klein BM. Structural properties of ordered high-melting-temperature intermetallic alloys from first-principles total-energy calculations. Phys Rev B. 1990 May; 41(15):10311–23. PMID: 9993438

62. Hammer L, Blum V, Schmidt C, Wieckhorst O, Meier W, Müller S, et al. Role of Co antisite segregation in the CoAl(111) surface. Phys Rev B. 2005 Feb; 71(7):075413.

63. Liu XL, VanLeeuwen BK, Shang SS-L, Du Y, Liu Z-K. On the scaling factor in Debye-Grüneisen model: A case study of the Mg-Zn binary system. Comput Mater Sci. 2015 Feb; 98:34–41.

64. Stein F, He C, Dupin N. Melting behaviour and homogeneity range of B2 CoAl and updated thermodynamic description of the Al–Co system. Intermetallics. 2013 Aug; 39:58–68.

65. Pavl J, Vřeš ál J, Šob M. Ab initio study of formation energy and magnetism of sigma phase in Cr–Fe and Cr–Co systems. Intermetallics. 2010 Feb; 18(2):212–20.

66. Bell HB, Hajra JP, Putland FH, Spencer PJ. The Determination of the Thermodynamic Properties of Cobalt–Chromium Alloys Using Solid-Electrolyte EMF and High-Temperature Calorimetric Techniques. Met Sci. 1973 Jan; 7(1):185–90.

67. Downie DB, Arslan F. Enthalpies of formation of (cobalt + chromium) alloys at 473 K. J Chem Thermodyn. 1983 Jul; 15(7):645–9.

68. Moskvitina ES, Kuznetsov VN, Guzei LS. Refinement of the Co-Cr-Al Phase-Diagram. Vestn Mosk Univ Seriya 2 Khimiya (Moscow Univ Chem Bull). 1992; 33(4):373–4.